CO_2 Mobility Control with Foam for Enhanced Oil Recovery and Associated Storage

Multi-scale Approach for Field Application

by

Mohan Sharma

Thesis submitted in fulfilment of
the requirements for the degree of
PHILOSOPHIAE DOCTOR
(PhD)

University of
Stavanger

Faculty of Science and Technology
Institute of Energy Resources
2019

Summary

The sustainable development scenario envisioned by the international organizations and government agencies incorporates two key elements — access to affordable and clean energy to all, and substantial decline in greenhouse gases emission to achieve objectives of Paris Agreement adopted in December 2015. According to a report issued by the U.S. Energy Information Administration, the world energy consumption is expected to increase by 30% from now until 2040. Out of all energy sources, oil will remain the largest source of energy, providing one-third of the world's energy demand through this projection period. Since the oil production from the developed fields will decline in future, it becomes imperative to implement technologies to enhance oil recovery beyond primary and secondary development stages.

Carbon dioxide (CO_2) has been commercially used for Enhanced Oil Recovery (EOR) for nearly five decades in onshore fields in the USA. Some of these projects are still operational with additional oil recovery ranging between 15 to 20% of oil initially in-place. In addition, CO_2 storage in geologic formations via CO_2 utilization for EOR offers safe and long term storage, and is considered as one of the best alternatives for dealing with carbon emissions. At the end of the CO_2 EOR project when the operation becomes uneconomic and the field is decommissioned, effectively all of the CO_2 that was purchased during the project life gets stored incidentally. While EOR projects treat CO_2 as an additional cost, the operators may receive carbon credits or other types of subsidies for CO_2 storage, making CO_2 EOR economically more attractive than other geologic storage options such as injecting in aquifers and depleted reservoirs.

The industry has a proven track record of safely injecting CO_2 into geologic formations, and it is well understood that CO_2 EOR can add value by increasing oil recovery while reducing carbon emissions.

However, based on the knowledge gained from field-scale projects, it has been realised that a substantial volume of reservoir remains unswept during CO_2 floods leading to poor performance.

Foam, which is generated using a surfactant, has the potential to overcome the challenges of unstable displacement during CO_2 injection. A few field pilots have been performed in past. However, only limited information is available to de-risk the technology for implementation in a high-cost and high-risk environment such as Norwegian Continental Shelf. An international collaboration has been setup between universities and oil companies to perform two field pilots to advance the technology of using foam as mobility control agent for CO_2 EOR, with a focus on integrated reservoir modelling to assist technology transfer to other fields.

This thesis investigates the mechanisms involved in CO_2-Foam displacement, at both small and large scales, for one of the pilots in a carbonate reservoir. The thesis builds upon six scientific papers that present the aspects of a multi-scale approach, and integrate findings from studies performed at pore-scale, core-scale and field-scale. The first step was to obtain a guesstimate of the pilot performance for early evaluation of the concept and qualifying the reservoir for field trial. Paper I provides an overview of laboratory studies performed with analogue core material and reservoir modelling performed with limited field data. A list of uncertainties was generated based upon discussions with the stakeholders. A pilot is typically designed to reduce these uncertainties for scale-up to field-wide implementation. The study confirmed value addition by foam to the ongoing CO_2 injection. The initial cost estimate based upon this study was found acceptable by the field operator to proceed to the next stage of detailed design.

A pore-scale study was then performed to evaluate CO_2-Foam performance in silicon-wafer micromodels, as presented in Paper II. In-situ foam generation and flow diversion was observed under dynamic

conditions, while long-term foam stability was quantified under static conditions based on findings from experiment running over three days.

The findings from the initial study were used to guide pilot area selection and experiments' design as described in Paper III. The experiments were performed with reservoir core materials to obtain foam model parameters, using a surfactant concentration of 0.5wt% and foam quality of 0.7 which was found most optimal for field application. Additional coreflood experiments were performed, using co-injection and surfactant-alternating-gas (SAG) slugs, to further investigate the choice of injection strategy as presented in Paper IV. Core-scale simulations were run to validate waterflood and CO_2-Foam EOR experiments, using best estimates for relative permeability for different phases and foam model parameters, which were used further in a 3D reservoir model for the pilot area.

In order to understand the large-scale foam behaviour, it is paramount that an appropriate field data acquisition program is planned to get right data. Baseline surveys were discussed with the field operator and are being conducted, which are outlined in Paper V. The baseline data collection program includes injection profiling, pressure fall-off test and an interwell tracer test. It is planned to repeat these surveys after the pilot. In addition surface rates and injection pressure will be monitored to assess the pilot performance.

Fit-for-purpose reservoir modelling and simulation techniques were used to generate a 3D reservoir model for the pilot area which was calibrated to historical production data. A workflow was developed to obtain a revised estimate of uncertainties in the model, which is explained in Paper VI. The initial geologic model was calibrated to 40 years of waterflood and over four years CO_2 injection data. The history match quality was verified by comparing the model response to observed data for injection profiles and interwell tracer test, which were not included in the history matching cycle. The future reservoir management plans

and surface operations were discussed with the operator, and the pilot performance prediction was revised subject to changes since the initial study (Paper I). The findings from relevant laboratory studies were analysed. The uncertainties in foam model parameter were coupled with reservoir model's uncertainties to obtain reliable forecast for the pilot performance in terms of distributions for key performance indicators such as cumulative oil production and CO_2 retention. SAG with 10 days of surfactant injection and 20 days of CO_2 injection was found most appropriate for field application, with possibility of revision based upon the initial pilot response. The pilot is planned to begin Q1 2019. The data obtained from the pilot will be used to further calibrate the model using the workflow mentioned earlier, and improve our understanding about large-scale foam displacement.

Acknowledgements

Mohan Sharma

List of Publications

I. **Sharma, M.**, Alcorn, Z.P., Fredriksen, S.B., Fernø, M.A., Graue, A. 2017. Numerical Modelling Study for Designing CO_2-Foam Field Pilot. EAGE 19th European Symposium on Improved Oil Recovery, Stavanger, Norway, 24-27 April.

   Accepted for publication in *Petro-physics and Rock Physics of Carbonate Reservoirs*, Springer Nature Singapore.

II. Rognmo, A.U., Fredriksen, S.B., Alcorn, Z.P., **Sharma, M.**, Føyen, T.L., Eide, Ø., Graue, A., Fernø, M.A. 2018. Pore-to-Core EOR Upscaling for CO_2-Foam for CCUS. SPE EUROPEC 80th EAGE Annual Conference and Exhibition, Copenhagen, Denmark, June 11-14.

   Accepted for publication in *SPE Journal*.

III. Alcorn, Z.P., Fredriksen, S.B., **Sharma, M.**, Rognmo, A.U., Føyen, T.L., Fernø, M.A., Graue, A. 2018. An Integrated CO_2 Foam EOR Pilot Program with Combined CCUS in an Onshore Texas Heterogeneous Carbonate Field. SPE IOR Symposium, Tulsa, Oklahoma, USA, April 14-18.

   Accepted for publication in *SPE Reservoir Evaluation and Engineering*.

IV. Fredriksen, S.B., Alcorn, Z.P., **Sharma, M.**, Wergeland, C., Fernø, M.A., Graue, A., Ersland, G. 2018. Core-Scale Sensitivity Study of CO_2 Foam Injection Strategies for Mobility Control, Enhanced Oil Recovery and CO_2 Storage.

   Submitted for publication.

V.   Alcorn, Z.P., **Sharma, M.**, Fredriksen, S.B., Rognmo, A.U., Fernø, M.A., Graue, A. 2018. CO_2 Foam Field Pilot Test for EOR and CO_2 Storage in a Heterogeneous Carbonate Reservoir: Operational Design, Data Collection and Pilot Monitoring Program. EAGE 80th Annual Conference and Exhibition, Copenhagen, Denmark, 11-14 June.

To be submitted for publication.

VI. **Sharma, M.**, Alcorn, Z.P., Fredriksen, S.B., Rognmo, A.U., Fernø, M.A., Skjæveland, S.M., Graue, A. 2019. Model Calibration for Forecasting CO_2-Foam EOR Field Pilot Performance in a Carbonate Reservoir.

Submitted for publication.

This thesis is based on the above six papers.

Additional Publications

I. **Sharma, M.**, Taware, S.V. and Datta-Gupta, A. 2016. Optimizing CO_2 Floods Using Rate Control with Smart Wells Under Geologic Uncertainty. SPE Abu Dhabi International Petroleum Exhibition & Conference, Abu Dhabi, UAE, 7-10 November.

II. Taware, S.V., Alhuthali, A.H., **Sharma, M.**, Datta-Gupta, A. 2016. Optimal rate control under geologic uncertainty: Waterflood and EOR processes. *Optimization and Engineering* **18** (1), 63-86.

III. Alcorn, Z.P., **Sharma, M.**, Fredriksen, S. B., Fernø, M.A., and Graue, A. 2017. CO_2 Foam EOR Field Pilot: Pilot Design, Geologic and Reservoir Modelling, Laboratory Investigations, and Application of a Reservoir Management Workflow. EAGE 19th European Symposium on Improved Oil Recovery, Stavanger, Norway, 24-27 April.

Other Disseminations

I. **Sharma, M.**, Fernø, M.A., Skjæveland, S.M., Graue, A. 2016. CO_2 Foam EOR Field Pilots. Poster presentation at IOR Norway 2016.

II. **Sharma, M.**, Alcorn, Z.P., Fredriksen, S.B., Rognmo, A.U., Fernø, M.A., Skjæveland, S.M., Graue, A. 2017. CO_2-Foam EOR Field Pilot in an Onshore Carbonate Reservoir. Seminar at Department of Geoscience & Engineering, TU Delft.

Table of Contents

Table of Figures

xvii

xviii

List of Tables

Nomenclature and Abbreviations

Nomenclature

epcap	Parameter to capture shear-thinning behavior in low quality regime
epdry	Parameter controlling the abruptness of foam collapse
epoil	Parameter controlling the effect of oil saturation
epsurf	Parameter controlling the effect of surfactant concentration
fmcap	Parameter set to smallest capillary number expected in simulation
fmdry	Water saturation in vicinity of which foam collapses
fmmob	Reference gas mobility-reduction factor for foam
fmoil	Reference high oil saturation for foam collapse
fmsurf	Reference surfactant concentration
Kh	Permeability-thickness
k	Permeability
s	Skin factor
f_g	Foam quality
f_g^*	Foam quality at transition between low and high qualities
f_g^+	Limiting Capillary Pressure
k_{rg}^{nf}	Gas relative permeability without foam
k_{rg}^{f}	Gas relative permeability with foam
k_{rg}^{0}	Gas end-point relative permeability
k_{rog}^{0}	Oil end-point relative permeability in presence of gas
k_{row}^{0}	Oil end-point relative permeability in presence of water (no gas)
k_{rw}^{0}	Water end-point relative permeability
k_{rog}	Oil relative permeability in presence of gas
k_{row}	Oil relative permeability in presence of water (no gas)
k_{rg}	Gas relative permeability
k_{rw}	Water relative permeability
N_c	Capillary number
n_g	Corey exponents to gas
n_{og}	Corey exponents to oil in presence of gas and connate water
n_{ow}	Corey exponent to oil in presence of water
n_w	Corey exponent for water
Pc*	Limiting Capillary Pressure
q_g	Gas flow rate
q_w	Water flow rate
r_o	Pressure equivalent radius of a grid

r_w	Wellbore radius
S_g	Gas saturation
S_{gcon}	Connate gas saturation
S_l	Liquid saturation
S_{org}	Residual oil saturation to gas
S_{orw}	Residual oil saturation to water
S_{wcon}	Connate water saturation
S_w	Water saturation
S_w^*	Water saturation at transition between low and high qualities
u_t	Total velocity
∇P	Pressure gradient
σ	Interfacial tension
μ	Viscosity
v	Velocity

Abbreviations

CCUS	Carbon capture, utilization and storage
CO_2	Carbon dioxide
EOR	Enhanced oil recovery
ES	Evolution strategy
ft/d	feet per day
Gt	Gigatonnes
HCPV	Hydrocarbon pore volume
HQ	High-quality
KPI	Key performance indicator
LHC	Latin hypercube
LQ	Low-quality
Mscfd	Thousand standard cubic feet per day
MMP	Minimum Miscibility Pressure
MP	Mismatch parameter
MPG	Minimum Pressure Gradient
MPZ	Main producing zone
MRF	Mobility reduction factor
NPD	Norwegian Petroleum Directorate
OIIP	Oil Initially In-Place
PB	Plackett-Burmann
PIMULT	Productivity (Injectivity) index multiplier
psi	pound per square inch
PV	Pore volume

PVT	Pressure Volume Temperature
ROZ	Residual oil zone
SAG	Surfactant alternating gas
SCAL	Special core analysis
Sm^3	Standard cubic metre
STB/D	Stock tank barrels per day
UP	Uncertainty parameter
VRR	Voidage replacement ratio
WAG	Water alternating gas
Wt %	Weight percent

Part 1

1   Introduction

1.1   Motivation

According to a report issued by the U.S. Energy Information Administration, the world energy consumption is expected to rise by 30% from now until 2040. Most of this increase in energy demand is anticipated to come from non-OECD countries especially China and south Asia, because of growing population and strong economic growth. The industrial sector, which includes mining, manufacturing, agriculture and construction, will account for more than 50% over this projection period. Although renewable energy and nuclear power are the fastest growing forms of energy, fossil fuels are expected to continue meeting most of world's energy demand until 2040. Out of all the fossil fuels, oil will remain the largest source of energy, providing one-third of the world's energy demand through the projection period. With a decline in oil production from existing fields lying between 4 to 12% annually, it becomes imperative to continue discovering large oil reservoirs, and implement technologies to enhance oil recovery from existing fields.

On the other hand, dependence upon fossil fuels has led to a rapid increase in carbon dioxide (CO_2) emissions since the industrial revolution, which has disrupted the global carbon cycle. The signs of global warming and climate change are becoming more pronounced around the world. In case of no action, the global temperature is expected to rise by 4.5°C above the pre-industrial temperature level. This would result in physical and ecological problems such as extreme weather events, sea-level rise, disrupted water supply and food shortage. The world nations adopted a goal to limit warming to well below 2°C and to pursue efforts to limit the temperature increase to no more than 1.5°C, at United Nations Climate Change conference 2015 held in Paris.

CO_2 has been successfully used for Enhanced Oil Recovery (EOR) in fields resulting in an additional oil recovery between 15 to 20% of oil

initially in-place (OIIP). In addition, at the end of the CO_2 EOR project when the operation becomes uneconomic and the field is decommissioned, effectively all of the CO_2 purchased during the project life gets stored incidentally. CO_2 EOR is likely the first and most economic option for addressing the concern of climate change, until other technologies develop further and become more viable.

CO_2 EOR technology has evolved significantly over last five decades. A large number of commercial CO_2 floods have been operated since the first CO_2 injection in SACROC Unit in 1972 (Merchant 2010). Some of these projects are still operational with CO_2 injection reaching over 80% hydrocarbon pore volume (HCPV), with a few mature CO_2 floods exceeding 500% HCPV. Based on the knowledge gained from these field-scale projects, it has been realised that the sweep efficiency in field is lower than that observed in laboratory, owing to low density and viscosity of CO_2, and reservoir heterogeneity. This results in viscous fingering, gravity segregation and poor sweep (Jarrell et al. 1990). Several technologies have been tested to improve CO_2 flood performance including gel or polymer treatment (Enick et al. 2012), cementing for zonal isolation, alternating CO_2 injection with water, and smart completions with inflow control valves (Sharma et al. 2016), with limited to moderate success for in-depth mobility control.

The laboratory studies confirm the viability of foam for CO_2 mobility control away from the injector. Previous field trials with foam (Heller et al. 1985, Holm and Garrison 1988, Jonas et al. 1990, Chou et al. 1992, Hoefner and Evans 1995, Harpole and Hallenbeck 1996, Sanders et al. 2012, Mukherjee et al. 2016) have demonstrated the benefits of this technology to variable extent, with some meeting all planned objectives. However, the displacement mechanisms with foam are still not well understood at larger scales. Therefore, two field trials have been planned to test the effectiveness of foam in enhancing oil recovery and increasing CO_2 retention at field scale.

1.2 Research Goals

According to a study conducted by the Norwegian Petroleum Directorate (NPD) in 2017, 27 of the largest fields on Norwegian Continental Shelf (NCS) will contain about 2000 million Sm^3 residual oil after water injection. The technical potential for EOR was evaluated for these 27 fields, and the solution with the biggest potential for each field was chosen. It was found that NCS has a huge EOR potential of 320–860 million Sm^3, with a base estimate of 592 million Sm^3 additional oil recovery (Figure 1). The recovery with gas injection, including both CO_2 and hydrocarbon gases, exceeds that for Low salinity/polymer flooding, which is ranked highest in terms of EOR potential for NCS (Figure 2).

Foam has the ability to overcome the challenges of unstable displacement during CO_2 and hydrocarbon gas injection which limits the EOR potential (Heller 1994). It has however been realised that further field trials with foam are needed to quantify the benefits of the technology, and understand the full value chain. Almost all previous field trials with foam have been done onshore because of relatively lower cost, smaller well spacing and higher injectant availably. Therefore, as a precursor to an offshore field trial on NCS, it was decided to perform field trials onshore in the USA.
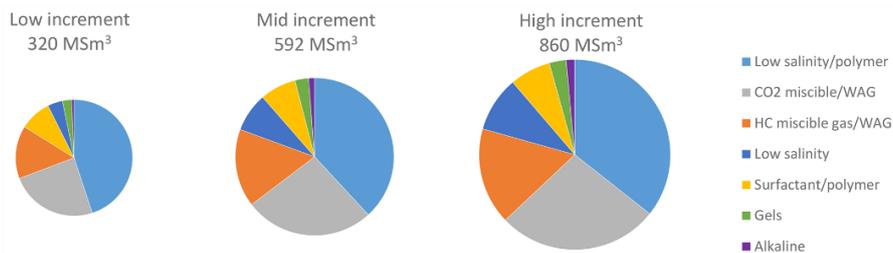
Figure 1: Relative contribution of EOR techniques for Low, Mid and High estimates of EOR potential on NCS. (Reference: NPD)
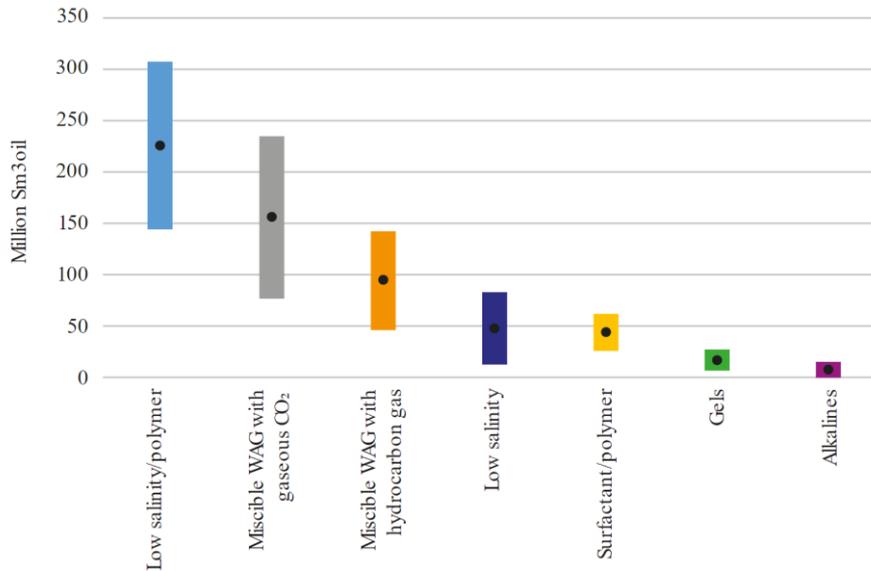
Figure 2: Mid-range estimates and uncertainty ranges for the methods included in the technical EOR potential study. (Reference: NPD)

An international collaboration has been setup between seven universities and five oil companies (headed by Petroleum and Process Technology Research Group at University of Bergen) to advance the technology of using foam as mobility control agent for CO_2 EOR. The field pilots that have been run so far have shown varying results, inferred mainly from interwell tracer studies and production data analysis. The focus of the ongoing collaboration is to use integrated reservoir modelling to assist technology transfer to high risk and high cost environment. The project involves understanding the mechanisms of CO_2-Foam displacement at small-scale by conducting relevant laboratory studies, and at large-scale by running field pilots in two heterogeneous reservoirs. Fit-for-purpose reservoir modelling and simulation techniques will be used to integrate data from different scales, and guide up-scaling of the governing displacement mechanisms from lab to field.

1.3   Thesis Outline

As a part of the overall project, it is planned to run pilot with foam in two fields in west Texas – a carbonate reservoir and a sandstone reservoir. This thesis focusses upon the modelling studies and data acquisition planning performed for the first pilot in the carbonate reservoir. The reservoir has been waterflooded for more than fifty years, and a significant part of it has been on continuous CO_2 injection for last five years. An inverted five-spot pattern, which had rapid CO_2 breakthrough in adjacent producers and is currently recycling significant amounts of CO_2, was selected for the field trial. The pilot is planned for two years with surfactant-alternating-gas injection in the first year, followed by continuous CO_2 injection in the second year. Integration of data from conventional and special core-scale injection studies, geological modelling and flow simulation, and results from pilot study will provide insights into understanding complex flow dynamics across multiple scales.

This thesis is divided into two parts. The first part summarizes the research, and consists of five chapters, each of which is divided into sub-sections. The remainder of the first part is organized as following:

- Chapter 2 reviews CO_2 EOR and associated storage, and foam flow in porous media.
- Chapter 3 focusses on the different elements of the scale-up process including laboratory studies, numerical studies and field data acquisition.
- Chapter 4 discusses the results obtained from the lab-scale and field-scale numerical modelling study.
- Chapter 5 contains the conclusions, and work plans for near future.

The second part consists of six papers which have been published or submitted to a journal.

2   Theory

2.1   CO₂ Injection

2.1.1   Enhanced Oil Recovery

The life of an oil field typically involves two stages — primary production, where oil is allowed to come up to surface from own pressure resulting in decline in field pressure; and secondary production, where pressure is maintained by injecting water to make up for the volume of oil produced. There are, however, two problems associated with waterflood:

- It has poor volumetric sweep efficiency, which means that water does not reach all parts of the reservoir.
- It has poor displacement efficiency, which means that water leaves behind oil trapped in pores in swept areas.

At the end of the waterflood, the residual oil exists as a discontinuous phase of droplets trapped by displacing water in a water-wet system. Waterfloding of an oil-wet system results in a different fluid distribution, where displacing water has entered a sufficient number of pore channels to stop oil flow in an oil-wet system at the end of the waterflood. The residual oil exists as a film around matrix grains, and may occupy entire pore space in the smaller flow channels. As shown in Figure 3, the residual oil can be mobilized by increasing the capillary number(N_c), which corresponds to the ratio of viscous to capillary forces (Lake et al. 2014):

$$N_c = \frac{k \, \nabla P}{\sigma} = \frac{v \, \mu}{\sigma} \qquad (2.1)$$

where k is permeability, ∇P is pressure gradient, σ is interfacial tension, v and μ are superficial velocity and viscosity of displacing phase,

respectively. The capillary number can be increased by either increasing viscous forces, or decreasing interfacial tension force.
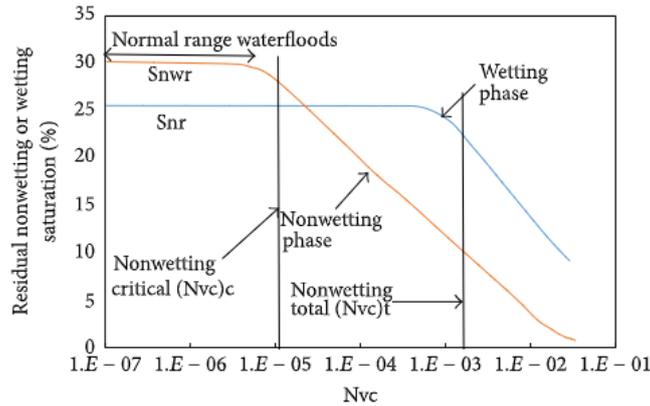
Figure 3: Capillary desaturation curve. (Reference: Green and Willhite 1998)

Enhanced oil recovery, the third stage in field life, addresses one or both of the problems associated with waterflood to recover residual oil. The EOR techniques are broadly divided into four categories — Chemical, Gas, Microbial and Thermal. Gas injection is a proven EOR technique, which relies on decreasing interfacial forces between the injected solvent (CO_2, hydrocarbon gases or N_2) and the residual oil. It has been seen from laboratory coreflood studies and field pilots that gas can displace oil efficiently where it sweeps bringing down the residual oil saturation from over 30% after waterflood to less than 10%, resulting in high displacement efficiency.

The microscopic sweep efficiency for gas injection depends on the extent to which the gas and oil phases are miscible i.e. form a single homogeneous phase when mixed in all proportions without an interface. Gas based EOR can therefore be grouped into two broad categories — miscible and immiscible, depending on reservoir pressure, temperature and oil properties. At a constant temperature, the lowest pressure at which miscibility occurs is defined as the minimum miscibility pressure (MMP). The miscible displacement, which occurs near or above MMP,

involves exchange of hydrocarbon components between oil and injected solvent. Gases such as ethane, propane and butane mix directly with reservoir oil without any multiphase behaviour, developing 'first-contact miscibility'. On the other hand, gases such as methane and CO_2 form a transition zone with oil (Figure 4), leading to 'multi-contact miscibility' through component exchanges.

At the point of complete miscibility, when the interfacial tension approaches zero, the injected solvent and the residual oil start to flow together as a single phase resulting in increase in volume of the combined oil-solvent phase relative to water phase. Under immiscible conditions, when reservoir pressure is significantly lower than MMP, the injected gas and oil do not form a single phase. The gas is however soluble in oil, which causes oil swelling and viscosity reduction helping recover additional oil under immiscible conditions. A miscible gas EOR process therefore achieves higher recovery than the immiscible process.
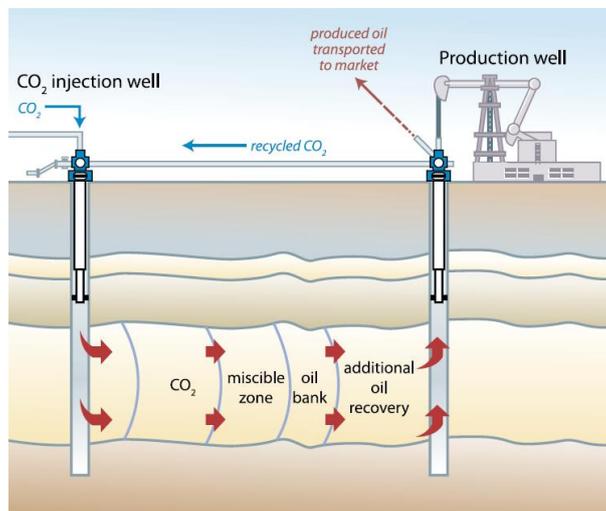
Figure 4: Enhanced oil recovery with CO_2 injection. (Reference: IPCC SR CCS)

When compared to other gases, CO_2 has more favourable properties for use as an EOR agent. It can extract heavier components upto C30 and expands oil to higher extent. CO_2 achieves miscibility at lower pressures,

allowing miscible injection in reservoirs at a depth greater than 800 m (2500 ft). Also, at those depths, supercritical CO_2 has liquid-like density which results in relatively less gravity segregation with respect to oil, and more efficient utilization of underground storage space.

From the field-scale CO_2 EOR projects, it has been realised that overall sweep is poor due to — areal and vertical reservoir heterogeneity; viscous instability due to low gas viscosity compared oil and water viscosities; and gravity override due to gas density lower than that for oil and water. Based on field data from various locations, a typical value for Dykstra-Parsons coefficient (Dykstra and Parsons 1950), which characterizes reservoir heterogeneity, is 0.75. For a 5-layer reservoir with equal layer thickness, this would correspond to permeabilities of 20, 50, 80, 170 and 680 mD, meaning that the highest permeability layer has conductivity 34 times that for lowest permeability layer. By itself, in homogeneous reservoir, viscous instability (gas displacing oil or water) leads to fingering and early gas breakthrough resulting in poor volumetric sweep. Viscous imbalance coupled with reservoir heterogeneity makes heterogeneity much worse. Because of lower density, gas rapidly moves to top of reservoir in homogeneous reservoirs. Even though heterogeneity makes effect of gravity less severe, it usually is a concern for EOR depending upon reservoir geology, well spacing and well completions.

2.1.2 Associated Storage

Because of additional costs involved in purchasing CO_2, the field-scale CO_2 injection is designed as a closed loop system (Figure 5). After breakthrough, the CO_2 that gets produced back is separated from hydrocarbon and water, dried, compressed and re-injected. As the EOR project matures, the recycled CO_2 volumes increase while purchased CO_2 volumes decrease, along with drop in oil production rate. When the oil production (due to ongoing CO_2 injection) from a significant portion of the field becomes uneconomic, the operator tends to stop buying new

CO_2. The recycled CO_2 is allocated to remaining economic areas within the field. Once the oil production from the entire field becomes uneconomic, the wells are plugged and abandoned; and the project is stopped. As a result, effectively all of the CO_2 purchased during the project life gets stored in the reservoir, which is referred to as 'Associated' or 'Incidental' storage.
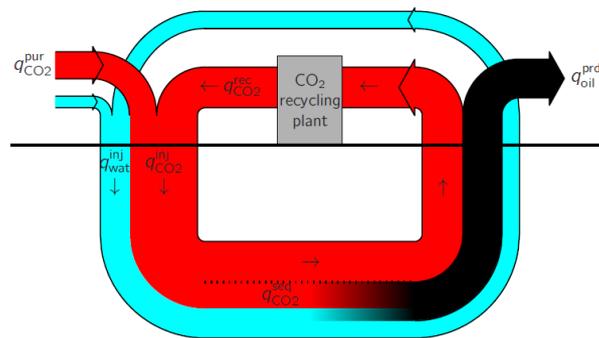
Figure 5: Fluid flows in a CO_2 EOR project. (Reference: Veld et al. 2013)

CO_2 storage in aquifers, in the context of carbon capture and storage (CCS), can be referred to as 'Non-Associated' storage to distinguish it from storing CO_2 through EOR, as both occur in geologic formations. The main differences between associated and non-associated storage are:

- Site characterisation: Availability of more well data and historical production data from primary and secondary stages of field development allows better design a CO_2 EOR project. The associated storage can be quantified with higher confidence through improved site characterisation.
- Pressure management: During CO_2 EOR, the operator strives to maintain a balance between the production and injection volumes, to keep reservoir pressure at a desired level. After CO_2 saturation and reservoir pressure have reached a desired level, the voidage replacement ratio (VRR) is maintained close to 1. Since non-associated storage does not involve any offsetting fluid production,

the reservoir pressure is expected to increase to fracture pressure much earlier. Mimicking oil production operations by drilling pressure relief wells for non-associated storage would only add to capital and operational cost with no revenues.

- Areal footprint: Since associated storage involves production of pre-existing reservoir fluids (typically hydrocarbon and brine), CO_2 gest access to far higher fraction of total pore space compared to that in non-associated storage. This means that a given quantity of CO_2 can be stored subsurface below a relatively smaller surface area with associated storage, which may make the logistics easier and overall operation economic.

Until late 1990s, naturally occurring underground CO_2 fields were the main source of CO_2 needed for EOR in the USA. Though an engineered storage solution is different from a natural accumulation, CO_2 injected at carefully selected site can be stored underground for long periods of time (up to 1000 years). For injection in aquifers, CO_2 gets trapped by a combination of following permanent storage mechanisms:

- Hydrodynamic / Structural / Stratigraphic trapping: CO_2 being less dense than formation brine, rises buoyantly until it encounters a seal that has a capillary entry pressure greater than the buoyancy or hydrodynamic force. As shown in Figure 6, the seal can be either a structural trap (anticline, fault) or strartigraphic trap (unconformity, change in rocktype, pinchout).
- Residual / Capillary trapping: During the counter-current flow of CO_2 and formation brine as CO_2 migrates up, a relatively more wetting phase enters the pores previously occupied by less-wetting CO_2 phase (Krevor et al. 2015). This results in a significant saturation of CO_2 becoming trapped as discontinuous immobile phase (Figure 7a).
- Solubility / Dissolution trapping: When CO_2 comes in contact with formation fluid, mass transfer occurs with CO_2 dissolving into water until an equilibrium state is reached (Figure 7b).

- Mineral trapping: The injected CO_2 dissolved in formation brine initiates geochemical reactions over longer period of time (Figure 8), which enables conversion of CO_2 into a stable mineral phase.
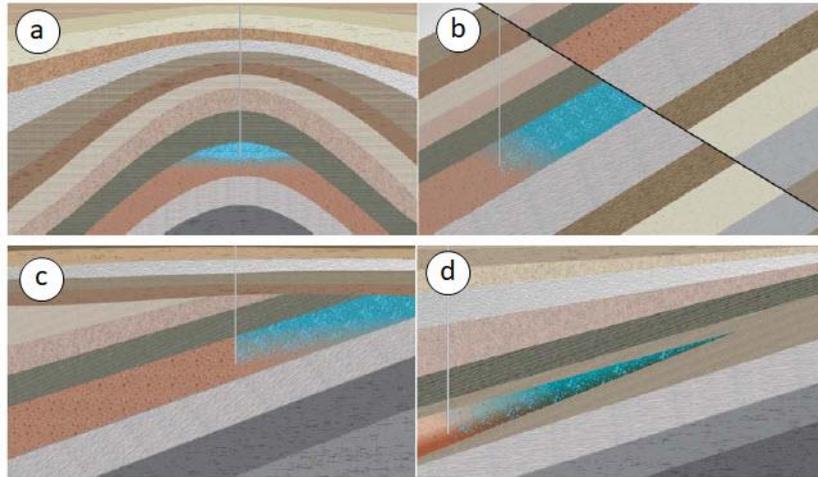
Figure 6: Structural and stratigraphic trapping (a) Anticline (b) Fault (c) Unconformity (d) Pinch-out (Reference: CO₂CRC)
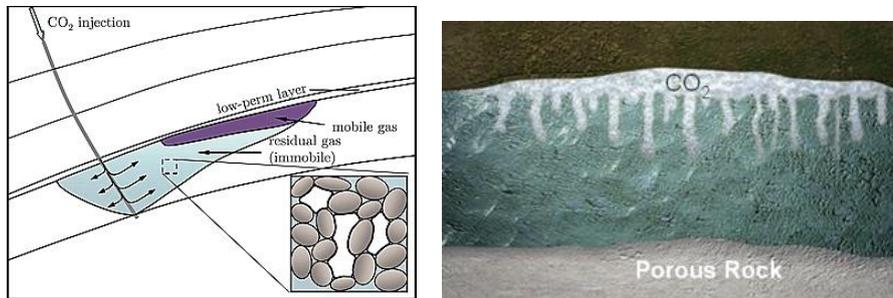
Figure 7: (a) Residual CO_2 left behind as the plume migrates upward during the post-injection period. (Reference: Juanes et al. 2006) (b) Solubility trapping.

Oil and gas fields, either producing or depleted, are good candidates for storage because the reservoirs have held hydrocarbons for millions of years; and seismic and well data can be used to quantify the storage potential. According to IPCC's Special Report on Carbon dioxide Capture and Storage, the discovered oil and gas fields worldwide have a storage capacity of approximately 675–900 Gt CO_2. In an active miscible

flood, CO_2 is retained i.e. not recycled due to — storage as supercritical CO_2, dissolution in inaccessible formation water, dissolution in inaccessible oil, adsorption to rock surface and loss outside of target reservoir volume.
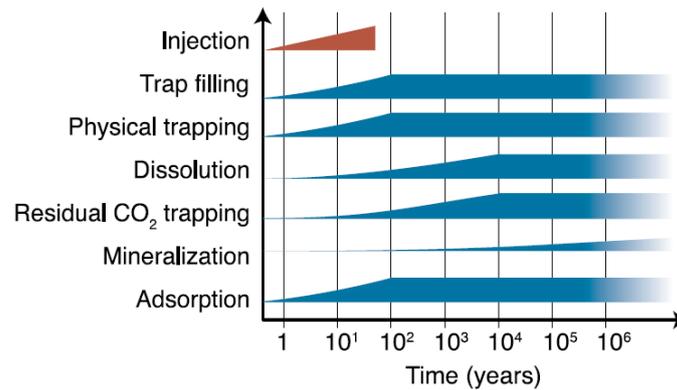
Figure 8: Time taken by various mechanisms to contribute to CO_2 trapping with respect to injection. (Reference: IPCC SR CCS)

2.2   Sweep Improvement with Foam

The causes of the poor sweep efficiency during EOR can be addressed by using foam (Bond and Holbrook 1958). Foam is a dispersion of gas in liquid, where gas gets trapped in bubbles that are separated by thin liquid films called 'lamellae', as shown in Figure 9. These lamellae are stabilized by adding 'surface active agent', referred to as surfactant, which can adsorb onto the gas/liquid interface. Two bubbles coming together have a thin water (soap) film between the two interfaces.

Foam can improve volumetric sweep by addressing all three limitations of Gas-based EOR:
- In heterogeneous formations, foam reduces mobility more in high permeability layers than in low permeability layers. This results in gas diversion to poorly swept or unswept regions in a reservoir. Foam also forms as gas moves upward through sharp permeability boundaries, and thus can address gravity segregation issue.

- All foams reduce gas mobility, and therefore reduces tendency of gas fingering through oil and water.
- Foam increases viscous pressure gradient in competition with gravity, and thereby increases the distance of three-phase zone around injector.
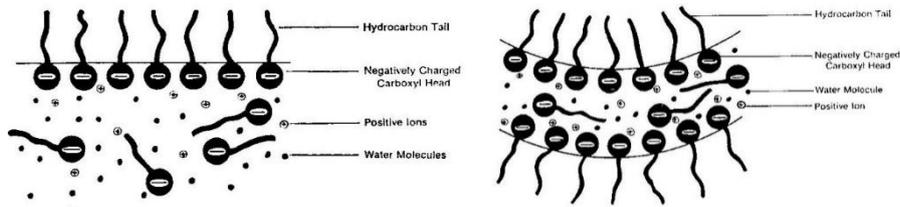
Figure 9: (a) Surfactant distribution at water-gas interface. (b) Thin film with two interfaces. (Reference: Isenberg 1992)

The direct effect of foam on microscopic sweep at reservoir scale, however, remains unresolved. The surfactant in foam reduces oil-water interfacial tension moderately, but not enough to mobilize residual oil. In laboratory, foam builds pressure gradients large enough to mobilize oil (Eq. 2.1). However, this large pressure gradient is difficult to achieve for field applications, and direct effect of foam on large-scale displacement efficiency requires further study. The additional oil recovery due to foam is therefore mostly attributed to improved volumetric sweep.

For CO_2 injection in an oil reservoir, the storage efficiency gets hampered due to CO_2 channelling through high permeability streaks or regions. Application of foam ensures CO_2 diversion into bulk of reservoir at moderate to low permeability, which improves associated CO_2 storage. CO_2 soluble surfactants may be used to keep the leakage paths blocked for a longer time, ensuring enhanced storage security. Also, it has been found from laboratory studies that foam mobilizes the water behind the foam front, allowing more room for CO_2 than in conventional injection schemes.

17

2.3   Foam Flow in Porous Media

2.3.1   Surfactant Chemistry

Surfactants are amphiphiles, where the prefix 'amphi' means dual and 'philos' means affinity. An amphiphilic substance consists of two parts:

- On one end, a polar group that contains heteroatoms such as O, S, P, or N, included in functional groups such as alcohol, thiol, ether, ester, acid, sulfate, sulfonate, phosphate, amine, amide etc.
- On the other end, an essentially apolar group which is in general an hydrocarbon chain of the alkyl or alkylbenzene type, sometimes with halogen atoms or a few non-ionized oxygen atoms.

The polar portion exhibits a strong affinity for polar solvents, particularly water, and it is often called hydrophilic part, whereas the apolar part is called hydrophobe or lipophilic. Because of its dual affinity, an amphiphilic molecule does not feel 'at ease' in any solvent, be it polar or non-polar, since there is always one of the two groups which does not like that environment. This is why amphiphilic molecules exhibit a strong tendency to migrate to interfaces and to orientate so that the polar group lies in water and the apolar group is placed out of it, and eventually in gas or oil (Figure 9).

The surfactants are classified based on their dissociation in water as:

- Anionic surfactants, which dissociate into an amphiphilic anion and a cation. They are the most commonly used surfactants. They include alkylbenzene sulfonates (detergents), (fatty acid) soaps, lauryl sulfate (foaming agent), di-alkyl sulfosuccinate (wetting agent), lignosulfonates (dispersants) etc. Anionic surfactants account for about 50 % of the world production.
- Cationic surfactants, which dissociate into an amphiphilic cation and an anion. These surfactants are more expensive than anionics, because of a high pressure hydrogenation reaction to be carried out during their synthesis. They are only used in when there is no

cheaper substitute, i.e. as positively charged substance which is able to adsorb on negatively charged substrates to produce antistatic.

- Zwitterionic surfactants, where a single surfactant molecule exhibit both anionic and cationic dissociations. These include synthetic products like betaines or sulfobetaines and natural substances such as amino acids and phospholipids.
- Non-ionic surfactants, which come as a close second to Anionic surfactants with about 45% of the overall industrial production. They do not ionize in water, because their hydrophilic group is of a non-dissociable type, such as alcohol, phenol, ether, ester, or amide. A large proportion of these nonionic surfactants are made hydrophilic by the presence of a polyethylene glycol chain, obtained by the polycondensation of ethylene oxide. As far as the lipophilic group is concerned, it is often of the alkyl or alkylbenzene type.

2.3.2 Foam Apparent Viscosity

Foam is not a new thermodynamic phase, and gas and liquid each retain their respective densities. The trapping of gas in separate bubbles reduces the mobility, which can be significant depending upon the proportion of stationary lamella (which completely block the flow of gas) and moving lamellae (Figure 10). A pressure drop is required to move individual lamella. The laboratory studies show that if multiple bubbles occupy a single pore, they would rapidly merge because of gas diffusion resulting in bubbles as large as the individual pore (Rossen 1996).
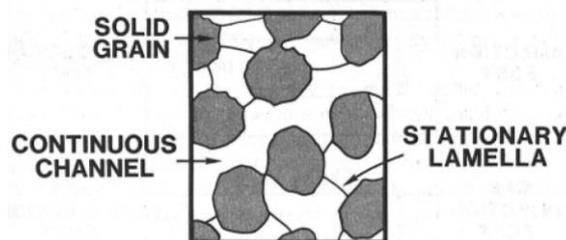
Figure 10: Reduced flow with foam. (Reference: Falls et al. 1988)

19

The components contributing to flow resistance were studied in uniform smooth capillaries (Hirasaki and Lawson 1985). A conceptual model for the relative permeability of two-phase flow was the bundle of capillary tubes model where the wetting phase flowed in the smaller capillaries and the non-wetting phase flowed in the larger capillaries. The relationship between the flow rate and pressure drop was then described by the Hagen-Poiseuille Iaw. The flow of a discontinuous non wetting phase like foam, however, cannot be described by the Hagen-Poiseuille law. The relationship between flow rate and pressure drop for the flow of foam through a capillary is described by an apparent viscosity that is required to modify the Hagen-Poiseuille law for the flow of foam.

Measurements done in laboratory show that the most important variables affecting foam viscosity is foam texture and quality. The number of bubbles per unit volume is known as the foam texture. Foam of finer texture has more lamellae per unit volume and, as a result offer greater resistance to flow. Finely textured foams are therefore also referred to as strong foams. The foam quality f_g, is defined as the gas fractional flow in foam:

$$f_g = \frac{q_g}{q_g + q_w} \qquad (2.2)$$

The principal factors affecting apparent viscosity of foam in uniform capillaries are dynamic changes at gas and liquid interfaces (Figure 11). The apparent viscosity of foam in a smooth capillary is the sum of three contributions:

- Slugs of liquid between gas bubbles resist flow.
- Viscous and capillary forces result in interfaces that are deformed against the restoring force of surface tension. The extent of this deformation and the resulting bubble shape partially determine apparent viscosity as a function of flow rate.
- Interface at the leading end of a bubble expands accompanied by compression at the trailing end. This sweeping action causes surface

active material to be depleted at the front and to accumulate at the back of the bubble. The result is a surface tension gradient that resists flow.

Other parameters like ratio of bubble radius to capillary radius, velocity and surface tension gradient influence the contribution from an individual element. Even though actual porous media for a reservoir is heterogeneous with different pore and pore-throat size across a control volume, the apparent viscosity of foam in uniform smooth capillaries is indeed one component of the mobility of foam in porous media.
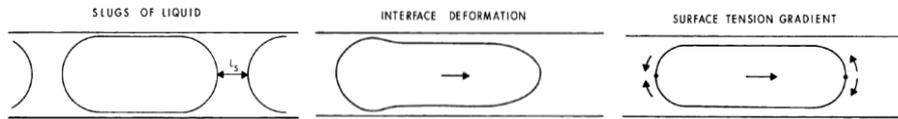
Figure 11: Mechanisms controlling apparent viscosity of foam in uniform capillary. (Reference: Hirasaki and Lawson 1985)

2.3.3 Foam Generation

The key mechanisms behind lamella creation are (Ransohoff et al. 1988):

- Capillary snap-off, illustrated in Figure 12a, occurs when liquid is displaced by gas in a pore throat to form a discontinuous gas bubble. Foam generation by capillary snap-off depends on the capillary pressure dropping below half of capillary entry pressure. This can happen with step increase of permeability by at least a factor of 4 or at the end of the core. The snap-off mechanism creates separate gas bubbles, which makes the gas phase more discontinuous resulting in strong foam.
- Lamella division shown in Figure 12b, only occurs when foam is already present, and a moving lamella approaches a branch point. The lamella then gets divided into two or more lamellae, and new gas bubbles are created. It however requires the pressure gradient to exceed minimum pressure gradient (MPG) for this mechanism to be relevant for foam generation as shown in Figure 13 and Figure 14.

It is therefore highly likely that foam generates near the well where ∇P is large, especially in alternating-slug processes. Separate gas bubbles are formed similar to the snap-off mechanism, reducing the relative permeability to gas phase significantly.
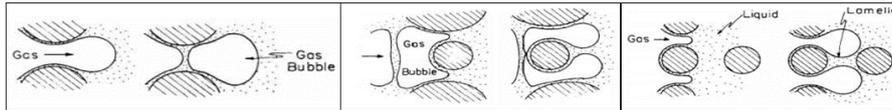
Figure 12: Lamella creation mechanisms (a) Snap-off (b) Lamella division (c) Leave-behind. (Reference: Ransohoff and Radke 1988)
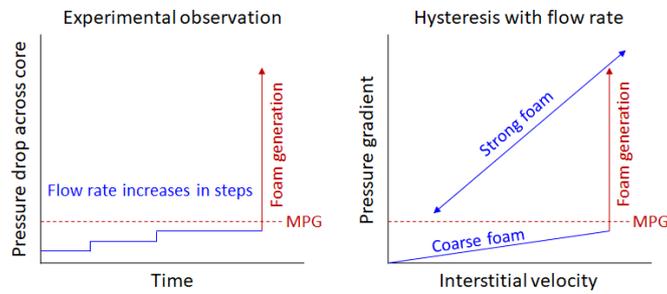
Figure 13: Minimum Pressure Gradient (MPG) required to create strong foam. (Reference: Gauglitz et al. 2002)
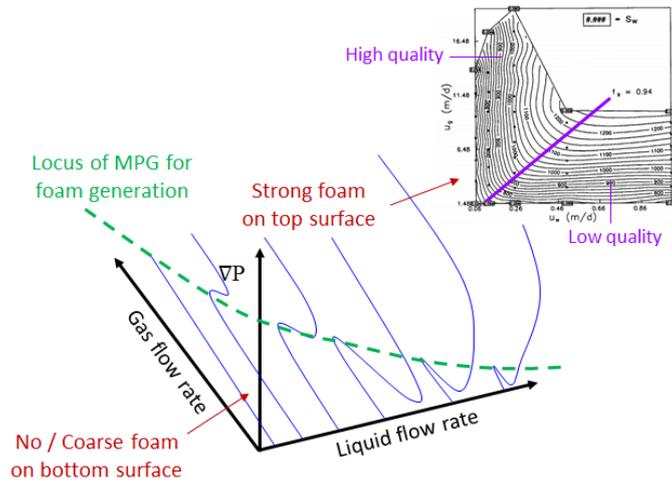
Figure 14: Minimum Pressure Gradient (MPG) as function of gas and liquid velocities, with pressure drop contours for strong foam (Reference: Osterloh and Jante 1992), in top right corner.

- The last mechanism called Leave-behind is illustrated in Figure 12c, and occurs when two gas fronts move towards the same liquid-filled pore space from different directions. The gas fronts will force the liquid in the pore space into a lamella. As this mechanism creates a large number of lamellae, gas pathways are blocked and the relative permeability to gas phase is reduced. Leave-behind does not form separate gas bubbles, which results in relatively weak foam.

2.3.4 Foam Destruction

Displacement with foam requires the lamellae to survive in reservoir, and therefore its effectiveness depends on its stability. The stability of foam lamellae is controlled by:

- Limiting capillary pressure
- Oil type and saturation
- Gas composition
- Solid substrate, depending upon wettability and capillary pressure

As the gas fractional flow is increased, which is equivalent to reducing water saturation, the capillary pressure at first increases and then approaches a characteristic value called the 'limiting capillary pressure' Pc* (Figure 15a). If the gas fractional flow in increased further, coalescence coarsens foam texture, the liquid saturation remains constant and the relative gas mobility becomes proportional to fg/fw (Figure 15b). As it dries out, foam collapses abruptly as a function of capillary pressure or water saturation. The limiting capillary pressure depends upon type of surfactant and its concentration, gas velocity (decreasing function) and permeability (decreasing function).

A major concern about the application of foam in oil reservoirs is the stability of foam in the presence of oil. To be effective in achieving good mobility control, it is crucial that foam remains stable when it comes in contact with oil. The available experimental data in porous media present varied results in terms of foam–oil interaction. It has been suggested that

foam stability depends on the composition of the oil phase such that the presence of light components is detrimental to foam stability.
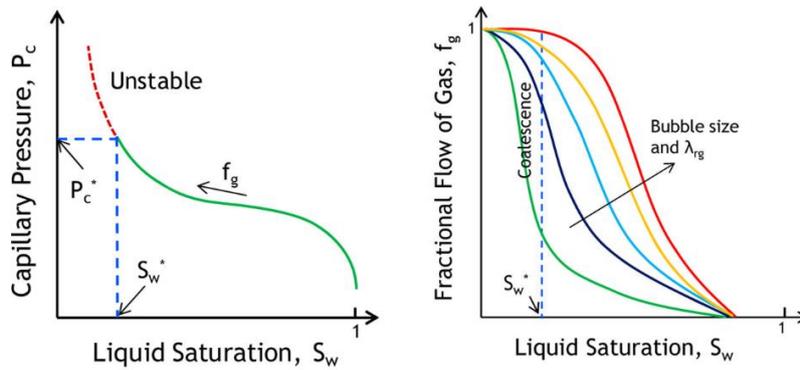
Figure 15: (a) Limiting capillary pressure Pc*. (b) Bubble size variation at Sw*. (Reference: Lotfollahi et al. 2016)
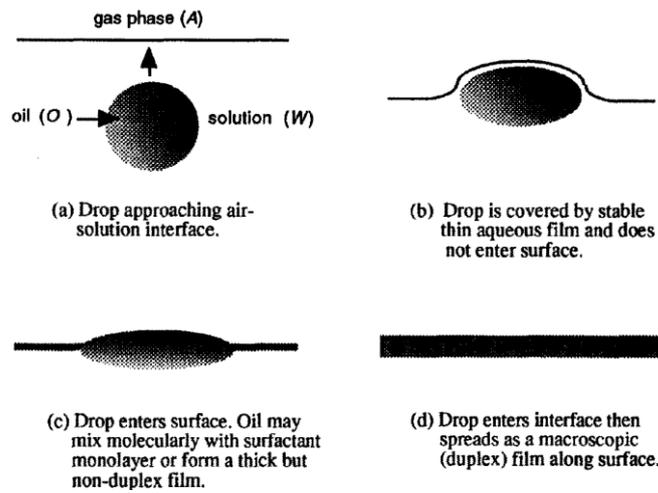
Figure 16: Possible states of gas-water interface in presence of oil. (Reference: Aveyard et al. 1994)

As shown in Figure 16, the underlying foam stability mechanism in the presence of oil depends upon aqueous film thinning due to entry of oil drop, oil spreading on the gas–water interface, occurrence of an unstable bridge across the foam film, and stability of pseudo-emulsion film, which

is a thin aqueous film separating the approaching oil drop and gas–water interface. The effect of oil on foam is not yet fully resolved. Figure 17 shows a schematic for formation of an oil bank, which is expected to result in a no-foam region next to it chased by foam of increasing strength.
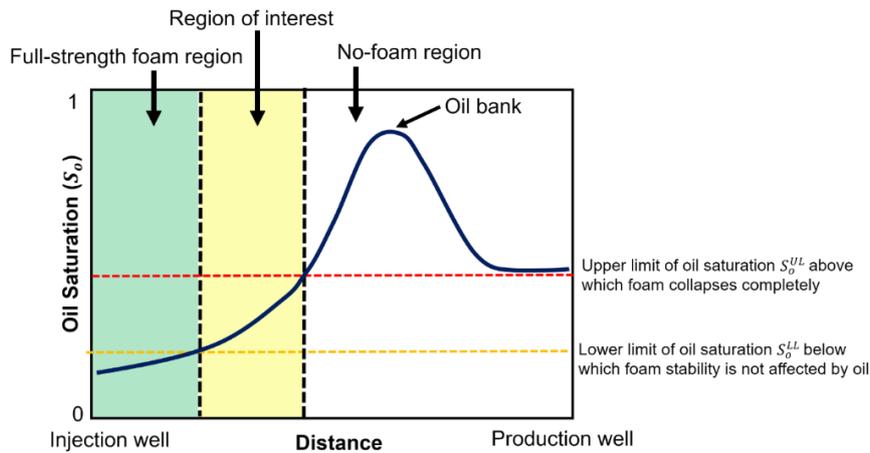
Figure 17: Foam strength dependence upon oil saturation. (Reference: Amirmoshiri et al. 2018)

2.3.5 Foam Flow Regimes

Extensive studies have been done to characterize foam behaviour at core scale in absence of oil. The results for strong foam (above the locus of minimum pressure gradient in Figure 14) confirm presence of two foam flow regimes — High-quality (HQ) and Low quality (LQ). Figure 18 shows the pressure gradient contours for strong foam (Osterloh and Jante 1992, Kim et al. 2005, Ma et al. 2012) as a function of gas and liquid velocity.

In the high-quality regime (also referred as dry foam), ∇P is nearly independent of gas rate and foam behavior is controlled by limiting capillary pressure Pc*. As a result, Sw is nearly independent of flow rates and stays close to Sw*. Foam can be modestly shear-thinning, shear-thickening or Newtonian based on observation from laboratory studies.

25

The behaviour is however represented as Newtonian in the model described later. In the low-quality regime (also referred as wet foam), ∇P is nearly independent of liquid rate and foam behavior is controlled by gas trapping and mobilization. Sw depends on flow rates, and foam exhibits strong shear-thinning behavior. At intersection between regimes ∇P reaches its maximum value, gas mobility is reduced by a given factor and Sw = Sw*.
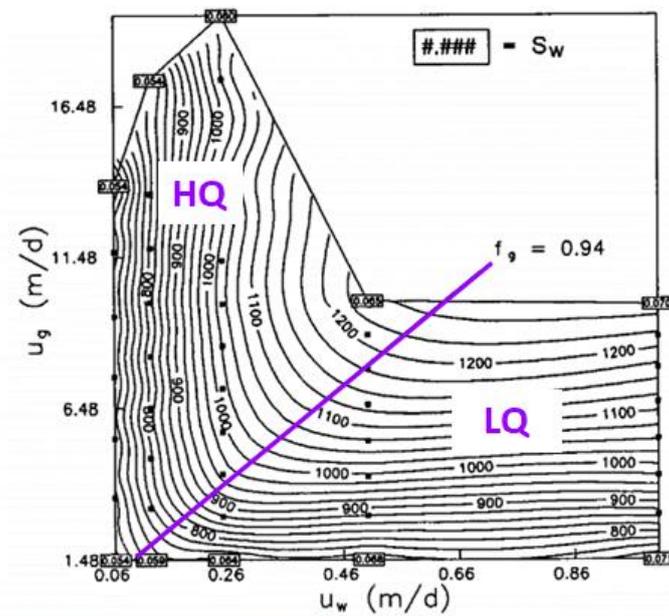
Figure 18: Steady-state pressure drop contours (psi) as a function of water and gas velocities for foam flood in a sandpack (Reference: Osterloh and Jante 1992). The dots represents steady-state pressure-drop measurement.

3   Scale-up Methodology

3.1   Field Overview

The field selected for the pilot study is located onshore in Permian basin, west Texas, USA (Figure 19). The field produces from the San Andres unit, which is a heterogeneous carbonate formation with porosity in the range of 3 – 28 % and permeability in the range of 1 – 300 mD. The reservoir has a net pay of 110 ft with reservoir top at a depth of 5300 ft from surface. The reservoir exhibits large vertical heterogeneity with Dykstra-Parsons coefficient of 0.79 and Lorenz coefficient of 0.84. Based on the regional data, it has been identified that the reservoir consists of two zones (Figure 20):

- Main Pay Zone (MPZ), which has produced by primary depletion and waterflood.
- Residual Oil Zone (ROZ), which is thought to be formed by structural tilting or seal breach events, and has been naturally waterflooded over geologic time. This zone has significant immobile oil which cannot be drained by primary or secondary mechanisms.

The field came online in early 1940s and produced 12% of OIIP until late 1960s. Waterflood began in early 1970s with wells on an 80-acre pattern. The field was developed throughout early 1980s with infill drilling to establish 40-acre peripheral waterflood patterns. However, with a low primary plus secondary recovery of only 22% of OIIP by late 1980s, the operator realized the need to reduce pattern size. An infill program was run to develop field on a 20-acre five spot pattern. Infill drilling yielded excellent results with increase in oil production rate from 400 STB/D to 1200 STB/D. However, a steep decline in production and high residual oil saturations in the reservoir rock after waterflood indicated the potential for tertiary oil recovery. Tertiary CO_2 injection for EOR started in eastern part of the field in October 2013 to target

remaining oil, and was further expanded to other patterns. This resulted in an increase in oil production rate from 250 STB/D in October 2013 to 800 STB/D in March 2018 (Figure 21). The peripheral producers of most of the patterns experienced CO_2 breakthrough in a short period, with breakthrough occurring within three months from start of CO_2 injection in some patterns. The reservoir has poor volumetric sweep due to reservoir heterogeneity and unfavourable mobility of CO_2, which makes it a good candidate to test foam for improving sweep and reducing CO_2 recycling.
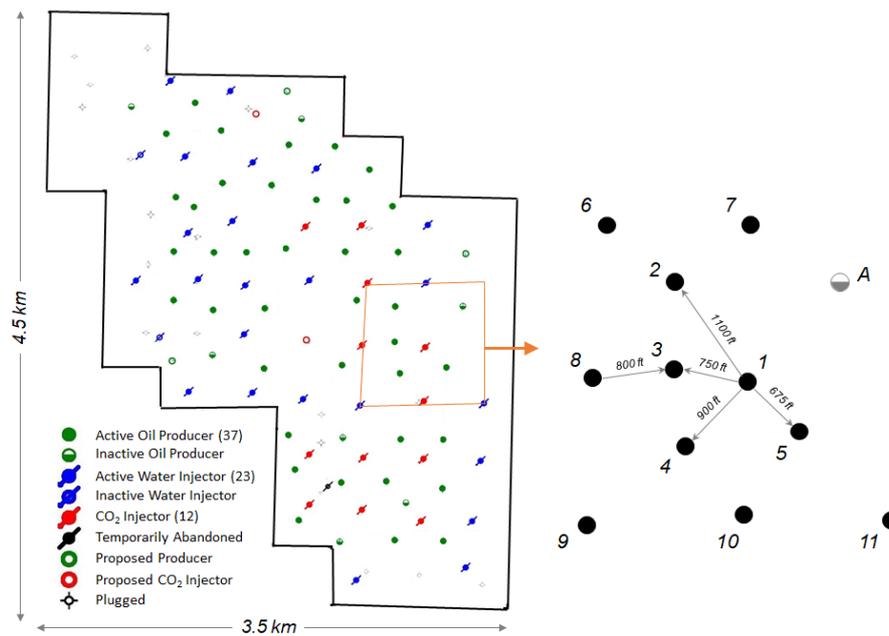
Figure 19: Field layout and location of selected pilot area. Surfactant will be injected in well 1.
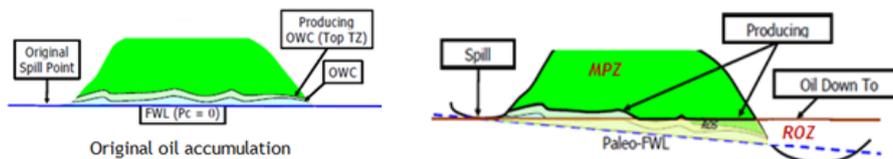
Figure 20: Effect of tilting on initial hydrocarbon distribution. (Reference: Honarpour et al. 2010)
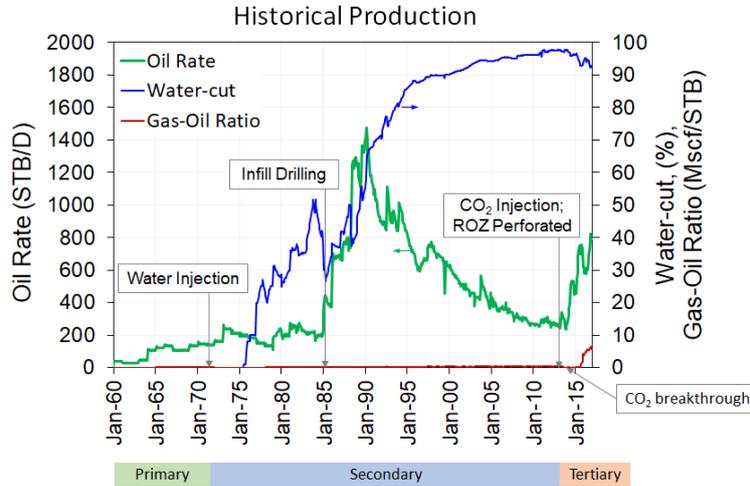
Figure 21: Field historical production.

3.1.1 Pilot Selection

The site selection for field trial was based on following criteria:

- Geology representative of entire field, to allow surfactant injection in other patterns post-pilot without resorting to detailed modelling.
- Short CO_2 breakthrough time for ongoing CO_2 injection, to allow shorter timeframe to demonstrate value of foam.
- High gas-oil ratio, to allow use of production data to confirm foam generation in-situ.
- Good initial well injectivity, to allow injection at desired rates considering flow resistance due to foam generation in high permeability layers.

After discussions with the field operator, an inverted five-spot pattern around well 1 (Figure 19) was selected. Well 1 was drilled in 1980, and was competed as a producer in MPZ. It was the first well that was re-completed in September 2013 to include ROZ when it turned into CO_2 injector. CO_2 breakthrough occurred at wells 3 and 5 in 8 and 4 months respectively, which are around 700 ft from well 1. Figure 22 shows the gas-oil ratio for wells 3 and 5 since start of CO_2 injection. The

completion in well 1 allows co-injection of CO_2 and surfactant, if required; and it has a profile to hang pressure gauge for accurate bottom-hole pressure measurement. Since the well status has changed during historic water flood and CO_2 injection, a prefix of 'P','WI' or 'GI' denotes the state of the well as producer, water injector or CO_2 injector, respectively.
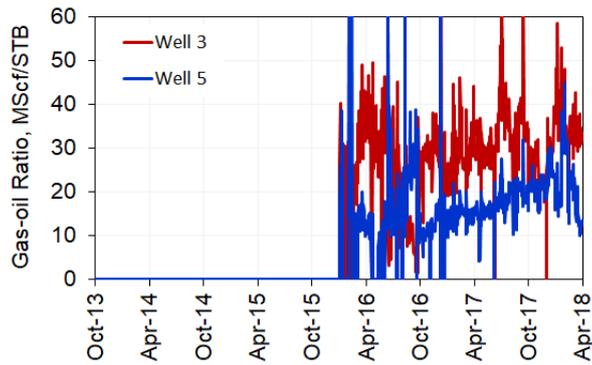
Figure 22: Gas-oil ratio for wells 3 and 5.

3.1.2 Reservoir Management Plan

The hydrostatic pressure corresponding to reservoir top is 2300 psi. The current reservoir pressure has been estimated to be 600–800 psi higher than the hydrostatic pressure, because of injection at a higher voidage replacement ratio since start of CO_2 injection in 2013. The injectors have been operating at flowing bottom-hole pressure of 3950 psi for a few years, which is close to fracture pressure. The CO_2 injection rate has varied historically between 1 to 3 MMscfd, depending on the reservoir pressure and well injectivity.

The reservoir management plan going forward is to depressurise the reservoir by injecting at a lower rate, at levels almost half of historic injection rate. For the pilot area, this corresponds to reduction in injection rate from 0.1 pore volume (PV) a year to 0.05 PV a year. A disposal well, completed in a separate deeper reservoir, is being used to depressurise

the reservoir before start of pilot. The gas injectors, after conversion from either a producer or a water injector, have been on continuous CO_2 injection in past. The revised base plan considers water alternating gas (WAG) injection with water injection for one year followed by CO_2 injection for six months. Based on discussions with operator, it has been agreed to implement surfactant alternating gas (SAG) injection in the chosen injector. The pilot will run for a year followed by continuous CO_2 injection for next year. The numerical modelling thus considers two scenarios — WAG and SAG, to demonstrate the value of foam.

3.2 Laboratory Studies

Several laboratory studies were performed to gain a comprehensive understanding of mechanisms governing 1D foam dynamics. A range of surfactants including cationic, non-ionic and zwitterionic were explored to identify candidates that have the potential to satisfy all the key requirements for CO_2-Foams in carbonate reservoirs (Nguyen et al. 2015). The foaming ability, stability, reduction of interfacial tension, adsorption and compatibility with formation fluids was examined as a function of the surfactant formulation. The selected surfactant was used to perform experiments to characterise foam stability and strength.

3.2.1 Characterizing Foam Stability

Silicon-wafer micromodels were used to mimic foam generation and decay in two-dimensional pore structure, under dynamic and static conditions. The experiments were performed in absence of oil. Bulk foam stability tests were then performed to test the foam stability in presence of oil. Additionally, coreflood EOR experiments were performed to characterize effect of oil on foam stability (Farajzadeh et al. 2012) in a bigger porous media relative to micromodel.

3.2.2 *Characterizing Foam Strength*

The effect of foam quality and flow rate were considered to characterize variation of foam strength.

- Steady-state pressure drop were measured for constant total injection rate with foam quality varying from 0.3 to 1. This is referred to as foam quality scan. Though the data collected for a fixed total flow rate is limited, as shown by redline in Figure 23, it has information for both high and low quality regimes which can be used to obtain foam model parameters as explained later.

- In a separate experiment, steady-state pressure drop was measured for constant foam quality (below transition fg under wet foam condition) with total injection rate varying from 1 to 10 ft/d. This is referred to as foam rate scan. Figure 24 shows the trend of foam apparent viscosity with superficial velocity at fixed foam quality (Zeng et al. 2016).

Both the scans were done in absence of oil. The use of these scans to derive foam model parameters is explained in next section.
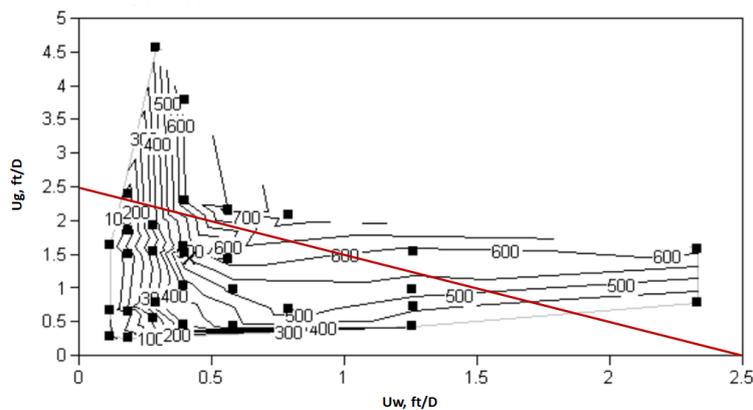
Figure 23: Steady-state pressure gradient contours (psi/ft) as a function of water and gas velocities (Reference: Alvarez et al. 2001). A scan at fixed total superficial velocity (2.5 ft/d), but varying foam quality, is shown as red line.
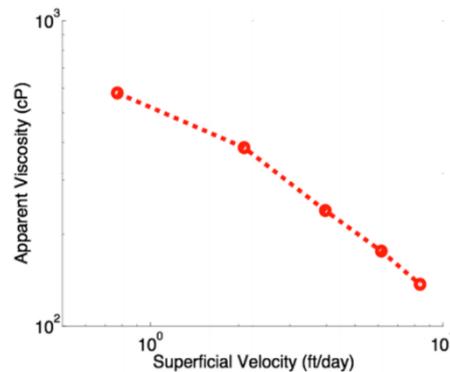
Figure 24: Flow rate scan for N_2 and surfactant solution using 6.7 in Bentheimer sandstone (0.65 Darcy) core at ambient temperature at fixed foam quality of 0.78 (Reference: Zheng et al. 2016).

3.3   Numerical Modelling

3.3.1   Modelling 1D Foam Behaviour

To a good approximation, foam has no effect on water flow, and water relative permeability remains the same function of water saturation. On the other hand, foam has large effect on gas flow in porous media. Foam traps a large fraction (almost 90–95%) of gas, reducing amount of gas flowing, and thus krg. Drag on foam lamellae increases resistance to bubbles that are flowing thereby increasing gas viscosity μg. These two effects are related to number of lamellae per unit volume of pore space and can be represented separately. However, as they appear in Darcy's law together as a ratio, most of the models lump both these effects into either krg or μg.

There are two general approaches available to model foam transport:
- Explicit-texture population-balance model (Falls et al. 1988, Rossen et al. 1999), allows direct simulation of foam creation, propagation, and coalescence that is observed in laboratory core experiments.
- Implicit-texture local-equilibrium model (Cheng et al. 2000, Alvarez et al. 2001), uses an empirical relation to capture the effect

of surfactant concentration, water saturation, oil saturation, shear thinning due to flow velocity etc. on foam mobility.

The major challenge with developing a mechanistic foam simulator for explicit-texture approach is tracking changes in foam texture, which in turn, depends upon dynamic mechanisms of in-situ lamella creation and coalescence. Because of complex foam dynamics and challenges associated with extracting model parameters from coreflood experiments for mechanistic population-balance approach, the implicit-texture approach is more appropriate to model large-scale foam behaviour. In this approach, the gas permeability in presence of foam (k_{rg}^f) is modified by multiplying the gas relative permeability without foam (k_{rg}^{nf}) at a specific water saturation with a mobility reduction factor (MRF), which is a function of various factors.

$$k_{rg}^f = k_{rg}^{nf} \times MRF \qquad (3.1)$$

The mobility reduction factor is dependent upon water saturation, shear rate, surfactant concentration, oil saturation and oil composition as shown by the expression (ECLIPSE 2018):

$$MRF = \frac{1}{1 + fmmob \times F_{water} \times F_{shear} \times F_{surf} \times F_{oil}} \qquad (3.2)$$

where *fmmob* refers to the maximum gas mobility reduction that can be achieved. F_{water}, F_{shear}, F_{surf}, and F_{oil}, with expressions below, capture the water saturation, shear rate, surfactant concentration and oil saturation dependence respectively, with all lying in the range of 0 to 1. The capillary number N_c represents the relative effect of viscous and capillary forces.

$$F_{water} = 0.5 + \frac{arctan[epdry(S_w - fmdry)]}{\pi} \qquad (3.3)$$

$$F_{shear} = \begin{cases} \left(\frac{fmcap}{N_c}\right)^{epcap} & if \ N_c > fmcap \\ 1 & otherwise \end{cases} \quad (3.4)$$

$$F_{surf} = \left(\frac{Surfactant \ concentration}{fmsurf}\right)^{epsurf} \quad (3.5)$$

$$F_{oil} = \left(1 - \frac{S_o}{fmoil}\right)^{epoil} \quad (3.6)$$

Foam model parameters like *fmmob*, *fmdry*, *epdry*, *fmcap*, *epcap*, *fmsurf*, *epsurf*, *fmoil* and *epoil* are obtained by fitting different set of laboratory data.

As shown in Figure 23, representative ∇P contour lines from laboratory measured data can be extrapolated in both the regimes to the point of intersection. At intersection, Sw = Sw* (*fmdry*) and ∇P reaches its maximum value. Assuming that base water and gas permeabilities are known functions of water saturation for the core used, *fmdry* is identified from measured krw in high-quality regime. Gas mobility gets reduced by a factor at the intersection which can be used to obtain *fmmob*. *epcap* is based on shear-thinning in low-quality regime, while large *epdry* will give a vertical trend in high-quality regime.

Using the above approach however requires measurement of multiple steady state pressure drops for different combinations of gas and water flow rates, which is very time consuming and impractical. The foam model parameters (*fmmob*, *fmdry*, *epdry*, *fmcap and epcap*) can be obtained with a limited data set from a foam quality scan of co-injection experiment by following the steps below:

- Initial estimation using best-fit straight line for high-quality regime and a convex curve for low-quality regime, both intersecting at fg* (Boeije and Rossen 2015, Kibodeaux and Rossen 1997).
- Regression to improve the match between experimental data and empirical model response for foam quality and rate scans.

In the high-quality regime, foam behaviour is considered Newtonian and the water saturation remains close to Sw*. As a result, ∇P can be assumed a linear function of fg.

$$u_t(1 - f_g) = - \frac{k k_{rw}(S_w^*)}{\mu_w} \times \nabla P \qquad (3.7)$$

$$\nabla P = C \, (1 - f_g) \qquad (3.8)$$
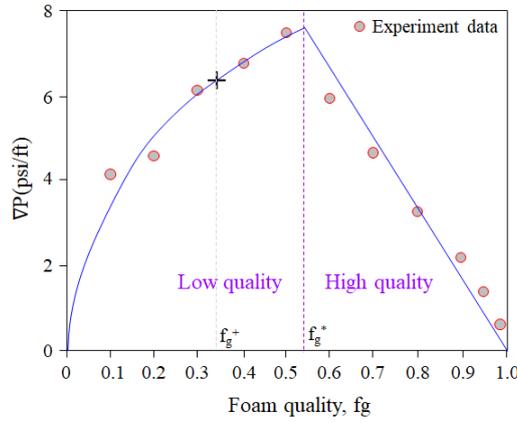
Figure 25: Fitting foam quality scan to obtain initial estimate of foam model parameters.

As shown in Figure 25, the best fit in high-quality regime is a straight line passing through (fg, ∇P) = (1, 0). Since the low-quality regime exhibits non-linear behaviour due to shear thinning, the first estimate is free hand convex plot through data. The intersection between these two curves occurs at fg^*. Krw(Sw*) can be obtained using Darcy's law for the transition point as:

$$k_{rw}(S_w^*) = \frac{u_t \, \mu_w \, (1 - f_g^*)}{k \, \nabla P(f_g^*)} \qquad (3.9)$$

fmdry, which is Sw*, can then be obtained from the known relation between Krw and Sw. Once Sw* is known, *fmmob* can be obtained using the relations below based on Darcy's law for gas phase at fg^*:

$$MRF(f_g^*) = \frac{k_{rg}^f}{k_{rg}^{nf}} = \frac{u_t \, \mu_g \, f_g^*}{k \, \nabla P(f_g^*) \, k_{rg}(S_w^*)} \qquad (3.10)$$

$$fmmob = \frac{1}{MRF(f_g^*)} - 1 \qquad (3.11)$$

The limiting case for *epdry* corresponds to sharp transition due to abrupt change between regimes. This can be achieved by assuming a large value of *epdry* at this stage, lying in the range of 10,000-100,000. Because of this assumption, Fwater does not play a role in low-quality regime i.e. Fwater = 1 for fg < fg*. At this stage, it is also assumed that the gas relative permeability in absence of foam in the low-quality regime remains close to the value at Sw*. A point is then picked from the data for low-quality regime, not too close to fg*, which can be called fg+.

Applying Darcy's law to the gas phase to this point results in the expression below, which can be used to derive *epcap*:

$$u_t \, f_g^+ = \frac{k \, k_{rg}(S_w^*) \, \nabla P(f_g^+)}{\mu_g} \frac{1}{1 + fmmob \left(\dfrac{\nabla P(f_g^*)}{\nabla P(f_g^+)} \right)^{epcap}} \qquad (3.12)$$

$$epcap = \frac{log \left[\dfrac{1}{fmmob} \left(\dfrac{k \, k_{rg}(S_w^*) \, \nabla P(f_g^+)}{\mu_g \, u_t \, f_g^+} - 1 \right) \right]}{log \left(\dfrac{\nabla P(f_g^*)}{\nabla P(f_g^+)} \right)} \qquad (3.13)$$

k and σ_{wg} are assumed constant, which allows replacing the ratio of capillary numbers in Fshear by ratio of pressure gradients. *fmcap* can be derived using the lower limit of ∇P below which non-Newtonian foam

behaviour is not expected. At this stage, ∇P_{low} can be based on 3D simulation, or assumed a user-specified fraction of $\nabla P(f_g^*)$:

$$fmcap = \frac{k \, \nabla P_{low}}{\sigma_{wg}} \qquad (3.14)$$

Foam parameters obtained using the above approach serve as an initial estimate for least-square fitting routine (MatLab), which was used to simultaneously reduce the misfit between laboratory data and empirical model prediction for foam quality and rate scans.

Aqueous solutions with different surfactant concentrations can be used to perform experiments to obtain *fmsurf* and *epsrf*. Since foam shows a complex behaviour in presence of oil, the first step for obtaining foam model parameters involves obtaining steady-state pressure data in absence of oil. In a separate experiment, coreflood can be performed with oil present in core, to obtain *fmoil* and *epoil*.

3.3.2 Modelling 3D Foam Behaviour

Integrated Reservoir Model

Integrated reservoir modelling is an approach to combine information from multiple sources (seismic, well logs, pressure transient tests, tracer tests, production data etc.) to generate a robust 3D subsurface description of the reservoir. This reservoir model then is used for field development planning subject to the uncertainties in modelling inputs, and understanding the risks associated with decision-making. The overall modelling process consists of two stages:

A. Static (Geologic) Modelling

As shown in Figure 26, the static model is the final product of following processes in general (Cannon 2018):

- Structural modelling: The geophysical surveys (2D seismic lines, 3D seismic volumes, checkshots etc.) provide depth-converted surfaces (horizons) corresponding to geologic units and faults, which are used to setup the reservoir structure. A geologic unit bounded between seismic horizons can be further split into zones based upon well log data.
- Stratigraphic modelling: Similar log responses (and interpretations) in wells are correlated across the reservoir, to determine the similarity of rock bodies at different locations in reservoir.
- Facies modelling: A facies is a body of rock with specific attributes (like depositional structure, texture, composition, variation post-deposition through diagenesis etc.) that are distinct from adjacent rock. Cores and petrophysical logs are typically used to identify and characterize the most relevant facies types at well level. The facies are then distributed throughout the 3D model using either stochastic or deterministic geostatistical techniques.
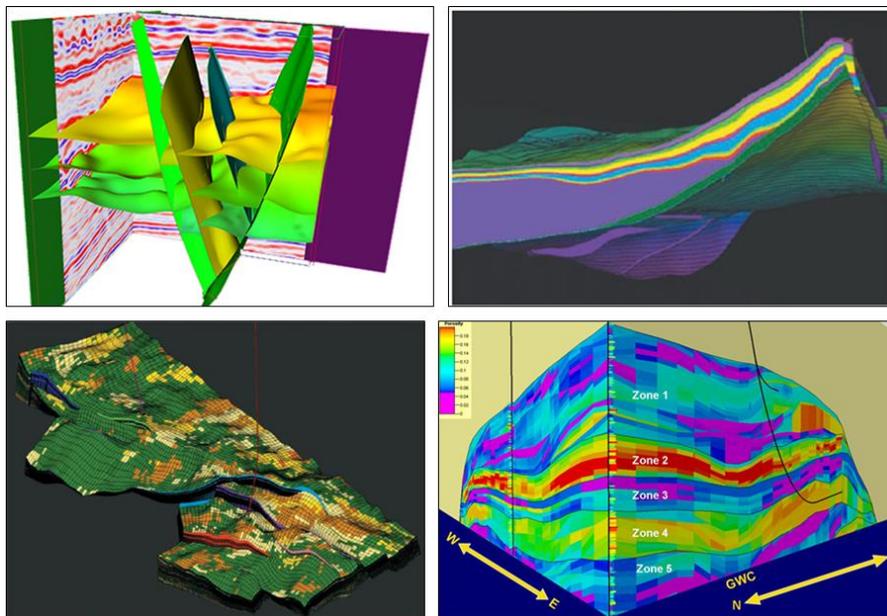
Figure 26: Static modelling (from top left to bottom right) — Structural modelling, Stratigraphic modelling, Facies modelling and Petrophysical modelling. (Reference: www.oil-gasportal.com)

- Petrophysical modelling: The intrinsic properties of a reservoir like porosity, permeability and initial water saturation are obtained at the well locations using petrophysical logs. Core data is used as a basis for calibrating the interpretations from logs. These properties are linked to facies, and distributed throughout the 3D model using geostatistical techniquies.

B. Dynamic (Simulation) Modelling

The dynamic model is created by integrating static model with following:

- Pressure and Saturation dependent properties: A fluid model is required to model the pressure-volume-temperature (PVT) characteristics of fluids present in reservoir and injected into reservoir. Saturation functions (capillary pressure and relative permeability) are required to calculate the forces driving fluids from pore space and the mobility of each phase.
- Initial conditions: The initial pressure, phase saturations and composition (for compositional simulation) needs to be available for the dynamic model before simulating the reservoir behavior. The initial conditions can be defined through – Equilibration (by defining fluid contacts and reference pressure, and assuming fluids in hydrostatic equilibrium), Enumeration (be defining initial state for each cell) and Restart (by using an intermediate point from another simulation).
- Wells and Surface facility: The completions, along with well paths, need to be defined to establish connections between reservoir and wells. Incorporating lift curves for wells and pipelines, and performance curves for surface equipment in the simulation allows using the model for prediction at specific surface constraint(s).
- Field management strategy: The drainage strategy, well and group hierarchy, production and injection limits etc. define how the field development evolves with time. This has two phases — 'History', when actual measured production rates and pressures from field are

known and 'Prediction', when production strategy is setup to determine hydrocarbon recovery.

Model Calibration and Forecasting

There exist uncertainties in the modelling inputs because of absence of information or limited data availability. Since the main objective of reservoir modelling is to create a reliable forecast that reflects all available information, the reservoir model was calibrated to reduce the uncertainties before using it for pilot design. The workflow that was used for assisted history matching is outlined in Figure 27 and explained in Paper VI.
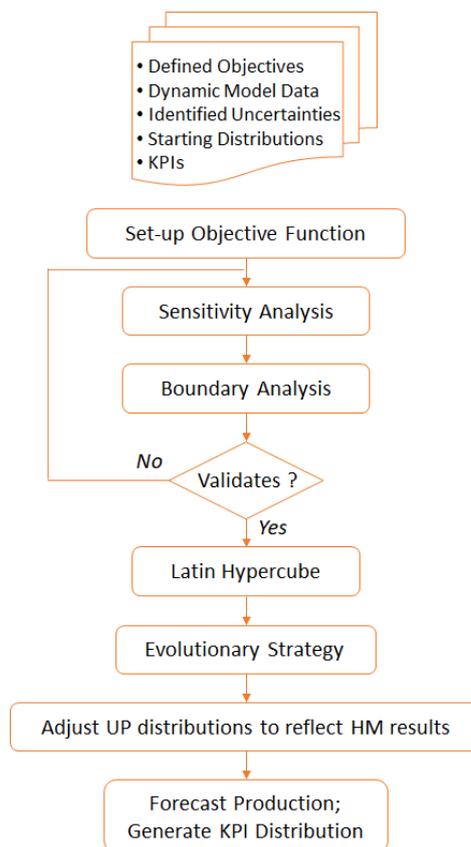
Figure 27: History matching and forecasting workflow.

The workflow transforms uncertainty about input information into an ensemble of predictions that describe the uncertainty in production. As we proceeded, initial views about uncertainties were revised to get a reasonable fit to observations using more than one set of values for model parameters. The steps of the history matching and forecasting workflow are briefly explained below:

A. Model Calibration

- Setting up an Uncertainty Matrix: A matrix was setup with uncertainty parameters (UPs) after discussion with different stakeholders which listed model (static and dynamic) parameters, their ranges and distributions. The initial matrix was setup based on the understanding about reservoir dynamics, which was revised during the history matching process as needed.
- Setting up the Objective Function: The progress of the history matching process depends on the quality of the setup of the objective function, which is the misfit or mismatch between the observed data and the simulator response. This objective function, which is the weighted sum of mismatch parameters (MPs), is then minimized for the set of UPs using an optimization algorithms.
- Model validation: In order to ensure that simulations based on the input range of UPs cover measured data and match shape for simulated cases, the model setup was validated using Sensitivity and Boundary analyses. The sensitivity analysis involves running simulations by varying one variable at a time to get relative impact of each UP on various MPs in form of Tornado plot. The boundary analysis involves running simulations using Plackett-Burmann (PB) sampling, where low values of some UPs were combined with high values of other UPs.
- Selecting starting points for Assisted History Matching: Latin Hypercube (LHC) sampling technique was used to generate a large number simulations. Pareto plots and Correlation charts generated based on these LHC runs were used to understand the relation

among MPs and dependence of MPs on UPs. Multiple start points were selected to initialize history matching.

- Completing history matching: Evolution strategy (ES) was used for assisted history matching, which is one implementation of an evolutionary algorithm (Back 1996, Schulze-Riegert et al. 2002) with local and global search capabilities. In addition to a sufficient match quality, the other criteria that were found important for a successful history match were to — have sampled a wide enough selection from the input UP distribution, and to have obtained as many alternative solutions as realistically possible.

B. Forecasting

- Transition into Prediction: The well controls typically changes from controlling on set rates (voidage rate, liquid rate, oil rate) for history matching to controlling on set pressures (normally tubing-head pressure) for prediction, which introduces a discontinuity in well performance. We handled this issue of a smooth and physically reasonable transition into prediction by applying the same process to the prediction as applied during history matching. As mentioned in Section 3.1.2, the injectors will operate on a constant injection rate at levels almost half of historic injection rate, which is used as primary constraint for prediction. Well injectivity was tuned to reduce the misfit between observed data and model's response before using flowing bottom-hole pressure as secondary constraint. All producers in the field have been on artificial lift for a very long time, with no flowing bottom hole pressure data available. The producers are kept on constant liquid rate at same level reported on last step in historic data, assuming no modification in the lift capacity during prediction phase. This ensured smooth transition from history match phase to prediction phase.

- Forecasting pilot performance: The base values for foam model parameters were obtained by fitting different set of laboratory data mentioned earlier. In order to account for the effect of permeability,

the grid was divided into three regions depending upon the grid cell permeability — less than 10mD, 10–50 mD and greater than 50mD. These regions were assigned different *fmmob*, fmdry and *epdry*. Because of limited availability of core material, assumptions were made for the low and high values of the foam model parameters, considering 10–20% deviation from base value. The grid cells connecting to proposed injector were refined areally from 50 ft x 50 ft to 10 ft x 10 ft by introducing local grid refinement. In order to model foam dry-out during SAG near injector (Leeftink et al. 2015), the cells within the refined grid which were connected to the injector were assigned an *fmmob* of 0. This allowed modelling of complete foam collapse within a radius of 5 ft around injector to mimic dry-out. The UPs that were introduced to model foam behavior while forecasting pilot performance, were combined with the UPs from history matching phase, to generate a large number of LHC cases under two scenarios mentioned in Section 3.1.2. For each case, simulations were run using the sampled values of the UPs for all three phases — waterflood, CO_2 injection and forecast for three years. To ensure continuity, the initial pressure, saturation and composition for each case for second and third phase were based on the values extracted from the last step of previous phase. Several KPIs were identified to confirm pilot's success, out of which following two were under focus for numerical modelling study — increase in oil production, and increase in CO_2 retention factor, with foam over base case. CO_2 retention factor was evaluated as

$$CO_2 \ Retention = \frac{CO_2 \ Injected - CO_2 \ Produced}{CO_2 \ Injected} \qquad (3.15)$$

In the above expression, produced CO_2 volume corresponds to recycled CO_2 volume assuming no CO_2 loss at surface, while injected CO_2 volume corresponds to sum of purchased and recycled CO_2 volumes. CO_2 storage is slightly different from CO_2 retention, as given below (Melzer 2012),

$$CO_2 \ Storage \ = \frac{CO_2 \ Injected - CO_2 \ Produced - CO_2 \ Losses}{Purchased \ CO_2 \ Injected} \quad (3.16)$$

Since the above definition requires the operator to disclose the purchased volumes in addition to measurement of losses, CO_2 retention was found a more suitable metric for this study. The results obtained from the LHC cases were used to study – KPIs trend with time, distribution at a specific time and the relation between KPIs and UPs.

3.4 Field Data Acquisition

As mentioned earlier, one of the main reasons to run the field trial onshore is to assist technology transfer through numerical modelling to high-risk and high-cost environments. Field data acquisition, including both baseline and repeat survey, is of paramount importance to reduce uncertainties in the model and the process. The planned surveillance strategy therefore focuses on obtaining relevant data from wells and reservoir to meet the following pilot objectives:

- Verify in-situ foam generation
- Increased oil production
- Increased CO_2 Retention

3.4.1 Well Data

The flowing tubing-head pressure for well 1 will be continuously monitored during pilot, with an increase suggesting in-situ foam generation. The injection rate for all the wells has been reduced compared to historic rates to depressurize the reservoir. Well 1 will be injecting at a target (low) rate before and during pilot as long as the bottom-hole pressure does not exceed fracture pressure. The bottom-hole flowing pressure limit corresponds to tubing-head pressure of 1450 psi and 1900 psi for water and CO_2 respectively.

It has been planned to hang a pressure gauge on an electric line wire, close to reservoir top, with real-time surface readout. This will allow better control on surface operations, especially injection rates, because of the risk of operating close to fracture pressure. A wellhead lubricator assembly will be required throughout the pilot, which may have a problem with maintaining long-term seal against surface pressure. Downhole pressure monitoring with electric line is also not recommended for extended tests due to exposure of the wire to a corrosive environment. Therefore, if needed, the downhole gauge will be pooled-out-of-hole (POOH) during water injection periods for inspection, and will be run-in-hole (RIH) before switching to CO_2. Installation of a permanent downhole gauge would require retrieving the completions (tubing and packer) using a workover rig, and was not considered because of significant increase in project cost. Installation of electronic memory pressure gauge in the profile nipple was not considered fit-for-purpose because of unavailability of real-time data and frequent operations required to POOH gauge and RIH again with new battery.

The baseline and repeat injection profiles will be recorded for well 1, to confirm diversion of CO_2 to low permeability layers with in-situ foam generation. This will however require POOH the pressure gauge. No petrophysical logging is planned to measure change in oil saturation at the injector during pilot. Also, no monitoring well will be drilled in-between the existing wells for the pilot.

The producers 2, 3, 4 and 5 will be tested daily for three phase production rates. In-situ foam generation can be verified with drop in gas-oil ratio for wells 3 and 5, which are recycling most of the CO_2 injected in well 1. Produced water samples for wells 3 and 5 will also be collected and analyzed to detect presence of surfactant in laboratories. As mentioned earlier, all producers are on artificial lift. The zones producing CO_2 cannot be identified using production logging because of presence of lift equipment and inability of the wells to self-flow for more than a few

hours. A temperature profiling will be done if any producer in the pilot area needs to be worked over before pilot to change the lift equipments.

3.4.2   Reservoir Data

The change in interwell flow behaviour because of foam will be characterized using:

- Tracer test: An interwell tracer study was initiated in January 2018, with injection of a passive non-radioactive gas tracer (Khan et al. 2016) in well 1, to characterize the communication between well 1 and surrounding producers. The interwell tracer study will be repeated at the end of the pilot with a different gas tracer.
- Pressure fall-off test: A baseline fall-off test, with downhole pressure measurement, is planned for well 1 to improve reservoir characterization and identify reservoir features like fractures, faults and presence of distinct mobility regions around injector. The fall-off test will be repeated at the end of the pilot depending upon the quality of data collected during the baseline test.

4   Results and Discussion

This section summarizes the main results from the scientific papers published as part of this thesis.

4.1   Laboratory Studies

A non-ionic water-soluble surfactant (Surfonic L24-22) was selected for field pilot based on surfactant screening studies for the reservoir (Nguyen et al. 2015). Surfonic L24-22 is a linear alcohol ethoxylate produced by the addition of ethylene oxide (EO) to linear, primary alcohols. It is a 22 mole ethoxylate of linear, primary 12-14 carbon number alcohol.

4.1.1   Pore-scale Foam Stability Tests

Paper II presents a qualitative and quantitative evaluation of CO_2-Foam behaviour at pore-scale using silicon-wafer micromodels. A baseline test was performed using co-injection without surfactant in the micromodel. Visual observations (Figure 28a) showed gas phase spanning over several pores with no separation by liquid films, suggesting low reduction in CO_2 mobility. The test was repeated with surfactant added to the aqueous phase which resulted in generation of strong foam. Figure 28b shows that both continuous and discontinuous CO_2-Foam were generated as shown by blue and yellow circles, respectively. In contrast to the baseline test, flow diversion occurred around sites with discontinuous foam generation, towards regions of continuous CO_2-Foam or no foam. Fluctuations in flow paths were observed due to foam coalescence and regeneration.

In addition, foam stability was measured at elevated pressures under static conditions for a period of 72 hours. Figure 29 shows the observed trend for normalized bubble concentration (ratio of number of bubbles at each time step to initial number of bubbles) with time for a fixed field-

of-view. The bubble coalescence rate was high in the beginning, which decreased with time until it reached a stable value after around 30 hours. 37% of the original bubbles remained after 72 hours, suggesting good foam stability under static conditions. The foam half-life (corresponding to bubble concentration of 50% of original) was found to be 13.3 hours. During this period, the aqueous phase was released due to coalescence, and became mobile (Figure 30).
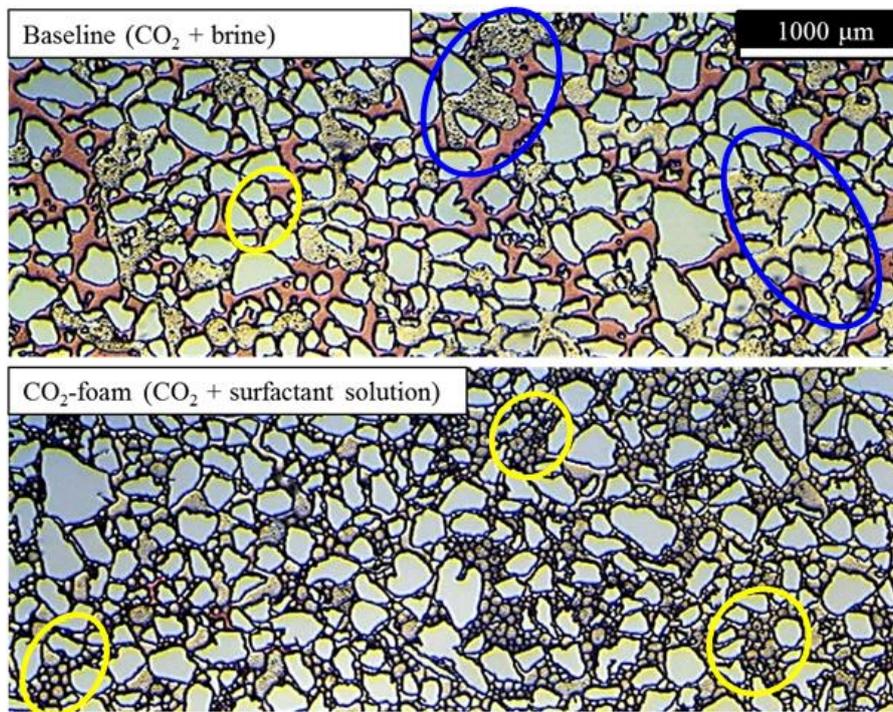
Figure 28: CO_2-brine co-injection at 9 MPa, 20ºC and gas fraction of 0.7 (a) Without surfactant (b) With surfactant. Matrix grains are shown as grey uniform coloured area, water as red and CO_2 as darker grey bubbles. Continuous CO_2 bubble spanning over multiple pores is shown as blue circle, while fine textured foam with multiple bubbles occupying single pore is shown as yellow circle. (Reference: Paper II)
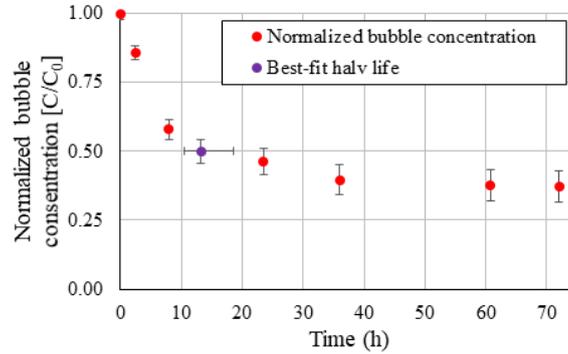
Figure 29: Reduction in normalized CO_2-Foam bubble concentration (red points) with time under static conditions at 9 MPa, 20ºC. The half-life concentration is shown as purple point. (Reference: Paper II)
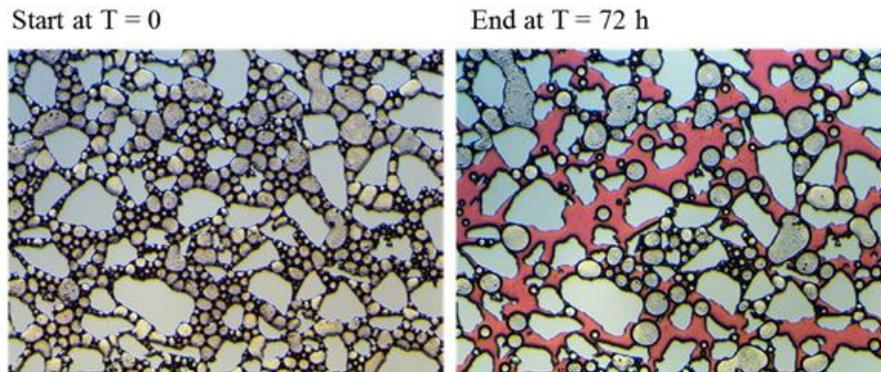
Figure 30: Visual assessment of static foam stability for field-of-view section (a) Start of Static test (b) End of Static test after 3 days. Matrix grains are shown as grey uniform coloured area, water as red and CO_2 as darker grey bubbles. (Reference: Paper II)

4.1.2 Bulk-foam Stability Tests

The pore-scale micromodel study suggested foam stability in absence of oil. Bulk-foam stability tests were performed to observe the effect of oil on foam decay for two different surfactant concentrations — 0.5wt% and 1wt%.Baseline tests were performed in absence of oil, and the height of the foam column was considered to represent foam's stability at a given time. Figure 31 shows the foam decay profiles (in terms of normalized height) for the two surfactant concentration. 1wt% solution (blue curve)

gave a higher half-life time of 10.5 min compared to that for 0.5wt% solution (green curve) of 6.7 min in absence of oil. The field pilot injection, however, is planned at 0.5wt% concentration, because of favourable economics.
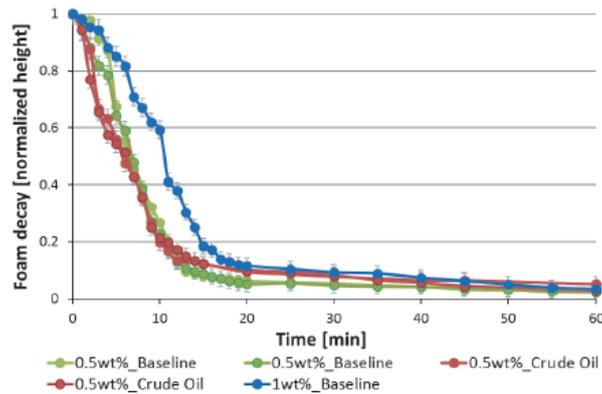
Figure 31: Bulk-foam decay profiles. Baseline experiments in absence of foam for 0.5wt% and 1wt% surfactant solution are shown by green and blue curves, respectively. Experiments in presence of oil for 0.5wt% surfactant solution are shown by red curves. (Reference: Paper IV)

To test the foam stability in presence of oil, 5vol% dead oil was added to the mix prior to foam generation. Two tests with 0.5wt% concentration were performed, which are shown by red curves in Figure 31. The results suggested that oil destabilizes the foam, and reduces the half-life by 12% from 6.7 min to 5.9 min. However, the oil did not completely kill the foam, which confirmed suitability of selected surfactant and 0.5wt% concentration for the field trial.

4.1.3 Foam Quality and Rate Scans

As published in Papers II to IV, foam quality and rate scans were performed for various possible combinations of parameters such as:

- Core material: Outcrop limestone core, Reservoir core
- Wettability: Water-wet, Oil-wet
- Surfactant concentration: 0.5wt%, 1wt%
- Oil content: No oil, Oil at residual oil saturation

Figure 32 shows the experimental data for foam scans considered for further use in numerical modelling.
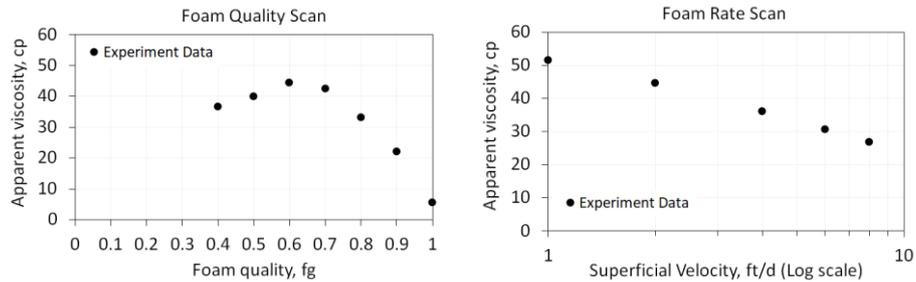
Figure 32: Experimental data considered for use in pilot simulation (a) Quality scan (b) Rate scan. (Reference: Paper II)

4.1.4 CO_2-Foam EOR Corefloods

As published in Papers III and IV, CO_2 EOR coreflood experiments were performed using reservoir core material (oil-wet), reservoir brine and crude oil. Figure 33 compares the saturation profiles for water, CO_2 and CO_2-Foam injection for a set of related experiments. CO_2-Foam was pre-generated due to short core plug lengths. Waterflood recovery was around 32% with a long tail production, which is typical for oil-wet reservoirs. No additional oil was recovered during surfactant pre-flood. Similar recoveries were observed with CO_2-Foam for both 0.5wt% and 1wt% surfactant concentration.

Pure CO_2 injection (red curve) after waterflood resulted in additional oil recovery by 37% OIIP. The recovery from CO_2-Foam flood (immediately after waterflood) was found to be lower than the recovery during pure CO_2 flood, likely due to interference from liquid films hindering direct miscibility between CO_2 and oil. When pure CO_2 injection was followed by CO_2-Foam, additional 15% OIIP was recovered, reducing Sor to 0.04. This is lower than the Sor observed in slim-tube experiment of 0.1, suggesting effectiveness of foam in improving oil recovery.
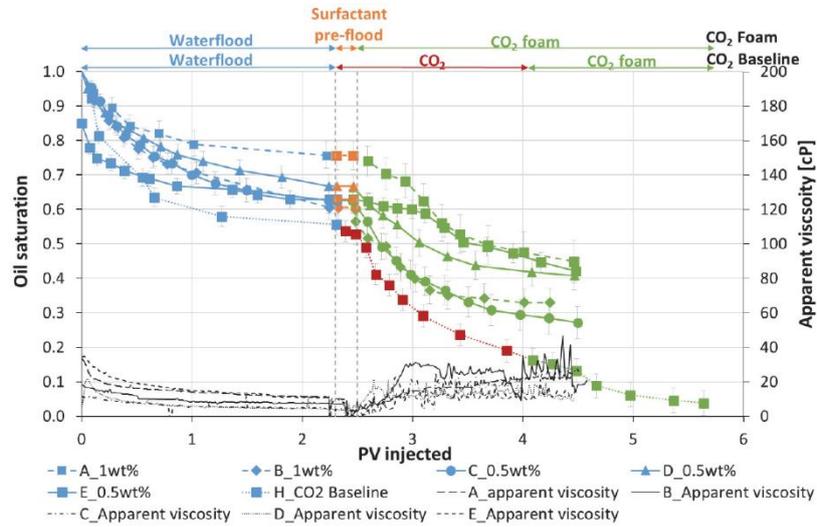
Figure 33: Oil saturation and apparent viscosity versus pore volume injected for five CO_2-Foam EOR experiments (A, B, C, D and E) and one CO_2 flood. Waterflooding is shown as blue, surfactant pre-flood as orange, CO_2 flood as red and CO_2-Foam co-injection as green. Surfactant concentration of 0.5 wt% and 1wt% is shown as solid and dashed curve, respectively. (Reference: Paper III)

4.2 Numerical Modelling Studies

The following sections describe the setup of initial reservoir model, calibration to production data, and integration with laboratory inputs for forecasting the pilot response.

4.2.1 Geologic Model

The field produces from San Andres reservoir, a heterogeneous carbonate formation which consists of cyclical sequences of subtidal and intertidal deposits interbedded with shaley mudstone layers. These mudstone layers act to limit vertical communication throughout the reservoir and are considered as barriers to vertical flow. The subtidal dolostone facies make up the bulk of the reservoir rock, which has well developed porosity, later enhanced through leaching and subsequent dedolomitization (Wang et al. 1998).

The core data was available for well A, which was drilled and cased, but was not completed for production. Gamma ray, neutron, density, and resistivity logs were used to tie the core analysis to log data, and define flow units. Lithology was determined from gamma ray and resistivity logs, while porosity was calculated from the neutron and density logs. The porosity varies between 0.03 to 0.28 with an average of 0.12, while permeability varies between 1 to 300 mD with a low average of 7 mD. MPZ and ROZ were divided into four and two flow zones respectively, each separated by impermeable units. Three petrophysical classes (Wang et al. 1998) were identified based on core data (Figure 34). The main reservoir zones are composed of grainstones and packstones (class 1 and 2) interbedded with low permeability shaley mudstones (class 3). The range in permeability values for petrophysical classes 1 and 2 arises from dissolution of carbonate material resulting in high values.
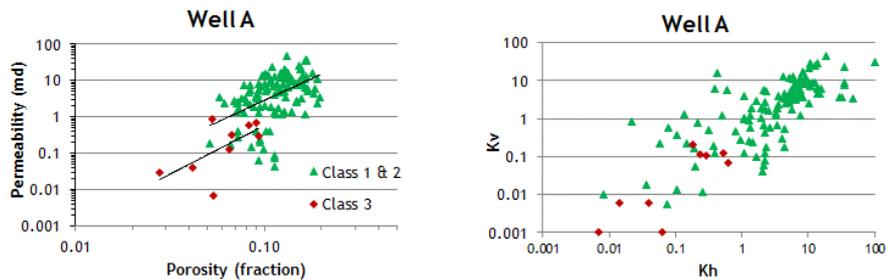
Figure 34: Core data for Well A (a) Porosity-permeability relation (b) Vertical permeability.

A 3D geologic model was setup for a sector using Petrel (Schlumberger) which included the wells (Figure 19) in the pilot area, and peripheral water and CO_2 injectors. The tops of the reservoir flow zones and impermeable zones were interpolated in the pilot area using information available at well level, which were used to build the geologic framework. Due to absence of seismic data, reservoir flow zones were assumed continuous in the interwell region unless they pinched out due to absence of a zone at any well. The model had 28 layers with areal grid cell dimensions of 50 feet. Facies model was prepared based on the cores and logs data available from the wells. The petrophysical properties were

populated stochastically in the interwell region constrained to facies distribution. The layers – 4, 8, 10 and 16, which correspond to the grain dominated facies of Petrophysical class 1, were input deterministically after the initial geomodel was built. The petrophysical properties for these 'Enhanced Permeability Zones' were assigned a constant value throughout the layer. The permeability distribution in the geomodel for a cross-section connecting wells 8, 3, 1, 5 and 10 (Figure 35) highlights the vertical heterogeneity in the reservoir.

It was realized that large uncertainties exist in modelling inputs because of absence of seismic information, and limited logs and cores. The geologic model was therefore matched to available production data to reduce the uncertainties, before using it for pilot design.
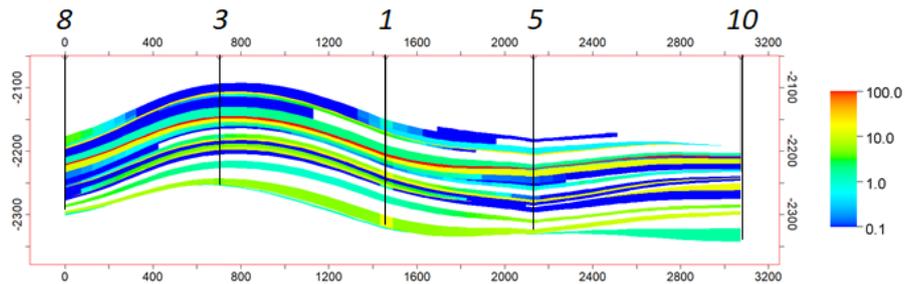
Figure 35: Cross-section along wells 8, 3, 1, 5 and 10 showing permeability in geologic model. (Reference: Paper VI)

4.2.2 Fluid and Rock Characterization

Table 1 lists the fluid composition for reservoir oil for MPZ and ROZ. Since oil in ROZ is immobile, a downhole oil sample could not be collected. The operator combined the stock tank oil sample from MPZ with synthetic gas (adjusted for gas composition from ROZ) for PVT studies. Peng-Robinson (PR) equation of state (EoS) model with six components was tuned to PVT data that was available for oil sample from MPZ. The model included 2 C7+ components, while the lighter components were lumped as CO_2, N_2+C1, H_2S+C2+C3, C4+C5+C6.

The reported C7+ fraction was split using Gamma distribution, followed by Gaussian quadrature based lumping. The critical properties were estimated using Lee-Kesler correlation. Pc, Tc and volume shift for the 2 C7+ components; and binary interaction coefficients for CO_2 and hydrocarbon components were tuned to get a match on the PVT data, including swelling factor and saturation pressure for swollen fluid. Pedersen model was tuned to fit the oil viscosity data, while keeping previously mentioned parameters out of regression. Figure 36 shows the fluid model fit to available experimental data from differential liberation, swelling and constant composition expansion tests, where experimental data is shown as circles and the line correspond to the response from the tuned EoS.

Component	Fluid Composition (mol %)	
	MPZ	ROZ
N_2	0.51	0.04
CO_2	2.47	0.02
H_2S	1.96	0
C1	24.65	20.1
C2	9.1	9.07
C3	7.57	6.95
iC4	1.41	0.04
nC4	4.03	3.9
iC5	1.76	0.04
nC5	2.03	2.49
C6	3.54	2.69
C7+	40.97	54.66

Table 1: MPZ and ROZ fluid composition. (Reference: Honarpour et al. 2010)

From laboratory measurements, it was found that the reservoir has mixed wettability with a tendency towards oil-wet behaviour, similar to other carbonate reservoirs. Base water-oil relative permeability (Figure 37) was obtained by tuning the parameters for Corey-type model to available coreflood data. Straight-line relative permeability with end-point of 1 were assumed for miscible oil displacement by CO_2 for the base case. The values for parameters of Corey-type model for all three phases were

allowed to vary during the history matching phases as explained later. Due to availability of limited special core analysis data, single set of relative permeability curves were used for all petrophysical classes.
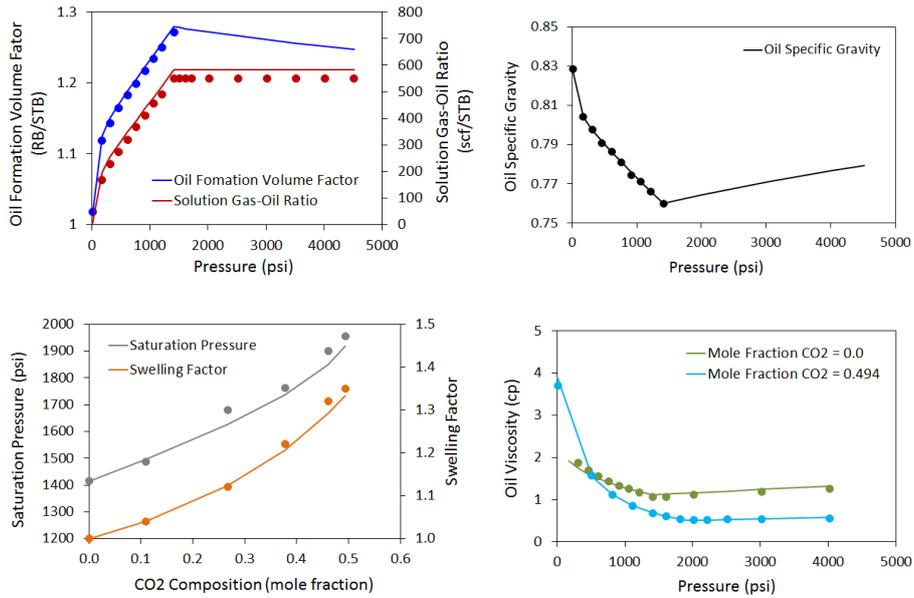
Figure 36: Fluid model fit to available PVT data including Differential liberation, Swelling test and Viscosity measurements. (Reference: Paper I)
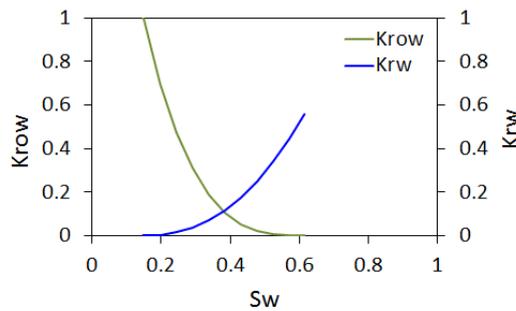
Figure 37: Base water-oil relative permeability. (Reference: Paper I)

4.2.3 Model Initialization

The hydrostatic reservoir pressure is 2300 psi at top of MPZ. Reservoir pressure has not been recorded since start of field production (around 1980 for the pilot area) until recently in 2017. From the infill wells that were drilled late in field life (a few years before start of CO_2 injection), it was inferred that the reservoir was around hydrostatic condition based on the drilling mud weight. Due to unavailability of reservoir pressure data, it was assumed that the reservoir was at hydrostatic pressure at start of water injection in the pilot area, and stayed close to hydrostatic condition during the waterflood. Based upon the gas-oil ratio (GOR) trend which stayed below solution GOR during waterflood, it was assumed that the reservoir pressure never went below the bubble point pressure of 1400 psi. Two-phase black oil model, with oil and water phases, was therefore found sufficient to model historical waterflood.

The initial water saturation in the model for waterflood simulation was assigned through enumeration, with MPZ at saturation of 0.1 based on laboratory SCAL studies. Pressure-retained cores that were extracted from an infill well suggested Remaining Oil Saturation (ROS) between 0.1 and 0.4 for ROZ, with an average of 0.32 (Honarpour et al. 2010). ROS for ROZ did not show any correlation with rock properties like porosity, permeability or a function of these two. ROS measured on cores recovered using Sponge coring was found to be between 0.1 and 0.38 with an average of 0.3. This was in good agreement with data from pressure-retained cores. ROZ was therefore assigned a higher water saturation of 0.68, which is much higher than irreducible water saturation due to natural water flooding that occurred during geological times.

Instead of continuing with black-oil fluid model, a compositional simulation model based on tuned EoS was used to simulate historical CO_2 injection. The pressure and water saturation were initialized from the state post waterflood simulation. The oil composition was based on data available from PVT study. Because of reservoir pressure staying

above bubble-point pressure throughout waterflood, it was assumed that the oil composition is uniform and no free gas is present in the reservoir at start of CO_2 injection.

4.2.4 Waterflood Match

Monthly production and injection data was available for 30 years from 1981 to 2013 for wells in the pilot area, which was used to calibrate the geologic model. As mentioned earlier, a black-oil fluid model with oil and water phase was used to model this period. Fluids were assumed to have constant compressibility and viscosity. Oil and water relative permeabilities were parameterized using Corey relation, with base values based on SCAL measurement:

$$k_{row} = k_{row}^0 \left(\frac{S_o - S_{orw}}{1 - S_{orw} - S_{wcon}} \right)^{n_{ow}} \tag{4.1}$$

$$k_{rw} = k_{rw}^0 \left(\frac{S_w - S_{wcon}}{1 - S_{orw} - S_{wcon}} \right)^{n_w} \tag{4.2}$$

where, k_{row}^0 and k_{rw}^0 are oil and water end-point relative permeability, while n_{ow} and n_w are Corey exponents for oil (in presence of water) and water respectively.

The wells were completed only in MPZ based on available well completion information. For simulation of historical waterflood, the producers were kept on historic liquid rate control, while the injectors were kept on historic water injection rate adjusted in proportion to the area they were feeding in the sector model (Figure 38). As shown in Figure 39, the geologic model was found to deviate significantly from the observed cumulative oil production trend for all the producers.
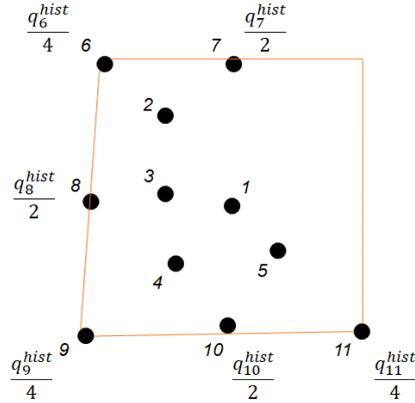
Figure 38: Rates for injectors - 6, 7, 8, 9, 10 and 11 adjusted in proportion to area fed in sector model. (Reference: Paper VI)
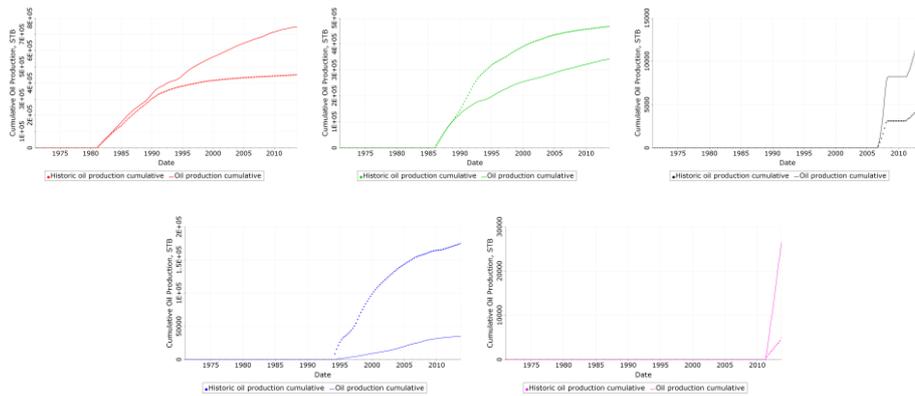
Figure 39: Mismatch in cumulative oil production based upon base geologic model for producers P-1, P-2, P-3, P-4 and P-5. (Reference: Paper VI)

The mismatch between simulated and observed cumulative oil production for each producer were added, with weighting in proportion to fraction of cumulative oil produced by that well, to form the objective function. The steps outlined in Figure 27 were followed to identify 15 most influential UPs (Table 2), and complete history match by reducing the objective function. Sector cumulative oil production and water-cut for cases selected to update the range for the UPs after history match are shown in Figure 40a and Figure 40b, respectively. Similarly, the cumulative oil production for the five producers (P-1, P-2, P-3, P-4 and

P-5) for the selected cases is shown in Figure 41. Table 2 shows the updated UPs (range and distribution) after match.

Parameter	Region	Layer	Distribution	Min	Max	Mean	Std Dev	P10	P90
SwCrit	All	All	Log Normal			0.24	0.03	0.21	0.27
Sorw	All	All	Normal			0.41	0.03	0.37	0.44
KroSwMin	All	All	Uniform	0.59	0.80			0.61	0.78
KrwSorw	All	All	Uniform	0.61	0.80			0.63	0.78
Nw	All	All	Uniform	1.04	1.31			1.07	1.28
Now	All	All	Log Normal			5.03	0.44	4.48	5.60
PVMult1	A	1 - 16	Triangular			1.91	0.02	1.72	2.14
PVMult2	B	1 - 16	Log Normal			0.98	0.08	0.88	1.08
PVMult3	C	1 - 16	Normal			0.10	0.01	0.08	0.11
PVMult4	D	1 - 16	Uniform	0.08	0.12			0.08	0.12
PVMult5	E	1 - 16	Uniform	6.52	8.45			6.71	8.25
PVMult6	F	1 - 16	Uniform	0.08	0.12			0.08	0.12
PermMult1	A, B, E	1 - 16	Uniform	0.43	0.58			0.44	0.57
PermMult2	C, D, F	1 - 16	Uniform	1.28	1.72			1.32	1.68
KYKX	All	All	Uniform	0.59	0.79			0.61	0.77

Table 2: Updated uncertainty parameters (range and distribution) based upon waterflood match (Reference: Paper VI)
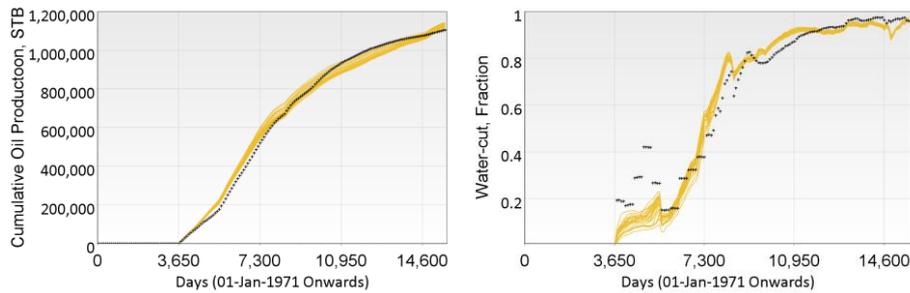
Figure 40: Simulation results at sector level for cases selected to update (posterior) uncertainty parameter ranges after running ES (a) Cumulative oil production (b) Water-cut. (Reference: Paper VI)
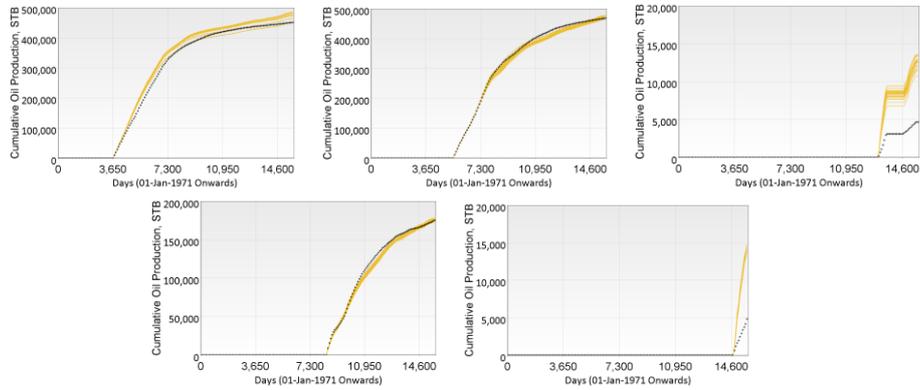
Figure 41: Cumulative oil production for producers P-1, P-2, P-3, P-4 and P-5, for cases selected to update (posterior) uncertainty parameter ranges after running ES. (Reference: Paper VI)

4.2.5 CO$_2$ Injection Match

Daily allocated oil and water production rate, and measured injection rate data was available for wells in the pilot area for around four years from October 2013 to March 2018 (Figure 42). The data was used to further calibrate the model for pilot area before using it for making predictions. Even though gas breakthrough was observed within four months of start of CO$_2$ injection in well 1, gas production could only be measured after two years from January 2016 onwards because of some facility constraints. Bottom-hole pressure measured in a well at a close distance to pilot area after three days of shut-in suggested increase in reservoir pressure from hydrostatic (2300 psi) in October 2013 to 3300 psi in July 2017. It was the only information available for reservoir pressure during historical CO$_2$ injection period. Flowing tubing-head pressure data was available for injectors from January 2016 onwards. No flowing pressure data was available for producers. Production logs could not be acquired because of presence of lift equipment in producers, low well productivity and high operational costs.
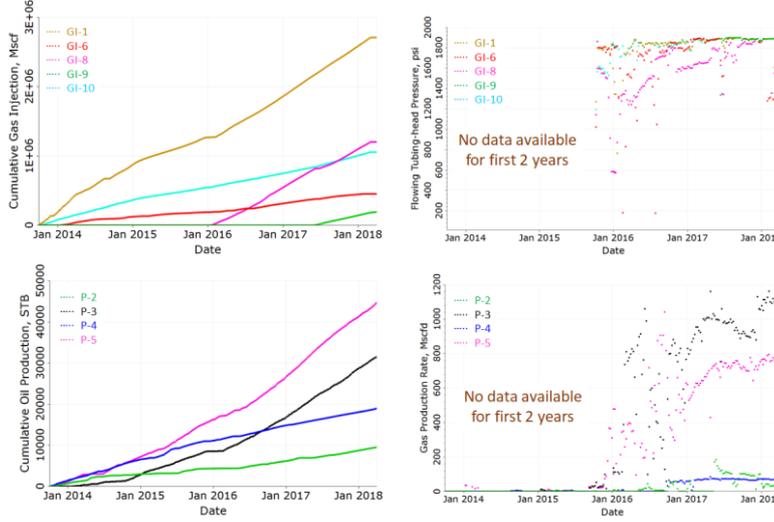
Figure 42: Well performance during CO_2 injection (a) Cumulative CO_2 injection (b) Tubing-head pressure (c) Cumulative oil production (d) Gas production rate. (Reference: Paper VI)

The compositional model setup has been explained earlier in section 4.2.2. Separate saturation functions were specified for drainage and imbibition processes for water and gas to capture hysteresis effects. The relative permeabilities were parameterized to allow variation in critical gas saturation, relative permeability end-points, and Corey exponents during history match process:

$$k_{rog} = k_{rog}^0 \left(\frac{S_l - S_{org} - S_{wcon}}{1 - S_{gcon} - S_{org} - S_{wcon}} \right)^{n_{og}} \qquad (4.3)$$

$$k_{rg} = k_{rg}^0 \left(\frac{S_g - S_{gcon}}{1 - S_{gcon} - S_{org} - S_{wcon}} \right)^{n_g} \qquad (4.4)$$

where, k_{rog}^0 and k_{rg}^0 are oil and gas end-point relative permeability, while n_{og} and n_g are Corey exponents to oil (in presence of gas) and gas respectively. Killough's non-wetting model was used to model hysteresis (ECLIPSE 2018).

64

The producers and CO_2 injectors were completed in both MPZ and ROZ based on available well completion information, in-line with the perforation activities performed in field at the start of CO_2 injection. For simulation of historical CO_2 injection, the producers were kept on historic liquid rate control, while the injectors were kept on historic water or CO_2 injection rate adjusted in proportion to the area they were feeding in the sector model (Figure 38).

The mismatch between simulated and observed response for — cumulative oil production for each producer, gas production rate for last two years and flowing bottom-hole pressure for injectors, were added with weighting in proportion to fraction of cumulative oil produced by that well, to form the objective function. The weighting was expected to improve the match for P-3 and P-5, which are the key producers for pilot with surfactant injection planned in well 1. The steps outlined in Figure 27 were followed to identify 43 most influential UPs (Table 3), and complete history match for CO_2 injection phase by reducing the objective function. UPs were setup for modifying pore volume and transmissibility in interwell regions for MPZ and ROZ; three-phase relative permeabilities; and well injectivities. All studies for CO_2 match were performed by fixing the 15 UPs from waterflood match at their mean values.

Sector cumulative oil production, water-cut and gas-oil ratio for cases selected to update the range for the UPs after history match are shown in Figure 43b through Figure 43d, respectively. The relative error in cumulative oil production was reduced to less than 10% after history match. The cumulative oil production, water-cut and gas-oil ratio for P-3 are shown in Figure 44. Table 3 shows the updated UPs (range and distribution) after CO_2 injection match.
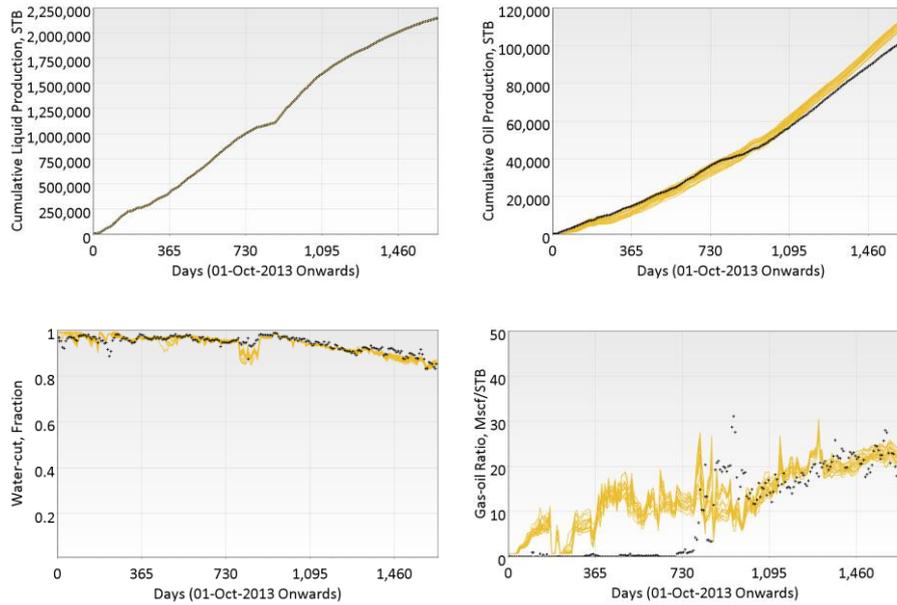
Figure 43: Simulation results at sector level for cases selected to update (posterior) uncertainty parameter ranges (a) Cumulative liquid production, showing producers do not switch from the assigned liquid rate control (b) Cumulative oil production (c) Water-cut (d) Gas-oil ratio. (Reference: Paper VI)
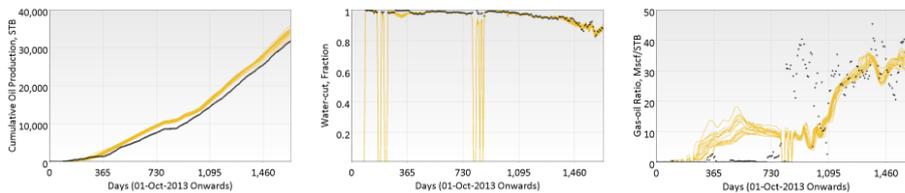
Figure 44: Simulation results for P-3 for cases selected to update (posterior) uncertainty parameter ranges after running ES (a) Cumulative oil production (b) Water-cut (c) Gas-oil ratio. (Reference: Paper VI)

Parameter	Layer(s)	Distribution	Min	Max	Mean	Std Dev	P10	P90
Krg@Connate Liquid	All	Uniform	0.90	1.00			0.91	0.99
Ng	All	Uniform	1.00	1.10			1.01	1.09
Nog	All	Uniform	1.00	1.20			1.02	1.08
SgCritIMB	All	Log-Normal			0.28	0.01	0.26	0.29
SgCritDRN	All	Triangular			0.32	2E-4	0.30	0.34

SwCritDRN	All	Normal			0.33	0.02	0.31	0.36
M4 (Wells 1 - 5: PV Mult)	1 - 16	Log-Normal			5.03	0.27	4.69	5.38
M5 (Wells 1 - 5: Trans Mult)	1 - 16	Normal			0.20	0.02	0.17	0.23
M6 (Wells 5 - 10: PV Mult)	1 - 16	Log-Normal			5.01	0.29	4.64	5.38
M7 (Wells 5 - 10: Trans Mult)	1 - 16	Uniform	0.80	1.00			0.82	0.98
M9 (Wells 1 - 3: Trans Mult)	1 - 16	Uniform	0.17	0.24			0.17	0.24
LY8A (Wells 1 - 3: Trans Mult)	8	Log-Normal			1.99	0.22	1.72	2.27
LY8B (Wells 3 - 8: Trans Mult)	8	Uniform	1.64	2.44			1.72	2.36
OP2 (Wells 1 - 3 Inner Region: Trans Mult)	4	Uniform	1.65	2.38			1.72	2.31
OP3 (Wells 1 - 3 Outer Region: Trans Mult)	4	Log-Normal			1.97	0.22	1.70	2.25
OP4 (Wells 1 - 3 Inner Region: Trans Mult)	7, 8	Log-Normal			1.99	0.23	1.71	2.28
OP5 (Wells 1 - 3 Outer Region: Trans Mult)	7, 8	Uniform	1.58	2.42			1.66	2.34
OP6 (Wells 1 - 3 Inner Region: Trans Mult)	10	Uniform	1.64	2.39			1.72	2.32
OP7 (Wells 1 - 3 Outer Region: Trans Mult)	10	Uniform	1.56	2.40			1.64	2.32
OP10 (Wells 1 - 5 Inner Region: Trans Mult)	4	Normal			1.00	0.13	0.84	1.16
OP11 (Wells 1 - 5 Outer Region: Trans Mult)	4	Log-Normal			1.92	0.22	1.65	2.21
OP12 (Wells 1 - 5 Inner Region: Trans Mult)	7, 8	Uniform	0.80	1.21			0.84	1.17
OP13 (Wells 1 - 5 Outer Region: Trans Mult)	7, 8	Log-Normal			1.97	0.23	1.68	2.27
OP14 (Wells 1 - 5 Inner Region: Trans Mult)	10	Uniform	0.80	1.20			0.84	1.16
OP15 (Wells 1 - 5 Outer Region: Trans Mult)	10	Uniform	1.61	2.39			1.69	2.31
R7 (Wells 5 - 10: PV Mult)	18 - 28	Log-Normal			0.10	0.01	0.09	0.11
R9 (Wells 2 - 6: PV Mult)	18 - 28	Log-Normal			0.10	0.01	0.09	0.11
R10 (Wells 2 - 6: Trans Mult)	18 - 28	Uniform	0.40	0.60			0.42	0.58
R14 (Wells 3 - 8: Trans Mult)	18 - 28	Uniform	1.23	1.81			1.29	1.75
R16 (Wells 1 - 5: Trans Mult)	18 - 28	Log-Normal			2.07	0.18	1.85	2.31
R18 (Wells 2 - 6: Trans Mult)	19	Uniform	0.40	0.61			0.42	0.59
WPIMULT_GI1	Completion	Log-Normal			0.06	0.01	0.05	0.06
WPIMULT_GI6	Completion	Uniform	0.25	0.35			0.26	0.34
WPIMULT_GI8	Completion	Uniform	0.45	0.66			0.47	0.64
WPIMULT_GI9	Completion	Uniform	2.00	3.03			2.10	2.93

WPIMULT_GI10	Completion	Uniform	0.04	0.08			0.04	0.08
WPIMULT_WI1	Completion	Uniform	0.30	0.50			0.32	0.48
WPIMULT_WI6	Completion	Uniform	0.20	0.30			0.21	0.29
WPIMULT_WI7	Completion	Uniform	0.15	0.20			0.16	0.19
WPIMULT_WI8	Completion	Uniform	1.99	3.03			2.09	2.93
WPIMULT_WI9	Completion	Uniform	6.98	8.04			7.09	7.94
WPIMULT_WI10	Completion	Uniform	1.98	2.93			2.08	2.84
WPIMULT_WI11	Completion	Uniform	0.20	0.30			0.21	0.29

Table 3: Updated uncertainty parameters (range and distribution) based upon CO_2 injection match (Reference: Paper VI)

The cell connection transmissibility factor had to be significantly reduced for most of the wells, which is defined as:

$$Cell\ Connection\ Factor = \frac{PIMULT * Kh}{\ln\left(\frac{r_o}{r_w}\right) + s} \qquad (4.5)$$

where $PIMULT$ is a user-specified number, Kh is the effective permeability times the net thickness of the connection, r_o is the 'pressure equivalent radius' of the grid block, r_w is the wellbore radius and *s* is the skin factor. The flowing bottom-hole pressure after match for well 1 (pilot injector) is shown in Figure 45. The ratio between the connection factors for history matched models to the geologic model, which was setup using petrophysical logs, was found to be 0.1 to 0.4, suggesting near-well damage.

Injection profiles have been recorded for GI-1 at a year's interval since start of CO_2 injection using radioactive tracer logging tool (Figure 46a). The technique though economic for small fields, has poor vertical resolution and can only identify zones of injection broadly. Therefore, the profiles were not used directly for history matching. The fractions of injected CO_2 entering into each of the two pay zones were calculated for the simulation model, and were compared with the observed fractions for

the four profiles to test the predictive capability of the history matched models. Because well 1 was a producer during waterflood phase with completions only in MPZ, this zone was expected to be depleted around well 1, compared to ROZ, at the start of CO_2 injection. CO_2 therefore preferentially flowed into MPZ until local equilibration between the zones was achieved. The fraction of injected CO_2 entering into MPZ reduced from 100% at the beginning of CO_2 injection (2013) to around 70% in 2 years. The calibrated models were found to track the variation in relative injectivity with time (Figure 46b).
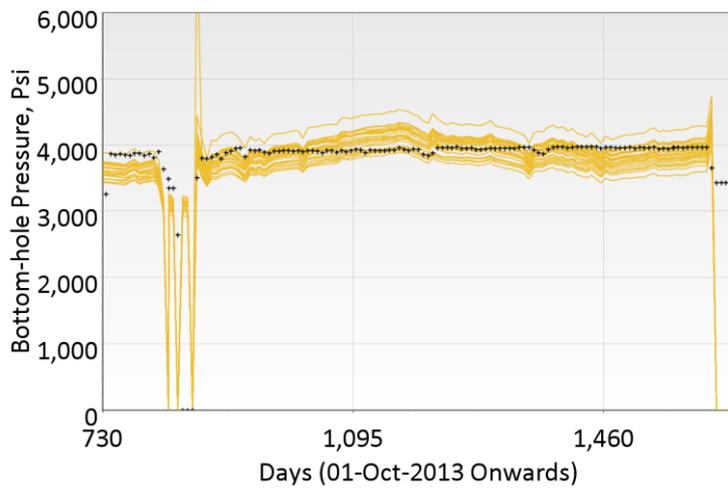
Figure 45: Flowing bottom-hole pressure for GI-1 for cases selected to update posterior uncertainty parameter ranges. (Reference: Paper VI)
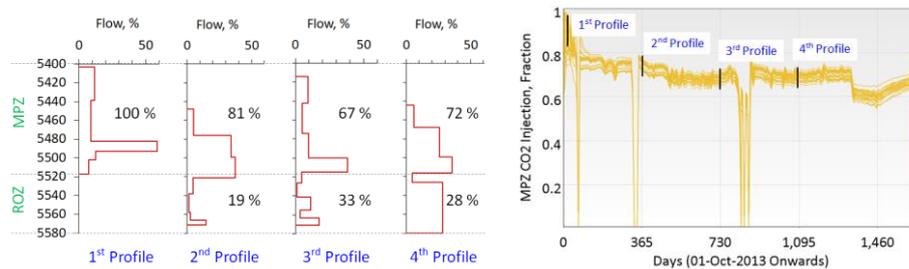
Figure 46: Fraction of CO_2 injected into GI-1 entering into MPZ for (a) Actual injection profiles (b) Cases selected after CO_2 injection match. (Reference: Paper VI)

69

In order to characterize the baseline communication between GI-1 and surrounding producers, a passive non-radioactive gas tracer was injected in GI-1 on 9 January 2018. The first set of data received from the field for the interwell tracer study showed tracer breakthrough in both P-3 and P-5 in 17 days, and no tracer production in P-2 and P-4. P-3 and P-5 have produced 16.5% and 6% of injected tracer until March 2018. The tracer study is still in progress, with a reduced sampling frequency of one sample every two weeks for all wells. The tracer response was therefore not included in the current history matching cycle. The simulation results for the cumulative tracer production for both P-3 and P-5, as a fraction of the total amount of tracer injected, are shown in Figure 47. Though the models predicts lower tracer production, which is expected due to absence of high resolution features in the current model, their performance was found acceptable for use in prediction.
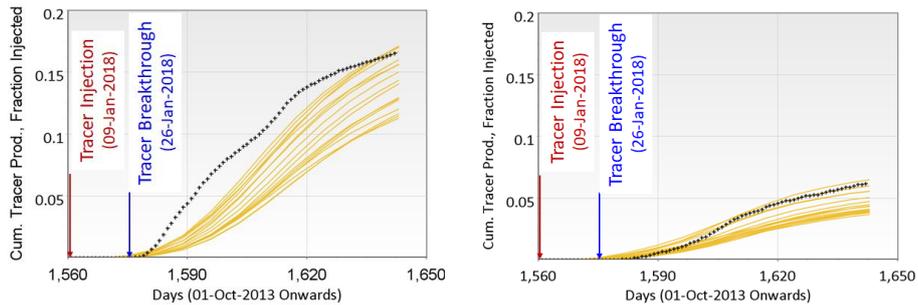
Figure 47: Cumulative tracer production, as fraction of injected volume, for cases selected to update posterior uncertainty parameter ranges (a) P-3 (b) P-5. (Reference: Paper VI)

4.2.6 Foam Model Parameters

The surfactant selected for the pilot was found to have very low adsorption of 0.08 mg/g (Jian et al. 2016) on reservoir material in laboratory. Because of significant increase in runtime of the base model with introduction of surfactant adsorption, it was excluded from the prediction study.

To account for the effect of permeability on foam behaviour, the reservoir model was divided into three regions depending upon the grid cell permeability as — Region 1 with permeability less than 10 mD, Region 2 with permeability in range of 10 to 50 mD and Region 3 with permeability greater than 50 mD. These regions were assigned different *fmmob*, *fmdry* and *epdry*.

Only limited reservoir core was available for laboratory studies. Most of the experiments were performed with reservoir core having permeability in range of 20 to 30 mD, which corresponds to Region 2. The base values for *fmmob*, *fmdry* and *epdry* for Region 2 were obtained by fitting empirical foam model to quality scan data (Figure 48a) through regression. The base values for *fmcap* and *epcap* were obtained by fitting the empirical foam model to rate scan data (Figure 48b), assuming *fmmob*, *fmdry* and *epdry* (estimated earlier) to be invariable for regression. Assumption were made about *fmmob*, *fmdry* and *epdry* to characterize foam behaviour for regions 1 and 3. It was assumed that no foam generates in Region 1, while apparent viscosity of foam in Region 3 was assumed twice as that of in Region 2. The range considered for these parameters for pilot performance prediction is listed in Table 4.
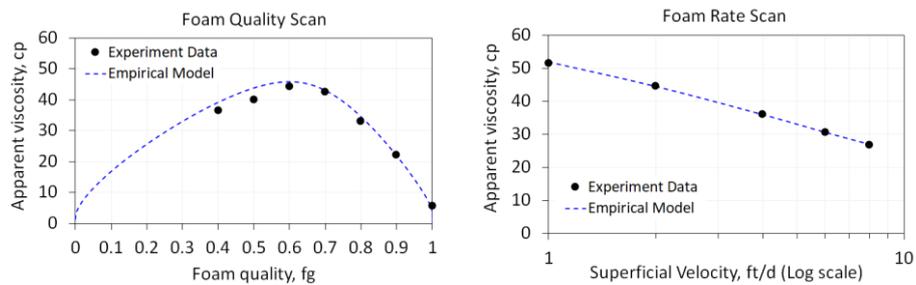
Figure 48: Experimental data and empirical foam model fit to (a) Quality scan (b) Rate scan. (Reference: Papers II and VI)

The critical micellar concentration (CMC) was found to be 0.01 wt% (0.035 lb/bbl) for the selected surfactant. The minimum concentration for foam generation was set at CMC, while the reference concentration for transition from weak to strong foam was assumed five times the

71

CMC. The base value of fumsurf was therefore set as 0.05 wt% (0.175 lb/bbl). Due to unavailability of data to characterize the steepness in the change of mobility reduction due to surfactant concentration, the base value of *epsurf* was assumed 1. Based upon CO_2-Foam EOR experiments, the maximum oil saturation above which foam ceases to exit (*fmoil*) was considered as 0.28. Due to unavailability of data to characterize the steepness in the change of mobility reduction due to oil saturation, the base value of *epoil* was assumed 1. The range of values for all foam model parameters which were considered for pilot performance prediction are listed in Table 4. Assumptions were made for the low and high values of the foam model parameters, considering 10-20% deviation from base value.

Parameter	Region	Low	Base	High	Distribution	Remarks
fmmob	1		0			Assumed no foam generation
	2	500	630	750	Uniform	Base value based on Quality Scan
	3	900	1200	1500	Uniform	
fmdry	1		0.32			
	2	0.243	0.27	0.297	Uniform	Base value based on Quality Scan
	3	0.198	0.22	0.297	Uniform	
epdry	1		500			
	2	80	100	120	Uniform	Base value based on Quality Scan
	3	20	25	30	Uniform	
fmcap	All	6.2e-7	7.8e-7	9.4e-7	Uniform	Base value based on Rate Scan
epcap	All	0.52	0.65	0.78	Uniform	Base value based on Rate Scan
fmsurf	All	0.14	0.175	0.21	Uniform	Base value assumed 5 times of CMC
epsurf	All	0.8	1	1.2	Uniform	
fmoil	All	0.21	0.28	0.35	Uniform	Base value from EOR experiments
epoil	All	0.5	1	2	Uniform	

Table 4: Uncertainties in foam model parameters considered for forecasting (Reference: Paper VI)

4.2.7 Pilot Performance Predictions

A surfactant component was added to the aqueous phase to model foam behaviour (Islam and Farouq-Ali 1990). The aqueous phase only had the water component present during CO_2 injection match. Before using a particular model for making predictions, the regions were assigned depending upon updated permeability after history match, using a script. The simulator was found to lack reliable modelling of dry-out effect during SAG. A local grid refinement (LGR) was introduced around the pilot injector, where grid cells were refined areally from 50 ft x 50 ft to

10 ft x 10 ft. In order to model foam dry-out during SAG near injector, the innermost cells (within LGR) connecting to injector were assigned an *fmmob* of 0 to mimic foam absence within a radius of 5 ft around injector.

12 UPs that were introduced to model foam behavior were combined with 58 UPs from history matching phase, and LHC sampling was used to generate 100 cases under two scenarios. The first scenario (Figure 49a) is based on operators' current plan to implement 2:1 WAG with a year of water injection followed by six months of CO_2 injection. The second scenario (Figure 49b) considers 12 cycles of SAG, followed by continuous CO_2 injection. Based on discussions with the operator regarding field operational constraints, a SAG strategy with 10 days of surfactant injection and 20 days of CO_2 injection, was found most suitable. As mentioned earlier, water and CO_2 injection will be constrained to approximately half of the maximum rates that can be injected in well 1 at maximum allowable flowing bottom-hole pressure. This corresponds to water and CO_2 injection rate of 300 STB/D and 1000 Mscfd, respectively. For each case, simulations were run using the sampled values for both historical period (waterflood, CO_2 injection) and forecast period (three years). The grid-cell pressures, saturations and compositions for each case for CO_2 injection and forecast period were based on the values extracted from the last step of previous period.
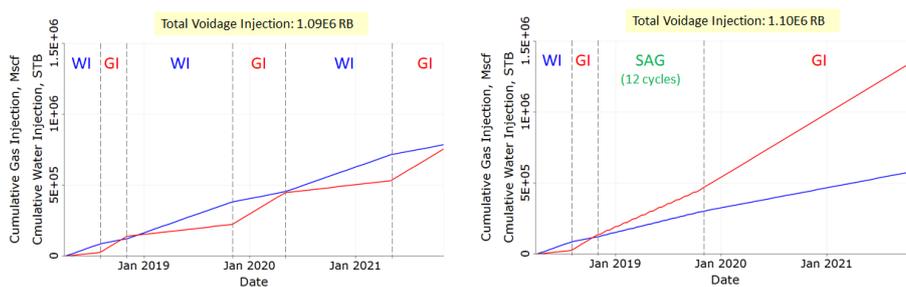
Figure 49: Injection scheme for (a) Base case scenario with WAG (b) Pilot with 12 SAG cycles followed by CO_2 injection. (Reference: Paper VI)
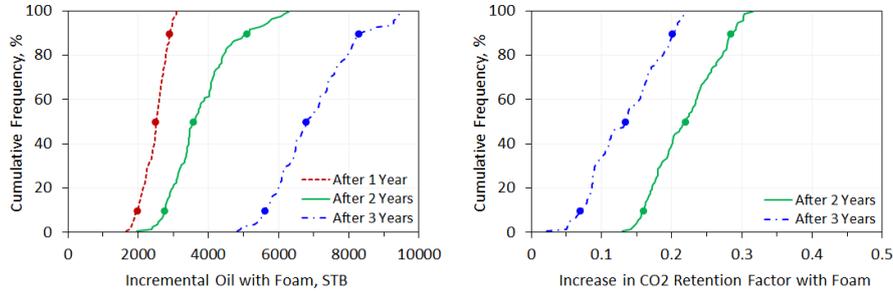
Figure 50: Cumulative distribution for (a) Incremental oil (b) Increase in CO_2 retention factor. (Reference: Paper VI)

The cumulative probability distributions for incremental oil for Scenario 2 with respect to Scenario 1 after 1 year, 2 years and 3 years of start of pilot are shown in Figure 50a. Similarly, the cumulative probability distribution for CO_2 retention factor for both the scenarios after 2 years and 3 years of start of pilot are shown in Figure 50b. Foam selectively generates in high permeability region, which allows diversion of CO_2 into low permeability regions, resulting in a higher oil recovery and CO_2 retention. P90, P50 and P10 values for incremental oil and increase in CO_2 retention with foam are listed in Table 5.

KPI	Time	P90	P50	P10
Incremental Oil, STB	1 Year	1900	2500	2800
	2 Years	2700	3500	5000
	3 Years	5600	6700	8200
Increase in CO_2 Retention Factor	2 Years	0.16	0.22	0.28
	3 Years	0.07	0.13	0.20

Table 5: Confidence intervals for KPIs based upon simulation cases (Reference: Paper VI)

5   Concluding Remarks

5.1   Conclusions

The oil industry has taken several initiatives in last decade to meet rising energy demand while lowering greenhouse gas emissions by increasing energy efficiency and advancing research in alternative energy sources. The industry has nearly five decades of experience in injecting CO_2 into oil reservoirs for EOR. Moreover, the associated CO_2 storage is expected to be effective for thousands of years. Based upon the laboratory studies, it is well understood that foam can be used to improve oil recovery and CO_2 storage efficiency during CO_2 EOR. However, there exists a knowledge gap about viability of the technology for field-scale applications. As part of this research work, CO_2-Foam field pilot was designed for an onshore heterogeneous carbonate reservoir in West Texas, USA. The objective of the overall research, which also includes another field pilot in a sandstone reservoir, is to develop a roadmap for implementing the technology of mobility control using foam for CO_2 EOR and storage on the NCS through low-cost onshore field trials.

The research work elucidates that foam can be used for CO_2 mobility control to improve sweep, which results in enhanced oil recovery and improved storage efficiency. The laboratory experiments for a field application should be designed to guide surfactant selection, its concentration and foam quality to ensure minimal surfactant loss to formation and other phases, and foam stability at reservoir conditions in presence of oil. The fact that foam behaviour varies with permeability should be considered while selecting reservoir core plugs to perform foam coreflood experiments. The well injectivity in current operating conditions and expected during foam pilot should be considered while choosing the injection strategy between co-injection and surfactant-alternating-gas injection. Knowing the reservoir state (pressure, saturations and compositions) by using appropriate techniques, at the

beginning and end of the pilot, will help understand the large-scale foam displacement. Since, limited data is available to characterize reservoir at a fine scale in most cases, we should incorporate uncertainties in model prediction based on uncertainties in available information. Depending upon resource availability to perform numerical studies and findings from the sensitivity study, uncertainty parameters which have low influence on key performance indicators can be excluded from the study.

The main conclusions for the pilot planned in the carbonate reservoir are:
- CO_2-Foam stability: Extensive work was done in laboratory to ensure foam stability at reservoir conditions.
    - The pore-scale behavior seen in micromodel suggested a half-life of 13.3 hours for CO_2-Foam under static conditions in absence of oil. The study was performed for a period of 72 hours, when 37% of the original bubbles were found to survive confirming long-term stability of CO_2-Foam.
    - The foaming ability of the selected surfactant in presence of oil was confirmed using bulk-foam stability test.
    - Foam-quality scan suggested that foam with high apparent viscosity can be generated with gas fraction of 0.7.

- CO_2-Foam EOR: CO_2 and surfactant co-injection after waterflood, at foam quality of 0.7, resulted in an additional recovery of 28.8% OIIP from reservoir core.
    - The recovery was lower than for pure CO_2 injection after waterflood, most likely due to liquid films and emulsion formations resulting in reduced contact between CO_2 and oil. However, CO_2 and surfactant co-injection after CO_2 injection, at quality of 0.7 resulted in an additional recovery of 15% OIIP.

- Foam model parameters: Because of complex foam dynamics and challenges associated with extracting model parameters from coreflood experiments, the implicit-texture approach was found more appropriate to model large-scale foam behaviour.

76

o Foam quality scan was used to obtain initial estimate of foam model parameters by using best-fit straight line for high-quality regime and a convex curve for low-quality regime.

o The initial estimate of foam model parameters served as an input to a least-square fitting routine in MatLab. The misfit between laboratory data and empirical model prediction for both foam quality and rate scans were simultaneously reduced to obtain representative foam parameters for use in forecasting.

- Integrated reservoir model: A 3D model was setup with appropriate resolution to capture reservoir heterogeneity.

    o Core data was available for a well in the pilot area which was used to obtain porosity-permeability relation and KvKh ratio for different petrophysical classes.

    o The model was initialized for pressure, saturation and composition based on information provided by the operator and available in literature.

- Model calibration and forecasting: The main objective of numerical modelling was to create a reliable forecast for the pilot phase.

    o A workflow for assisted history matching was developed, which was used to calibrate the base reservoir model. The distribution of the uncertainty parameters was updated to reduce the misfit between observed data and model response. Data for 30 years of waterflood and around 4 years of CO_2 injection was used to obtain a calibrated uncertainty parameters, mainly based on pore volume and interwell connectivity. An acceptable match was obtained for cumulative oil production and gas-oil ratio, both at sector and well levels.

    o The calibrated models captured the trend for CO_2 injection into MPZ obtained from historical injection profiles, despite being excluded from the history matching cycle. Similarly, the initial findings from the baseline interwell tracer study were excluded from the objective function setup. The calibrated models were

however found to predict tracer production to an acceptable level. Also, the findings supported presence of barriers in the pilot area, which were introduced during history matching.

- o Uncertainty parameters that were introduced to model foam behavior were combined with those from history matching to obtain cumulative distribution for incremental oil and increase in CO_2 retention with foam over operators' current reservoir management plan.
- o Workarounds were implemented to model mechanisms which are not currently captured by commercial simulators.

- Field data acquisition: The surveillance strategy was planned to obtain data to allow quantification of pilot success vis-à-vis pilot objectives and characterization of large-scale foam displacement.
    - o The flowing pressure of the proposed injector will be continuously monitored during the pilot. Baseline and repeat injection profiles will be recorded for the proposed injector to confirm CO_2 diversion to previously unswept layers. The surrounding producers will be tested frequently to obtain more reliable information on oil production rate and gas-oil ratio, instead of relying on allocation based on sparse tests.
    - o Baseline interwell gas tracer study is in progress, which will help characterize the communication between proposed injector and surrounding producers. The tracer study will be repeated at the end of the pilot with a different gas tracer. Baseline fall-off test is planned for the proposed injector to improve reservoir characterization and identify reservoir features like fractures, faults and presence of distinct mobility regions around the well. It is planned to repeat the fall-off test at the end of the pilot.

In summary, a systematic approach was developed to produce a basis for pilot performance expectations subject to uncertainties before start of actual operations. This approach is generic and can be applied to other pilot studies.

5.2   Future Work

The reservoir selected for the trial is currently being depressurized. A baseline interwell tracer study is in progress. It is planned to run baseline injection profiling and fall-off test in the proposed pilot injector. It is also planned to hang a pressure gauge on an electric line wire, close to reservoir top, with real-time surface readout, to allow better control on surface operations.

The injection wellsite currently has a WAG skid, where injection brine is delivered at a pressure of 1450 psi and CO_2 is delivered at a pressure of 1900 psi. Surface facilities for the pilot will require minor modifications to existing setup and additional equipment as shown in Figure 51. The planned operating procedure for pilot injection is outlined below:

- 15000 gallons (358 bbl) of brine will be pumped into a holding tank (A), where it will heated to 45°C using a hot oil truck (B).
- The surfactant will arrive as molten 100% product at the wellsite in 5000 gallon (120 bbl) heated tanker truck at 45°C (C).
- The surfactant from the truck and pre-heated water from holding tank will be passed through inline mixer (D) for partial dilution until all surfactant is transferred from the tanker truck to the holding tank.
- The surfactant solution will be circulated using a centrifugal pump (E) in a closed loop to obtain uniform 25 wt% solution.
- Since heating is required only while mixing, the hot oiler truck will be dispatched from field until next cycle, to avoid additional costs. The viscosity of 25 wt% surfactant solution is expected to vary thereafter from 20 to 70 cP depending on ambient surface temperature.
- The concentrated 25 wt% solution and injection brine will then be metered into the final dilution line (F) to desired volumetric ratios to obtain a concentration of 0.5 wt %. Based on the planned injection strategy, one batch of 25 wt% surfactant solution is expected to last for 5 to 6 SAG cycles (months).

In addition, an oxygen scavenger (1000 ppm Carbohydrazide) and Scale Inhibitor (50 ppm Phosphonate) will be added upstream of in-line mixer to limit surfactant degradation. Sampling ports will be available at different locations to ensure that sufficient amount of scavenger is always present to remove dissolved oxygen. Similarly, a sampling port will be available before wellhead to analyse for injected surfactant concentration. A refractometer will be used on-site for quick measurement of surfactant concentration.
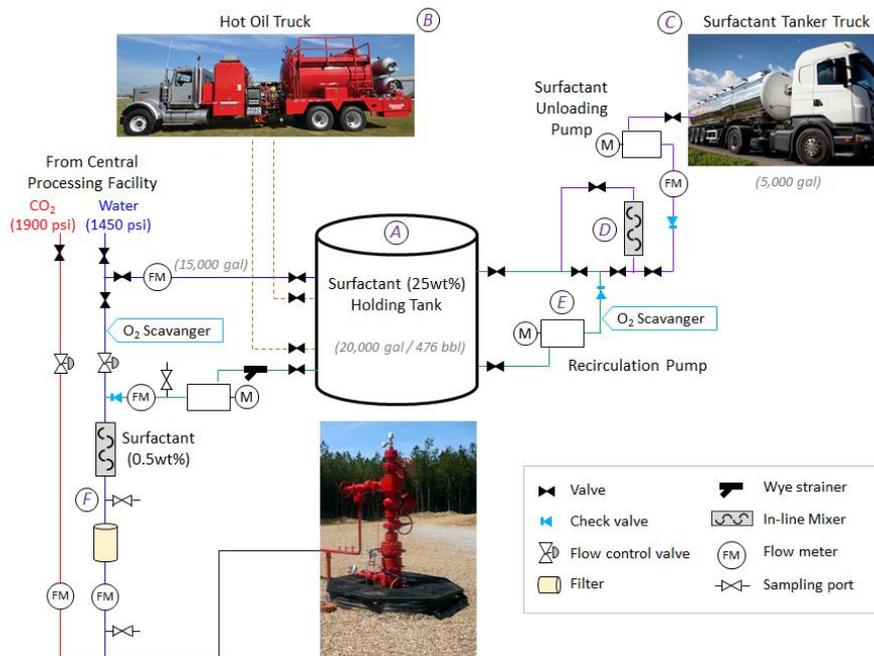
Figure 51: Schematic showing surface equipment for surfactant injection during pilot.

References

Alvarez, J.M., Rivas, H. and Rossen, W.R., 2001. A Unified Model for Steady-State Foam Behavior at High and Low Foam Qualities. *SPE J.* **6**, 325-333.

Amirmoshiri, M., Zeng, Y., Chen, Z., Singer, P.M., Puerto, M.C., Grier, H., Kamarul Bahrim, R.Z., Vincent-Bonnieu, S., Farajzadeh, R., Biswal, S.L. and Hirasaki, G.J. 2018. Probing the Effect of Oil Type and Saturation on Foam Flow in Porous Media: Core-Flooding and Nuclear Magnetic Resonance (NMR) Imaging. *Energy & Fuels* **32** (11), 11177-11189.

Aveyard, R., Binks, B.P., Fletcher, P.D.I., Peck, T.G. and Rutherford, C.E. 1994. Aspects of aqueous foam stability in the presence of hydrocarbon oils and solid particles. *Adv Colloid Interface Sci* **48**, 93-120.

Back, T., 1996. Evolutionary Algorithms in Theory and Practice. Oxford U. Press, Oxford, U.K.

Boeije, C. S., and Rossen, W. R. 2015. Fitting Foam-Simulation-Model Parameters to Data: I. Coinjection of Gas and Liquid. *SPE Res Eval Eng* **18** (02), 264 – 272.

Bond, D. C., and O. C. Holbrook 1958. Gas drive oil recovery process. U.S. Patent No. 1958, 2866507.

Cannon, S. 2018. Reservoir Modelling: A Practical Guide, first edition. Hoboken, NJ: John Wiley & Sons Inc.

Cheng, L., Reme, A.B., Shan, D., Coombe, D.A. and Rossen, W.R., 2000. Simulating Foam Processes at High and Low Foam Qualities. SPE/DOE Symposium on Improved Oil Recovery, Tulsa, OK, 3-5 April.

Chou, S.I., Vasicek, S.L., Pisio, D.L., Jasek, D.E. and Goodgame, J.A., 1992. CO_2 Foam Field Trial at North Ward-Estes. SPE Annual Technical Conference and Exhibition, Washington DC, 4-7 October.

Dykstra, H. and Parsons, R.L. 1950. The Prediction of Oil Recovery by Waterflooding in Secondary Recovery of Oil in the United States. 2nd Edition, API, Washington DC.

References

ECLIPSE Technical Description. 2018. Reservoir Simulation Software, Schlumberger.

Enick, R.M., Olsen, D.K., Ammer, J.R. and Schuller, W. 2012. Mobility and Conformance Control for CO_2 EOR via Thickeners, Foams, and Gels - A Literature Review of 40 Years of Research and Pilot Tests. SPE Improved Oil Recovery Symposium, Tulsa, Oklahoma, 14-18 April.

Falls, A.H., Hirasaki, G.J., Patzek, T.W., Gauglitz, D.A., Miller, D.D. and Ratulowski, J. 1988. Development of a Mechanistic Foam Simulator: The Population Balance and Generation by Snap-Off. *SPE Res Eng* **3**, 884-892.

Farajzadeh, R., Andrianov, A., Krastev, R., Hirasaki, G.J. and Rossen, W.R. 2012. Foam-Oil Interaction in Porous Media: Implications for Foam Assisted Enhanced Oil Recovery. *Adv. Colloid Interface Sci.* **183-184**, 1-13.

Gauglitz, P.A., Friedmann, F., Kam, S.I. and Rossen, W.R. 2002. Foam Generation in Homogeneous Porous Media. *Chem. Eng. Sci.* **57**, 4037-4052.

Green, D.W. and Willhite, G.P. 1998. Enhanced Oil Recovery, Society of Petroleum Engineers, Richardson, Texas, USA.

Harpole, K.J. and Hallenbeck, L.D. 1996. East Vacuum Grayburg San Andres Unit CO_2 Flood Ten Year Performance Review: Evolution of a Reservoir Management Strategy and Results of WAG Optimization. SPE Annual Technical Conference and Exhibition, Denver, Colorado, 6-9 October.

Heller, J.P., Boone, D.A. and Watts, R.J. 1985. Field Test of CO_2 Mobility Control at Rock Creek. SPE Annual Technical Conference and Exhibition, Las Vegas, Nevada, 22-26 September.

Heller, J.P. 1994. CO_2 Foams in Enhanced Oil Recovery. In Foams: Fundamentals and Applications in the Petroleum Industry, Advances in Chemistry 242, ed. L. L. Schramm, Chapter 5, 201-234. American Chemical Society.

Hirasaki, G. J. and Lawson, J. B. 1985. Mechanisms of Foam Flow in Porous Media: Apparent Viscosity in Smooth Capillaries. *SPE J.* **25**, 176–190.

Holm, L.W. and Garrison, W.H. 1988. CO_2 Diversion With Foam in an Immiscible CO_2 Field Project. *SPE Res Eng* **3** (1), 112-118.

Hoefner, M. L. and Evans, E. M. 1995. CO_2 Foam: Results from Four Developmental Field Trials. *SPE Res Eng* **10** (4), 273-281.

Honarpour, M.M., Nagarajan, N.R., Grijalba Cuenca, A., Valle, M. and Adesoye, K. 2010. Rock-Fluid Characterization for Miscible CO_2 Injection: Residual Oil Zone, Seminole Field, Permian Basin. SPE Annual Technical Conference and Exhibition, Florence, Italy, 19-22 September.

IPCC Special Report on Carbon Dioxide Capture and Storage. Metz, B., Davidson, O., Coninck, H. de, Loos, M. and Meyer, L. 2005 Cambridge, UK: Cambridge University Press.

Islam, M.R. and Farouq-Ali, S.M. 1990. Numerical Simulation of Foam Flow in Porous Media. *J Can Pet Technol* **29** (4), 47-51.

Isenberg, C. 1992. The Science of Soap Films and Soap Bubbles. Dover Publications Inc., New York.

Jarrell, P.M., Fox, C.E., Stein, M.H. and Webb, S.L. 1990. Practical Aspects of CO_2 Flooding. SPE Monograph Series, 22.

Jian, G., Puerto, M.C., Wehowsky, A., Dong, P., Johnston, K.P. and Hirasaki, G.J. 2016. Static Adsorption of an Ethoxylated Nonionic Surfactant on Carbonate Minerals. *Langmuir* **32** (40), 10244-10252.

Jonas, T.M., Chou, S.I. and Vasicek, S.L. 1990. Evaluation of a CO_2 Foam Field Trial: Rangely Weber Sand Unit. SPE Annual Technical Conference and Exhibition, New Orleans, Louisiana, 23-26 September.

Juanes, R., Spiteri, E.J., Orr Jr., F.M. and Blunt, M.J. 2006. Impact of relative permeability hysteresis on geological CO_2 storage. *Water Resources Research* **42** (12).

Khan, M.N., Iwama, H., Al-Neaimi, A., Al-Shehhi, O. and Chatterjee, M. 2016. A to Z of Gas Tracers – A Decade of Learning and Experience. SPE Abu Dhabi International Petroleum Exhibition & Conference, Abu Dhabi, UAE, 7-10 November.

References
___

Kibodeaux, K.R. and Rossen, W.R. 1997. Coreflood Study of Surfactant-Alternating-Gas Foam Processes: Implications for Field Design. SPE Western Regional Meeting, Long Beach, CA, June 25-27.

Kim, J.S., Dong, Y. and Rossen, W.R., 2005. Steady-State Flow Behavior of CO_2 Foam. *SPE J.* **10**, 405-415.

Krevor, S., Blunt, M J., Bension, S M., Pentland, C H., Reynolds, C., Al-Menhali, A., and Niu, B. 2015. Capillary trapping for geologic carbon dioxide storage – From pore scale physics to field scale implications. *International Journal of Greenhouse Gas Control* **40**, 221-237.

Lake, L.W., Johns, R.T., Rossen W.R. and Pope, G.A. 2014. Fundamentals of Enhanced Oil Recovery. Society of Petroleum Engineers, Richardson, Texas, USA.

Leeftink, T.N., Latooij, C.A. and Rossen, W.R. 2015. Injectivity errors in simulation of foam EOR. *J Petrol Sci Eng* **126**, 26-34.

Lotfollahi, M., Farajzadeh, R., Delshad, M., Varavei, A. and Rossen, W.R. 2016. Comparison of implicit-texture and population-balance foam models. *J Nat Gas Sci Eng* **31**, 184-197.

Ma, K., Biswal. S.L. and Hirasaki, G.J. 2012. Experimental and Simulation Studies of Foam in Porous Media at Steady State. AIChE Spring Meeting, Houston, TX, 1-5 April.

MatLab, The MathWorks, Inc., Natick, Massachusetts, United States.

Melzer, L.S. 2012. Carbon Dioxide Enhanced Oil Recovery (CO_2 EOR): Factors Involved in Adding Carbon Capture, Utilization and Storage (CCUS) to Enhanced Oil Recovery. Report prepared for the National Enhanced Oil Recovery Initiative, Center for Climate and Energy Solutions.

Merchant, D.H. 2010. Life Beyond 80: A look at Conventional WAG Recovery Beyond 80% HCPV Injection in CO_2 Tertiary Floods. SPE International Conference on CO_2 Capture, Storage, and Utilization, New Orleans, Louisiana, USA, 10-12 November.

Mukherjee, J., Nguyen, Q. P., Scherlin, J., Vanderwal, P.G. and Rozowski, P. 2016. CO_2 Foam Pilot in Salt Creek Field, Natrona County, Wyoming: Phase

III: Analysis of Pilot Performance. SPE Improved Oil Recovery Symposium, Tulsa, Oklahoma, USA, 11-13 April 2016.

Nguyen, Q.P., Hirasaki, G.J. and Johnston, K. P. 2015. Novel CO_2 Foam Concepts and Injection Schemes for Improving CO_2 Sweep Efficiency in Sandstone and Carbonate Hydrocarbon Formations. Technical Report, U.S. Department of Energy / National Energy Technology Laboratory.

Osterloh, W.T. and Jante, M.J. 1992. Effects of Gas and Liquid Velocity on Steady-State Foam Flow at High Temperature. SPE/DOE EOR symposium, Tulsa, OK, April 22-24.

Ransohoff, T.C. and Radke, C.J. 1988. Mechanisms of Foam Generation in Glass-Bead Packs. *J Res Eng* **3**, 573-585.

Rossen, W.R. 1996. Foams in Enhanced Oil Recovery. In Foams Theory, Measurements, and Applications. eds. Prud'homme, R.K. and Khan, S.A. volume 57, ch. 11, p 414-464, Marcel Dekker Inc., New York.

Rossen, W.R., Zeilinger, S.C., Shi, J.X. and Lim, M.T., 1999. Simplified Mechanistic Simulation of Foam Processes in Porous Media. *SPE J.* **4**, 279-287.

Sanders, A., Jones, R. M., Linroth, M.A. and Nguyen, Q. P. 2012. Implementation of a CO_2 Foam Pilot Study in the SACROC Field: Performance Evaluation. SPE Annual Technical Conference and Exhibition, San Antonio, Texas, USA, 8-10 October.

Schulze-Riegert, R.W., Axmann, J.K., Haase, O., Rian, D.T. and You, Y.,-L. 2002. Evolutionary Algorithms Applied to History Matching of Complex Reservoirs. *SPE Res Eval Eng* **5** (2), 163-173.

Sharma, M., Taware, S.V. and Datta-Gupta, A. 2016. Optimizing CO_2 Floods Using Rate Control with Smart Wells Under Geologic Uncertainty. SPE Abu Dhabi International Petroleum Exhibition & Conference, Abu Dhabi, UAE, 7-10 November.

Veld, K. van t, Mason, C.F. and Leach, A. 2013. The Economics of CO_2 Sequestration Through Enhanced Oil Recovery. *Energy Procedia* **37**, 6909-6919.

Wang, F.P., Lucia, J.F. and Kerans, C. 1998. Integrated Reservoir Characterization Study of a Carbonate Ramp Reservoir: Seminole San Andres Unit, Gaines County, Texas. *SPE Res Eval Eng* **1** (2), 105-113.

Zeng, Y., Muthuswamy, A., Ma, K., Wang, L., Farajzadeh, F., Puerto, M., Vincent-Bonnieu, S., Eftekhari, A.A., Wang, Y., Da, C., Joyce, J.C., Biswal, S.L. and Hirasaki, G.J. 2016. Insights on Foam Transport from a Texture-Implicit Local Equilibrium Model with an Improved Parameter Estimation Algorithm. *Ind Eng Chem Res*, **55** (28), 7819–7829.

Part 2

Paper I: Numerical Modelling Study for Designing CO₂-Foam Field Pilot

Sharma, M., Alcorn, Z.P., Fredriksen, S.B., Fernø, M.A., Graue, A.

Numerical Modelling Study for Designing CO2-Foam Field Pilot

M. Sharma[a,*], Z. P. Alcorn[b], S. B. Fredriksen[b], M. A. Fernø[b] and A. Graue[b]
[a] The National IOR Centre of Norway, University of Stavanger
[b] Department of Physics and Technology, University of Bergen

Abstract

Carbon dioxide has been successfully used in fields for tertiary oil recovery; and because of technical, commercial and environmental reasons, it has received considerable attention in recent years over other solvents. Based on experience with CO_2 flooding worldwide, it is well understood that despite its high local displacement efficiency, the process suffers from poor sweep efficiency due to reservoir heterogeneity, viscous instability and gravity override. Application of foam has been found to mitigate these limitations at laboratory scale, however understanding of CO_2-Foam flow behaviour at a larger scale is limited industry-wide. Some of the previous pilots have shown technical success especially near wellbore, but there exist a need to establish an integrated methodology to scale-up the CO_2-Foam technology efficiently and effectively.

As part of an ongoing research program, we have identified a field with heterogeneous carbonate reservoir onshore in west Texas, USA to run CO_2-Foam field trial. The research emphasizes on implementing a modelling, monitoring and verification approach as part of the roadmap. Static model created by integrating petrophysical logs and core data in-line with geologic framework, and dynamic model created based on analysis of reservoir engineering data including Routine Core Analysis (RCA), Special Core Analysis (SCAL), fluid phase behaviour, pressure data and coreflood experiments forms the basis for reservoir simulation study for the pilot area. In this paper, we provide an overview of different elements of numerical model and demonstrate application of a systematic approach to incorporate the uncertainties associated with model inputs, which is further used to guide resource allocation for baseline survey. The success will be validated via appropriate monitoring plan in the ongoing pilot research program.

Keywords

CO2, Foam, Mobility control, Field pilot, Uncertainty

1. Introduction

   CO_2 injection has proven to be an attractive technique for improving oil recovery in mature fields, which have been waterflooded for several years (Jarrell et al. 1990). Although CO_2 has properties making it favourable compared to other solvents, it also suffers from phenomena like gravity segregation, viscous fingering and channeling, eventually leading to poor sweep. Previous studies (Heller 1994, Kibodeaux and Rossen 1997, Turta and Singhal 1998, Fernø et al. 2015a) confirm the effectiveness of foam for mobility control at core scale. Figure 1 (Haugen et al. 2014) shows that for oil-wet fractured core plugs, use of foam can significantly improve tertiary recovery and sweep efficiency, especially under miscible conditions. Based on these studies, it is well understood that foam can improve conformance for solvent-based EOR by reducing gas mobility away from the injectors and selectively isolating high permeability zones within reservoir.

   The challenge is to ensure the scalability of displacement mechanisms to a larger scale, and development of a fit-for-purpose approach that will assist in advancing CO_2 foam technology to high risk and high cost environment. So, a field pilot research program has been initiated which aims at integrating traditional laboratory studies with data acquired from field pilot studies to get insights into fluid dynamics at multiple scales.

* Corresponding Author
Email: mohan.sharma@uis.no

A few field pilots have been run in past with varying extent of success. One of the earliest field pilot for foam-assisted CO_2 EOR was performed in the Wilmington field, located in southern California in 1984, which achieved the primary objectives (Holm and Garrison 1988). Since then field tests have been performed in Rock Creek, Virginia (Heller et al. 1985), Rangley Weber Sand Unit, Colarado (Jonas et al. 1990), North Ward/Estes, Texas (Chou et al. 1992), Slaughter, west Texas and Greater Areth, southeast Utah (Hoefner and Evans 1995), East Vacuum Grayburg/San Andres Unit, New Mexico (Harpole and Hallenbeck 1996), SACROC, Texas (Sanders et al. 2012) and Salt Creek (Mukherjee et al. 2014, 2016) with success to varying extent. Due to low oil prices and technical challenges involved in the process, foam has not been tested since the mid-90s. However, continued decline in conventional production and growing concern about climate change associated with emission of greenhouse gases has renewed interest over recent past in use of foam for mobility control as part of Carbon Capture, Utilization and Storage (CCUS).

This research works aims at scaling up CO_2 foam EOR from laboratory to field. In order to accomplish the objective, a heterogeneous carbonate reservoir has been identified onshore in west Texas, USA. Various stages of the project have been initiated, and the paper aims at providing an overview of different elements involved in this multidisciplinary research. Given the fact that there is limited data available for detailed reservoir characterization, a probabilistic approach has been applied to understand the impact of individual uncertainty parameter on key performance indicators. This has been used to transition the project through the 'Concept Select' and 'Define' phases to 'Execute' phase. As an outcome, an appropriate data acquisition strategy has been decided and agreed with the operator, to improve the baseline model, which will be used as a vehicle to obtain an injection strategy subject to reduced level of uncertainties.

2. Methodology

2.1. Field Overview

The Unit-A of the field selected for pilot study, which is located in Permian basin, west Texas (Figure 2), was developed throughout the 1940s and produced 12% of mapped oil initially in place until late 1960s. Waterflood began in early 1970s with infill drilling to establish 40-acre peripheral waterflood patterns. The Unit-B was developed throughout early 1980s. However, with a low primary plus secondary recovery of only 22% of OIIP by late 1980s, the operator realized the need to reduce pattern size. An infill program was run to develop both the units on a 20-acre five spot pattern. Infill drilling yielded excellent results with increase in production from 400 BOPD to 1200 BOPD. However, a steep decline in production and high residual oil saturations in the reservoir rock after waterflood indicated the potential for tertiary oil recovery.

It has been well identified from the regional data that the reservoir consists of two zones (Figure 3): Main Pay Zone (MPZ), and Residual Oil Zone (ROZ). MPZ has produced by primary depletion and waterflooded for over 50 years. ROZ is thought to be formed by structural tilting or seal breach events, and has been naturally waterflooded over geologic time. ROZ has significant immobile oil (20-40% of OOIP), which cannot be technically drained by primary or secondary mechanisms.

Tertiary CO_2 injection for EOR started in south-eastern part of the Unit-B in Oct-2013 to target remaining oil, both in MPZ and ROZ with commingled production and injection. This resulted in increased production rate from 10 BOPD to 15 BOPD. However, the peripheral producers of the pattern have already experienced CO_2 breakthrough, with breakthrough occurring as early as within 4 months from start of CO_2 injection. The reservoir heterogeneity and unfavourable mobility of CO_2 thus makes the reservoir a good candidate to improve sweep and reduce CO_2 recycling by foam injection.

Aligned with the operator's plans for field development, and to minimize the amount of time required to gather data, an injector-producer well pair was selected for the first foam injection trial. The selection of a well pair is advantageous for the use of CO_2 foam as interwell distances are greatly reduced, and reservoir response to foam can be seen at much shorter time intervals. After a careful analysis of possible well pairs in the south-eastern portion of the Unit-B, a well pair consisting of injector I1 and producer P5 was identified. Some of the criteria governing the choice of pilot area included continuity of reservoir flow zones, well injectivity, gas breakthrough time, well arrangement and well workover requirements etc.

2.2. Laboratory Studies

A range of surfactants including cationic, nonionic and zwitterionic were explored to identify candidates that have the potential to satisfy all the key requirements for CO_2 foams in carbonate reservoirs (Nguyen et al. 2015). The formation, texture, rheology and stability of CO_2 foams was examined as a function of the surfactant structure and formulation variables including temperature, pressure, water/ CO_2 ratio, surfactant concentration, salinity and concentration of oil. Furthermore, the partitioning of surfactants between oil and water, as well as CO_2 and water was examined in conjunction with adsorption measurements to develop strategies to optimize the transport of surfactants in reservoirs. A non-ionic water-soluble surfactant from Huntsman - Surfonic L24-22 was selected for field pilot based on surfactant screening studies for the reservoir (Jian et al. 2016). Surfonic L24-22 is a linear alcohol ethoxylate produced by the addition of ethylene oxide (EO) to linear, primary alcohols. It is a 22 mole ethoxylate of linear, primary 12-14 carbon number alcohol.

Because of material unavailability from the field (i.e. reservoir core and crude oil), limestone core from an analogous reservoir was used to obtain parameters for foam modelling. The cores were 100% saturated with synthetic reservoir brine made from analytical grade chemicals. A surfactant solution was made by adding 1 wt% Surfonic L24-22 to reservoir brine. The core-scale system was made up of two 2" limestone cores stacked vertically providing a total length of ~25cm. The cores were pre-flushed with surfactant solution prior to foam injection to reduce adsorption effects. To investigate the stability and generation of foam, gas and surfactant solution were co-injected at a total rate of 50ml/h (~2 ft/day) starting at a foam quality of 0.9 (i.e. CO_2 and surfactant solution was simultaneously injected at a ratio of 9:1). The pressure differential was measured across the cores as foam was generated in-situ. When differential pressure reached steady-state, the foam quality was reduced in steps of 0.1 to obtain a foam quality scan (Osterloh and Jante 1992, Xu and Rossen 2004, Kim et al. 2005). The process was repeated until a foam quality of 0.1 was achieved. The experiment was performed at supercritical conditions of 85 bar and 60°C.

There are two general approaches available to model foam transport. The first, explicit-texture population-balance model (Falls et al. 1988, Rossen et al. 1999), allows direct simulation of foam creation, propagation, and coalescence effects that can be observed in laboratory core experiments (Fernø et al. 2016). The second approach, an implicit-texture local-equilibrium model (Cheng et al. 2000¸Alvarez et al. 2001), uses an empirical relation to capture the effect of surfactant concentration, water saturation, oil saturation (Law et al. 1992, Farajzadeh et al. 2012), shear thinning due to flow velocity on foam mobility. The gas permeability in presence of foam (k_{rg}^f) is modified by multiplying the gas relative permeability without foam (k_{rg}^{nf}) at a specific water saturation with a mobility reduction factor (FM), which is a function of aforementioned factors. The water permeability in presence of foam remains unchanged.

$$k_{rg}^f = k_{rg}^{nf} \times FM \qquad (1)$$

Because of complex foam dynamics and challenges associated with extracting model parameters from coreflood experiments for mechanistic population-balance approach, the second approach was found more appropriate for foam scoping studies at field pilot scale. We studied the effect of water saturation, shear rate and surfactant concentration on mobility reduction factor in numerical modelling, given by the expression:

$$FM = \frac{1}{1 + fmmmob \times F_{water} \times F_{shear} \times F_{surf}} \qquad (2)$$

$fmmmob$ refers to the maximum gas mobility reduction that can be achieved. F_{water} , F_{shear} and F_{surf} with expressions below capture the water saturation, shear rate and surfactant concentration dependence, with all lying in the range of 0 to 1. The capillary number N_{ca} represents the relative effect of viscous and capillary forces.

$$F_{water} = 0.5 + \frac{arctan[epdry(S_w - fmdry)]}{\pi} \tag{3}$$

$$F_{shear} = \begin{cases} \left(\frac{fmcap}{N_{ca}}\right)^{epcap} & if\ N_{ca} > fmcap \\ 1 & otherwise \end{cases} \tag{4}$$

$$F_{surf} = \left(\frac{Surfactant\ concentration}{fmsurf}\right)^{epsurf} \tag{5}$$

The apparent foam viscosity was calculated at steady state based on the data generated from laboratory coreflood experiments. Regression was performed to obtain values for *fmmob*, *fmdry* and *epdry* (Ma et al. 2012), and an acceptable match to measured data was obtained at values of 180, 0.4 and 10000 for these parameters respectively (Figure 4). The values for *fmcap* and *epcap* were based on previous studies. The critical saturation at which foam collapses was considered as 0.475 for this study. *fmsurf*, which corresponds to reference concentration for transition from weak to strong foam was assumed to be ten times the critical micellar concentration (0.01 wt%) measure in lab. *epsurf* was assumed to be 1.

2.3. Geologic Model

The field produces from the San Andres reservoir, a heterogeneous carbonate formation consisting of subtidal to supratidal deposits. The formation was deposited during a regression of Guadalupian seas with minor rises in sea level creating a cyclical sequence of subtidal and intertidal deposits, interbedded with shaley mudstone layers. Mudstone layers act to limit vertical communication throughout the reservoir and can be thought of as barriers to flow. Subtidal dolostone facies make up the bulk of the reservoir rock, which are typically located deeper within the overall pay section. Reservoir rocks have well developed intercrystalline porosity, which has later been enhanced through leaching and subsequent dedolomitization (Wang et al. 1998).

To assist the pilot design, a sector model for the selected well pair and the peripheral producers was setup. The reservoir heterogeneity makes investigation of the continuity of reservoir flow zones in interwell region challenging. Identification of rock units with appreciable reservoir characteristics was based on the analysis of available petrophysical logs and well core. The information was used to establish a geologic framework for the pilot area (Alcorn et al. 2016).

Drill core and well log data were correlated in the pilot area. Gamma ray, neutron, density, and resistivity logs were used to tie the core analysis to log data and define flow units. Porosity was calculated from the neutron and density logs; lithology and saturation was determined from gamma ray and resistivity logs, respectively. The porosity for reservoir zones range between 0.12 to 0.15, whereas permeability varies between 1 mD to 300 mD with an average of 15 mD. Four and two flow zones were identified in MPZ and ROZ respectively, each separated by impermeable units.

A three-dimensional reservoir model was built for the pilot area using the structural and geocellular modeling capabilities of Petrel (Schlumberger 2015.1). The tops of the reservoir flow zones and impermeable zones were mapped, which were used to build the geologic framework. The grid has dimensions of 63 x 61 x 46 with approximately 120,000 active cells. Grid cell are 50ft x 50ft areally, and layer thickness varies from 1-10 feet depending upon mapped stratigraphic units. Facies model was prepared based on the hard data (cores and logs) available from the wells. Porosity, permeability, and water saturation derived at each well location provided values for grid cells penetrated by the well. Since limited information is available to characterize the reservoir, the modeling workflow began with a framework obtained deterministically, and moved towards a stochastic approach to obtain interwell property distribution. Static properties were extended to interwell regions through the calibration of individual petrophysical well data to the modelled facies distribution. Stochastic simulation of petrophysical properties was used with stratigraphic constraints to populate grid cell properties in interwell regions as shown in Figure 5 and Figure 6.

2.4. Simulation Model

A conventional finite-difference compositional model (ECLIPSE, Schlumberger 2015.1) was set-up using the tuned EoS model (Islam and Farouq-Ali 1990, Rossen 2013, Masoudi et al. 2015). In ECLIPSE, aqueous phase is traditionally modelled using a single component. We introduced a second component to model the surfactant component for the foam model. Foam adsorption and desorption were modelled using reversible chemical reaction. A component to model surfactant adsorbed to the rock was introduced. The effect of solid deposition on pore volume (or permeability) reduction was not included in the modelling. Foam decay was also modelled using a chemical reaction to convert the surfactant component to water. Other foam model parameters were specified as obtained from laboratory studies. Grid cells with permeability less than 5 mD were identified as a region property, and were assigned an fmmob of 0. All other grids cells were assigned the value obtained from laboratory study, which was varied during uncertainty study as explained in next section. The mathematical details of the foam model and chemical reaction model is available in the ECLIPSE Technical Description, and are not discussed here.

Fluid and rock characterization is important for reservoir performance prediction. Available data, including well surveys, was analysed to prepare inputs for an integrated baseline model. The composition for oil sample from MPZ was measured in laboratory (Honarpour et al. 2010). Because oil in ROZ is immobile and significant quantity of oil could not be collected, the operator used recombined sample of stock tank oil from MPZ and synthetic gas (adjusted for gas composition from ROZ) for PVT studies (Table 1). Data for routine tests and swelling experiment was available for oil sample from MPZ, which was used to tune Peng-Robinson (PR) equation of state (EoS) model. The Minimum Miscibility Pressure was measured using Slimtube test as 1500 psi. An 8-component model including 4 C7+ components was set up, where the lighter components were lumped as CO_2, N_2+C1, $H_2S+C2+C3$, $C4+C5+C6$. The C7+ fraction from reported composition was split using Gamma distribution, followed by Gaussian quadrature based lumping and critical property estimation using Lee-Kesler. Pc, Tc and volume shift for 4 C7+ components; and binary interaction coefficients for CO_2 and hydrocarbons were tuned to get a match on routine PVT and swelling test data. The tuned EoS was then used to match the oil viscosity data using Pedersen model. Previously mentioned parameters were excluded from the regression while tuning viscosity. Figure 7 and Figure 8 show the fluid model fit to available experiment data from differential liberation, swelling and constant composition expansion tests (test data as circles and tuned model as line). The cores recovered using pressure-retaining coring in an infill well for ROZ were used to measure oil and water saturation, mainly using Dean Stark extraction. Remaining Oil Saturation (ROS) ranged between 10-40 % with an average of 31.7 %, and did not show any significant correlation with rock properties like porosity, permeability or square root of the ratio of permeability to porosity. ROS measured on cores recovered using Sponge coring on four wells ranged from 10-38 % with an average of 29.8 %. This was in good agreement with data on pressure-retained cores. The observed water saturation in the ROZ is much higher than the Swirr from primary drainage capillary pressure due to natural water flooding that occurred during geological times. The water-oil relative permeability curve (Figure 9) has been obtained by tuning the parameters for Corey-type model to available laboratory coreflood data. Straight-line relative permeability function has been used for miscible oil displacement by CO_2 in numerical modelling.

Due to availability of limited production data, information derived from petrophysical logs and well surveys that were run prior to start of CO_2 injection, coupled with base geology model, forms the basis for reservoir simulation studies. The reservoir pressure for I1 was recently measured to be 3714 psia at 5300 ft. This depth is slightly above the topmost reservoir horizon for the pilot area, and was considered reference for simulation studies. The pressure recorded was higher than hydrostatic (2300 psi at reference depth), which increased during CO_2 injection over past 4 years. The operator is considering depressurizing the reservoir by completing a disposal well in a separate reservoir zone. Injection profiling was done for reservoir zone in I1 under flowing conditions with CO_2 injection at 1.2 MMscfd with approximately 300 psi pressure drop across perforations, suggesting good injectivity in MPZ and ROZ. The profile was used to tune the well model. Base CO_2 injection rate of 2 MMscfd and base water injection rate of 1000 BWPD has been used as well control for I1, in-line with current field observation. The wellhead injection pressure is constrained to keep bottom-hole pressure 250 psi below the formation fracture pressure.

Capturing the well injectivity is critical for designing the injection strategy, because injection of a low-mobility fluid like foam will increase the operating bottom-hole pressure to maintain set injection rate, and eventually reduction in injection rate when bottom-hole pressure reaches a set upper constraint. The issues that complicates prediction of well injectivity is the shear-thinning behavior of foam, which can lead to underestimation of injectivity with the use of Peacemen equation in the injection well grid block (Leeftink et al. 2015). Specifically during SAG, foam dries out below a critical water saturation near wellbore during gas cycle. This abrupt collapses increases gas mobility and injectivity significantly in near wellbore region. We addressed this issue by grid refinement around the injector at the cost of increased runtime.

To stay aligned with operator's philosophy of reservoir management, SAG injection was planned for pilot study to avoid any corrosion problems in surface facilities. We studied a scenario consisting of three alternate slugs of surfactant and CO_2 injection with one month frequency each at a similar voidage rate. A preflush slug of water precedes the surfactant-alternating-CO_2 injection. The water injected in this stage will be compatible with subsequent chemical water injection, and will contain a sacrificial agent to minimize surfactant losses from the surfactant slugs. The last CO_2 cycle is followed by chase water injection for two months, which will be continued to completion of the pilot during subsequent modelling work and field operations.

2.5. Pilot Simulation Study

It is well understood within the integrated reservoir modelling domain that forecasting has to take into account the existence of a wide range of uncertainties that are caused by the complexity and access to limited information about subsurface systems. As a result, even the most carefully constructed models do not exactly represent reality, and their fundamental equations do not exactly describe the actual physical behaviour. To recognize the effect of all sources of uncertainty, we implemented a probabilistic forecasting workflow (Figure 10). The model-based forecast is accompanied with an estimate of the uncertainty in the forecast, which can be made using an ensemble of forecasts. It is then implicitly assumed that a (tuned) set of values for model parameters would describe (imprecise) observations of past and future behaviour. With the availability of well pressure and production data, the workflow typically involves using post-history match probability distributions for the uncertain parameters (Fernø et al. 2015b). For our study, we found it sufficient to construct a set of equi-probable forecasts using the agreed range for uncertainty parameters (UPs). The workflow requires identifying the Key Performance Indicators (KPIs) for the prediction phase at the uncertainty framing sessions. For the pilot, these included incremental fluid volume production at end of pilot, injection pressure and breakthrough time for surfactant. There is limited information available for characterizing reservoir, rock behaviour and foam model parameters. Therefore, parameters available for ROZ were used for MPZ, where applicable; and an uncertainty matrix (Table 2) was setup after discussion with stakeholders.

3. Results

3.1. Sensitivity Analysis

Sensitivity analysis was run to evaluate how uncertainty in model inputs affects the model outputs. This involves generating simulations by varying one UP at a time from base value to low and high values. Tornado diagrams for KPIs were inspected after performing sensitivity analysis, where x-axis of such a diagram shows the relative change in the value of the selected KPI from base case. Each UP in the model has its own bar, where red and blue bars corresponds to low and high values of that UP, respectively. The width of each bar shows how much impact that UP can have on a selected KPI when varied through a range. The diagram is essentially a ranked list of UPs that was considered for designing surface operation plan and data acquisition program.

Based on the discussion with operator, the bottom-hole pressure for injector was found to be an important KPI because of flowing bottom-hole pressure close to fracture pressure. Foam generation is expected to reduce injectivity, and the rates will have to be constrained while maintaining injection pressure during pilot. Figure 11a shows the tornado diagram for bottom-hole pressure for injector at start of surfactant injection. As shown in the figure, the bottom-hole pressure for injector at start of

surfactant injection is more sensitive to permeability, water injection rate and initial fluid saturation compared to others. Figure 11b shows that the bottom-hole pressure for injector during first CO_2 slug injection (post surfactant slug) is also sensitive to foam model parameters, especially those controlling shear-thinning.

Various other KPIs were also identified like incremental oil production, amount of surfactant required, volumes of water and CO_2 required, drop in gas-oil ratio etc., out of which the first two were of more importance to the operator. Figure 12a shows the tornado diagram for cumulative oil production for pilot phase, which suggests that even though foam model parameters influence the additional recovery, the uncertainty in oil saturation for MPZ has highest influence on it. The data acquisition program should thus aim to reduce the uncertainty range in remaining oil saturation in MPZ before start of pilot. Figure 12b shows that the amount of surfactant required depends relatively more on permeability, water injection rate and initial oil saturation than other uncertain parameters.

3.2. Experimental Design

Sensitivity analysis was followed by experimental design study to evaluate uncertainty in predictions. Some of the UPs could be removed as most of the KPIs did not show much sensitivity to variation in them, however we carried all the UPs for further analysis as simulations could be run within available time. Moreover, there is the possibility that some parameters may have an influence on the simulation model in conjunction with other parameters, which gets captured in this step.

The UP ranges were sampled again using Latin Hypercube technique to generate approximately 10 times the 'number of UPs' simulation cases. Latin Hypercube takes the cumulative distribution function and splits the cumulative probability into equally large compartments. The number of compartments, and as a result the extent of detail, is determined by the number of simulations created. Each forecast used the same unique set of uncertainty parameter values for sampling to ensure that the entire parameter space is represented in the design matrix. After creating production profiles, discrete P90, P50 & P10 cases can be selected.

The preliminary study focussed on estimating the volume requirements for injectant fluid (water, CO_2) and surfactant. Figure 13 shows cumulative water injection for the pilot duration, including preflush and chase period. The mean of all the forecasts obtained from simulation, or the ensemble mean, provides good information on the most likely amount of water required during pilot, subject to known unknowns. Similarly, Figure 14 shows volume of CO_2 required during pilot phase. The amount of surfactant required for the pilot subject to various combination of UPs is shown in Figure 15, which suggests that 275,000 – 425,000 lbs of surfactant will be required for the pilot. The spread of the ensemble forecast indicates the confidence we can have in the predictions, where a large spread here indicates more uncertainty in predictions.

4. Discussion

The results from the pilot simulation study were discussed with the operator, to agree on field operations' plan including data acquisition. The operator measured the water injectivity for the proposed injector for pilot phase, which was a producer until 2013, and was on continuous CO_2 injection since then. The water injectivity was found to be around 600 bbl/d which is lower than the range (800-1000-1200), including the injectivity index multiplier (0.8-1-1.2), that was considered for this study. Given the fact that surfactant cost will be a significant share of the overall pilot cost, it was agreed to keep the total amount of surfactant to 200,000 lbs, and optimize the injection strategy in next phase of pilot design.

Because of limited margin on increasing injection pressure, the operator will drill a disposal well in a separate deeper reservoir to facilitate reservoir depressurization before initiating the pilot. However, because of availability of core from previous wells and understanding of vertical communication, no coring and vertical pressure profiling has been planned for this well.

One of the CO_2 injectors in a similar pattern, further south of the pilot area, will be converted form continuous CO_2 injector to Water-alternating- CO_2 (WAG) injector, with 2:1 water-gas slug size ratio. It has bene planned to use the change in injectivity during multiple WAG cycles and additional recovery as a baseline to the proposed SAG pilot.

The data acquisition program has been designed to reduce uncertainty on some of the heavy-hitters like interwell connectivity and fluid saturations. In addition to surface monitoring, the plan for data acquisition, based on this study, includes injection profiling, tracer study and cross-well seismic. An interwell gas tracer study will be performed to understand the baseline volumetric sweep pattern for each producer with respect to proposed injector I1. The petrophysical logs that are available for the wells will be reprocessed to estimate remaining oil saturation post waterflood based on information from similar reservoirs in west Texas. Measuring saturation by running new petrophysical log or performing partitioning interwell tracer study was found to be expensive. The numerical model will be initialized using these saturations and calibrated for historical CO_2 injection, before simulating foam injection. The planned surveys will thus help reduce the uncertainty in performance prediction.

Foam model parameters based either on experiments performed with limestone core from an analogous reservoir or on assumptions were also found to impact the KPIs. It was decided to perform experiments with reservoir core and fluids under representative conditions to obtain more reliable foam model.

5. Conclusions

The design and performance prediction for the field pilot relies heavily on the numerical model generated by integrating multidisciplinary inputs. Given the fact that a limited data is available for reservoir characterization, the uncertainty analysis produces a basis for pilot performance expectations prior to start of field operations. We presented the analysis for one specific scenario with three SAG cycles. The results of this analysis were used to design the data acquisition program, within available resources, to assist in improved reservoir characterization. Laboratory work is currently ongoing to investigate mobility control during CO_2 injection and foam stability using selected surfactant at reservoir pressure and temperature using core material from the formation. The additional baseline surveys will shed more light on interwell connectivity and fluid distribution. The reservoir model is thus expected to grow in complexity over time as more data becomes available, which will used as a basis to derive an optimal injection strategy.

Acknowledgements

Nomenclature

fmmob	Maximum gas mobility reduction factor
fmdry	Foam model parameter in Fwater
epdry	Foam model parameter in Fwater
fmcap	Foam model parameter in Fshear
epcap	Foam model parameter in Fshear
fmsurf	Foam model parameter in Fsurf
epsurf	Foam model parameter in Fsurf
BOPD	Barrels of oil per day
BWPD	Barrels of water per day
CCUS	Carbon Capture, Utilization and Storage
CCE	Constant Composition Expansion
EoS	Equation of State
FM	Mobility reduction factor
KPI	Key Performance Indicator

MMscfd	Million standard cubic feet per day
MPZ	Main Pay Zone
OIIP	Oil Initially In Place
PR	Peng-Robinson
ROZ	Residual Oil Zone
SAG	Surfactant-alternating-Gas
Sorw	Residual oil saturation for water
UP	Uncertainty Parameter
USBM	U.S. Bureau of Mines
WAG	Water-alternating-Gas (CO_2)

References

Alcorn, Z.P., Fernø, M. and Graue, A., 2016. Workflow for Optimal Injection of CO_2 to Enhance Oil Recovery in Mature Oil Fields: A Preliminary Study for a Field Pilot Program. SPE Bergen One-Day Seminar, Bergen, Norway, 20 April.

Alvarez, J.M., Rivas, H., and Rossen, W.R., 2001. A Unified Model for Steady-State Foam Behavior at High and Low Foam Qualities. SPE J. 6, 325-333.

Cheng, L., Reme, A.B., Shan, D., Coombe, D.A. and Rossen, W.R., 2000. Simulating Foam Processes at High and Low Foam Qualities. SPE/DOE Symposium on Improved Oil Recovery, Tulsa, OK, 3-5 April.

Chou, S.I., Vasicek, S.L., Pisio, D.L., Jasek, D.E. and Goodgame, J.A., 1992. CO_2 Foam Field Trial at North Ward-Estes. SPE Annual Technical Conference and Exhibition, Washington, D.C., 4-7 October.

Falls, A.H., Hirasaki, G.J., Patzek, T.W., Gauglitz, D.A., Miller, D.D. and Ratulowski, J., 1988. Development of a Mechanistic Foam Simulator: The Population Balance and Generation by Snap-Off. SPE Res. Eng. 3, 884-892.

Farajzadeh, R., Andrianov, A., Krastev, R., Hirasaki, G.J. and Rossen, W.R., 2012. Foam-Oil Interaction in Porous Media: Implications for Foam Assisted Enhanced Oil Recovery. Adv. Colloid Interface Sci. 183-184, 1-13.

Fernø, M.A., Eide, Ø., Steinsbø, M., Langlo, S.A.W., Christophersen, A., Skibenes, A., Ydstebø, T. and Graue, A., 2015. Mobility control during CO_2 EOR in fractured carbonates using foam: Laboratory evaluation and numerical simulations. J. Petrol. Sci. Eng. 135, 442-451.

Fernø, M.A., Steinsbø, M., Eide, Ø., Ahmed, A., Ahmed, K., Graue, A., 2015. Parametric study of oil recovery during CO_2 injections in fractured chalk: Influence of fracture permeability, diffusion length and water saturation. J. Nat. Gas Sci. Eng. 27 (2), 1063-1073.

Fernø, M.A., Gauteplass, J., Pancharoen, M., Haugen, Å., Graue, A., Kovscek, A.R. and Hirasaki, G., 2016. Experimental Study of Foam Generation, Sweep Efficiency, and Flow in a Fracture Network. SPE J. 21 (4), 1140-1150.

Harpole, K.J. and Hallenbeck, L.D., 1996. East Vacuum Grayburg San Andres Unit CO_2 Flood Ten Year Performance Review: Evolution of a Reservoir Management Strategy and Results of WAG Optimization. SPE Annual Technical Conference and Exhibition, Denver, Colorado, 6-9 October.

Haugen, A., Mani, N., Svenningsen, S., Brattekås, B., Graue, A., Ersland, G. and Fernø, M.A., 2014. Miscible and Immiscible Foam Injection for Mobility Control and EOR in Fractured Oil-Wet Carbonate Rocks. Trans. Por. Med. 104, 109-131.

Heller, J.P., 1994. CO_2 Foams in Enhanced Oil Recovery. In Foams: Fundamentals and Applications in the Petroleum Industry, Advances in Chemistry 242, ed. L. L. Schramm, Chapter 5, 201-234. American Chemical Society.

Heller, J.P., Boone, D.A. and Watts, R.J., 1985. Field Test of CO_2 Mobility Control at Rock Creek. SPE Annual Technical Conference and Exhibition, Las Vegas, Nevada, 22-26 September.

Holm, L.W. and Garrison, W.H., 1988. CO_2 Diversion With Foam in an Immiscible CO_2 Field Project. SPE Res. Eng. 3 (1), 112-118.

Hoefner, M. L. and Evans, E. M., 1995. CO_2 Foam: Results from Four Developmental Field Trials. SPE Res. Eng. 10 (4), 273-281.

Honarpour, M.M., Nagarajan, N.R., Grijalba Cuenca, A., Valle, M. and Adesoye, K., 2010. Rock-Fluid Characterization for Miscible CO_2 Injection: Residual Oil Zone, Seminole Field, Permian Basin. SPE Annual Technical Conference and Exhibition, Florence, Italy, 19-22 September.

Islam, M.R. and Farouq-Ali, S.M., 1990. Numerical Simulation of Foam Flow in Porous Media. J. Can. Pet. Tech. 29(4), 47-51.

Jarrell, P.M., Fox, C.E., Stein, M.H. and Webb, S.L., 1990. Practical Aspects of CO_2 Flooding. SPE Monograph Series, 22.

Jian, G., Puerto, M.C., Wehowsky, A., Dong, P., Johnston, K.P. and Hirasaki, G.J., 2016. Static Adsorption of an Ethoxylated Nonionic Surfactant on Carbonate Minerals. Langmuir 32(40), 10244-10252.

Jonas, T.M., Chou, S.I. and Vasicek, S.L., 1990. Evaluation of a CO_2 Foam Field Trial: Rangely Weber Sand Unit. SPE Annual Technical Conference and Exhibition, New Orleans, Louisiana, 23-26 September.

Kibodeaux, K.R. and Rossen, W.R., 1997. Coreflood Study of Surfactant-Alternating-Gas Foam Processes: Implications for Field Design. SPE Western Regional Meeting, Long Beach, CA, June 25-27.

Kim, J.S., Dong, Y. and Rossen, W.R., 2005. Steady-State Flow Behavior of CO_2 Foam. SPE J. 10, 405-415.

Law, D.H., Yang, Z.M. and Stone, T., 1992. Effect of Presence of Oil on Foam Performance: A Field Simulation Study. SPE Symposium on Reservoir Simulation, Houston, TX, Feb. 6-8.

Leeftink, T.N., Latooij, C.A. and Rossen, W.R., 2015. Injectivity errors in simulation of foam EOR. J. Petrol. Sci. Eng. 126, 26-34.

Ma, K., Biswal. S.L. and Hirasaki, G.J., 2012. Experimental and Simulation Studies of Foam in Porous Media at Steady State. AIChE Spring Meeting, Houston, TX, 1-5 April.

Masoudi, R., Giddins, M. A., Karkooti, H., Jalan, S. and Gil, A.A.V., 2015. Foam Simulation from Coreflood to Field Scale. Presented at the SPE Asia Pacific Enhanced Oil Recovery Conference, Kuala Lumpur, Malaysia, 11-13 August.

Mukherjee, J., Norris, S. O., Nguyen, Q. P., Scherlin, J.M., Vanderwal, P.G. and Abbas, S., 2014. CO_2 Foam Pilot in Salt Creek Field, Natrona County, WY: Phase I: Laboratory Work, Reservoir Simulation, and Initial Design. Paper SPE 169166 presented at the SPE Improved Oil Recovery Symposium, Tulsa, Oklahoma, USA, 12-16 April.

Mukherjee, J., Nguyen, Q. P., Scherlin, J., Vanderwal, P.G. and Rozowski, P., 2016. CO_2 Foam Pilot in Salt Creek Field, Natrona County, Wyoming: Phase III: Analysis of Pilot Performance. Presented at the SPE Improved Oil Recovery Symposium, Tulsa, Oklahoma, USA, 11-13 April 2016.

Nguyen, Q.P., Hirasaki, G.J. and Johnston, K. P., 2015. Novel CO_2 Foam Concepts and Injection Schemes for Improving CO_2 Sweep Efficiency in Sandstone and Carbonate Hydrocarbon Formations. Technical Report, U.S. Department of Energy / National Energy Technology Laboratory.

Osterloh, W.T. and Jante, M.J., 1992. Effects of Gas and Liquid Velocity on Steady-State Foam Flow at High Temperature. SPE/DOE EOR symposium, Tulsa, OK, April 22-24.

Rossen, W.R., Zeilinger, S.C., Shi, J.X. and Lim, M.T., 1999. Simplified Mechanistic Simulation of Foam Processes in Porous Media. SPE J. 4, 279-287.

Rossen, W.R., 2013. Numerical Challenges in Foam Simulation: A Review. SPE Annual Technical Conference and Exhibition, New Orleans, Louisiana, USA, 30 September - 2 October.

Sanders, A., Jones, R. M., Linroth, M.A. and Nguyen, Q. P., 2012. Implementation of a CO_2 Foam Pilot Study in the SACROC Field: Performance Evaluation. Presented at the SPE Annual Technical Conference and Exhibition, San Antonio, Texas, USA, 8-10 October.

Schlumberger, 2015. Technical Description. ECLIPSE Reservoir Simulation Software.

Turta, A.T. and Singhal, A.K., 1998. Field Foam Applications in Enhanced Oil Recovery Projects: Screening and Design Aspects. Presented at the SPE International Conference and Exhibition, Beijing, China, 2-6 November.

Wang, F.P., Lucia, J.F. and Kerans, C., 1998. Integrated Reservoir Characterization Study of a Carbonate Ramp Reservoir: Seminole San Andres Unit, Gaines County, Texas. SPE Res. Eval. Eng. 1(2), 105-113.

Xu, Q. and Rossen, W.R., 2004. Experimental Study of Gas Injection in Surfactant-Alternating-Gas Foam Process. SPE Res. Eval. Eng. 7, 438-448.

Component	Fluid Composition (mol %)	
	MPZ	ROZ
N_2	0.51	0.04
CO_2	2.47	0.02
H_2S	1.96	0
C1	24.65	20.1
C2	9.1	9.07
C3	7.57	6.95
iC4	1.41	0.04
nC4	4.03	3.9
iC5	1.76	0.04
nC5	2.03	2.49
C6	3.54	2.69
C7+	40.97	54.66

Table 1 MPZ and ROZ fluid composition

Parameter	Description	Low	Base	High	Unit	Distribution
Static Model						
POROMULT	Pore volume multiplier	0.9	1	1.1		Uniform
PERMMULT	Horizontal permeability multiplier	0.75	1	1.25		Uniform
KVKH	Vertical to Horizontal permeability ratio	0.05	1	0.2		Uniform
Foam Model						
FMMOB	Reference foam mobility reduction factor	160	180	200		Uniform
FMDRY	Water-saturation dependence parameter	0.397	0.4	0.403		Uniform
EPDRY	Water-saturation dependence parameter	1000	10000	50000		Uniform
FMCAP	Shear-rate dependence parameter	1e-09	1e-08	1e-07		Uniform
EPCAP	Shear-rate dependence parameter	0.1	0.5	2		Uniform
Initialization						
SWIMPZ	Water saturation @ Start of Sim - MPZ	0.5	0.55	0.6		Uniform
SWIROZ	Water saturation @ Start of Sim - ROZ	0.62	0.68	0.75		Uniform
Well Model						
WATINJRATE	Injection Rate - Water slug	800	1000	1200	BWPD	Uniform
GASINJRATE	Injection Rate - Gas slug	1.6	2	2.4	MMscfd	Uniform
MAXINJPRES	Maximum injection pressure	4800	5000	5200	psia	Uniform
PIMULTWATINJ	Injectivity multiplier - Water slug	0.8	1	1.2		Uniform
PIMULTGASINJ	Injectivity multiplier - Gas slug	0.8	1	1.2		Uniform

Table 2 Uncertainty matrix for pilot simulation study
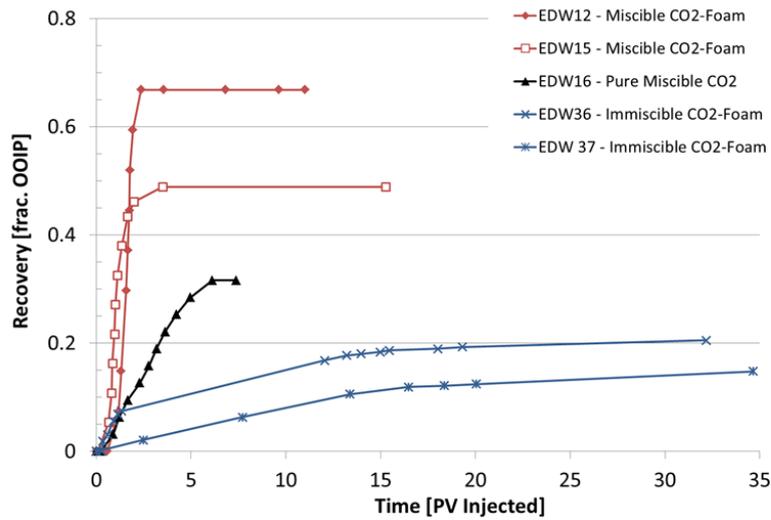
Figure 1 Comparison of oil recovery (in % OOIP) for pure CO_2 injection and CO_2-foam injection in oil-wet core plugs (Edwards Limestone). Mobility control by foam injection increased both rate of recovery and ultimate recovery significantly. Miscible foam injections produce more oil than immiscible foam injections.
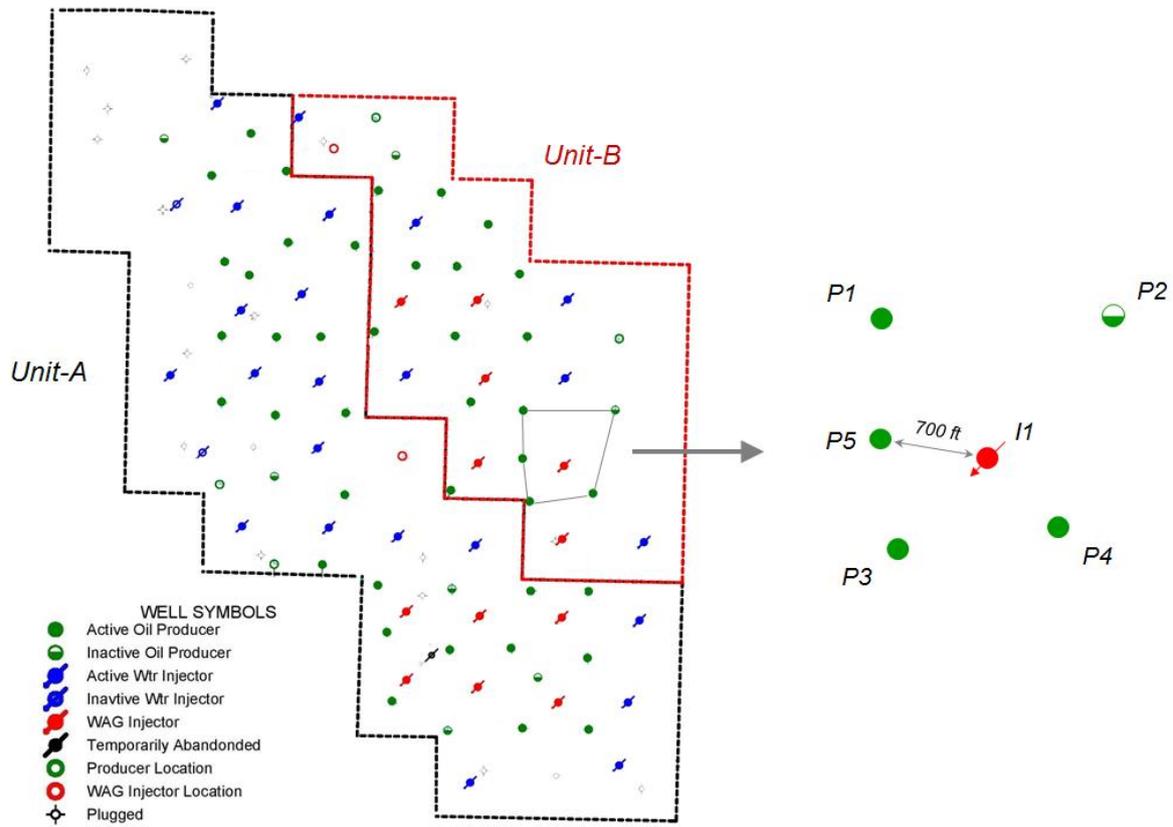
Figure 2 Field layout and location of selected pilot area
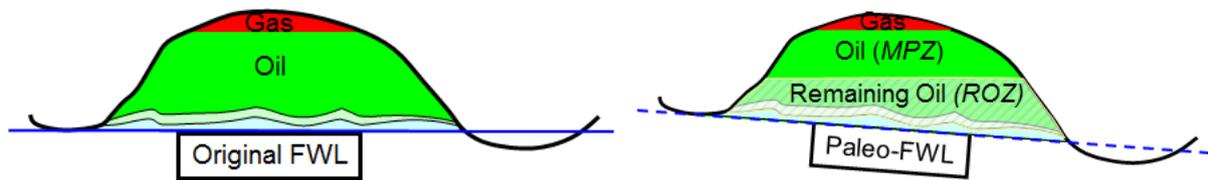
Figure 3 Effect of tilting on initial hydrocarbon distribution
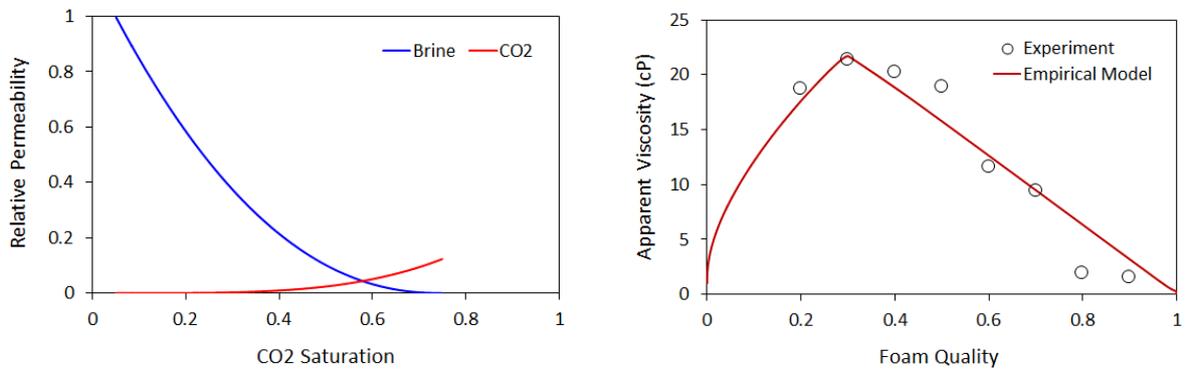
Figure 4 (a) CO_2-brine relative permeability for analogous limestone (b) Foam quality scan data fit to empirical model
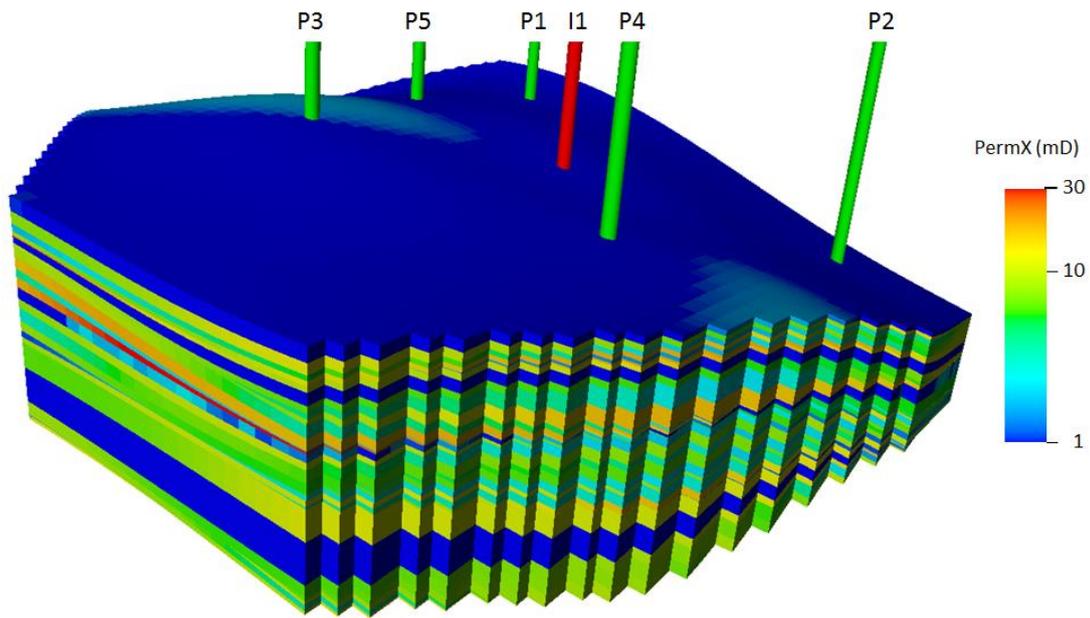
Figure 5 Permeability distribution in base geologic model
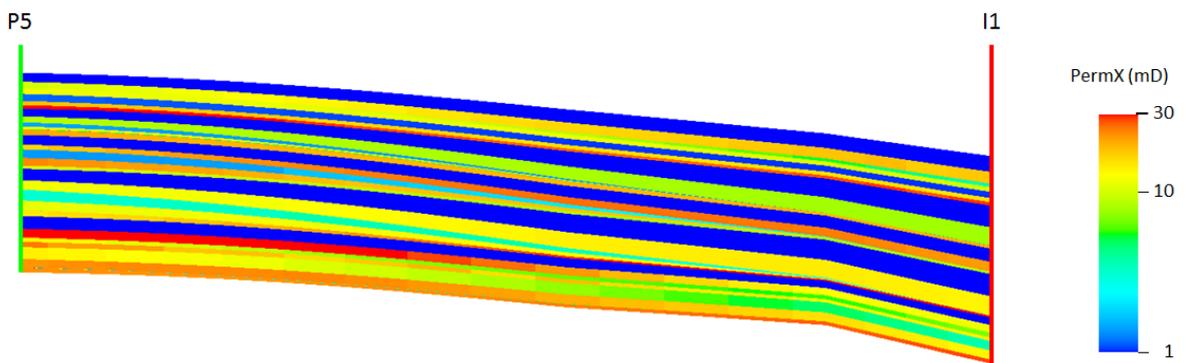
Figure 6 Cross-section (permeability) across I1 and P5
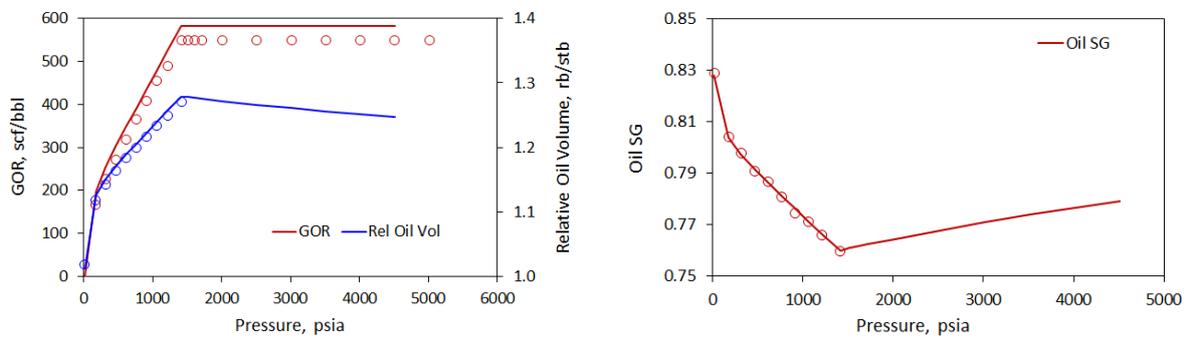
Figure 7 Fluid model fit to PVT data: Differential Liberation
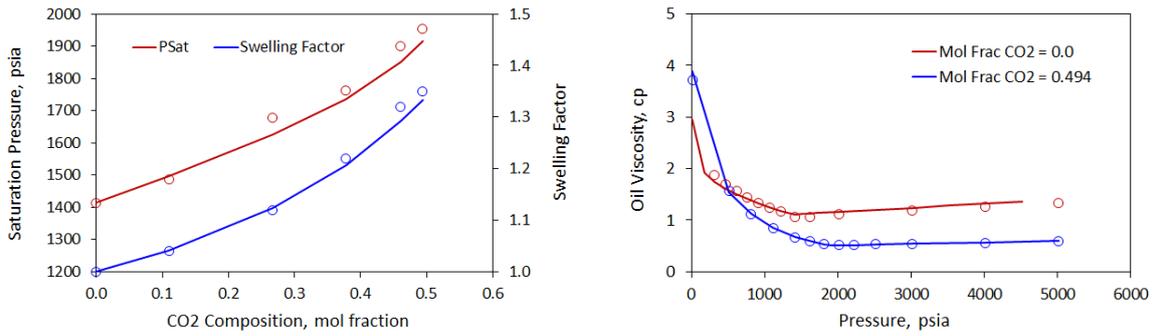
Figure 8 Fluid model fit to PVT data: Swelling and CCE/Viscosity (Oil+ CO_2)
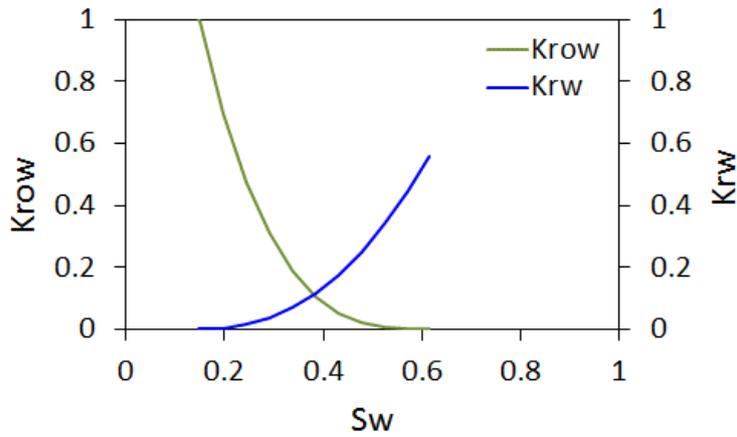
Figure 9 Water-Oil imbibition relative permeability
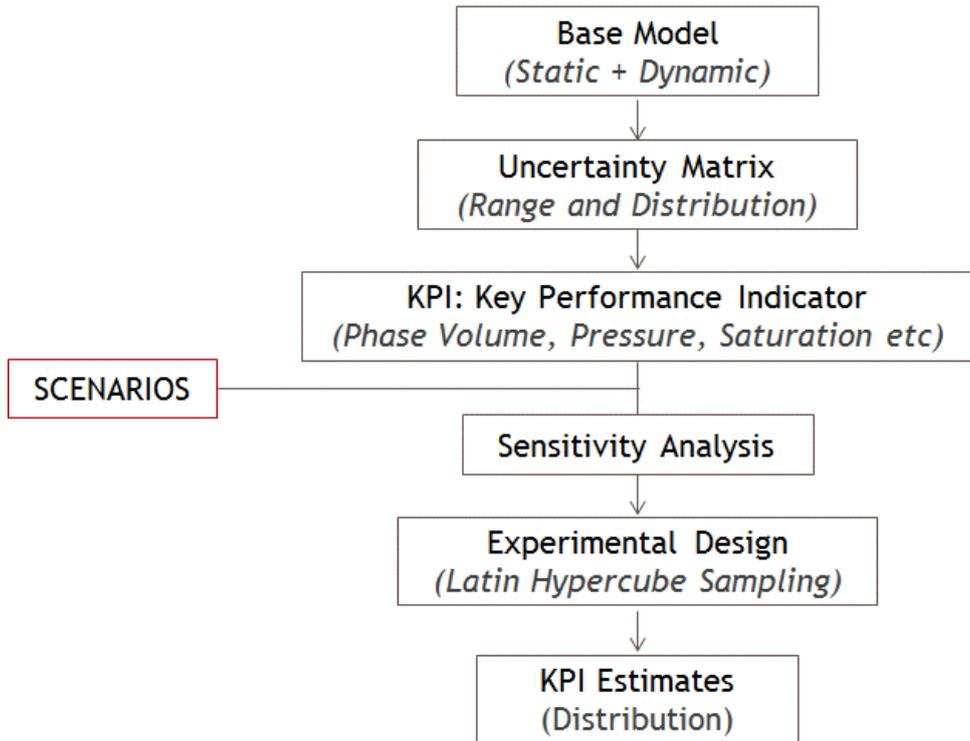
Figure 10 Workflow for forecasting under uncertainty
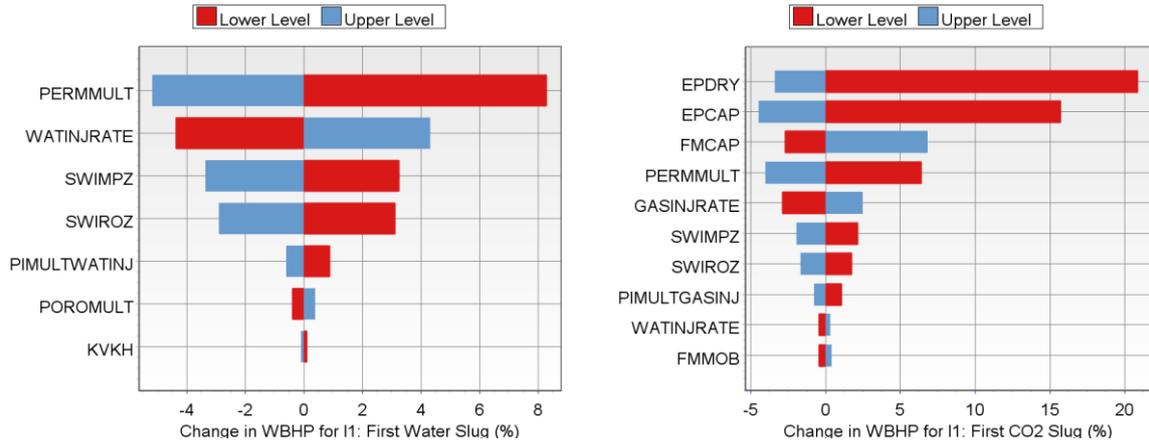
Figure 11 Sensitivity analysis capturing the key uncertainty parameters influencing bottom-hole pressure for injector under (a) surfactant injection (b) CO_2 injection
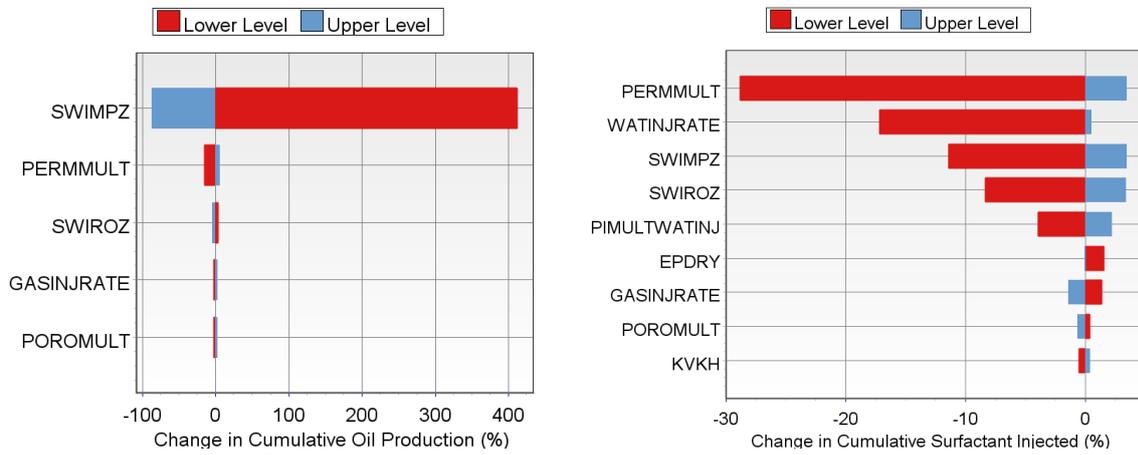
Figure 12 Sensitivity analysis capturing the key uncertainty parameters influencing (a) Cumulative oil production (b) Cumulative surfactant injection for pilot.
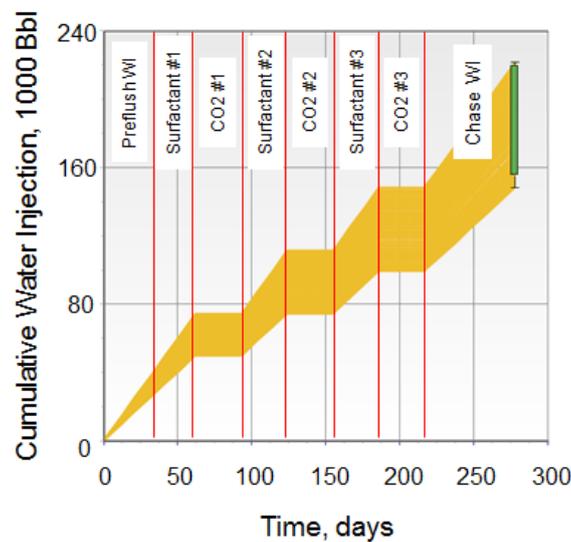
Figure 13 Uncertainty in volume of water required for pilot duration
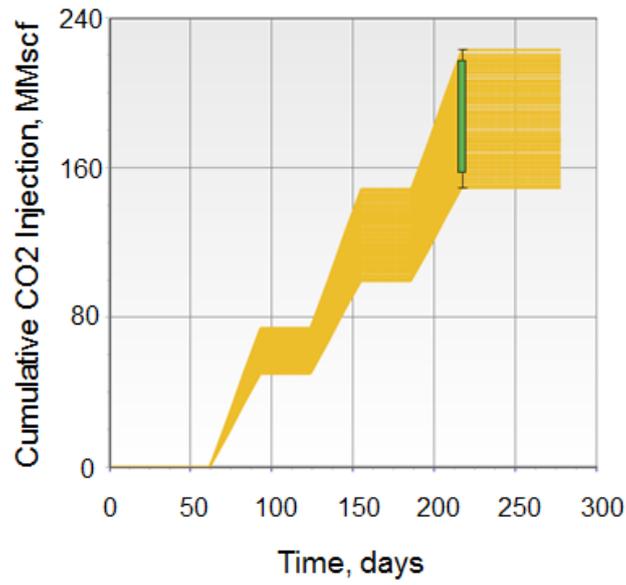
Figure 14 Uncertainty in volume of CO_2 required for pilot duration
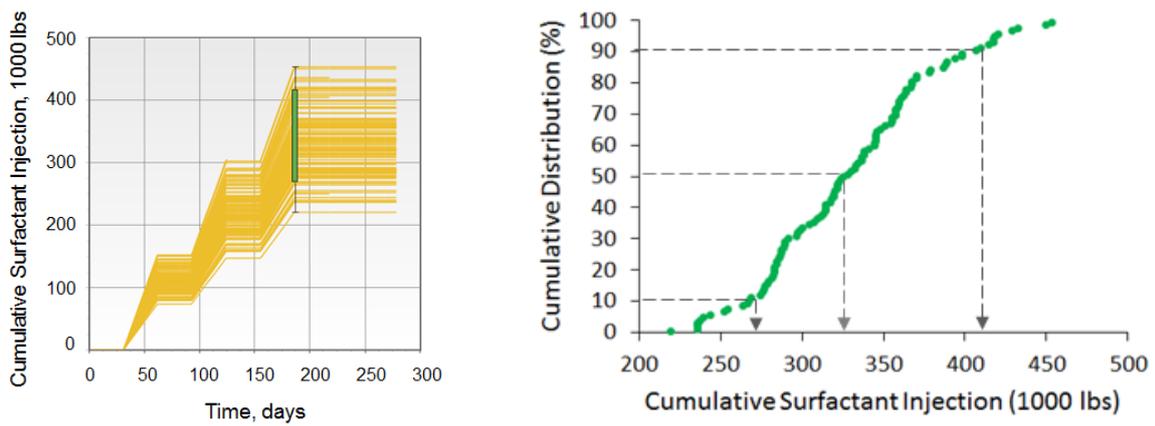
Figure 15 Uncertainty in amount of surfactant required for pilot duration

Paper II: Pore-to-Core EOR Upscaling for CO₂-Foam for CCUS

Rognmo, A.U., Fredriksen, S.B., Alcorn, Z.P., Sharma, M., Føyen, T.L., Eide, Ø., Graue, A., Fernø, M.A.

Please fill in the name of the event you are preparing this manuscript for.	SPE EUROPEC featured at the 80th EAGE Annual Conference and Exhibition 2018		
Please fill in your 6-digit SPE manuscript number.	SPE-190869-MS		
Please fill in your manuscript title.	Pore-to-Core EOR Upscaling for CO2-foam for CCUS		
Please fill in your author name(s) and company affiliation.			
Given Name	Surname		Company
Arthur Uno	Rognmo		University of Bergen
Sunniva Brudvik	Fredriksen		University of Bergen
Zachary Paul	Alcorn		University of Bergen
Mohan	Sharma		University of Stavanger
Tore	Føyen		University of Bergen, SINTEF Industry
Øyvind	Eide		University of Bergen
Arne	Graue		University of Bergen
Martin	Fernø		University of Bergen

Abstract

An ongoing CO_2-foam upscaling research project aims to advance CO_2-foam technology that accelerate and increase oil recovery, with reduced operational costs and carbon footprint during CO_2 EOR. Laboratory CO_2-foam behavior will be upscaled to pilot scale in an onshore carbonate reservoirs in Texas, USA. Important CO_2-foam properties such as local foam generation, bubble texture, apparent viscosity and shear-thinning behavior with a nonionic surfactant were evaluated using Pore-to-Core upscaling to develop accurate numerical tools for field pilot prediction of increased sweep efficiency and CO_2 utilization. On pore-scale, high-pressure silicon-wafer micromodels showed in-situ foam generation and stable liquid films over time during no-flow conditions. Intra-pore foam bubbles corroborated high apparent foam viscosities measured at core-scale. CO_2-foam apparent viscosity was measured at different rates (foam rate scans) and different gas fractions (foam quality scans) at core-scale. The highest mobility reduction (foam apparent viscosity) was observed between 0.60-0.70 gas fraction. The maximum foam apparent viscosity was 44.3 ($\pm$0.5) mPas, 600 times higher than that of pure CO_2, compared with baseline viscosity (reference case, without surfactant) that was 1.7 ($\pm$0.6) mPas, measured at identical conditions. CO_2-foam showed shear-thinning behavior with approximately 50% reduction in apparent viscosity when the superficial velocity was increased from 1 ft/day to 8 ft/day. Strong foam was generated in EOR corefloods at gas fraction 0.70, resulting in an apparent viscosity of 39.1 mPas. Foam parameters derived from core-scale foam floods was used for numerical upscaling and field pilot performance assesment.

Introduction

CO_2 injection for reservoir pressure support and enhanced oil recovery (EOR) is a proven technology with over 50 years of commercial experience (Taber et al. 1997; Jarrell and Jones 2002; Enick et al. 2012). Challenges related to differences in density and viscosity of the injected CO_2 and the in-situ reservoir fluids results in front instabilities (viscous fingering and gravitational segregation) during oil displacement. This gives rise to early CO_2 breakthrough, sub-optimal volumetric sweep efficiency and lower oil recovery. Water alternating gas (WAG) has emerged as a common technology to mitigate front instabilities where CO_2 and water are injected in alternating sequences to reduce CO_2 mobility. WAG injections stabilize the CO_2 front during oil displacement by increasing local water saturations and thereby decreasing CO_2 relative permeability (i.e., lowering its mobility). WAG has been extensively tested and implemented both at laboratory and field scale (Bennion and Bachu 2005; Bennion and Bachu 2007; Merchant 2010; Enick et al. 2012).

Reduced CO_2 mobility during CO_2 EOR is desirable due to several factors, including i) improved oil recovery (increased volumetric sweep); ii) reduced CO_2 utilization factor (reducing CO_2 costs); iii) increased CO_2 storage potential. One alternative to the commonly used WAG injection is in-situ generation of foam where liquid films (lamellae) surround the gaseous phase (CO_2) (Schramm 1994; Schramm 2000). Strong foam can be obtained by dissolving a foam stabilizer in the aqueous phase and injecting with CO_2 to mix in the reservoir (either in a surfactant alternating gas (SAG) sequence or as a co-injection). Foams are inherently thermodynamically unstable and a foam stabilizer (i.e., nanoparticles or surfactants) increases lamellae stability and provides a stronger foam with a significant reduction in CO_2 mobility that benefits EOR processes (Li et al. 2010; Rognmo et al. 2017; Rognmo et al. 2018). Also, using CO_2 for production purposes with associated storage (CCUS; Carbon Capture Utilization and Storage) contributes to reduce environmental impact from oil production. Several CO_2-foam field pilots using surfactants are reported as technical successes in the literature (Jonas et al. 1990; Chou et al. 1992; Hoefner et al. 1995; Henry et al. 1996; Sanders et al. 2012; Moffitt et al. 2015).

This experimental study is part of a field pilot research program to improve CO_2-foam EOR in carbonate reservoirs. The laboratory results presented here, at pore- and core-scale, provide an integrated approach to test and upscale a foam system for field implementation. High-pressure silicon-wafer micromodels enable direct pore-scale visualization which provides insight into foam texture, foam stability and fluid flow diversion, therby verifying the foam system's ability to reduce CO_2 mobility and generate lamella. Once verified, the foam system is tested in core plugs to evaluate foam stability at different gas fractions and injection rates, before being implemented on core plugs saturated with oil to measure the EOR potential from foam flood. The next step to the upscaling approach is the use of numerical models to accurately describe the behavior of foam at the field scale, based upon the observations at the core-scale. Abovementioned measurements are performed to provide input into numerical models, including CO_2/brine relative permeability, dynamic foam strength and foam shear thinning behavior. A more detailed description of the field pilot can be found elsewhere (Alcorn et al. 2016; Sharma et al. 2017).

Methods and Materials

The following section describes the experimental preparations, procedures, fluids, rock materials and micromodel used in this study.

Fluids

Synthetic reservoir brine (brine A, see **Table 1**) was made from analytical grade chemicals and distilled water. A commercially available nonionic surfactant (Huntsman International LLC, CAS no. 68551-12-2) was selected based on recent surfactant screening (Nguyen et al. 2015; Jian et al. 2016). The waxy solid surfactant was used as received, and mixed with brine A to obtain a 1 wt% surfactant concentration.

Fluid	Composition	Density [g/cm3]	Viscosity [mPas]	Condition
Brine A	27.1 g/L NaCl 2.76 g/L $MgCl_2 \cdot 6H_2O$ 5.82 g/LCaCl$_2 \cdot 2H_2O$ 0.46 g/L KCl	1.025	1.08	20°C / 0.1 MPa
		1.009	0.51	40°C / 0.1 MPa
[a]CO_2	> 99.999% CO_2	0.843	0.0788	20°C / 9.0 MPa (liquid)
		0.814	0.0735	40°C / 17.5 MPa (supercritical)
		0.685	0.055	60°C / 17.9 MPa (supercritical)
[a]Decane	$C_{10}H_{22}$	0.715	0.663	60°C / 17.9 MPa
Surfactant solution	1 wt% nonionic surfactant in brine A	1.027	-	-

[a]) (Lemmon et al. 2018)

Table 1 - Fluid properties.

Micromodel

Two-dimensional (2D) micromodels gain insight into pore-level displacement mechanisms that control multiphase fluid flow at core-scale (Gauteplass et al. 2015; Fredriksen et al. 2016). Etched silicon-wafer micromodels connected to a microfluidic flow rig with a high-resolution camera microscope enabled direct pore-scale visualization of fluid saturations, fluid flow interactions and displacement processes during CO_2-foam flow. The micromodels inherit the essential characteristics of a porous media (**Table 2**), and a detailed description of the manufacturing process can be found elsewhere (Hornbrook et al. 1991; Buchgraber et al. 2012). Fluid distribution ports are located in each corner and channels (termed "fractures") connects the ports horizontally opposite each other (see **Figure 1**).
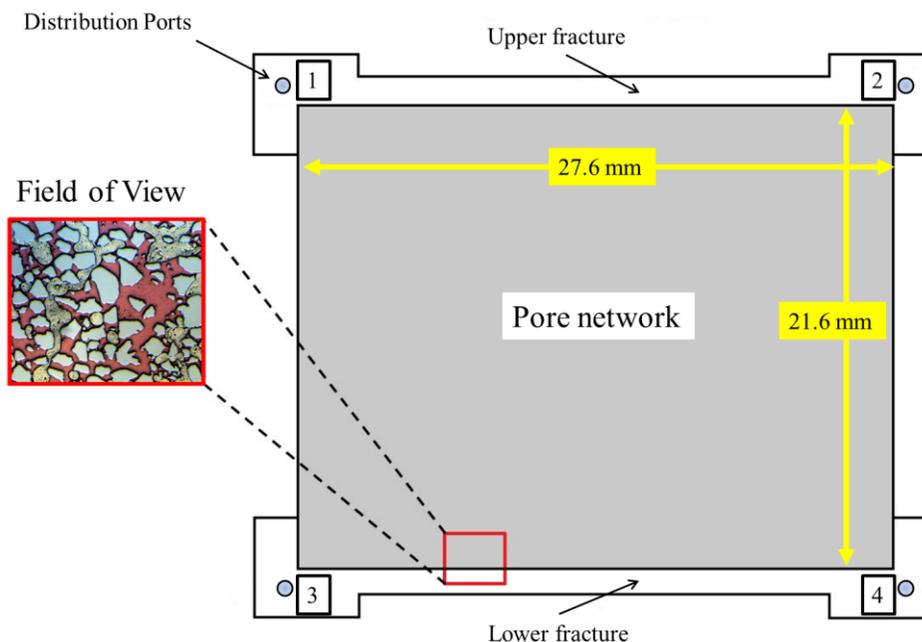
Figure 1 - Sketch of the silicon-wafer micromodels used for 2D visualization of multi-phase fluid flow during CO_2-foam injection.

Micromodel ID	Length [cm]	Width [cm]	Coordination number	Porosity [%]	Permeability [mD]	Grain size [μm]
HP_1	2.76	2.16	1-6	~60	2.9	10-400

Table 2 - Micromodel properties.

Rock Material

CO_2-foam scans were performed on a cleaned reservoir core plug (see **Table 3**) from the field pilot area of the East Seminole (ES) carbonate field in west Texas (Alcorn et al. 2016; Sharma et al. 2017). Due to lack of reservoir core material, CO_2-foam scans and EOR injections were also performed using an outcrop carbonate core plug with comparable rock properties. Hence, reported behavior might be affected by rock material, but is expected to mimic reservoir behavior. The reservoir core plug was drilled horizontally (parallel to bedding) from a borehole core from an offset producer in the pilot well pattern (see **Figure 2**). The core plug was cleaned for 72 hours in a Dean Stark apparatus with a 1:1 solution (by volume) of toluene and methanol, extracting any residual fluids.
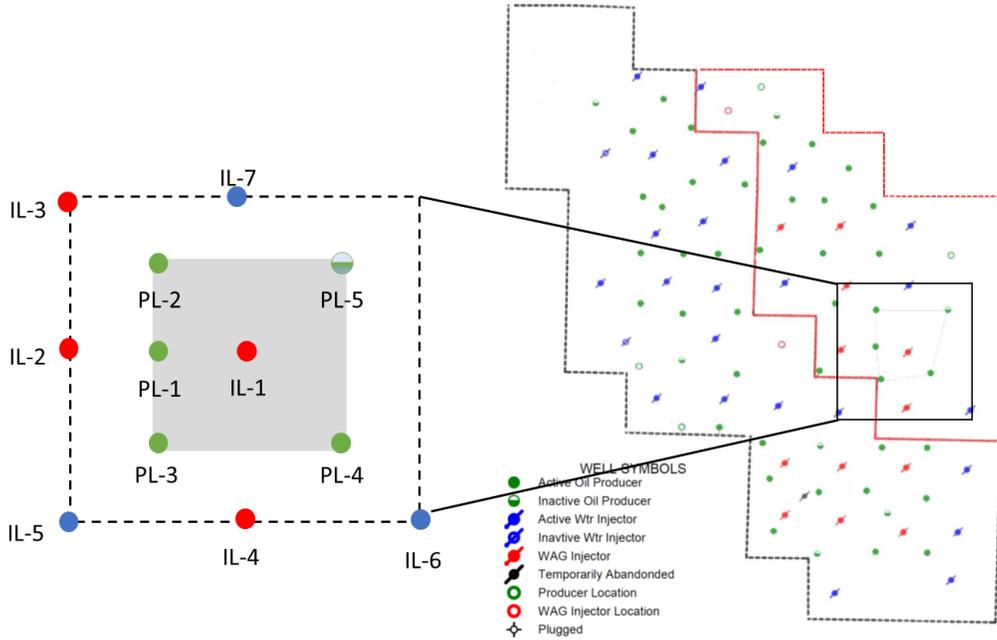
Figure 2 – Well map showing field pilot location (gray shaded area) in the East Seminole field, West Texas. The reservoir core plug used in this study was drilled from the offset producer PL-5.

Core ID	Length [cm]	Diameter [cm]	Pore Volume [ml]	Porosity [%]	Permeability [mD]
Reservoir	5.7	5.0	15.2	13.8	22.1
Outcrop	7.5	5.0	35.3	24.2	20.5
EOR 1 fg=0.8	24.9	4.8	111.6	24.5	13.9
EOR 2 fg=0.7	24.4	5.0	105.7	22.3	15.5

Table 3 – Core plug properties.

Experimental Procedures

Foam was generated by coinjecting CO_2 and surfactant solution at constant flow rate with varying gas fractions at the pore- and core scale. The gas fraction (f_g), is the ratio of injection rate of gas (q_g) to total volumetric injection rate of water (q_w) and gas at experimental conditions.

$$f_g = \frac{q_g}{q_g + q_w} . \quad \dots\dots\dots\dots\dots\dots\dots\dots\dots\dots\dots\dots\dots\dots\dots\dots\dots\dots\dots\dots\dots\dots\dots(1)$$

Foam strength was quantitatively evaluated by the apparent foam viscosity, calculated from steady-state pressure gradient at each gas fraction during foam quality scans and at each injection rate during foam rate scans.

$$\mu_{app} = \frac{k\Delta p}{u_l + u_g}, \quad \dots\dots\dots\dots\dots\dots\dots\dots\dots\dots\dots\dots\dots\dots\dots\dots\dots\dots\dots\dots\dots\dots(2)$$

where k is the absolute permeability, Δp is the pressure gradient over the core plug, and u_l and u_g are the superficial velocities of liquid and gas, respectively (Ma et al. 2013; Jones et al. 2016). From experimental results we find the optimal gas fraction i.e., the gas with the highest foam apparent viscosity and largest reduction in CO_2 mobility.

Part 1: Pore-scale

Foam Visualization

Pore-level foam texture, stability and flow diversion were evaluated in silicon-wafer micromodels at 9.0

(± 0.5) MPa absolute pore pressure and 20ºC (± 1ºC) using an in-house microfluidic setup (see **Figure 3**) with a constant gas fraction of 0.70. Gravity effects were minimized by placing the micromodel horizontally for all runs.
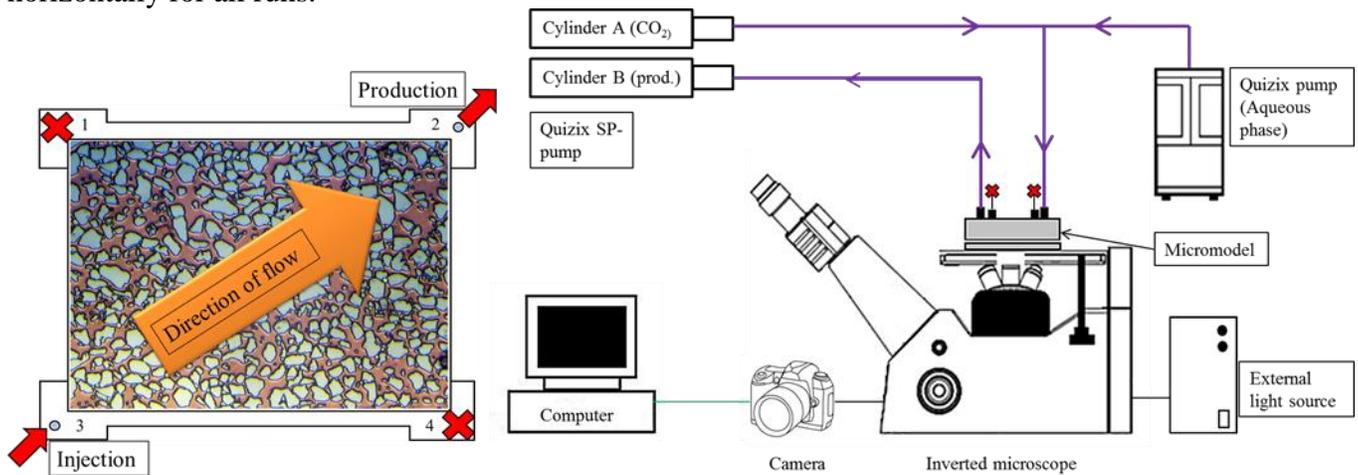
Figure 3 – Left: illustration of port configuration during co-injection of CO_2 and water (baseline) or CO_2 and surfactant solution (foam). Inlet is port 3 and outlet is port 2, whereas ports 1 and 4 remained closed for the duration of the injection tests. The orange arrow indicates general direction of flow (and pressure gradient) for the micromodel injections. Right: Experimental setup showing the high-pressure microfluidic flow rig. Fluid flow lines and flow direction in purple.

Part 2: Core-scale

Foam Scans

Core plugs were fully (100%) saturated with brine A under vacuum at room temperature. All injections were performed at 17.5 MPa (± 0.3 MPa) absolute pore pressure, measured at the outlet of the core, and at reservoir temperature, 40ºC (± 0.1ºC), and 60ºC (± 0.1ºC) for the reservoir core plug and the outcrop core plug, respectively. To reduce pressure fluctuations during the foam runs, and achieve steady pressure gradients, the produced fluids were collected in a piston accumulator held at pore pressure at the outlet by a N_2-loaded backpressure regulator (BPR). This reduced the adverse effects from rapid CO_2 expansion in the BPR (when pressure and temperature decreases) as distilled water (downstream of the piston) flowed through the BPR rather than CO_2. Pressure gradients were measured for a quantitative analysis and evaluation of the foam generation and strength during fluid flow.

CO_2-foam scans were performed to measure foam strength (apparent foam viscosity) as a function of injection rate (foam rate scan) and gas fraction (foam quality scan). CO_2-foam quality scans (co-injection of CO_2 and surfactant solution) are benchmarked against identical baseline runs without surfactant solution (co-injection of CO_2 and brine A) to evaluate foam performance. Equal initial water saturation (S_w = 1.0) was established before each run by injecting more than 10 PV aqueous phase with a high injection rate of 8 ft/day. Adsorption was satisfied before every surfactant run, to reduce injection time until steady-state.

CO_2-foam quality scans were conducted using the following injection sequence: 1) Baseline: foam quality scans used a drainage-like, monotonically increasing gas fraction sequence to determine foam apparent viscosities at different gas fractions. Brine and CO_2 were co-injected starting at a gas fraction of 0.10 and was increased by 20%-points for the first increment and 10%-points thereafter (from 0.30 to 0.90), obtaining steady-state flow conditions at each gas fraction. Apparent viscosities were calculated from pressure gradients at gas fractions 0.1, 0.3, 0.4, 0.5, 0.6, 0.7, 0.8 and 0.9, with Eq. 2. 2) CO_2-foam quality scans used a drainage-like, monotonically increasing gas fraction sequence to determine optimal foam gas fraction: surfactant solution and CO_2 were co-injected starting at gas fraction 0.30 and increasing the volumetric gas fraction with 10%-points to 1.0. Apparent viscosities were calculated using pressure gradients at gas factions 0.3, 0.4, 0.5, 0.6, 0.7, 0.8, 0.9 and 1.0. CO_2-foam rate scans were conducted with

a constant gas fraction of 0.70, increasing the injection rate (given as superficial velocity) from 1 to 8 ft/day and obtaining steady-state flow conditions at each rate. Apparent viscosities were calculated using pressure gradients at injection rates 1, 2, 4, 6 and 8 ft/day.

Foam EOR
Core plugs were fully (100%) saturated with brine A under vacuum at room temperature and drained with mineral oil (n-Decane) to a low water saturation (S_{wi}) at experimental conditions (17.9 MPa and 60ºC). Approximately 1.1 pore volume (PV) of brine A was injected during the waterfloods (WF) at a superficial velocity (v_s) of 1 ft/day (injection rate 23 to 25 mL/h). Co-injections (CO_2-foam) were performed with gas fractions of 0.70 and 0.80 for 2.0 PV. Pressure gradients and cumulative oil production were recorded over time to determine oil recovery and foam performance in the presence of oil.

Part 3: Core-Scale Derived Parameters for Numerical Upscaling
An integral part of the upscaling process is the use of numerical models to accurately describe the behavior of foam at the field scale, based upon observations at the core-scale. Therefore, several measurements were preformed to provide input into numerical models, including CO_2/brine relative permeability, dynamic foam strength and foam shear thinning behavior.

Relative Permeability
A set of laboratory injections were performed on a reservoir core plug at reservoir conditions, i.e.17.5 MPa ($\pm$ 0.3 MPa) absolute pore pressure and at 40ºC ($\pm$ 0.1ºC), to obtain CO_2/brine relative permeabilities for numerical modeling and upscaling. Steady-state pressure gradients were recorded at irreducible fluid saturations to calculate effective permeabilities, and Corey correlations were used to estimate two-and three-phase relative permeability curves. All injections were performed horizontally with an initial water saturation of 100% (brine A). Average water and gas saturations were determined by mass balance and the injection sequence followed four steps: 1) CO_2 injection at constant superficial velocity of 2.0 ft/day (obtaining irreducible water saturation S_{wc}); 2) brine injection at constant superficial velocity of 0.25 ft/day (obtaining residual gas saturation S_{gr}) ; 3) brine injection at constant superficial velocity of 0.50 ft/day (obtaining residual gas saturation at higher rate $S_{gr,2}$); 4) CO_2 injection at constant superficial velocity of 2.0 ft/day (obtaining hysteresis water saturation $S_{wc,hysteresis}$).

Foam Model Parameters
Laboratory foam scans constitute the basis for the implicit-texture local-equilibrium foam model that capture the effects of foam mobility, foam viscosity as a function of velocity, surfactant concentration, water and oil saturations (Law et al. 1992; Cheng et al. 2000; Alvarez et al. 2001; Farajzadeh et al. 2012; Sharma et al. 2017). To account for the decrease in gas mobility during foam floods the model scales the gas relative permeability for no foam floods (k_{rg}^{nf}) by a mobility reduction factor (FM), whereas the water relative permeability remains unchanged.

$$k_{rg}^{f} = k_{rg}^{nf} \cdot FM, \quad \dots\dots\dots\dots\dots\dots\dots\dots\dots\dots\dots\dots\dots\dots\dots\dots\dots\dots\dots\dots\dots\dots\dots\dots\dots\dots\dots\dots(3)$$

where k_{rg}^{f} is the relative gas mobility during foam flooding. FM incorporates the effect of water saturation change and injection rate, and is given as

$$FM = \frac{1}{1+fmmob \cdot F_{water} \cdot F_{shear}}, \quad \dots\dots\dots\dots\dots\dots\dots\dots\dots\dots\dots\dots\dots\dots\dots\dots\dots\dots\dots\dots\dots\dots(4)$$

where fmmob is the minimum gas mobility achieved, F_{water} and F_{shear} incorporates the dependence of water saturation and shear rate with values between 0 and 1. A more detailed description of numerical simulation

and regression alanysis for matching coreflood data can be found in Sharma et al. (2017).

Results and Discussion

A comprehensive analysis of foamability, foam flow and foam texture was conducted to investigate the foam stabilizing effect of adding the nonionic surfactant to synthetic reservoir brine during co-injection in carbonate systems. Quantitative evaluation of foam strength (foam apparent viscosity) was performed using core plugs and corroborated with qualitative (visual) assessment of foam texture and flow diversion at pore-scale using a micromodel. In addition, quantitative pore-level evaluation of static foam strength during half-life tests at elevated pressures enabled an improved understanding of mechanisms present during multiphase fluid flow with and without surfactants added to the aqueous phase.

Part 1: Pore-Scale

Co-injection Without Surfactant

A baseline flow test was performed in micromodel to evaluate the two-phase system without surfactant present. Visual observations showed few gas bubbles per unit area and the gas phase spanning over several pores without being separated by liquid films (see **Figure 4**). This is referred to as a continuous-gas foam (Schramm 1994) and is characterized by high multi-phase fluid flow potential and low reduction in CO_2 mobility. There was no lamella generation observed and the water phase was continuous throughout the porous media. CO_2 flow occured primarily in medium to large pores, whereas the smaller pores remained water saturated during co-injection. The few CO_2 bubbles observed were located in pores surrounded by narrow pore throats, suggesting gas trapping by snap-off.
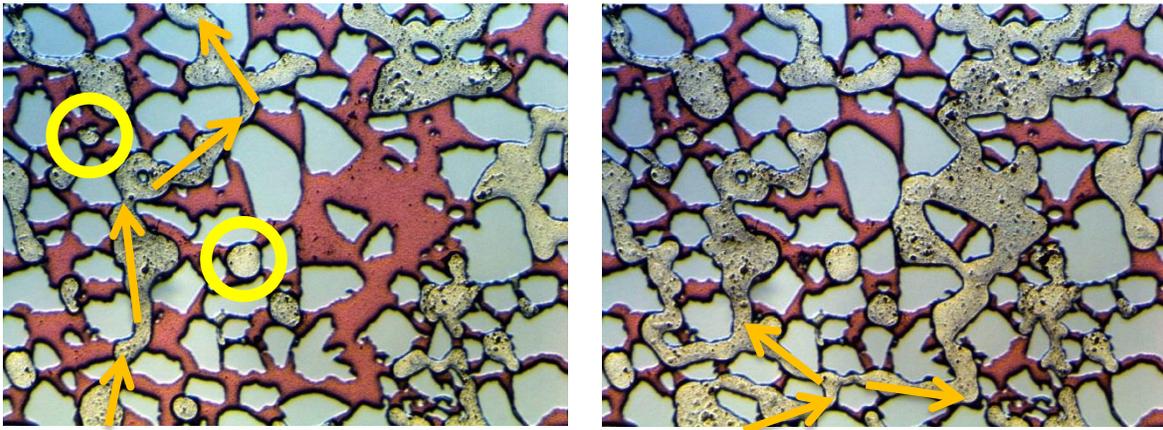
Figure 4 - Baseline co-injection of brine and CO_2 at 9.0 MPa, 20⁰C and at gas fraction of 0.70. The light blue regions are solid grains, the water phase is red and CO_2 is gray. The continuous CO_2 phase spanning several pores, suggested limited CO_2 mobility reduction. The orange arrows indicate CO_2 flow zones within the field of view. Water primarily saturated smaller pores and was continuous throughout the pore space, whereas CO_2 flow occured in the medium to large pores. Isolated CO_2 bubbles are indicated in yellow circles.

Co-Injection with Surfactant

To evaluate in-situ foam generation by adding the surfactant to the aqueous phase (concentration: 1 wt%), a co-injection at the same conditions as the baseline was performed (**Figure 5**). A strong CO_2-foam was generated, with high bubble concentration where most pores were filled with multiple bubbles. This is an important observation as it greatly increases the amount of lamellae per unit area and decreases CO_2 mobility. In contrast to baseline, the CO_2 phase did not span several pores and flow diversion occurred in correspondence with local foam generation and coalescence, governing the local fluid flow potential and therefor the volumetric flowrate.
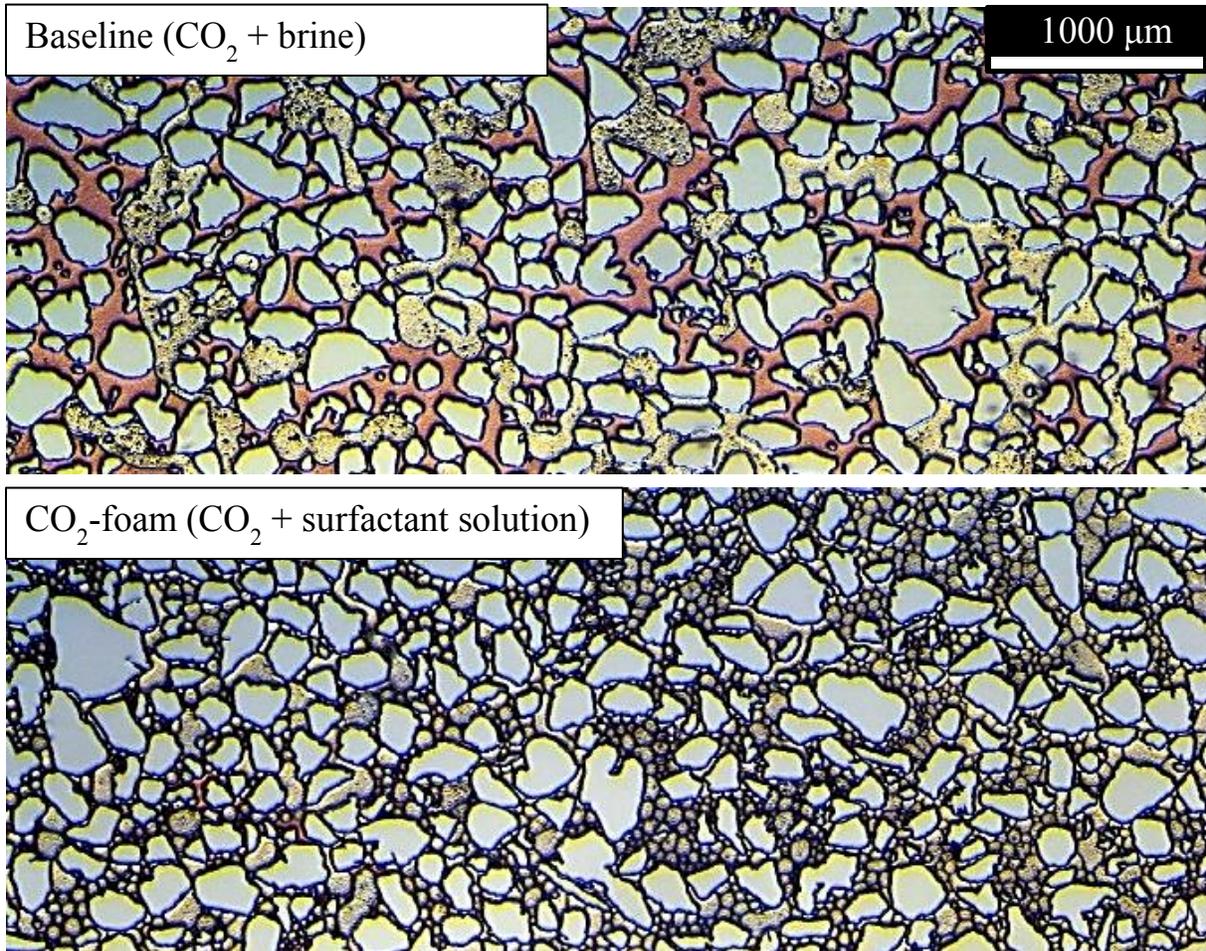
Figure 5 – Comparison between co-injection without (top) and with (bottom) surfactant at 9.0 MPa, 20ºC and at gas fraction = 0.70. The light blue regions are solid grains, the water phase is red and CO_2 is gray. Bubble concentration is 2-3 orders of magnitude higher for the runs with surfactant, hence the lamella concentration is significantly higher and traps most of the water in liquid films. The distribution of water without foam is "free" present in the smaller pores and covering the (water-wet) grains.

Static Foam Strength from Visual Observations

To determine the static foam strength (thermodynamic stability) at elevated pressure, foam coalescence was measured during no-flow, static conditions for 72 hours. The normalized bubble concentration (ratio of number of bubbles at each time step to initial number of bubbles) in the field of view enabled quantification of foam strength as a function of time (see **Figure 6**). The coalescence rate decreased for the first 30 hours before asymptotically approaching a constant normalized bubble concentration of 0.37 (±0.06), after 70 hours.
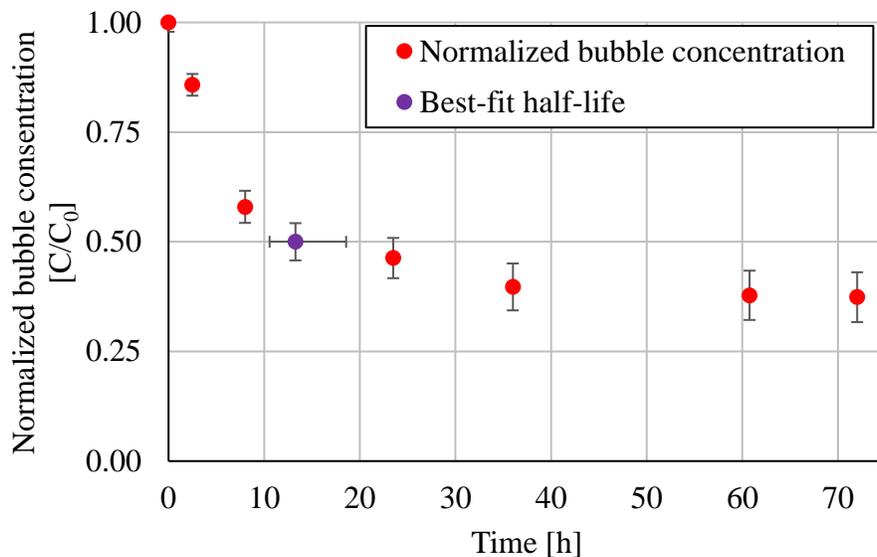
Figure 6 - Normalized bubble concentration (red dots) in field of view as a function of time after foam generation at static (no-flow) conditions. Purple dot represents the half-life of the bubbles and is calculated from a best-fit regression analysis. Uncertainties are given as experimental measurement uncertainty from the mean value.

CO_2-foam half-life was estimated from Figure 6 using a best-fit four parameter logistic (4PL) regression:

$$y = d + \frac{a-d}{1+\left(\frac{x}{c}\right)^b}$$

The half-life was 13.3 (±0.6) hour, i.e., the number of bubbles was reduced by 50% due to coalescence and the ability to reduce CO_2 mobility was weakened. During coalescence, the aqueous phase was released from lamellae that collapsed, and became mobile (see **Figure 7**).
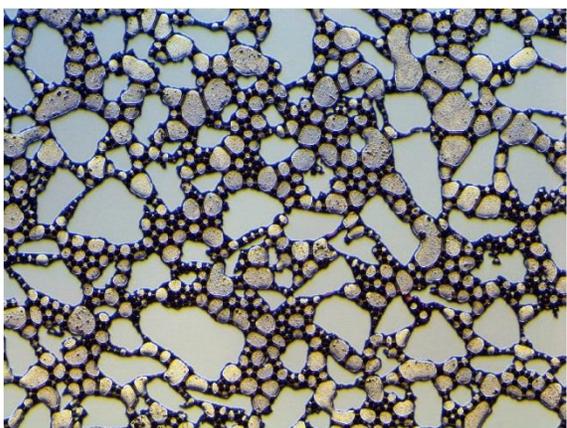
Start at t = 0 h   End at t = 72 h
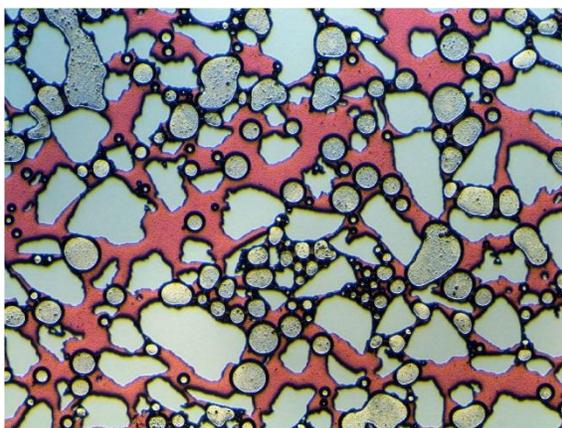
Figure 7 - Foam coalescence and half-life during static (no-flow) conditions at 9.0 MPa and 20ºC. The light blue regions are solid grains, the aqueous phase (surfactant solution) is red and CO_2 is gray. Left: bubble concentration at start of static test (t = 0 h). Right: bubble concentration at end of static test after 3 days (t = 72.0 h).

Fluid Flow Divergence
The ability of the surfactant to generate and stabilize foam decrease CO_2 mobility and increase sweep efficiency by flow diversion from zones with high bubble density (low flow potential) to low bubble density zones (high flow potential). Local zones (tens of pores) with high bubble concentration reoccurred

over time due to favorable foam generation conditions and diverted flow to zones with lower bubble concentration. Hence, stationary, stable bubbles locally reduce CO_2 flow to zero. Because the volumetric injection rate was kept constant, fluid flow was diverted from regions with high bubble concentration, increasing the areal sweep efficiency in the micromodel.

Part 2: Core-Scale

A numerical foam model is needed to upscale laboratory foam data to field scale. Several laboratory measurements on a reservoir core plug were performed to obtain input parameters for the empirical model, including relative permeability between CO_2 and brine, foam strength and foam shear thinning behavior.

Foam Scans

Core-scale foam scans (**Figure 8**) demonstrated that: 1) apparent viscosity (foam strength) was highest at gas fractions between 0.60 and 0.70 for both outcrop ($f_g^* = 0.70$, $\mu_{app} = 35$mPas) and reservoir core plug ($f_g^* = 0.60$, $\mu_{app} = 44$mPas); 2) the surfactant stabilizing effect was significant for gas fractions larger than 0.30. The highest apparent viscosity (1.80 mPas) for the baseline (without surfactant solution) was observed at gas fraction 0.50. Foam scan on outcrop core plug is published in Fredriksen et at. 2018.

In the reservoir core plug the apparent viscosity during foam scan from gas fraction = 1.0 (pure CO_2 injection) was 76 times higher ($\mu_{app,CO2} = 5.6$ mPas) than viscosity of pure CO_2 ($\mu_{CO2}=0.074$). This suggests reduced fluid flow potential as a result of trapped (immobile) gas from foam generation, with little or no dry-out effect (which would lead to bubble coalescence and increased CO_2 mobility) after more than 2.0 PV CO_2 injected. This is consistent with the high foam stability observed at pore-scale.
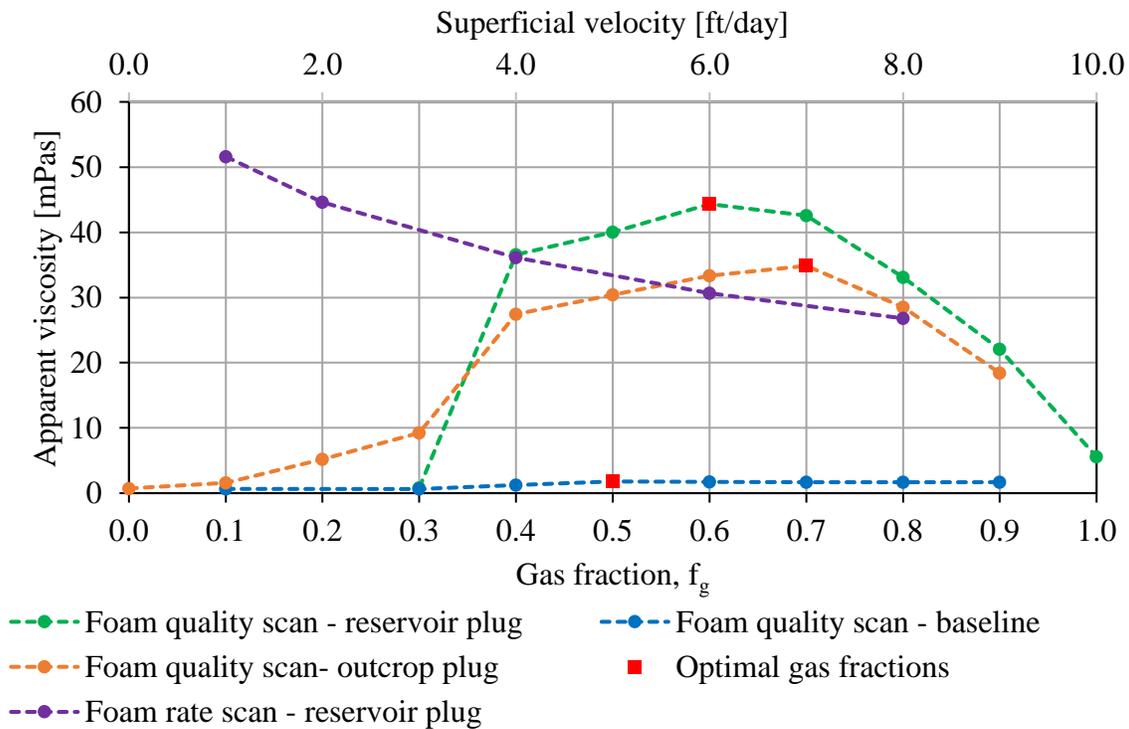
Figure 8 - Apparent viscosity as a function of superficial velocity (purple: secondary x-axis, top) and gas fraction (green, orange and blue: primary x-axis, bottom) during drainage-like injection sequence. Blue dots represent measured points for baseline; co-injection of brine and CO_2. Green dots represent measured points for surfactant stabilized foam in reservoir core; co-injection of surfactant solution and CO_2. Orange dots represent measured points for surfactant stabilized foam in carbonate outcrop core (reservoir analogue). The optimal gas fraction for each run is represented with a red square, indicating the interval 0.60-0.70 to be optimal for foam injection in the reservoir rock and analogue. Apparent viscosity versus superficial velocity show foam shear thinning behavior for co-injections with constant gas fraction (0.70) and increasing superficial velocity (purple: secondary x-axis).

Foam EOR

To evaluate the effect of gas fraction on oil recovery, CO_2 storage and CO_2 mobility reduction, two corefloods were run on carbonate outcrop core plugs with $f_g^* = 0.70$ (optimal gas fraction found during foam scan) and $f_g = 0.80$. Crude oil from the reservoir was not available so a mineral oil (n-Decane) was selected for the oil phase. Brine A was injected for $1.05 - 1.10$ PV until oil production rate was zero. A co-injection of surfactant solution and CO_2 was performed for 2.0 PV at a superficial velocity of 1 ft/day (~25 mL/h) as a tertiary EOR process (see **Figure 9**). Incremental oil recovery (%-points increase) was equal for the two foam floods (see **Table 4**), whereas significantly higher CO_2-foam apparent viscosity was observed for gas fraction 0.70.

Experiment ID	$R_{f,WF}$ [% OOIP]	$R_{f,final}$ [% OOIP]	$\Delta R_{f,co-inj}$ [% OOIP]	CO_2 stored [% PV]	App.visc. WF [mPas]	App.visc.foam [mPas]	App.visc. increase	VEE
f_g=0.7	31.2	63.9	32.7	63.2	4.5	39.1	768 %	3.1
f_g=0.8	42.6	75.2	32.6	42.2	2.5	2.9	14 %	1.9

Table 4 – Experimental parameters for tertiary EOR at fg=0.70 and fg=0.80. Apparent viscosity is calculated from the average pressure gradient for the last 0.1 PV for the respective injection sequence (WF or co-injection) and the volume element exchange (VEE) is calculated as the ratio of volume element CO_2 stored to volume element oil recovered, at experimental conditions.

For the lower gas fraction (0.70) the rate of recovery increased by 20% for the first 0.50 PV injected after WF, compared to gas fraction of 0.80. The CO_2 storage potential for each gas fraction was calculated from the ratio of volume element of CO_2 stored to volume element of oil produced (VEE, Table 4). The VEE values show that both gas fractions stored more CO_2 (in terms of VEE) than produced oil (VEE > 1), and that CO_2 storage effect was 50% higher for f_g=0.70 relative to f_g=0.80. Hence, as incremental oil recovery was equal for the two cases, the stronger foam at f_g=0.70 mobilized more water from the pore space resulting in higher CO_2 storage potential (see **Figure 10**).
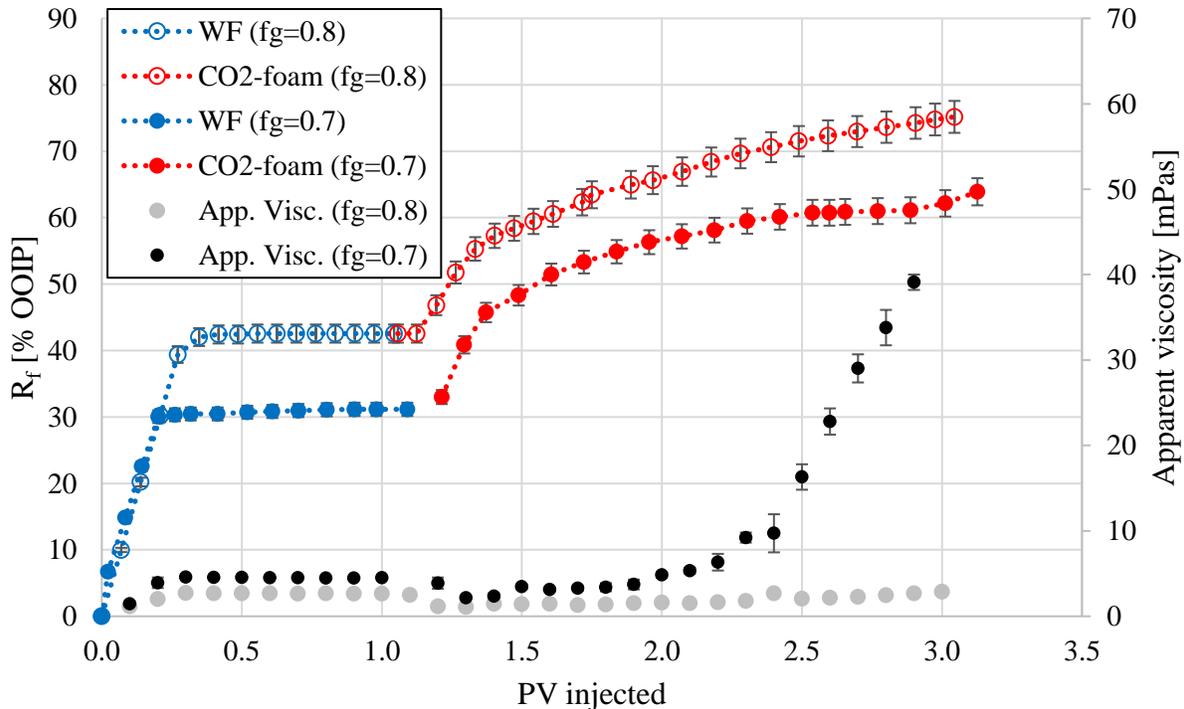
Figure 9 - Recovery factor and accompanying apparent viscosity plotted as a function of pore volumes injected for waterflood and CO_2-foam injection in outcrop carbonate core plugs for EOR. Uncertainties are given as one standard deviation from the mean, for the pressure graphs, and experimental measurement uncertainty for the recovery factor graphs.
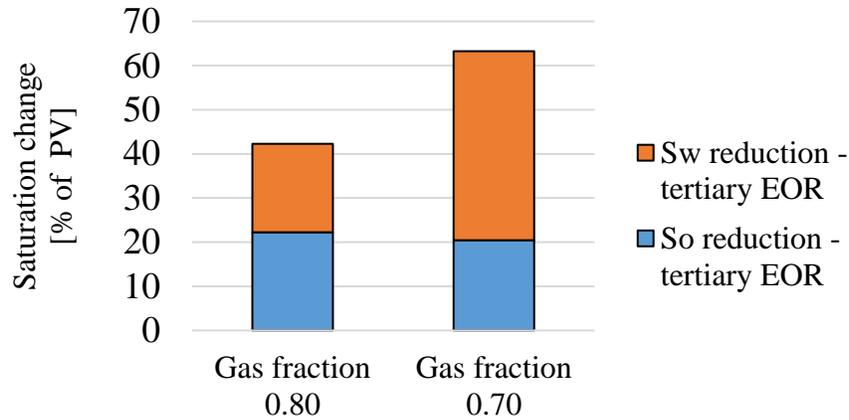
Figure 10 – Saturation change during tertiary EOR (co-injection of surfactant solution and CO₂) at two different gas fractions. The height of each column (blue + orange) equals the total CO₂ storage (CO₂ saturation when co-injection is stopped). The blue part is the oil saturation decrease (displaced by CO₂) and the orange part is the water saturation decrease (displaced by CO₂).

Part 3: Core-Scale Derived Parameters for Numerical Upscaling

A numerical foam model is needed to upscale laboratory foam data to field scale. Several laboratory measurements on a reservoir core plug were performed to obtain input parameters for the empirical model, including relative permeability between CO_2 and brine, foam strength and foam shear thinning behavior.

Relative permeability

Relative permeability curves were constructed from experimental data points (). Because a small system size overestimate irreducible water saturation S_{wc} due to capillary end-effects, the k_{rg} at S_{wc} value for numerical modeling was based on two-phase brine/oil drainage measurements from previous injection tests (**Figure 11**).
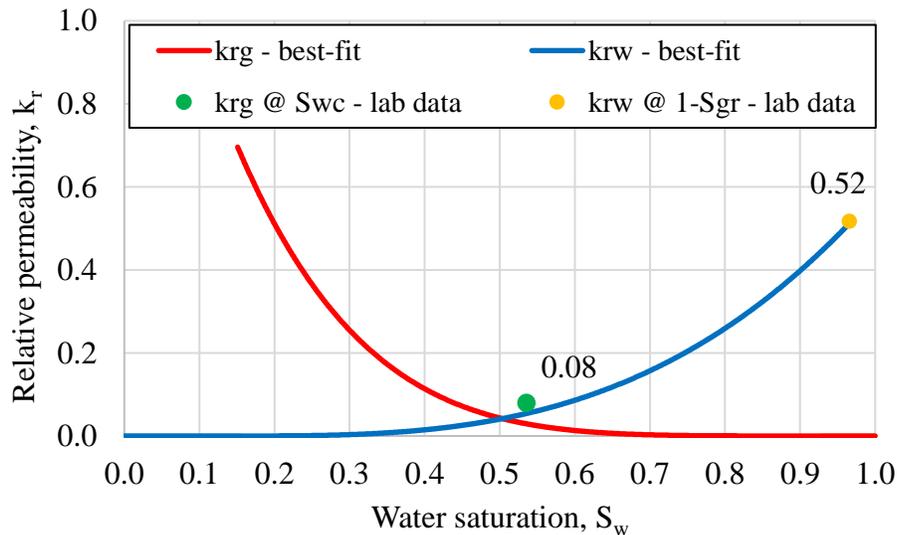
Figure 11 – Relative permeability curves for CO₂ and brine at reservoir conditions in reservoir core plugs. Solid lines shows the best-fit estimate for relative permeability for CO₂ (red) and brine (blue) as a function of water saturation. Green and yellow points are laboratory data for relative permeability of water at irreducible gas saturation (yellow) and relative permeability of gas at irreducible water saturation (green). The short core plug resulted in a high irreducible saturation (S_wc=0.54) and was set to Swc=0.15 in the best-fit estimate to reflect a more realistic scale value.

Foam Model Parameters

Curve fitting regression analysis performed on laboratory data from foam quality and rate scans on the reservoir core plug estimated a best-fit function for the foam behavior and values for fmmob (192), fmdry (0.4) and epdry (84) was obtained (see **Figure 12**). Definitions of the parameters can be found elsewhere

(Ma et al. 2013; Sharma et al. 2017).
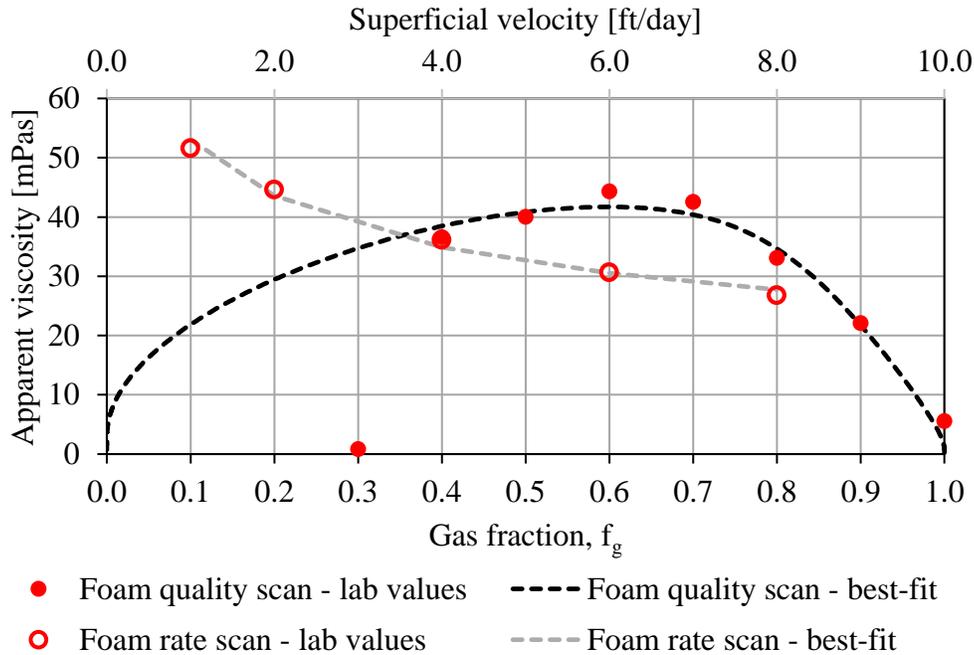
Figure 12 – Foam model fit to experimental data. Red solid dots show laboratory data from CO_2-foam scans (primary x-axis) with black dotted best-fit regression analysis. Red open sircles are laboratory data from gas rate scans (secondary x-axis) with gray dotted best-fit regression analysis.

Conclusions

The laboratory results presented here at pore- and core-scale provide an integrated approach to test and upscale a foam system for field implementaion. In this paper we have evaluated foam system by CO_2 mobility reduction, foam generation, strength, and stability as part of an ongoing field pilot research program. The following key observations were made using a carbonate outcrop and reservoir core material:

- The screened and selected surfactant for the field pilot test significantly decreased CO_2 mobility, corroborated by pore-scale foam generation and flow observations and quantification of foam strength at the core-scale.
- The formation of lamellae (quantified by CO_2-bubble concentration) significantly reduced CO_2 mobility, leading to increased sweep efficiency at the pore-scale. The bubble half-life was 13.3 hours, and long-term foam stability was observed with 37% of initial bubble concentration remaining in the pore space after 3 days at static conditions.
- The optimal gas fraction was 0.60 (reservoir core plug) and 0.70 (carbonate analogue), with apparent viscosities ~600 times higher compared to pure CO_2.
- CO_2 storage potential during CCUS projects increases with foam strength because stronger foam (higher apparent viscosity) mobilize water from the pore space during EOR which allows more pore space for CO_2 storage. The optimal gas fraction (f_g=0.70) produced a stronger foam during tertiary EOR CO_2-foam compared with fg=0.80, and increased the CO_2 storage by 50%.

Acknowledgements

Nomenclature

%*	Percentage Points
2D	Two-dimensional
BPR	Backpressure Regulator
C_0	Initial Bubble Concentration
CCUS	Carbon Capture Utilization and Storage
EOR	Enhanced Oil Recovery
fg	Gas Fraction
fg*	Optimal gas fraction
FM	Mobility reduction factor
k_r	Relative Permeability
k_{rg}	Gas Relative Permeability
k_{rg}^{f}	Gas Relative Permeability Foam
k_{rg}^{nf}	Gas Relative Permeability No Foam
k_{rw}	Water Relative Permeability
PV	Pore Volume
q_g	Injection Rate of Water
q_w	Injection Rate of Water
R_f	Recovery Factor
SAG	Surfactant Alternating Gas
S_{gr}	Irreducible Gas Saturation
S_{wc}	Irreducible Water Saturation
$S_{wc,hysteresis}$	Irreducible Water Saturation with Hysteresis
VEE	Volume Element Exchange
WAG	Water Alternating Gas
WF	Waterflood
Wt%	Weight Percent

References

Alcorn, Zachary P., Martin Fernø, Arne Graue. 2016. Workflow for Optimal Injection of CO2 to Enhance Oil Recovery in Mature Oil Fields: A Preliminary Study for a Field Pilot Program. Proc., SPE Bergen One Day Seminar, Grieghallen, Bergen, Norway. SPE-180029-MS. https://doi.org/10.2118/180029-MS

Alvarez, J. M., H. J. Rivas, W. R. Rossen. 2001. Unified Model for Steady-State Foam Behavior at High and Low Foam Qualities. *SPE Journal* **6** (03). SPE-74141-PA.
https://doi.org/10.2118/74141-PA.

Bennion, Brant, Stefan Bachu. 2005. Relative Permeability Characteristics for Supercritical CO2 Displacing Water in a Variety of Potential Sequestration Zones. Proc., SPE Annual Technical Conference and Exhibition, Dallas, Texas. SPE-95547-MS. https://doi.org/10.2118/95547-MS.

Bennion, Douglas Brant, Stefan Bachu. 2007. Permeability and Relative Permeability Measurements at Reservoir Conditions for CO2-Water Systems in Ultra Low Permeability Confining Caprocks. Proc., EUROPEC/EAGE Conference and Exhibition, London, U.K. SPE-106995-MS. https://doi.org/10.2118/106995-MS.

Buchgraber, M., M. Al-Dossary, C. M. Ross et al. 2012. Creation of a dual-porosity micromodel for pore-level visualization of multiphase flow. *Journal of Petroleum Science and Engineering* **86**

(Supplement C): 27-38. https://doi.org/10.1016/j.petrol.2012.03.012.

Cheng, L., A. B. Reme, D. Shan et al. 2000. Simulating Foam Processes at High and Low Foam Qualities. Proc., SPE/DOE Improved Oil Recovery Symposium, Tulsa, Oklahoma. SPE-59287-MS. https://doi.org/10.2118/59287-MS.

Chou, S. I., S. L. Vasicek, D. L. Pisio et al. 1992. CO2 Foam Field Trial at North Ward-Estes. Proc. SPE Annual Technical Conference and Exhibition, 4-7 October, Washington, D.C. SPE-24643-MS. https://doi.org/10.2118/24643-MS.

Enick, Robert Michael, David Kenneth Olsen, James Robert Ammer et al. 2012. Mobility and Conformance Control for CO2 EOR via Thickeners, Foams, and Gels -- A Literature Review of 40 Years of Research and Pilot Tests. Proc. SPE Improved Oil Recovery Symposium, 14-18 April, Tulsa, Oklahoma, USA. SPE-154122-MS. https://doi.org/10.2118/154122-MS.

Farajzadeh, R., A. Andrianov, R. Krastev et al. 2012. Foam–oil interaction in porous media: Implications for foam assisted enhanced oil recovery. *Advances in Colloid and Interface Science* **183-184**: 1-13. https://doi.org/10.1016/j.cis.2012.07.002.

Fredriksen, Sunniva B., Arthur Uno Rognmo, Martin A. Fernø. 2016. Pore-Scale Mechanisms During Low Salinity Waterflooding: Water Diffusion and Osmosis for Oil Mobilization. Proc., SPE Bergen One Day Seminar, Grieghallen, Bergen, Norway. SPE-180060-MS. https://doi.org/10.2118/180060-MS.

Fredriksen, S.B., Alcorn, Z.P., Frøland, A., Viken, A., Rognmo, A.U., Seland, J.G., Ersland, G., Fernø, M.A. and Graue, A. 2018. Surfactant Pre-Floods during CO_2 Foam for Integrated Enhanced Oil Recovery in Fractured Oil-Wet Carbonates. SPE Improved Oil recovery Conference, 14-18 April, Tulsa, Oklahoma. SPE-190168-MS. https://doi.org/10.2118/190168-MS.

Gauteplass, Jarand, Kuldeep Chaudhary, Anthony R. Kovscek et al. 2015. Pore-level foam generation and flow for mobility control in fractured systems. *Colloids and Surfaces A: Physicochemical and Engineering Aspects* **468**: 184-192. https://doi.org/10.1016/j.colsurfa.2014.12.043.

Henry, Richard L., D. Ramsey Fisher, Stephen P. Pennell et al. 1996. Field Test of Foam to Reduce CO2 Cycling. Proc. SPE/DOE Improved Oil Recovery Symposium, 21-24 April, Tulsa, Oklahoma. SPE-35402-MS. https://doi.org/10.2118/35402-MS.

Hoefner, M. L., E. M. Evans, J. J. Buckles et al. 1995. CO2 Foam: Results From Four Developmental Field Trials. *SPE Reservoir Engineering* 10 (04). SPE-27787-PA. https://doi.org/10.2118/27787-PA.

Hornbrook, J. W., L. M. Castanier, P. A. Pettit. 1991. Observation of Foam/Oil Interactions in a New, High-Resolution Micromodel. Proc. SPE Annual Technical Conference and Exhibition, 6-9 October, Dallas, Texas. SPE-22631-MS. https://doi.org/10.2118/22631-MS.

Jarrell, Perry M., Russell T. Jones. 2002. *Practical aspects of CO2 flooding*, SPE Monograph Series Vol. 22.

Jian, Guoqing, Maura C. Puerto, Anna Wehowsky et al. 2016. Static Adsorption of an Ethoxylated Nonionic Surfactant on Carbonate Minerals. *Langmuir* **32** (40): 10244-10252. http://dx.doi.org/10.1021/acs.langmuir.6b01975.

Jonas, T. M., S. I. Chou, S. L. Vasicek. 1990. Evaluation of a C02 Foam Field Trial: Rangely Weber Sand Unit. Proc. SPE Annual Technical Conference and Exhibition, 23-26 September, New Orleans, Louisiana. SPE-20468-MS. https://doi.org/10.2118/20468-MS.

Jones, S. A., G. Laskaris, S. Vincent-Bonnieu et al. 2016. Surfactant Effect On Foam: From Core Flood Experiments To Implicit-Texture Foam-Model Parameters. Proc., SPE Improved Oil Recovery Conference, Tulsa, Oklahoma, USA. SPE-179637-MS. https://doi.org/10.2118/179637-MS.

Law, D. H. S., Z. M. Yang, T. W. Stone. 1992. Effect of the Presence of Oil on Foam Performance: A Field Simulation Study. *SPE Reservoir Engineering* **7** (02). SPE-18421-PA. https://doi.org/10.2118/18421-PA.

Lemmon, E.W. , M.O. McLinden, D.G. Friend. 2018. Thermophysical Properties of Fluid Systems. In *in NIST Chemistry WebBook, NIST Standard Reference Database Number 69, Eds. P.J. Linstrom*

and W.G. Mallard, National Institute of Standards and Technology, Gaithersburg MD, 20899.

Ma, Kun, Jose L. Lopez-Salinas, Maura C. Puerto et al. 2013. Estimation of Parameters for the Simulation of Foam Flow through Porous Media. Part 1: The Dry-Out Effect. *Energy & Fuels* **27** (5): 2363-2375. https://doi.org/10.1021/ef302036s.

Merchant, David H. 2010. Life Beyond 80: A Look at Conventional WAG Recovery Beyond 80% HCPV Injected in CO2 Tertiary Floods. Proc., SPE International Conference on CO2 Capture, Storage, and Utilization, New Orleans, Louisiana, USA. SPE-139516-MS. https://doi.org/10.2118/139516-MS.

Moffitt, Paul, Doug Pecore, Mark Trees et al. 2015. East Vacuum Grayburg San Andres Unit, 30 Years of CO2 Flooding: Accomplishments, Challenges and Opportunities. Proc. SPE Annual Technical Conference and Exhibition, 28-30 September, Houston, Texas, USA. SPE-175000-MS. https://doi.org/10.2118/175000-MS.

Nguyen, Quoc, George Hirasaki, Keith Johnston. 2015. Novel CO2 Foam Concepts and Injection Schemes for Improving CO2 Sweep Efficiency in Sandstone and Carbonate Hydrocarbon Formations, Univ. of Texas, Austin, TX (United States).

Rognmo, A. U., S. Heldal, M. A. Fernø. 2018. Silica nanoparticles to stabilize CO2-foam for improved CO2 utilization: Enhanced CO2 storage and oil recovery from mature oil reservoirs. *Fuel* **216**: 621-626. https://doi.org/10.1016/j.fuel.2017.11.144.

Rognmo, A. U., H. Horjen, M. A. Fernø. 2017. Nanotechnology for improved CO2 utilization in CCS: Laboratory study of CO2-foam flow and silica nanoparticle retention in porous media. *International Journal of Greenhouse Gas Control* **64** (Supplement C): 113-118. https://doi.org/10.1016/j.ijggc.2017.07.010.

Sanders, Aaron, Raymond Michael Jones, Arwa Rabie et al. 2012. Implementation of a CO2 Foam Pilot Study in the SACROC Field: Performance Evaluation. Proc. SPE Annual Technical Conference and Exhibition, 8-10 October, San Antonio, Texas, USA. SPE-160016-MS. https://doi.org/10.2118/160016-MS.

Schramm, Laurier L. 1994. *Foams : fundamentals and applications in the petroleum industry*, Vol. 242. Washington, DC: Advances in chemistry series, American Chemical Society (Reprint). https://doi.org/10.1021/ba-1994-0242.

Schramm, Laurier L. 2000. *Surfactants : fundamentals and applications in the petroleum industry*. Cambridge, Cambridge University Press (Reprint).

Sharma, M., Z P. Alcorn, S B. Fredriksen et al. Numerical Modeling Study for Designing CO2-foam Field Pilot. IOR 2017 - 19th European Symposium on Improved Oil Recovery Stavanger, Norway, 24 April. https://doi.org/10.3997/2214-4609.201700339.

Taber, J. J., F. D. Martin, R. S. Seright. 1997. EOR Screening Criteria Revisited - Part 1: Introduction to Screening Criteria and Enhanced Recovery Field Projects. *SPE Reservoir Engineering* **12** (03). SPE-35385-PA. https://doi.org/10.2118/35385-PA.

Paper III: An Integrated CO₂ Foam EOR Pilot Program with Combined CCUS in an Onshore Texas Heterogeneous Carbonate Field

Alcorn, Z.P., Fredriksen, S.B., Sharma, M., Rognmo, A.U., Føyen, T.L., Fernø, M.A., Graue, A.

SPE-190204-MS

An Integrated CO$_2$ Foam EOR Pilot Program with Combined CCUS in an Onshore Texas Heterogeneous Carbonate Field

Z.P. Alcorn[1], S.B. Fredriksen[1], M. Sharma[2], A.U. Rognmo[1], T.L. Føyen[1,3], M.A. Fernø[1], and A. Graue[1]
[1]Department of Physics and Technology, University of Bergen, [2]The National IOR Centre of Norway, University of Stavanger, [3]SINTEF Industry

Abstract

A CO$_2$ foam enhanced oil recovery (EOR) field pilot research program has been initiated to advance the technology of CO$_2$ foam for mobility control in a heterogeneous carbonate reservoir. Increased oil recovery with associated anthropogenic CO$_2$ storage is a promising technology for mitigating global warming as part of carbon capture, utilization, and storage (CCUS). Previous field tests with CO$_2$ foam report various results due to injectivity problems and the difficulty of attributing fluid displacement specifically to CO$_2$ foam. Thus, a comprehensive integrated multiscale methodology is required for project design to better link laboratory and field scale displacement mechanisms. This study presents an integrated upscaling approach for designing a miscible CO$_2$ foam field trial, including pilot well selection criteria and laboratory corefloods combined with reservoir scale simulation to offer recommendations for injection of alternating slugs of surfactant solution and CO$_2$ (SAG) while assessing CO$_2$ storage potential.

Laboratory investigations include dynamic aging, foam stability scans, CO$_2$ foam EOR corefloods with associated CO$_2$ storage, and unsteady state CO$_2$/water endpoint relative permeability measurements. Tertiary CO$_2$ foam EOR corefloods at oil wet conditions result in a total recovery factor of 80% OOIP with an incremental recovery of 30% OOIP by CO$_2$ foam after waterflooding. Stable CO$_2$ foam, using aqueous surfactants with a gas fraction of 0.70, provided mobility reduction factors up to 340 compared with pure CO$_2$ injection at reservoir conditions. Oil recovery, gas mobility reduction, producing gas oil ratio (GOR), and CO$_2$ utilization at field pilot scale was investigated with a validated numerical model. Simulation studies show the effectiveness of foam to reduce gas mobility, improve CO$_2$ utilization, and decrease GOR.

Introduction

A site has been selected for a CO$_2$ foam field pilot test in East Seminole Field, which produces from a heterogeneous carbonate reservoir in the Permian basin of west Texas. The field pilot research program aims to advance the technology of CO$_2$ foam for mobility control for enhanced oil recovery (EOR) and CO$_2$ storage. Growing concerns regarding greenhouse gas emissions has led to the increased use of CO$_2$

for EOR and storage as part of carbon, capture, utilization, and storage (CCUS). CO_2 EOR is a mature technology with more than 40 years of experience in the Permian Basin. CO_2 flood performance is often hindered by the unfavorable mobility ratio of CO_2 to reservoir fluids which can lead to gravity segregation, viscous fingering, and poor volumetric sweep efficiency (Hanssen et al. 1994; Lake et al. 2014). The unfavorable mobility ratio and adverse CO_2 properties, mostly density and viscosity, can be mitigated by the use of foam (Heller 1966; Holm 1980; Haugen et al. 2013; Fernø et al. 2015). Foam reduces the relative permeability and the effects of low viscosity of injected CO_2, and can divert flow from high permeability well swept zones to low permeability unswept regions (Rossen 1996).

Field implementation of CO_2 foam presents unique challenges to balance injectivity, gas mobility reduction, well performance, and operational constraints. Typically, CO_2 foam is injected through simultaneous injection of CO_2 and surfactant solution (coinjection) or through the use of alternating slugs of surfactant solution and CO_2 (SAG). While some past field tests have reported success of CO_2 foam reducing gas mobility and improving oil recovery, others present mixed results due to injectivity issues and difficulty in attributing fluid displacement specifically to CO_2 foam (Heller et al. 1985; Chou et al. 1992; Stephenson et al. 1993; Hoefner and Evans 1995; Martin et al. 1995). A more thorough integration of laboratory experiments with interwell simulation and field scale experience can enhance existing knowledge of size-dependent CO_2 foam displacement mechanisms. Thus, an integrated laboratory to field scale methodology is required for project design to advance the understanding of the connection between size-dependent displacement mechanisms of CO_2 foam.

This study presents an integrated upscaling approach for designing a CO_2 foam field trial, including pilot well selection criteria, comprehensive laboratory coreflood experiments combined with reservoir scale simulation to offer recommendations for a SAG injection schedule. Laboratory tests determining optimal foam flooding parameters with reservoir cores are used in validated field scale simulation models to guide injection design and advance the understanding of size-dependent displacement mechanisms encountered throughout the field pilot research program. Moreover, laboratory work offers recommendations for foam system design parameters for field implementation.

East Seminole Field
East Seminole Field is located in the Permian Basin of west Texas (**Figure 1**) and was discovered in the early 1940s with estimated original oil in place (OOIP) of 38 million barrels. The field was developed throughout the 1960s, producing 12% OOIP through pressure depletion. Waterfloods began in the early 1970s and continued into the 1980s with strategic infill drilling, reducing the well spacing from 40 to 20 acres. Waterflooding proved to increase oil recovery with characteristics of increased reservoir pressure, decreased gas oil ratio, and short fill up time resulting in cumulative primary and secondary recoveries of 22% OOIP (Gray 1989).

Tertiary CO_2 floods began in inverted 40 acre 5-spot patterns in 2013 in the eastern portion of the field. Miscible CO_2 injection initially increased oil production and reservoir pressure. However, rapid CO_2 breakthrough, high producing GOR, and CO_2 channeling was soon observed in peripheral production wells. CO_2 performance suffers due to reservoir heterogeneity and unfavorable mobility ratio between injected CO_2 and reservoir fluids resulting in poor areal sweep efficiency, high producing GOR, and CO_2 channeling.
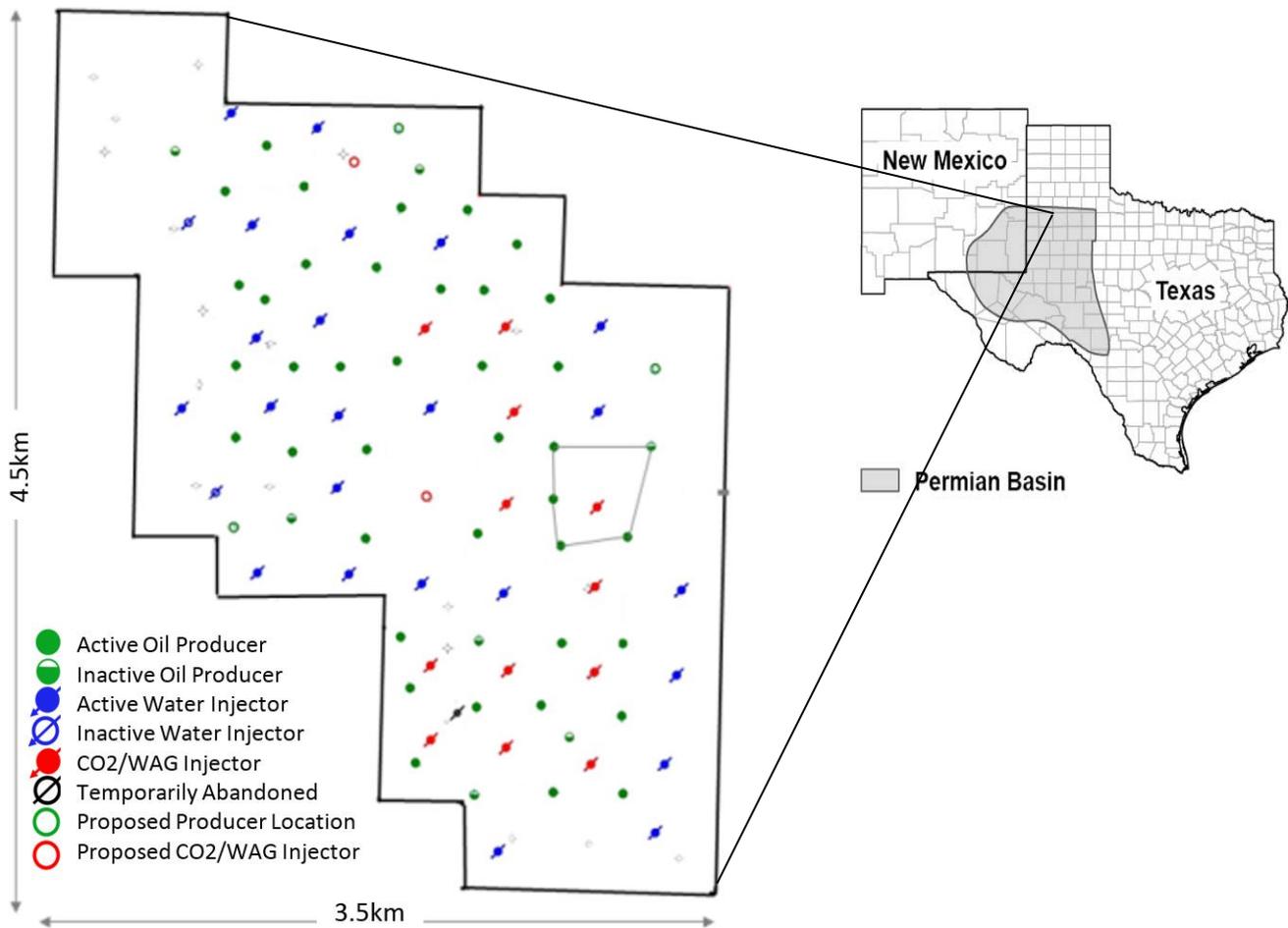
Figure 1–Field location map in the Permian Basin of west Texas. Shaded area shows extent of the Permian Basin.

Reservoir Characterization

East Seminole Field produces from the San Andres unit, a heterogeneous cyclical carbonate consisting of over 190 ft of subtidal, intertidal, and supratidal deposits. Net pay is 110 ft and is characterized by 12 to 15% porosity and an average permeability of 13 mD. Thin high permeability zones occur throughout the pay section with permeabilities up to 300 mD. Subtidal dolostone facies make up the bulk of the reservoir rock which are often interbedded with shaley mudstone layers. Mudstone layers act to limit vertical communication throughout the reservoir and are considered barriers to flow. Leaching and subsequent dedolomitization has resulted in well-developed intercrystalline porosity in the reservoir subtidal facies (Wang et al. 1998).

Initial reservoir pressure was 2500 psig at an average bottom hole temperature of 104°F and a formation fracture pressure of 3900 psig. The current reservoir pressure is 3200 psig, well above the 1500 psig minimum miscibility pressure (MMP) of CO_2 and crude oil. Current reservoir pressure is above the initial reservoir pressure due to the injection of produced water in a disposal well which was completed in one of the lower reservoir zones, in an offset pattern. This injection resulted in the elevated reservoir pressure of 3200 psig. The disposal well has since been deepened and injection into the reservoir zones has ceased, in an effort to decrease the reservoir pressure back to initially measured values. Reservoir wettability in the field is difficult to determine, but most oil reservoirs are considered to be neutral to slightly oil wet.

The field has produced from the San Andres main producing zone (MPZ) for over 50 years, through primary and secondary recovery. As seen in other areas of the Permian Basin, tilted fluid contacts presumed from basin activity and/or a breach of seal have created a deeper residual oil zone (ROZ).

Original hydrocarbon distributions were altered through basinal tilt, establishing the ROZ. These zones are thought to have been naturally waterflooded through hydrodynamic displacement and have been shown to contain considerable immobile oil (20 to 40% OOIP) which can be mobilized by CO_2 flood. Thus, the residual oil saturation in the ROZ is similar to waterflooded zones and establishes it as an economically attractive target for tertiary CO_2 recovery efforts.

Wells in East Seminole Field were deepened and completed into the ROZ as CO_2 floods were initiated in 2013. A more detailed explanation of the origin and genesis of the ROZ is given by Melzer et al. (2006). See **Table 1** for reservoir and fluid properties of the MPZ and ROZ.

Reservoir Characteristic	Value
Depth	5200 ft
Permeability	1 – 300 mD Ave. 13 mD
Porosity	3 – 28 % Ave. 12- 15 %
Pay Thickness	110 ft
Reservoir Pressure (initial)	2500 psig
Reservoir Pressure (current)	3200 psig
Temperature	104ºF
Oil Gravity	31º API
Initial Oil Saturation	0.65
Initial Water Saturation	0.35
Oil viscosity (reservoir conditions)	1.20 cP (at 2500 psig and 104 ºF)
Bubble Point Pressure	1805 psig
Formation Brine Salinity	70,000 ppm
S_{orw}	0.40 (Gray, 1989)
ROZ S_{orw}	0.25 (Honarpour et al. 2010)
ROZ ROS, waterflood	0.32 (Honarpour et al. 2010)
ROZ S_{orm}	0.12 (Honarpour et al. 2010)

Table 1–Reservoir and fluid properties of the San Andres

Heterogeneity measures (**Figure 2**) indicate a very heterogeneous reservoir with Lorenz coefficient of 0.84 and Dykstra-Parsons permeability variation coefficient of 0.79 (Dykstra and Parsons, 1950; Stiles, 1949; Schmalz and Rahme, 1950). Available core data was divided into four main reservoir flow zones (Zones 1 to 4) and used to determine the average Lorenz coefficient for the entire reservoir interval (Figure 2, left). High values of each heterogeneity measure indicate a large variation in permeability which causes CO_2 performance to suffer due CO_2 channeling through high permeability zones. Foam can mitigate these effects by diverting flow from high permeability, low oil saturated, well swept regions to low permeability, high oil saturated, unswept regions. Further, the inherent heterogeneity in platform carbonate formations presents a considerable opportunity to improve the performance of CO_2 injection. Foam has been shown to be more effective in heterogeneous systems at the core and field scale (Haugen et al. 2013; Harpole et al. 1994).
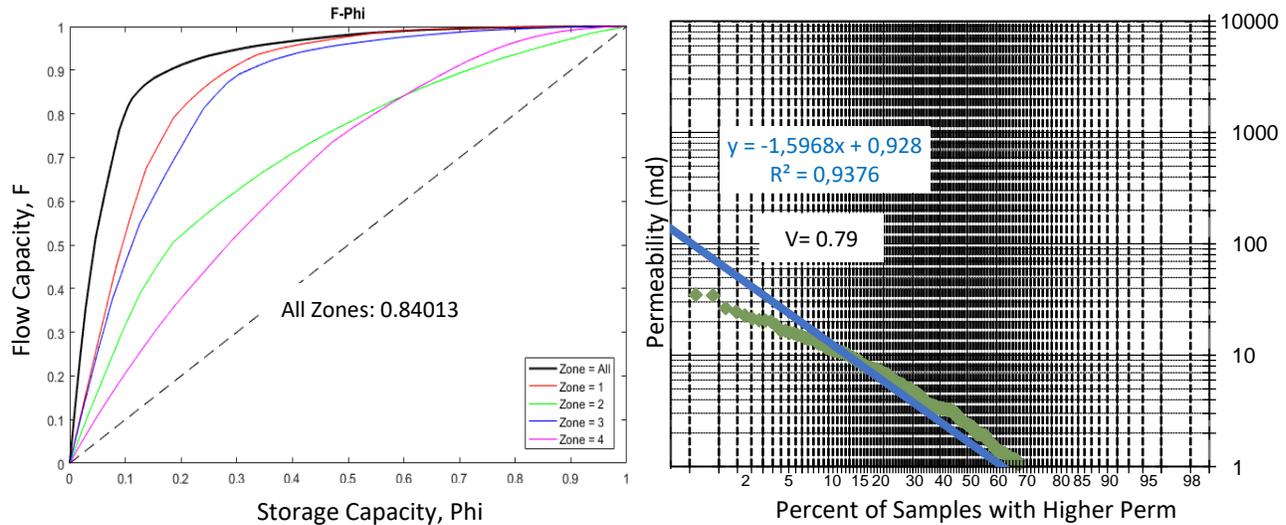
Figure 2–(a) Lorenz coefficient for four identified flow zones (Zone 1-4) and average of all zones (b) Dykstra-Parsons coefficient for available core data

Pilot Design

Once characterizing the reservoir and identifying the opportunity for a foam treatment, clearly defined objectives and definitions of success for CO_2 foam are identified by members of a multidisciplinary team. CO_2 foam injection aims to increase field performance and mitigate the technical challenges of CO_2 injection through achieving the following at East Seminole Field:

- Increase incremental oil production through improved CO_2 sweep efficiency
- Reduce the producing GOR while maintaining injectivity
- Improve CO_2 utilization
- Verify CO_2 storage and mobility control

Pilot Selection Criteria

Adhering to field development plans and minimizing the amount of time required to gather data, an injector-producer well pair was considered for the first CO_2 foam injection at East Seminole Field. The selection of a closely spaced well pair, with an interwell distance of 750 ft, is advantageous for the use of CO_2 foam as reservoir response to foam can be observed much sooner at shorter interwell distances, as opposed to the larger interwell distances associated with standard 5-spots and offshore fields. The field pilot location should contain representative reservoir zones and high well density. The southeastern portion of the field was chosen to analyze for well pair candidates.

Criteria must be followed for the selection of a successful well pair within the field pilot location that establishes a best case scenario to maximize the chance of success for the foam treatment and minimizes avoidable operational issues of selected wells (i.e. injectivity interruptions due to pressure buildup near the injection well). The following criteria were applied to select a well pair for implementation of CO_2 foam:

- The chosen producer in the well pair should experience rapid gas breakthrough from CO_2 injection ahead of the CO_2 foam, relative to surrounding production wells.
- A high gas oil ratio, relative to adjacent producers, should be observed in the selected production well.

- The injection well head pressure should be lower than comparable injection wells to offer a larger window for operational flexibility, to mitigate injectivity issues, since large pressure increases are expected during foam injection.
- The well pair should be in close proximity to minimize geological uncertainty and maximize interwell connectivity.

Respecting the selection criteria and to achieve the outlined objectives, a closely spaced well pair has been chosen consisting of one central injector (IL-1) and one producer (PL-1). The well pair is part of an inverted 40 acre 5-spot which also contains production wells PL-2, PL-3, and PL-4 (**Figure 3**). The selected pattern provides a site to experimentally study the injection of CO_2 foam for analysis on gross oil recovery, improved sweep efficiency, and foam's impacts on CO_2 mobility.
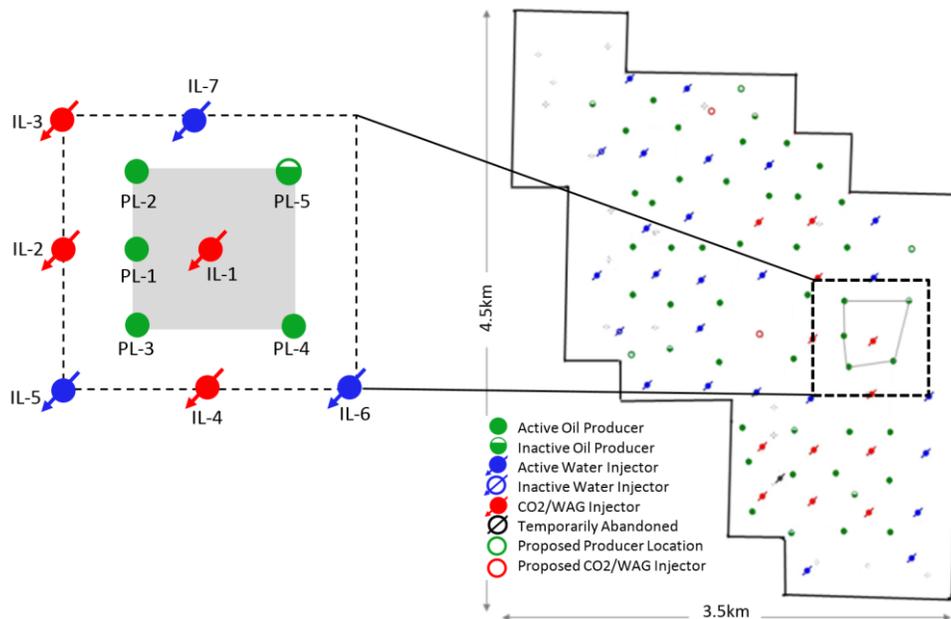
Figure 3–Well map showing location of selected pilot pattern (gray shaded area) and peripheral injection wells.

Continuity of reservoir flow zones, evidence of prior CO_2 breakthrough, close interwell distance, and production and injection history further facilitated the selection process (**Figure 4**). The current operating status of the wells was also considered to make the project economically feasible. The success of CO_2 foam within the well pair provides further insight into utilizing CO_2 foam technology in neighboring patterns and similar heterogeneous reservoirs.

Historical Production and Injection Analysis

Historical field data and petrophysical well logs for the selected well pair permit the following discussion which serves to support the well selection criteria and review well status for the pilot test. Analysis focuses on the selected well pair (IL-1 and PL-1) and a nearby CO_2 injector, IL-2, which likely influences the high producing GOR of PL-1. See **Figure 5** for recent injection and production history.

IL-1 was drilled as a production well by Mobil Producing Texas & N. Mexico Inc. in 1980 and completed to a depth of 5580 ft. Well behavior under primary depletion was typical of solution gas drive reservoirs with decreasing oil production rate and increasing water production. It operated under primary drainage conditions until being switched to injection at the end of July 2013. The well was fully converted to injection by August 2013, when it began injecting water for two months prior to the start of CO_2 injection. CO_2 injection began in October 2013 and continues today at an average rate of 2200 Mcf/day at a THP of 1900 psi. Initial reservoir response to CO_2 injection has been favorable as pressure has increased and no

problems with injectivity have been reported. The well site is also equipped with a WAG skid so minimal workovers and surface alterations will be required to prepare the well for CO_2 foam injection.

IL-2 was drilled in February 1986 and began injecting water in January 1987 at an average rate of 360 bbl/day. It was switched to CO_2 injection in January 2016 and continues to inject at an average rate of 3000 Mcf/day at a THP of 1900 psi. The producing GOR of PL-1 increased significantly shortly after IL-2 CO_2 injection (Figure 5), likely to due to the higher injection rate for IL-2 over IL-1 and/or enhanced permeability zones transporting injected CO_2 from IL-1 to PL-1.
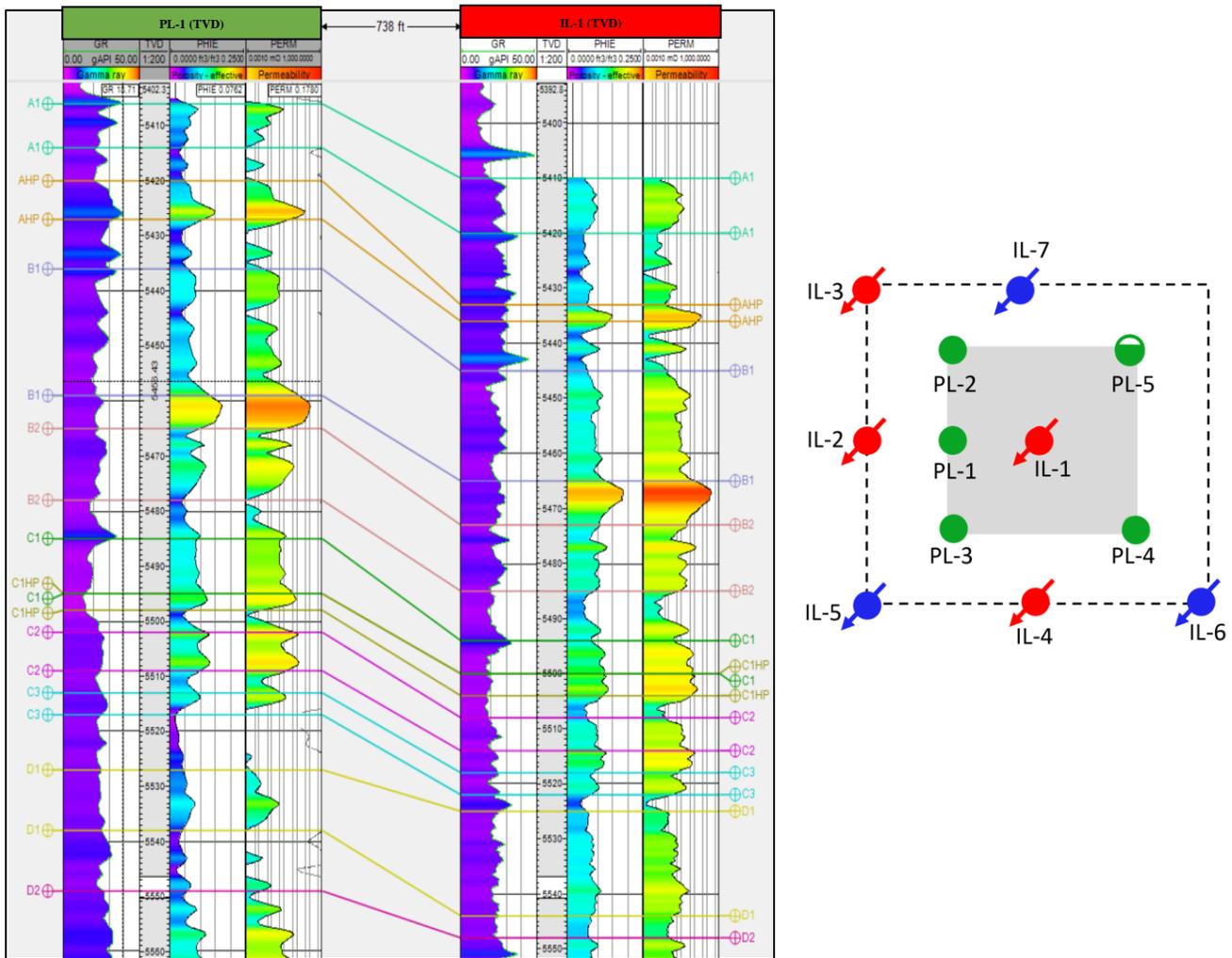
Figure 4–Gamma ray (GR), porosity (PHIE), and permeability (PERM) logs for the selected pilot injection well (IL-1) and production well (PL-1). Major flow zone divisions are shown between wells. Pilot well location map is shown at right (well symbols shown in Figure 3).

PL-1 was drilled in September 2006 and indicated a reservoir pressure of 2500 to 2700 psig (near hydrostatic). The well was opened for primary production in 2006 but by August 2014 the well had declined to an average oil production rate of 3 bbl/day. Oil recovery increased as CO_2 injection began in IL-1 in October 2013. The favorable response to CO_2 injection resulted in average daily oil production rates increasing to 15 bbl/day and a further increase in oil production to 38 bbl/day after IL-2 began injecting CO_2. However, CO_2 breakthrough occurred ten months after the start of CO_2 injection resulting in high producing GOR, CO_2 channeling, and poor CO_2 utilization (Figure 5).

Production rates soon stabilized around 25 bbl/day and gas production continued to rise. The well currently produces more gas than surrounding pattern production wells (**Figure 6**) and has a producing GOR of 35 Mcf/bbl compared to a GOR of 10 Mcf/bbl for adjacent production wells. The high producing GOR (Figure 5, black curve) and low incremental oil recovery indicates poor sweep efficiency and results in poor CO_2 utilization. The closer interwell distance (750 ft) to the CO_2 injection well, relative to other producers (1200 ft), minimizes geologic uncertainty and further presents opportunities for CO_2 foam to improve the performance of miscible CO_2 injection.
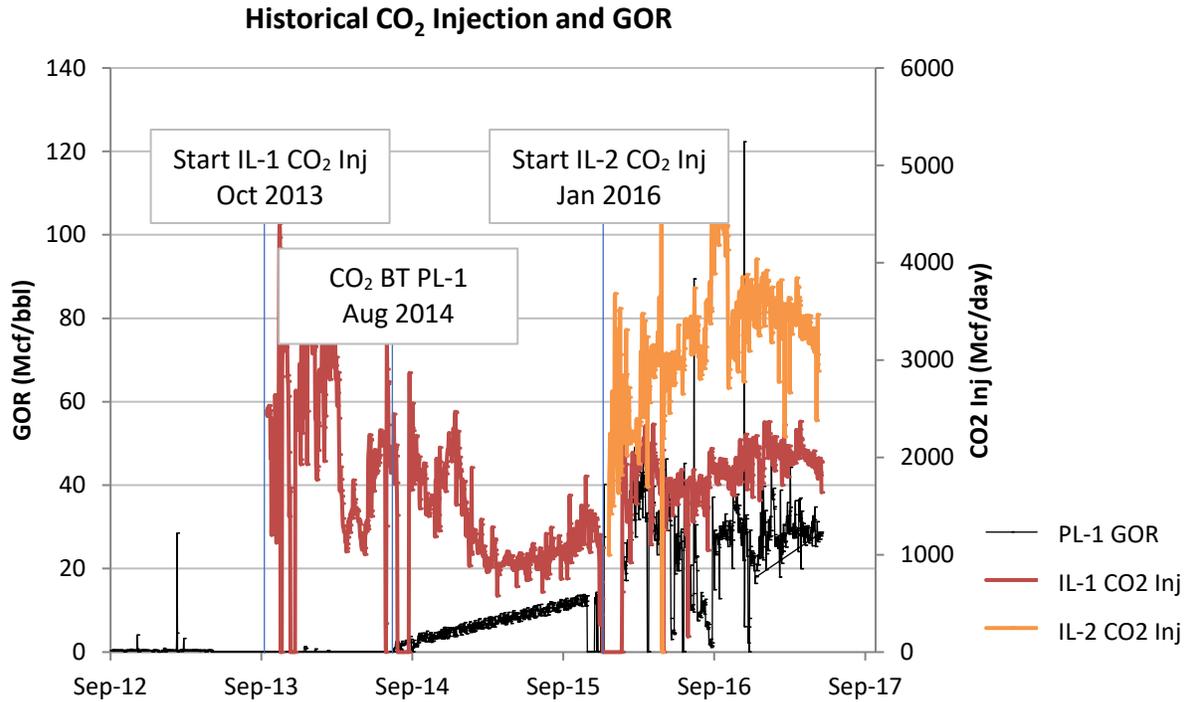
Figure 5–Plot of historical CO_2 injection for IL-1 and IL-2 and producing GOR for PL-1.
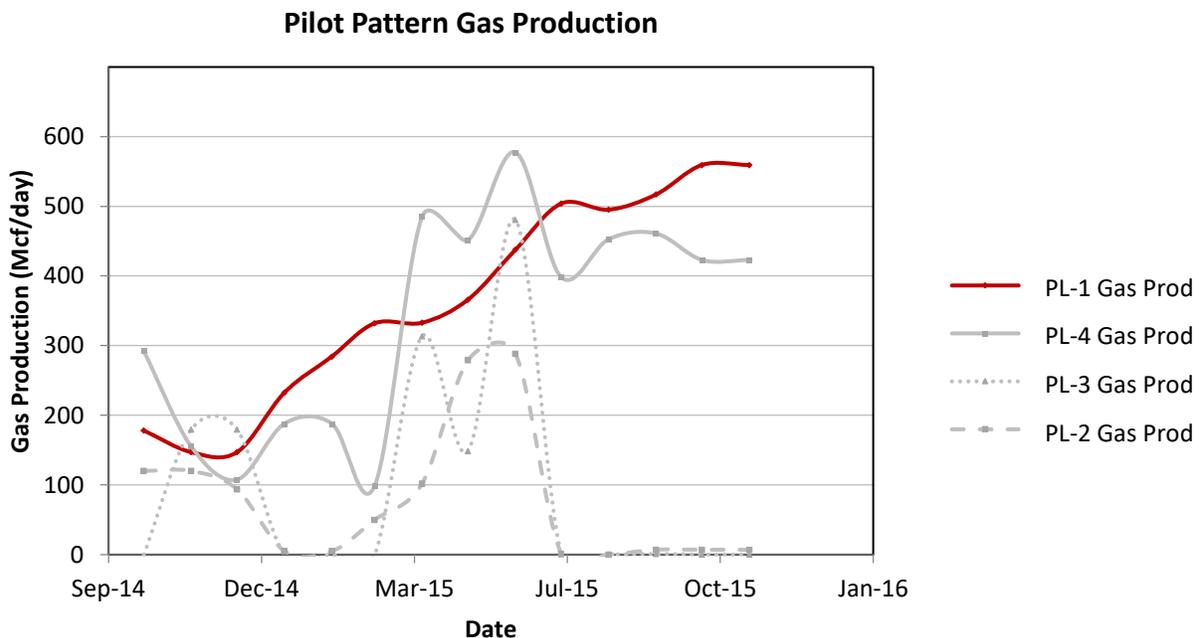
Figure 6–Gas production for wells in the pilot 5-spot pattern. Note the higher gas production in the selected well pair production well (PL-1).

Foam System Design

Foam system design parameters were determined at the laboratory core scale, on reservoir material from an offset producer in the pilot pattern, to offer recommendations for field implementation and provide input to numerical models to predict reservoir response to CO_2 foam injection at the field scale. Experimental work focuses on determining the optimal surfactant concentration and foam quality that generates strong and stable foam, given economic field constraints. Investigations include dynamic aging to reservoir conditions, foam quality/rate scans, CO_2 foam EOR corefloods at optimal gas fraction and flow rate, and CO_2/brine relative permeability experiments all conducted on reservoir rock and fluid material.

Core Preparation

The experimental work was performed on reservoir core material restored to neutral to weakly oil-wet reservoir wettability conditions. Nine 2 inch diameter cores were drilled, parallel to bedding, at different depths (TVD) from a drill core taken from a peripheral producer in the pilot pattern. The cores were cleaned in a Dean Stark apparatus with a 50/50 solution of toluene and methanol for 72 hours (Anderson 1986). The cores were dried at 60ºC until a stable weight was reached, and then saturated with mineral oil under vacuum. Oil permeabilities were measured at different injection rates and calculated by Darcy's law and porosities were calculated based on mass balance (**Table 2**).

The cores were aged dynamically to ensure a uniform reservoir wettability distribution throughout the pore space (Graue et al. 1994, 1999a, 1999b, 2001a and Fernø et al. 2010). Five pore volumes of reservoir crude oil were first injected, miscibly displacing the mineral oil used for saturation and to allow the rock surface to be in contact with the crude oil. Reservoir crude oil was then continually injected at a rate corresponding to 1 ft/day for 4 days in each direction, optimizing the adsorption equilibrium on the rock surface by wettability altering components present in the crude oil.

The Amott Harvey index (I_{AH}) was measured on three cores at different steps in the core preparation procedure to determine wettability after restoration and verify the aging process. Core "J" was aged in reservoir crude as received (no cleaning) showing an $I_{AH} = -0.04$ (neutral wet). The Amott Harvey index was 0.76 (water wet) for core "N" after cleaning in the Dean Stark apparatus (unaged) and -0.79 ± 0.13 (oil wet) for core "E" when aged after cleaning. Measurements verify the cleaning and aging procedure used to restore the remainder of core material and results provide insight into reservoir wettability in contact with reservoir crude oil. Amott Harvey values confirm the neutral to oil wet preference of the reservoir rock and a successful aging towards reservoir conditions.

Core ID	Core and fluid properties					Experiment				
	Porosity	Permeability (mD)	Length (cm)	PV (ml)	C_{surf} (wt%) $\pm$ 5.0E-04	Foam Quality	Foam Rate	EOR	Rel. Perm	I_{AH}
A	0.09 ± 9.35E-04	7.9 ± 0.1	5.5 ± 2.0E-03	9.4 ± 0.1	1.0			X	X	
B	0.11 ± 1.11E-03	32.3 ± 0.1	5.7 ± 2.0E-03	11.9 ± 0.1	1.0	X		X		
C	0.14 ± 1.39E-03	27.7 ± 0.1	5.7 ± 2.0E-03	15.0 ± 0.1	0.5			X	X	
D	0.15 ± 1.46E-03	15.3 ± 0.0	5.6 ± 2.0E-03	15.2 ± 0.1	0.5			X		
E	0.17 ± 1.63E-03	15.3 ± 0.0	5.1 ± 2.0E-03	15.6 ± 0.2	0.5	X		X		X
F	0.17 ± 1.69E-03	11.2 ± 0.0	5.9 ± 2.0E-03	18.7 ± 0.2	1.0	X	X			
G	0.17 ± 1.71E-03	7.9 ± 0.0	6.2 ± 2.0E-03	19.9 ± 0.2	1.0			X		
H	0.14 ± 1.38E-03	26.7 ± 0.1	5.0 ± 2.0E-03	12.8 ± 0.1	1.0	X		X		
I	0.11 ± 1.08E-03	13.4 ± 0.0	5.3 ± 2.0E-03	10.6 ± 0.1	1.0		X			
J	0.09 ± 1.91E-03	16.9 ± 0.5	4.2 ± 6.6E-03	7.5 ± 0.1	1.0			X		X
K	0.14 ± 1.36E-03	22.1 ± 0.1	5.7 ± 2.0E-03	15.2 ± 0.1	n/a				X	
L	0.16 ± 1.52E-03	3.8 ± 0.1	5.9± 2.0E-03	16.8 ± 0.2	n/a				X	
M	0.11 ± 1.32E-03	9.8 ± 0.1	4.5 ± 2.0E-03	9.4 ± 0.1	1.0	X (foam model)	X			
N	0.26 ± 1.65E-03	3.6 ± 0.1	5.5 ± 2.0E-03	16.6 ± 0.3	n/a					X

Table 2–Core and fluid properties used in experimental work.

Foam Quality and Rate Scans

The main objective of the foam quality scans was to determine the optimal gas fraction (f_g), or foam

quality, which generates the most efficient and highest apparent viscosity CO_2 foam with reservoir core and fluids, considering field scale economic constraints. The gas fraction provides information on the transition from low quality foam to a high quality foam regime. Gas fraction refers to the fraction of injected gas to liquid and can be defined as:

$$f_g = \frac{q_{gas}}{q_{gas} + q_{liquid}} \quad \dotfill \text{(1)}$$

where q_{gas} and q_{liquid} are the individual flow rates (with identical units) of gas and liquid, respectively. Foam apparent viscosity describes gas mobility reduction during foam flow and is used as an indicator of foam strength (Hirasaki and Lawson, 1985). Foam apparent viscosity is calculated by Equation 2,

$$\mu_{app} = \frac{k\nabla p}{(u_l + u_g)} \quad \dotfill \text{(2)}$$

where k is the permeability of the porous medium, ∇p is the pressure gradient measured across the core, and u_l and u_g are the superficial velocities of liquid and gas, respectively (Jones et al. 2015).

Foam quality scans were run on restored reservoir cores at residual oil saturation (S_{or}), after CO_2 foam displacement. The decision to conduct scans on cores a S_{or} was to investigate foam generation, stability and apparent viscosity in the presence of S_{or}, a more realistic condition encountered in the field. Once the optimal f_g was determined from the foam quality scans, a foam rate scan was conducted to determine the injection rate which generates the highest apparent viscosity foam at the specified f_g. Foam rate scans give an estimate of rate-dependency on shear-thinning foam behavior and provide an optimal injection rate for high viscosity foam generation. The optimal f_g and injection rate were then utilized in CO_2 foam EOR coreflood experiments.

Procedure
Foam quality scans were completed using a surfactant solution of Huntsman L24-22 and reservoir brine. Surfactant screening studies identified the non-ionic Huntsman L24-22 as the best foaming agent with minimal adsorption for the reservoir rock (Jian et al. 2016). The selected surfactant has also been shown to alter the wettability of oil wet rock towards neutral wet conditions, and thus may be capable of establishing capillary continuity across open fractures to provide a viscous component across isolated matrix blocks (Fredriksen et al. 2018; Graue et al. 2001b, 2002; Aspenes et al. 2002 and Fernø et al. 2007, 2012).

Three quality scans were run with 0.5 weight percent (wt%) surfactant solution whereas two were conducted with 1 wt% to investigate the impact of surfactant concentration (C_{surf}) on foam generation and stability. CO_2 and surfactant solution were coinjected at 1 ft/day starting at $f_g = 0.1$. As the pressure differential reached steady state, the gas fraction was increased from low to high by 10% (0.1 f_g intervals) until $f_g = 0.9$. Quality scans were conducted at reservoir conditions of 40ºC and 172 bar (2500 psi). See **Table 2** for core and fluid properties.

Foam rate scans were conducted at fixed quality ($f_g = 0.70$) to determine foam apparent viscosity and the effect of shear thinning on foam generation at different flood rates starting at 1ft/day. Once steady state was reached for each flow rate, the rate was changed to 2, 4, 6, and 8 ft/day. Foam rate scans were conducted at the same experimental conditions as the foam quality scans.

Results and Discussion
Foam quality was evaluated at different gas fractions to determine the optimal ratio of CO_2 and surfactant solution that generates strong foam in the reservoir core and fluid system. Apparent foam viscosity versus gas fraction (**Figure 7**) demonstrates that the highest apparent viscosity foam was generated at $f_g = 0.70$

(dashed line), when considering economically feasible f_g (high CO_2 fraction and low aqueous fraction). The relatively small reduction in foam apparent viscosity between $f_g = 0.30$ to 0.70 compared to $f_g = 0.70$ to 0.90 does not justify the choice of a more expensive CO_2 to surfactant solution ratio. Therefore, a gas fraction of 0.70 is recommended for field testing. However, the actual gas fraction for field implementation will be challenging to control due to injection mode strategy and multiple zones of injection and mixing near the wellbore. Nonetheless, the foam quality scans reveal a target of volume fractions for field injection.

The foam quality scans using 1 wt% surfactant solution (Figure 7, green curves) show slightly higher apparent viscosities when compared to scans with 0.5 wt% surfactant solution (Figure 7, blue curves). Apparent viscosities achieved with 0.5 wt% solutions at $f_g = 0.70$ were ~20 cP, sufficient for field testing, whereas the increase in apparent viscosity at 1 wt% surfactant is not large enough to warrant the use of a more concentrated solution. The impacts of surfactant concentration were further investigated in the EOR corefloods with crude oil present (see CO_2 Foam EOR corefloods).

The foam rate scans conducted at foam quality of 0.70 resulted in the highest calculated apparent viscosity at a flow rate of 1 ft/day (**Figure 8**). The rate scan using 0.5 wt% surfactant solution had the highest calculated apparent viscosity of 48 cP (Figure 8, blue circle), whereas the highest apparent viscosity for the 1 wt% surfactant solution was 27 cP (Figure 8, green circle). The range in apparent viscosities between the 0.5 wt% and 1 wt% surfactant solution can be attributed to variable permeabilities and S_{or} of the core material. The scan using 0.5 wt% surfactant solution had a core permeability of 27.7 mD and the scan using 1 wt% surfactant solution had a core permeability of 7.9 mD. This difference in permeability impacts the performance of foam. Core material with higher permeability has been shown to generate higher apparent viscosity foam than cores that have lower permeability values and higher capillary entry pressure (Lee et al. 1991). Rate scans show a decreasing apparent viscosity with increasing flow rate, demonstrating the shear thinning behavior of foam and increased gas phase mobility. For field application, shear thinning behavior is desirable near the injection well where flow rates are high and gas mobility reduction is modest.
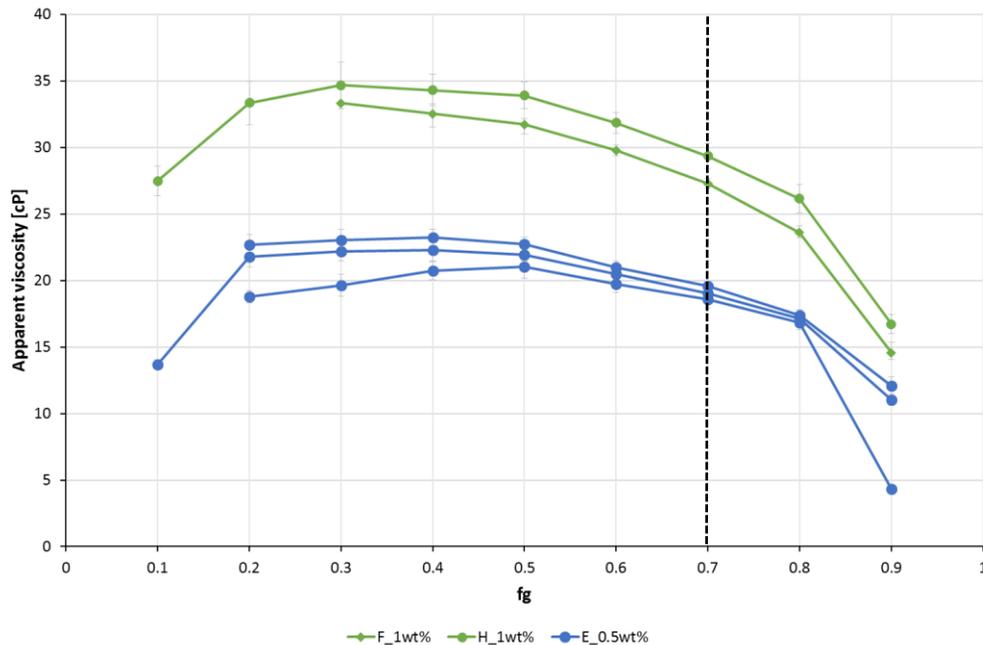
Figure 7–Apparent CO_2 foam viscosity versus gas fraction for five foam quality scans on reservoir core material at 40⁰C and 172 bar (2500 psi) at a rate of 1ft/day. Dashed line represents recommended gas fraction. Cores are at S_{or} prior to scan. Gray bars represent calculated uncertainties.
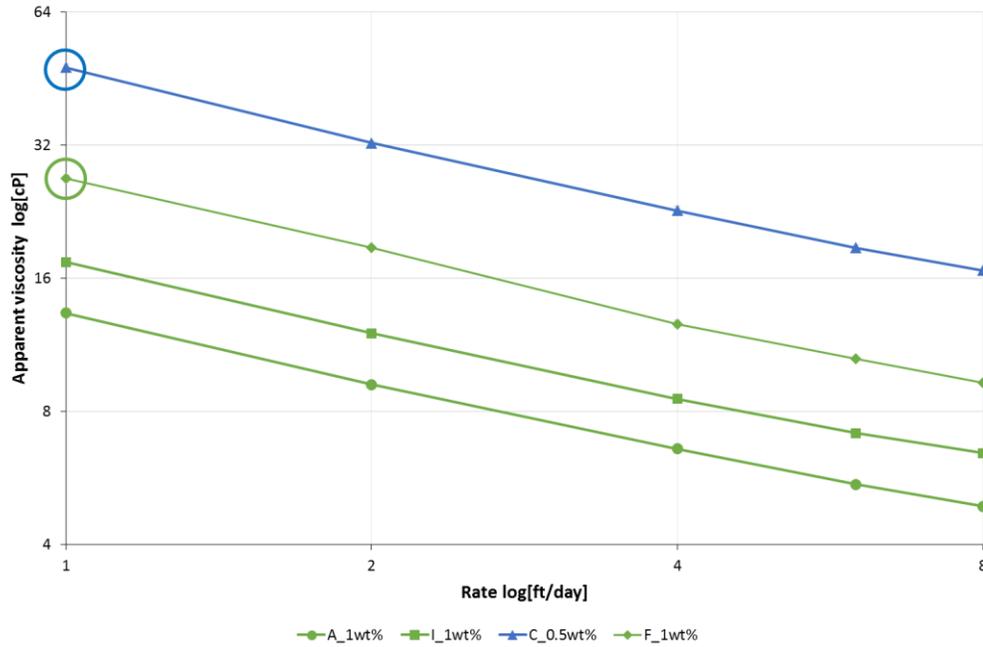
Figure 8–Log-log plot of apparent CO_2 foam viscosity versus flow rate for four foam rate scans conducted at f_g=0.70. Rate scans were conducted following the foam quality scans.

CO_2 Foam EOR Corefloods and Associated CO_2 Storage

CO_2 foam EOR corefloods aim to determine the optimal surfactant concentration used for field testing through analyzing recovery factor (Rf) and apparent viscosity by foam. CO_2 storage at reservoir conditions for the core scale system was also estimated. Secondary waterflooding was performed in all experiments prior to tertiary CO_2 foam injection. CO_2 foam injections were compared against a pure CO_2 flood.

Because foam is composed of distinct liquid and gas phases, foam mobility refers to the separate mobilities of gas and liquid in the presence of surfactant (Rossen 1996). During flooding, most of the continuous liquid phase travels to pore space it would in the absence of surfactant while the small amount of remaining liquid serves to stabilize lamella separating the discontinuous gas phase. Therefore, the mobility of liquid is mostly unaffected and gas mobility is greatly reduced. In this paper, CO_2 foam was evaluated by its apparent viscosity quantified from Equation 2, where a high apparent viscosity foam results in high CO_2 mobility reduction. When steady state was achieved during CO_2 foam flooding a mobility reduction factor (MRF) was calculated,

$$ MRF = \frac{\mu_{app,CO2foam}}{\mu_{,CO2}} \dots\dots\dots\dots\dots\dots\dots\dots\dots\dots\dots\dots\dots\dots\dots\dots\dots\dots\dots\dots\dots\dots\dots\dots\dots\dots\dots\dots\dots\dots\dots\dots (3) $$

where, $\mu_{,CO2}$ is the thermodynamic viscosity of pure CO_2 at reservoir temperature and pressure, and $\mu_{app,CO2foam}$ is the apparent viscosity of CO_2 foam calculated from its pressure gradient during flooding. Several mechanisms will contribute to the foam apparent viscosity during CO_2 foam flooding including lamella creation, trapped gas and oil-in-water emulsification, all of which increase pressure response and inferred higher apparent viscosities.

Procedure

Reservoir core material was cleaned and restored to reservoir conditions (see Core Preparation) and 100% oil saturated for the CO_2 EOR experiment and for the five CO_2 foam EOR experiments (Table 2). Cores were installed in a horizontally oriented Hassler core holder and pressurized to reservoir conditions of

40ºC (104ºF) and approximately 172 bar (~2500 psi). The CO_2 EOR experiment consisted of an initial waterflood, CO_2 flood, and a final CO_2 foam flood.

Three CO_2 foam EOR experiments used a 0.5 wt% surfactant concentration and two used 1 wt% surfactant concentration. An initial waterflood was performed followed by a surfactant pre-flush to satisfy surfactant adsorption and provide optimum foam conditions before conducting a tertiary CO_2 foam flood. The selected surfactant has previously been screened and was shown to have minimal adsorption of 0.08 mg/g on dolomite core material (Jian et al. 2016). All flood rates were 1 ft/day and CO_2 was coinjected with surfactant solution at a gas fraction of 0.70 through a foam pre-generator consisting of unconsolidated sand (due to short core lengths). CO_2 foam was injected for no more than two pore volumes considering the volumetric and economic limits of foam injection in field. Differential pressures were recorded during each flood to calculate apparent viscosity at steady state. In addition, mass balance calculations during the CO_2 foam floods provided an estimate of core scale CO_2 storage.

Results and Discussion
Figure 9 shows oil saturation and apparent viscosity (cP) versus pore volume (PV) injected for the CO_2 and the CO_2 foam injections. Waterflood recovery (blue curves) showed early water breakthrough and two-phase production from the start of injection. Waterflood recovery was on average $32.2 \pm 6.1\%$ OOIP. No oil was recovered during the subsequent surfactant pre-flood (orange curves). When introducing CO_2 foam (green curves), similar incremental recoveries were observed regardless of surfactant concentration. Using 0.5 wt% surfactant solution recovered an incremental of $28.5 \pm 6.0\%$ OOIP, whereas 1.0 wt% surfactant solution produced an additional $29.2 \pm 2.2\%$ OOIP.
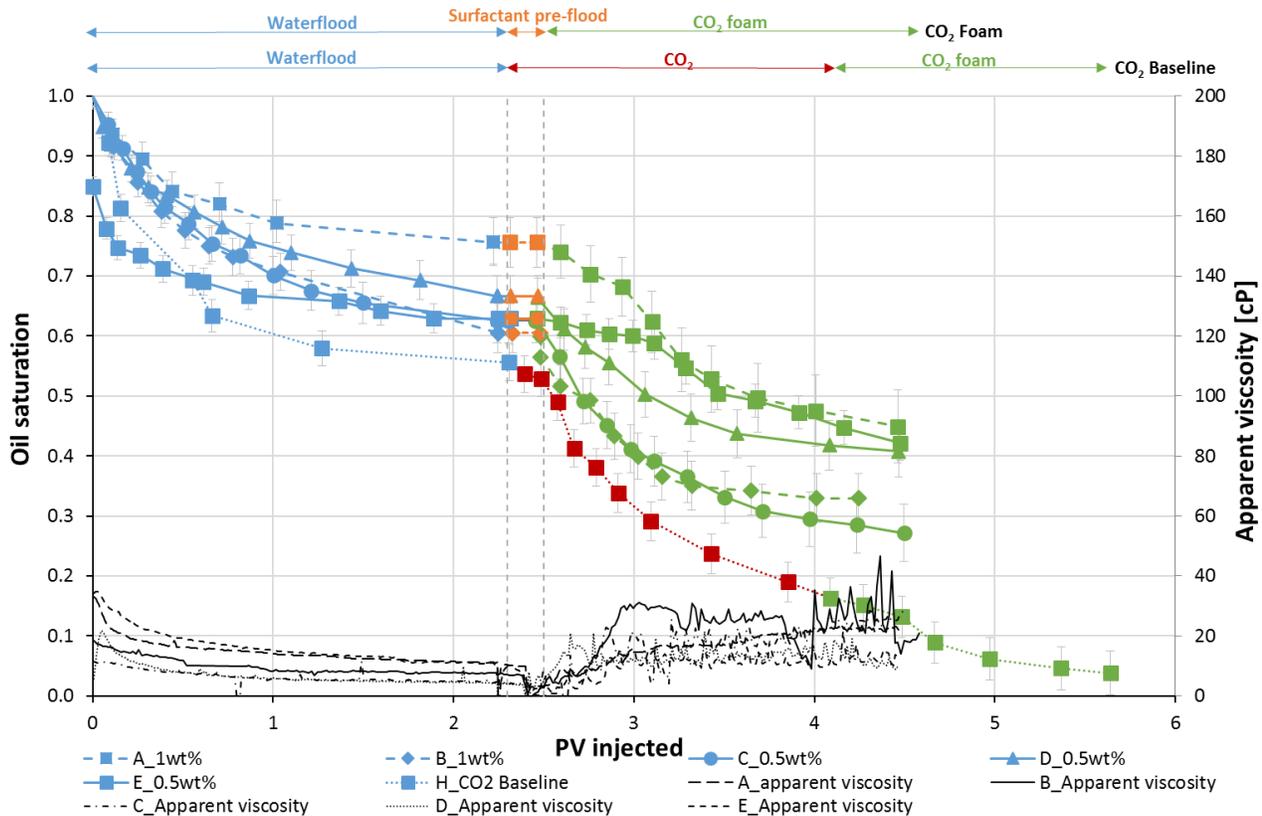
Figure 9–Oil saturation (fraction of PV) vs pore volume injected for the CO_2 EOR baseline after waterflooding (H) and five CO_2 foam EOR corefloods performed after waterflooding (A, B, C, D, E). Blue curves correspond to waterflood, orange to surfactant preflush, red to CO_2, and green to CO_2 foam. Stages of injection are also shown at the top of the graph. Differential pressures (black curves) are plotted on the secondary y-axis. Gray bars represent calculated uncertainties.

CO_2 foam injections were benchmarked against a pure CO_2 flood (red curve) after waterflood. An important note was that the pure CO_2 flood injected 30% more CO_2 ($f_g = 1.0$) compared to CO_2 foam (i.e. $f_g = 0.70$, $f_{surf} = 0.30$). A total of 1.7 PVs of CO_2 was injected during the CO_2 flood, recovering an additional $37 \pm 5\%$ OOIP, which was above average for all CO_2 foam floods (*i.e.* $28.8 \pm 3.9\%$ OOIP) in Figure 9. Additional recovery by CO_2 foam, after CO_2 injection, was 15% OOIP, reducing S_{or} to 0.04 ± 0.04, indicating improved recovery performance by foam even at low residual oil saturations.

The overall recovery of the CO_2 flood was greater than for the CO_2 foam floods due to increased CO_2 efficiency at the laboratory scale. This is mostly due to diffusion dominating the displacement in small core systems. Stable liquid films (lamella) form between the CO_2 and oil phase hindering miscibility and limiting displacement by diffusion during CO_2 foam floods. In addition, the analysis of effluent revealed oil-in-water emulsions of which also reduce displacement from diffusion and impact miscibility. This resulted in higher S_{or} for CO_2 foam ($S_{or} = 0.39$) versus the CO_2 flood ($S_{or} = 0.19$). Further, the higher volumes of CO_2 injected during the baseline CO_2 flood promoted miscibility and recovered more oil. At the field scale, the effect of lamellas and oil-in-water emulsions preventing miscibility between CO_2 and crude oil will be less dominant due to the longer exposure time associated with a field scale process (Taylor, 1998). The longer time scale will permit coalescence between oil and CO_2 as lamellas continuously collapse and regenerate, resulting in improved miscibile displacement and increased performance by CO_2 foam.

Field scale displacement is impacted more by reservoir heterogeneity and gravity effects and less by miscibility and diffusion. Thus, establishing viscous displacement forces during foam injection is critical to the success of the process. The benefits of foam at the laboratory scale should, therefore, not be assessed by increased oil recovery (compared to CO_2 flood) but by increased apparent viscosity, which is more important for fluid diversion at the field scale to mitigate the effects of reservoir heterogeneity and gravity.

A final evaluation of surfactant concentration was based on foam stability in terms of apparent viscosity during CO_2 foam injection (secondary y-axis, Figure 9). **Table 3** presents waterflood Rf, incremental Rf by CO_2 foam, MRF by CO_2 foam, and apparent viscosities for all EOR corefloods. The same range of overall Rf and MRF values were observed between 0.5 wt% and 1 wt% surfactant solutions. Average apparent foam viscosities (at the end of CO_2 foam) varied between 13 to 25 cP for all corefloods, independent of surfactant concentration. Similar values for overall recovery factor, apparent viscosity, and MRF does not justify the use of a more expensive 1 wt% surfactant solution in the field. Apparent viscosities of approximately 15 to 20 cP are observed for 0.5 wt% surfactant solution and are often sufficient for field application (Hirasaki 2017). Therefore, a surfactant solution of 0.5 wt% is recommended for field testing. In addition, a nominal surfactant preflush (0.15 PV) proved to satisfy surfactant adsorption losses and established favorable conditions for initial foam generation and also is suggested for field testing.

Core ID	C_{surf} (wt%) ± 5.0E-04	Rf_{WF} (%OOIP)	$Rf_{CO2\ foam}$ (%OOIP)	$\mu_{app\ CO2\ foam}$ (Pa·s)	$MRF_{CO2foam}$
A	1.0	24 ± 5%	31 ± 8%	0.022 ± 9.585E-05	307 ± 1
B	1.0	39 ± 3%	28 ± 5%	0.025 ± 0.002	348 ± 34
C	0.5	37 ± 4%	35 ± 6%	0.025 ± 4.980E-04	338 ± 7
D	0.5	34 ± 3%	26 ± 5%	0.013 ± 8.230E-04	177 ± 11
E	0.5	26 ± 3%	24 ± 4%	0.013 ± 9.476E-04	173 ± 13
G	1.0	48 ± 2%	36 ± 3%	0.017 ± 5.414E-04	239 ± 7
H	1.0	44 ± 3%	Incr. by CO_2: 37 ± 5% Incr. by CO_2 foam: 15 ± 7%	0.017 ± 2.666E-04	230 ± 4
J	1.0	43 ± 6%	48 ± 9%	0.022 ± 5.624E-04	306 ± 8

Table 3–Overview of CO_2 foam EOR corefloods showing Rf for waterflood and incremental Rf by CO_2 foam, apparent viscosities, and MRF by CO_2 foam.

Volumetric conservation during tertiary CO_2 foam corefloods provided an estimate of CO_2 storage for the core scale system at reservoir conditions (**Figure 10**). On average, less CO_2 was stored using the 0.5 wt% surfactant concentration (~42.2% PV) compared to the 1.0 wt% concentration (~54.6% PV). Storage potential for the 0.5 wt% surfactant solution was equal to the pure CO_2 flood storing 41.7% PV (H_CO_2 flood, Figure 10). Calculated apparent foam viscosities, however, were in the same range for all corefloods (Table 3) and could not explain the observed difference in storage potential. The influence on storage potential may be due to the fact that with less surfactant, wettability alteration and IFT reduction was reduced for the system providing less aid to the displacement process during foam.
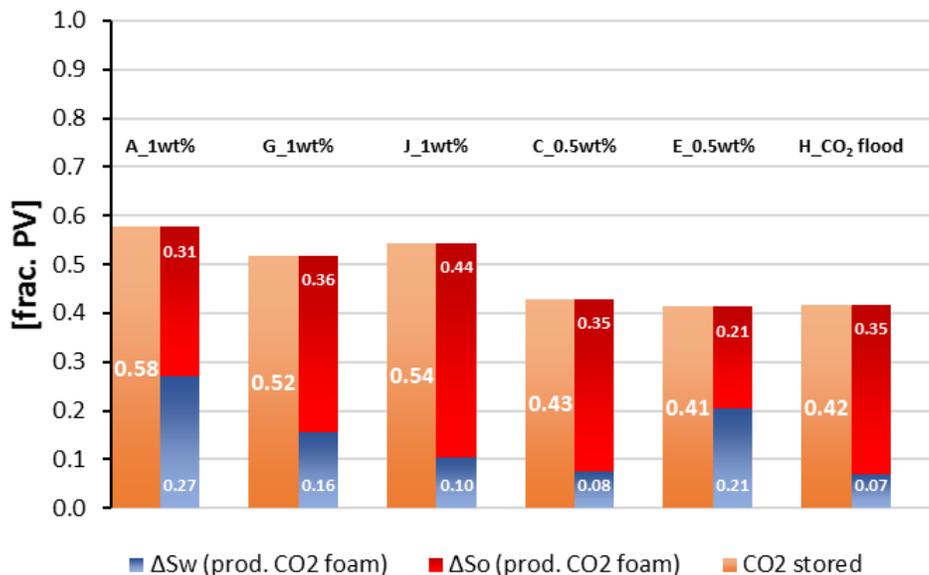
Figure 10–CO_2 storage potential during CO_2 foam EOR corefloods in oil-wet reservoir cores. Orange bars represent CO_2 stored in fraction of PV calculated from volumetric conservation, and the blue and red bars are change in water and oil saturation respectively during foam injection.

The values for CO_2 storage were compared to the saturation change of oil and water after CO_2 foam (red and blue bars, Figure 10). A direct correlation was observed between the amounts of CO_2 stored and saturation changes. In the oil-wet and oil saturated systems, CO_2 storage was governed by oil displacement as observed by the higher oil saturation changes compared to water. The effect became clear when plotting CO_2 storage as a function of oil production in **Figure 11**.

Figure 11 shows CO_2 stored as function of oil produced for four CO_2 foam floods (green curves) and the CO_2 flood (red curve). Increased CO_2 storage was observed from the start of injection as oil was continuously produced. However, the relationship between CO_2 stored and oil produced was above unity (black line) for all corefloods, meaning that a higher amount of CO_2 was stored compared to the amount of oil produced. The deviation from unity suggests that there are several displacement mechanisms occurring at the same time during CO_2 foam injection. CO_2 is displacing brine from the initial waterflood and oil from the pore-space in favor of CO_2 storage. Hence, a larger volume of CO_2 is stored from that of oil produced in Figure 11. In addition, some CO_2 will partially dissolve into the oil and water phase left behind in the pore-space.

Capillary trapping of CO_2 depends on reservoir wettability (Al-Menhali and Krevor 2016; Iglaur 2017). Studies have shown that significant trapping is expected if CO_2 is the non-wetting phase i.e. in water-wet saline aquifers where the rock remains unaltered by hydrocarbons (Al-Menhali and Krevor 2016). In the oil-wet system above the MMP, supercritical CO_2 may be intermediate-wetting towards the pore surface leading to film drainage and less CO_2 stored in terms of water displacement and capillary trapping (Chalbaud et al. 2007; Salathiel 1973).
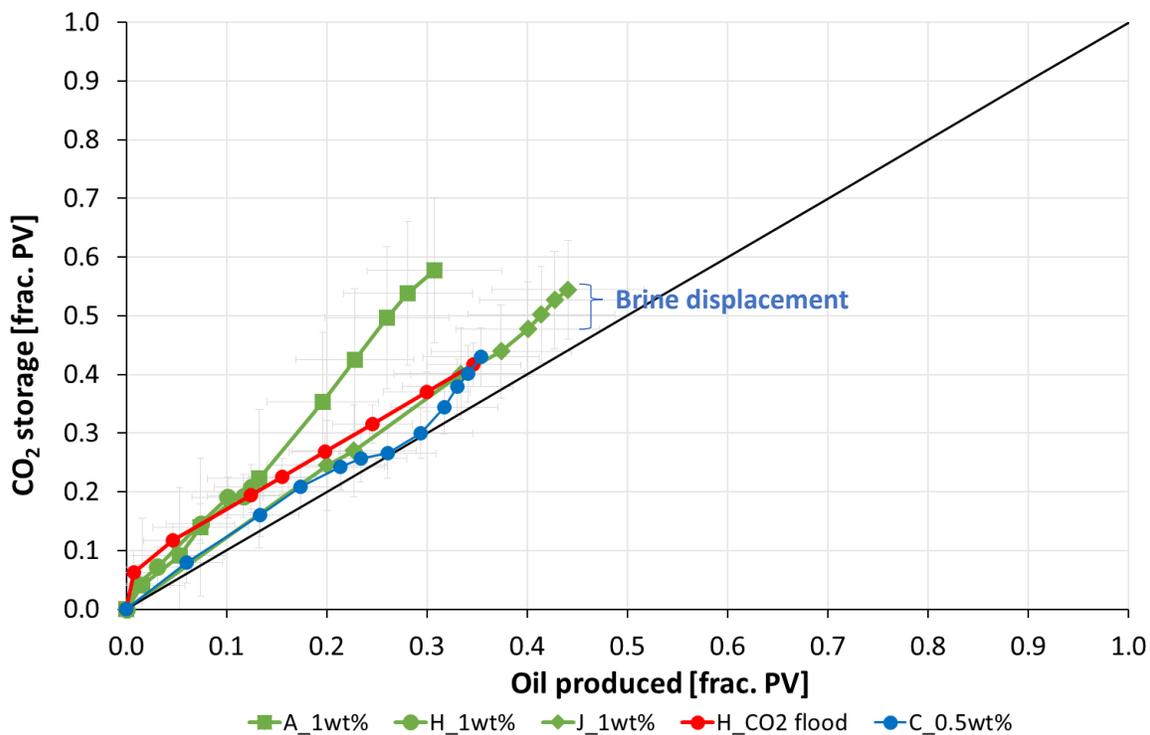
Figure 11–Oil production vs CO_2 stored during four CO_2 foam floods (green) and one CO_2 flood (red). A higher volume of CO_2 is stored compared to oil produced indicating brine displacement by CO_2 foam and CO_2 flood resulting in increased volume available for CO_2 storage. Black line represents unity with difference attributed to brine displacement. Gray bars show calculated uncertainties.

Figure 12 shows the relationship between the volume of CO_2 injected and CO_2 stored. The higher the residual oil saturation after waterflood, the more CO_2 is consequently stored within the pore network. Rapid CO_2 storage occurs during the first pore volume of CO_2 injected, after this the rate decreases with

the rate of oil production. Hence, on field scale, the storage potential will be greatest in the unswept zones where the residual oil saturation is highest, providing a valuable target for sequestration during mobility control by CO_2 foam. In addition, several displacement mechanisms occur simultaneously at reservoir scale, and capillary trapping will also occur in zones that have previously been waterflooded, providing a large potential for CO_2 storage for the reservoir as a whole.
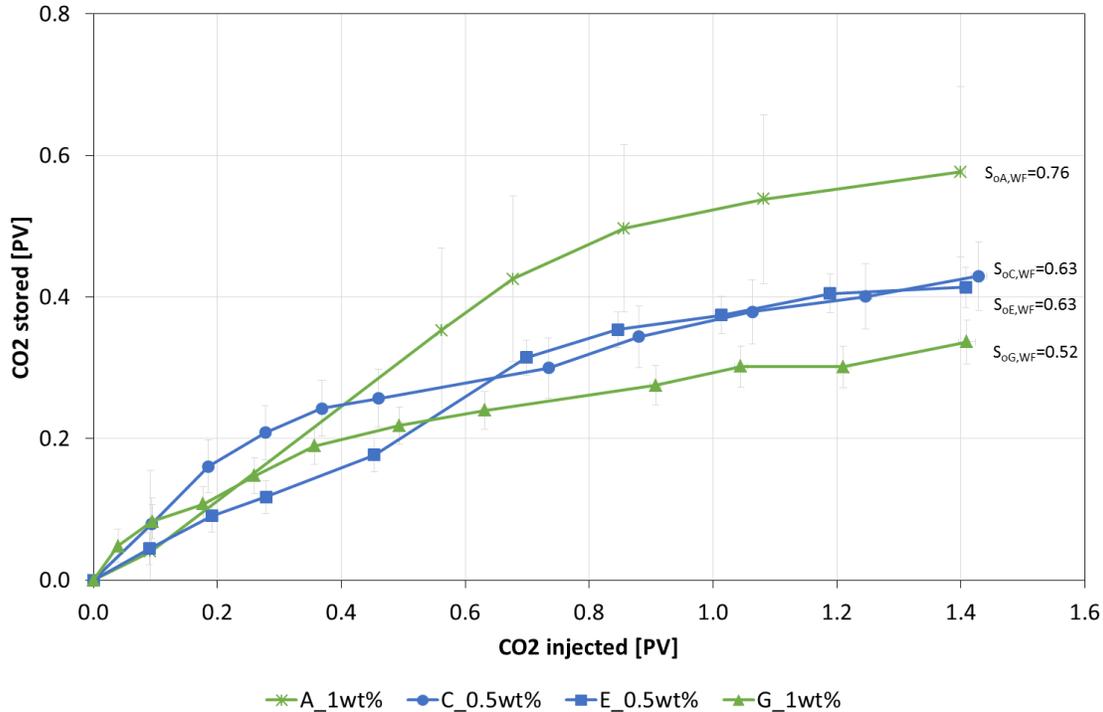
Figure 12–CO_2 injected vs CO_2 stored as functions of pore volumes during CO_2 foam EOR corefloods. Green and blue curves show experiments using 1wt% and 0.5wt% surfactant concentration, respectively. The potential for CO_2 storage depends on the residual oil after initial waterflood. Most of the CO_2 is stored during the first pore volume of CO_2 injected, when oil recovery is high. Gray bars represent calculated uncertainties.

CO2/Brine Relative Permeability

To obtain two and three-phase relative permeability curves for the numerical modeling, a set of core floods was performed in a CO_2/brine system using reservoir rock at reservoir conditions. By measuring the endpoint effective permeabilities, Corey correlations were used to give an estimation of the complete two- and three-phase relative permeability curves. The experiments consisted of four injection sequences in consecutive order: primary CO_2 drainage, primary brine injection, secondary brine injection (at higher volumetric flow rate) and secondary CO_2 drainage. The objective was to obtain the endpoint effective permeabilities at irreducible fluid saturation as a function of displacement process, and from these calculate the endpoint relative permeabilities (ratio of effective permeability to absolute permeability).

Procedure

To obtain the effective end-point permeabilities, fully brine saturated reservoir cores were installed in a horizontally placed Hassler core holder and pressurized to reservoir conditions. The core plugs were drained by injecting supercritical CO_2 at a constant superficial velocity of 2 ft/day until near steady-state flow conditions was achieved. Brine production was continuously measured during drainage and used to calculate average fluid saturations and the pressure drop was used to calculate the endpoint effective permeability of the CO_2. During the imbibition sequence, mass balance was used to calculate the amount of CO_2 produced and CO_2 trapped to determine saturations and permeability at two different endpoints.

Results

Two endpoint effective permeability measurements were performed to determine the fluid flow capacity of brine at irreducible CO_2 saturation, starting with the low rate (0.25 ft/day) and ending with the higher rate (0.50 ft/day). A secondary CO_2 drainage was conducted the exact same way as the primary CO_2 drainage. For increased statistical significance, the experimental procedure was performed on two different core plugs, at the same initial conditions. Average endpoint values were used to generate relative permeability curves by Corey type correlations and input into the numerical simulator for sensitivity studies (**Table 4**).

Process	Superficial velocity (ft/day)	S_g	krg,wi	krw,gi
1. Drainage	2.00	0.49	0.11	
1. Imbibition	0.25	0.23		0.21
2. Imbibition	0.50	0.11		0.47
2. Drainage	2.00	0.32	0.08	

Table 4–Relative permeability endpoints from unsteady state measurement showing endpoint relative permeability of gas at irreducible water (krg,wi) and relative permeability of water at irreducible gas (krw,gi).

Geologic and Reservoir Modeling

The structure of the static geologic model was generated based upon the integration of petrophysical well logs, core data, and regional stratigraphy to define the geologic framework in the extended pilot area. The extended pilot area includes the selected inverted 5-spot pilot pattern and peripheral injectors (Figure 3). The geologic framework was built through interpretation of cycles within the San Andres reservoir. In carbonate platform reservoirs, high frequency cyclicity and rock fabric units are the two critical scales for generating geologic and simulation scale models (Wang et al., 1994).

Stratigraphic tops were picked and correlated across the study area in all available well logs penetrating the San Andres formation. The formation was further subdivided based upon reservoir zones with appreciable reservoir characteristics (Figure 4). These zones serve as flow units and establish a broad layering scheme for populating grid cell properties at well nodes. Each reservoir flow unit and subdivision were input as depth specific well tops, converted to surfaces, and used to generate the structural and stratigraphic framework for the base static model grid using the structural and geocellular modeling capabilities of Petrel (Schlumberger 2015.1).

Porosity, permeability, and saturations were assigned to the geologic framework and correlated to flow zones and cycles through analysis of core data tied to gamma ray, neutron, density, and resistivity logs. Properties derived at each well location were used to constrain geostatistical methods to populate interwell regions. Due to the limited amount of information to characterize the reservoir, the modeling workflow began with a deterministic framework and moved toward more stochastic. The result was an extended pilot area model including the selected pilot pattern and peripheral injection wells, influencing well performance. The dynamic model was then created based on analysis of reservoir engineering data including RCA, SCAL, PVT, pressure data and coreflood experiments which formed the basis for the initial reservoir simulation study for the pilot area (Sharma et al., 2017).

Numerical Modeling

To assist pilot injection design and upscale the optimized laboratory foam system, numerical modeling with the 3D reservoir model was used to set up a compositional simulation case for the extended pilot area. The details of the initial extended pilot area simulation and fluid model can be found in Sharma et al. (2017). The initial geologic model has since been updated due to concerns over simulation run time and computational expense owing to the high amount of layers in the z-direction of initial realizations.

The geologic model was therefore revised, as used in this work, by upscaling and merging layers having less variance in petrophysical properties. The extended model grid had dimensions 59 x 58 x 28 with approximately 65,000 active grid cells. Individual grid cell sizes were 50 x 50 ft with thicknesses ranging from 1-10 ft. Porosities and permeabilities range from 1% to 19% and 0.01 md to 125 md, respectively.

An integral part of the upscaling process is the use of numerical models to accurately describe the behavior of foam at the field scale based upon observations at the core scale. Therefore, several measurements on reservoir cores plugs were performed to obtain input parameters for numerical simulations and the empirical foam model, including foam quality and rate scans and the previously discussed relative permeability measurements for the CO_2/brine system (Table 4). Foam model parameters (**Figure 13**), were obtained by fit-to-lab data from foam quality and rate scans, which were performed on water-wet, 100% water saturated reservoir core and fluids at reservoir conditions (2500 psi, 104ºF). See Table 1 for core properties. However, there is limited variation in apparent viscosity with foam quality, which restricts flexibility in controlling mobility reduction given that wells are operating close to fracture pressure.
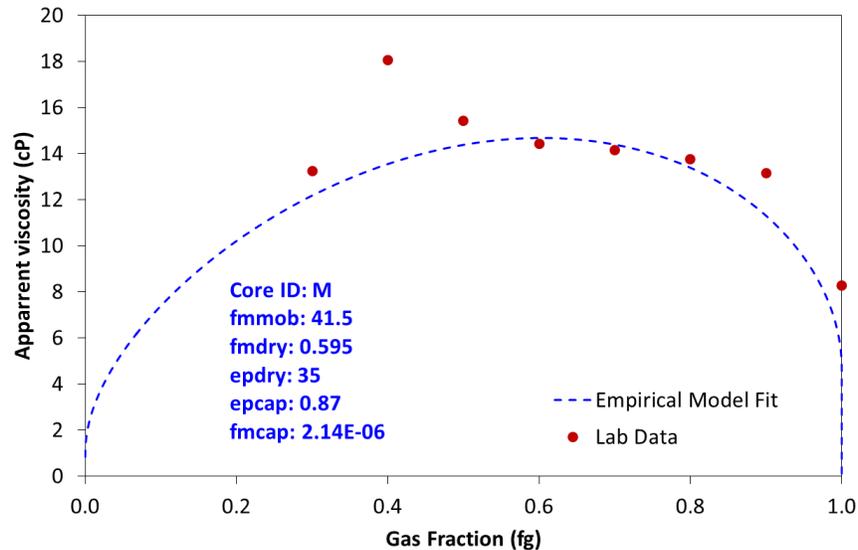
Figure 13–Empirical foam model fit to laboratory data for Core "M" Table 2 (measured with reservoir core and fluids at reservoir conditions).

Foam simulations were conducted on the extended pilot area model which has been history matched for the historical waterflood and CO_2 injection periods. Foam performance was assessed for its ability to reduce GOR, improve CO_2 utilization, and reduce CO_2 mobility while analyzing incremental oil recovery. CO_2 utilization refers to the volume of CO_2 used to produce a barrel of oil. The compositional model was set up with two aqueous phase components, water and surfactant, and six hydrocarbon phase components. Pressure and saturation (gas and water phase) at the start of simulation are based on values at last step of the CO_2 flood history match. Similarly, initial gas and water compositions were initialized explicitly using results from CO_2 injection match.

A fit for purpose model has been used to analyze foam for in depth mobility control, rather than near well conformance control. Thus, results of interwell flow behavior provide insights into foam's ability to reduce CO_2 mobility and decrease producing GOR of production wells at the expense of losing near well resolution. A number of methods have been shown to model near wellbore SAG processes which include using radial grids around injectors and applying fractional flow theory (Zhou and Rossen, 1995; Xu and Rossen, 2004; Kloet et al., 2009

Simulation Injection Design

Reservoir simulation cases were generated to investigate modes of SAG injection for the field test. Operational constraints control some aspects of field injection design method. For instance, simultaneous injection (coinjection) of CO_2 and surfactant solution brine can create carbonic acid which is known to cause corrosion in many standard oil field casings and pipelines (Matthews, 1989). Further, the pressure increases associated with coinjection for field application can lead to abrupt increases in bottom hole injection pressure, problematic when operating close to the fracture pressure of the formation. Therefore, it is preferred to inject alternating slugs of CO_2 and surfactant solution to minimize corrosion and offer more flexibility when injection pressure increases.

Considering SAG injection, scenarios were set up to investigate multiple cycle SAG, single cycle SAG, and rapid SAG. Their effect on oil recovery, GOR, gas mobility, and CO_2 utilization were compared to base case, water alternating gas (WAG) injection. All cases were initially ran for the same time duration (12 months) to determine injectivity reduction for each injection strategy. However, oil recovery in the model is sensitive to pore volume of CO_2 injected, which drops significantly during foam injection due to reduced injectivity. Therefore, additional cases were considered injecting the same cumulative volume of CO_2.

Base Case – Water Alternating Gas (WAG) Injection

The base case forecast was set up to investigate reservoir response to WAG injection, rather than implementation of a foam treatment, and permits comparison to SAG injection strategies. Three water cycles were injected for 1 month, with alternating 1 month slugs of CO_2 in between for a total duration of 6 months. The WAG scheme was followed by 6 months of chase CO_2 injection. Producers and injectors were on flowing bottom hole pressure (BHP) control with constraints of 1000psi and 4400psi, respectively.

In order to capture foam shear-thinning behavior at higher rates expected in near wellbore region, negative skin has been introduced at the injector. An alternate to introducing negative skin would be to use Local Grid Refinement around injector, at the expense of increased runtime. Well productivity indices have been tuned to get rates close to most recent field rates available at assumed pressures.

Surfactant Alternating Gas (SAG) Injection

A similar set up was used to model SAG injection. Three different SAG cases were generated to analyze the effects of slug volume and injection schedule on GOR, CO_2 utilization, and oil recovery. The first case considered multiple cycle SAG with an injection schedule identical to the WAG case. The next SAG injection was implemented with a large single cycle of surfactant solution for 3 months followed by CO_2 injection for 9 months. Rapid SAG injection was used in the final case where 6 cycles of surfactant and CO_2 were alternately injected for 10 days and 20 days, respectively for 6 months followed by chase CO_2 for 6 months. Surfactant concentration was set 0.5 wt% and a foam quality of 70% was targeted through volumetric ratios of slug sizes. The comparison of the base case WAG and multiple cycle SAG clearly indicates higher cumulative CO_2 injection and oil production by WAG injection (**Figure 14**).
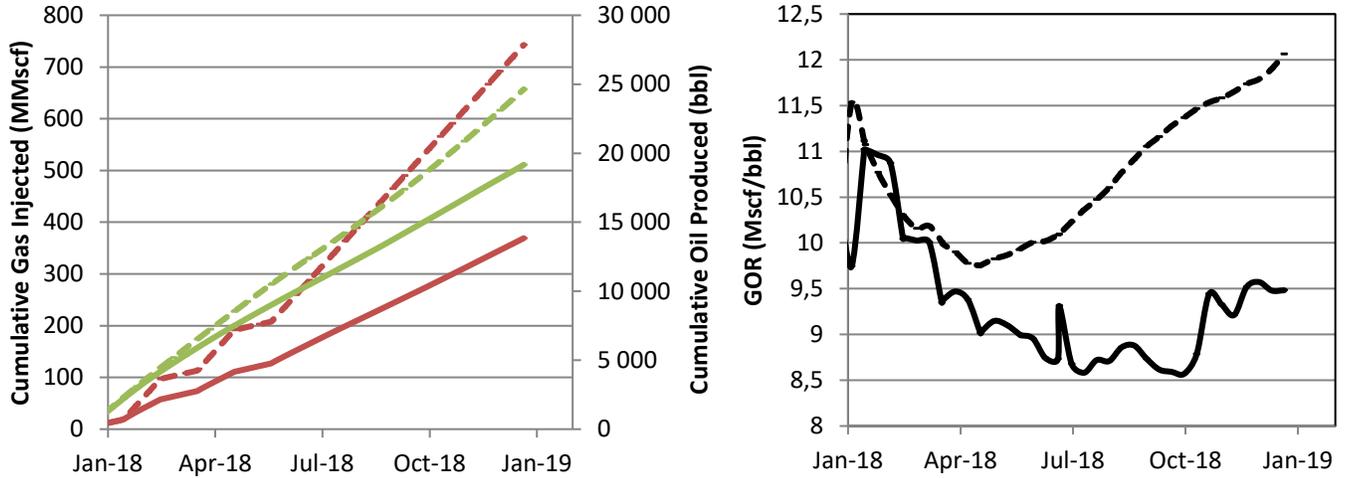
Figure 14–Base case WAG (dashed curves) compared to multiple cycle SAG injection (solid curves). Left: (a) cumulative gas injection (red curves) and oil production (green curves). Right: (b) field GOR.

As expected, SAG injection results in reduced CO_2 injectivity and a significantly lower producing GOR. Injectivity near the well, in SAG, is notably reduced through the formation of foam, indicated by the increase in injection well pressure (**Figure 15**). Injection rate is reduced to prevent the pressure from rising above the formation fracture pressure.
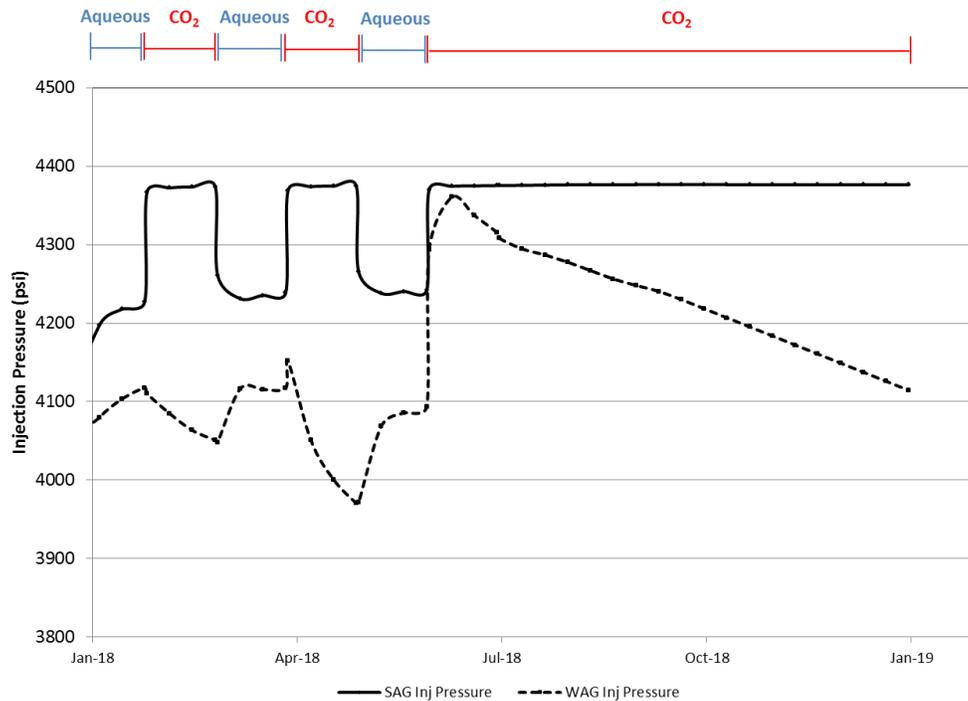
Figure 15–Injection pressure of WAG (dashed curve) and SAG (solid curve). Phases of injection are shown at top with aqueous phase during WAG and SAG consisting of water and surfactant solution, respectively.

All tested methods of SAG injection demonstrate the effectiveness of foam to reduce producing GOR and injectivity, and improve CO_2 utilization over WAG (**Figure 16, Table 5**). Single cycle SAG and rapid SAG both result in a reduction in GOR for all production wells. GOR for WAG continues to rise through the end of the 1 year simulation forecast while SAG methods curtail GOR increase through reducing CO_2 mobility. Multiple cycle SAG shows the lowest GOR mostly due to the largest injectivity reduction experienced during injection.
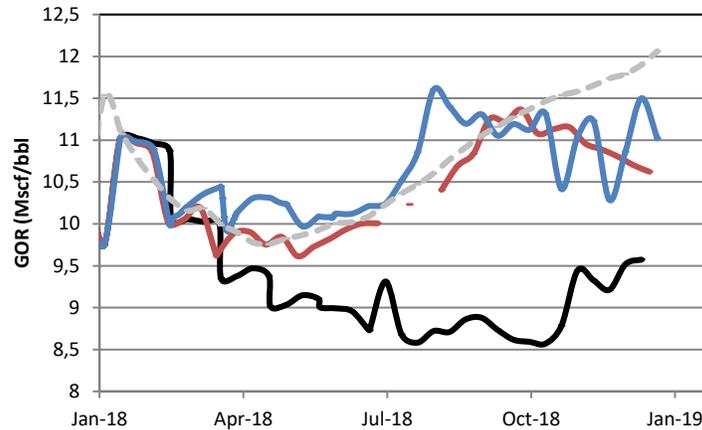
Figure 16–Field GOR of WAG (gray dashed curve), SAG (black curve), Single cycle SAG (red curve), and Rapid SAG (blue curve).

Case	CO_2 Utilization factor (Mscf/bbl)
WAG	30.14
SAG	19.26
Single Cycle SAG	20.47
Rapid SAG	21.30

Table 5–CO_2 utilization factor for each injection scenario

The results may present an optimistic production forecast, for WAG, due to model sensitivity to volume of CO_2 injected. Also, SAG may show a pessimistic production forecast due to numerical simulator limitations to properly capture foam effects on injectivity during gas slug injection in a SAG process, especially in the near wellbore region. For example, the water saturations that would have the greatest mobility reduction with foam are not experienced in the reservoir except within a shock front of negligible width. During gas injection, following surfactant, a shock front occurs at the leading edge of the gas bank from the initial state of the reservoir to a point of very low water fractional flow, where foam collapses (Kloet et al., 2009). In a finite-difference simulation, however, each grid block at the foam front passes through all those saturations, and thus the mobility reduction at the foam front is overestimated resulting in large reductions in injectivity.

In addition, injectivity is conventionally calculated assuming a uniform saturation and mobility in the injection-well grid block using the Peaceman equation. Injectivity in a simulation of a SAG process is extremely poor. In reality, the near-well region rapidly dries out and injectivity is much greater than estimated in a finite-difference simulation. The large injectivity reduction is compounded by limited variation in apparent viscosity with gas fraction from experimental data used to generate foam model parameters (Figure 13). This limits the flexibility in controlling mobility reduction. The foam quality scan used for obtaining foam model parameters varies from those reported in literature with partial dry-out even at high f_g and no change in foam regime over the range of f_g.The fit for purpose approach sacrifices near well resolution to capture the effects of foam in the interwell region, providing insights into in depth mobility control and impacts on production well GOR.

In an effort to mitigate some of the challenges associated with the model sensitivity to volumes of CO_2 injected, the base case WAG and multiple cycle SAG were run with the same cumulative volumes of injected CO_2 (**Figure 17**). The multiple cycle SAG case run time was extended for 6 months to account

for the increased volume of CO_2 to be injected. Results indicate a significant increase in cumulative oil production for SAG over WAG. When the same volume of CO_2 was injected, SAG produced 11,500 bbl more than WAG, a 46% increase.
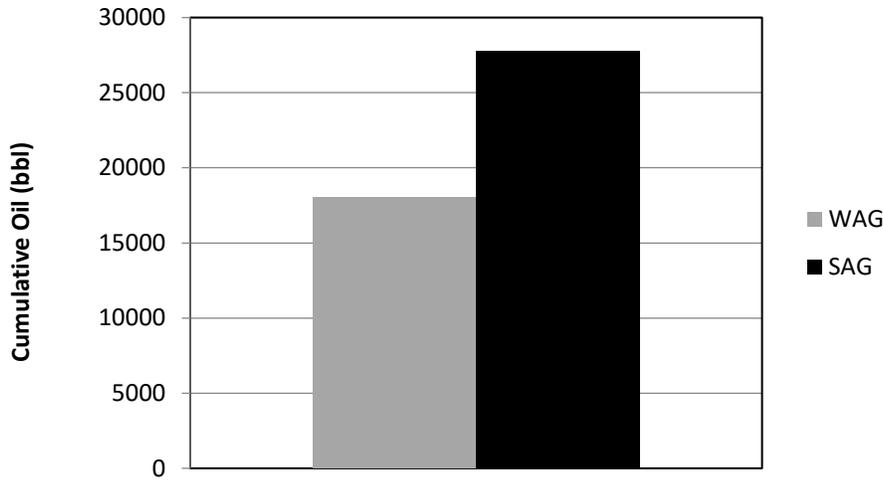
Figure 17–Comparison of cumulative oil produced for WAG (gray bar) and SAG (black bar) when injecting the same cumulative volume of CO_2.

Simulation results suggest that multiple cycle SAG and single cycle SAG are the two most attractive injection modes when considering CO_2 utilization improvement and reduction in GOR. CO_2 utilization was improved by nearly 35% while GOR was reduced by 20% on average for multiple cycle and single cycle SAG. At the current state of reservoir (over pressurized), SAG is inferior to WAG in terms of oil production. However, a drop in reservoir pressure will remove the limitation on throughput, which will make SAG attractive over the current strategy of continuous CO_2 injection or WAG. The operator has been depressurizing the reservoir since early 2018. Further, the reduced injectivity in the SAG simulations would likely not be as pronounced in the field test due to the simulator overestimating mobility reduction at the foam front and lacking foam dry out in the near wellbore region. Ongoing simulation work aims to reconcile these issues while also determining the applicability of a surfactant pre-flush. It is expected that an alternating slug injection scheme will provide the most flexibility, should injectivity issues arise, through minimizing the risk of fracturing the formation potentially creating problems beyond the remediation by foam.

Conclusions

An integrated multiscale field pilot research program has been initiated to advance the technology of CO_2 foam for in-depth mobility control for EOR and CO_2 storage. An inverted 40 acre 5-spot pattern has been selected for the first foam injection in East Seminole Field. Production well selection was based upon high producing GOR and rapid gas breakthrough. A pilot foam injector was selected which has a low well head injection pressure, suspected CO_2 channeling through high permeability zones, and close proximity to the production well.

Laboratory investigations which aim to determine the optimal foam system for field testing recommend a foam quality of 70% and a surfactant concentration of 0.5 wt%. CO_2 foam EOR corefloods, at the optimal surfactant concentration and foam quality, result in overall recovery factors of 80% OOIP and incremental recovery by CO_2 foam of 30% OOIP after waterflood. High differential pressures during CO_2 foam injection indicate generation of stable foam with mobility reduction factors by CO_2 foam up to 340, over CO_2 at reservoir conditions. The benefit of a nominal surfactant preflush has also been observed in

corefloods and is recommended for field implementation to minimize surfactant loss, maximize foam generation, and potentially establish capillary continuity across fractures if present. CO_2 storage assessed during the CO_2 foam EOR corefloods suggest that the storage potential in the field will be greatest in the unswept zones where the residual oil saturation is highest, providing a valuable target for sequestration during mobility control by CO_2 foam.

Foam injection design was investigated with a field scale simulation model to offer recommendations for SAG injection strategy. Comparison of foam cases to WAG injection clearly indicates reduction in CO_2 injectivity and producing GOR while improving CO_2 utilization during multiple cycle SAG, rapid SAG, and single cycle SAG injection. Multiple cycle SAG and single cycle SAG emerged as the two most attractive injection strategies with an improvement in CO_2 utilization by 35% and a 20% reduction in producing GOR, compared to WAG. Due to the inherent assumptions of the simulation model, it is recommended to design the injection strategy based upon technical feasibility in the field to minimize risk, primarily associated with the fracture pressure of the formation. The investigated alternating slug injection schemes will provide the most flexibility in the injection schedule, if injectivity is greatly reduced. Further, alternating slug injection will limit potential corrosion and offer better assessment to comparable WAG operations in other parts of field. Future simulation work aims to more accurately capture the effect of gas slug injection during SAG, near the wellbore, to account for injectivity changes and foam dry out.

The upscaling approach used in this work integrates comprehensive laboratory experiments, field scale simulation, and considers field economic and operational constraints for the application of CO_2 foam. Laboratory measured parameters make recommendations for foam system design which are used within simulation models. Field injection design is guided by the field scale simulations which offer suggestions for injection mode, accounting for field challenges. Overall, the ongoing field pilot research program offers an improvement to overall CO_2 foam field pilot project design which can be applied to many other fields where foam is appropriate to mitigate CO_2 flood challenges.

Acknowledgements

Nomenclature

f_g	Gas fraction or foam quality
f_{surf}	Surfactant solution fraction
C_{surf}	Surfactant concentration, weight percent in solution
$R_{f,tot}$	Total oil recovery, percent original oil in place
$R_{f,WF}$	Incremental oil recovery by waterflood
$R_{f,CO2\ foam}$	Incremental oil recovery by CO_2 foam
$\mu_{app,CO2foam}$	Apparent viscosity of CO_2 foam, Pa·s (often given in text in cP)
$MRF_{CO2Foam}$	Mobility Reduction Factor by CO_2 foam
S_g	Gas saturation, fraction of gas in pore volume
S_{orw}	Residual oil saturation to waterflood, fraction of residual oil in pore volume
Krg,wi	Endpoint relative permeability of gas
$Krw,\ gi$	Endpoint relative permeability of water
q_{gas}	Flow rate of gas for calculation of gas fraction, ml/hr (Eq. 1)
q_{liquid}	Flow rate of liquid for calculation of gas fraction, ml/hr (Eq. 1)
k	Permeability of the porous medium, m^2 (Eq. 2)

∇p	Pressure gradient measured across the core, Pa (Eq. 2)
u_l	Superficial velocity of liquid, m/s (Eq. 2)
u_g	Superficial velocity of gas, m/s (Eq. 2)
A	Cross sectional area of the core, m^2 (Eq. 2)
λ	Phase mobility
λ_1	Gas phase mobility when no surfactant solution is present
λ_2	Gas phase mobility when surfactant solution is present
MRF	Mobility Reduction Factor

Abbreviations

CCUS	Carbon, Capture Utilization, and Storage
EOR	Enhanced Oil Recovery
SAG	Surfactant Alternating Gas
WAG	Water Alternating Gas
MPZ	Main Producing Zone
ROZ	Residual Oil Zone
ROS	Remaining Oil Saturation
BT	Breakthrough
TVD	Total Vertical Depth
OOIP	Original Oil in Place
Wt %	Weight Percent
SCAL	Special Core Analysis
RCA	Routine Core Analysis
PVT	Pressure Volume Temperature
MMP	Minimum Miscibility Pressure
CCE	Constant Composition Expansion
PTA	Pressure Transient Analysis
GOR	Gas-Oil Ratio
MRF	Mobility Reduction Factor
PV	Pore Volume

SI Metric Conversion Factors	
Acre x 4.046873	E+03 = m^2
$^\circ$API 141.5/(131.5+ $^\circ$API)	= g/cm^3
bbl x 1.589873	E $-$ 01 = m^3
cp x 1.0	E $-$ 03 = Pa·s
$^\circ$F ($^\circ$F $-$ 32)/1.8	= $^\circ$C
ft x 3.048	E $-$ 01 = m
psi x 6.894757	E + 00 = kPa

References

Al-Menhali, A S., and Krevor, S. 2016. Capillary Trapping of CO2 in Oil Reservoirs: Observations in a Mixed-Wet Carbonate Rock. *Environmental Science and Technology* **50** (5): p. 2727-2734**.** DOI: 10.1021/acs.est.5b05925.

Aspenes, E., Graue, A., Baldwin, B. A., Moradi, A., Stevens, J., & Tobola, D. P. 2002. Fluid Flow in Fractures Visualized by MRI During Waterfloods at Various Wettability Conditions - Emphasis on Fracture Width and Flow Rate. Society of Petroleum Engineers. DOI:10.2118/77338-MS

Chalbaud, C., Robin, M., Bekri, S., and Egermann, P. 2007. Wettability Impact on CO_2 Storage in Aquifers: Visualization and Quantification using Micromodel Tests, Pore Network Model and Reservoir Simulations. International Symposium of the Society of Core Analysts, 10-12 September, Calgary, Canada.

Chou, S.I., Vasicek, S.L., Pisio, D.L., Jasek, D.E., Goodgame, J.A. 1992. CO2 Foam Field Trial at North Ward Estes. Presented at the 67th SPE Annual Technical Conference and Exhibition, Washington, D.C., October 4-7, 1992.

Dykstra, H. and Parsons, R.L. 1950. The Prediction of Oil Recovery by Waterflooding. *In* Secondary Recovery of Oil in the United States, second edition, p. 160–174. Washington, DC: API.

Fernø, M. A., Ersland, G., Haugen, A., Johannesen, E. B., Graue, A., Stevens, J., & Howard, J. J. 2007. Impacts From Fractures On Oil Recovery Mechanisms In Carbonate Rocks At Oil-Wet And Water-Wet Conditions - Visualizing Fluid Flow Across Fractures With MRI. Society of Petroleum Engineers. DOI:10.2118/108699-MS

Fernø, M.A., Torsvik, M., Haugland, S., Graue, A. 2010. Dynamic Laboratory Wettability Alteration. *Energy and Fuels* 2010, 24, p. 3950-3958 DOI: 10.1021/ef1001716 Fernø, M. A., Gauteplass, J., Pancharoen, M., Haugen, Å., Graue, A., Kovscek, A. R., & Hirasaki, G. 2014. Experimental Study of Foam Generation, Sweep Efficiency, and Flow in a Fracture Network. *Society of Petroleum Engineers Journal* **21** (04). DOI: 10.2118/170840-PA

Fernø, M. A., Haugen, A., & Graue, A. 2012. Surfactant Prefloods for Integrated EOR in Fractured, Oil-Wet Carbonate Reservoirs. Presented at the SPE Annual Technical Conference and Exhibition San Antonio, TX USA, 8-10 October 2012. DOI:10.2118/159213-MS

Fernø, M.A., Steinsbø, M., Eide, Ø., Ahmed, A., Ahmed, K., Graue, A. 2015. Parametric Study of Oil Recovery during CO_2 injections in Fractured Chalk: Influence of fracture permeability, diffusion length and water saturation, *Journal of Natural Gas Science & Engineering* (2015), DOI:10.1016/j.jngse.2015.09.052.

Fredriksen S.B., Alcorn, Z.P., Frøland, A., Viken, A., Rognmo, A.U., Seland, J.G., Ersland, G., Fernø, M.A., and Graue, A. 2018. Surfactant Pre-floods during CO_2 Foam for Integrated Enhanced Oil Recovery in Fractured Oil-Wet Carbonates. Presented at the SPE Improved Oil Recovery Conference, Tulsa, Oklahoma, USA, 14-18 April 2018. SPE-190168MS.

Graue, A., Tonheim, E., Baldwin, B.: 1994. Control and Alteration of Wettability in Low-Permeability Chalk, Rev. Proc.: 3rd International Symposium on Evaluation of Reservoir Wettability and Its Effect on Oil Recovery, U. of Wyoming, Laramie, WY., Sept. 1994, USA.

Graue, A., Eilertsen, T., Viksund, B.G., Moe, R. 1999a. Systematic Wettability Alteration by Aging Sandstone and Carbonate Rock in Crude Oil*, J. Petr. Sci. and Eng*., Vol. 24, 1999 (85-97).

Graue, A., Viksund, B.G., Baldwin, B.A. 1999b. Reproducible Wettability Alteration of Low-Permeable Outcrop Chalk", *SPE Res. Eval. and Eng*., Vol. 2, No. 2, April, 1999.

Graue, A., Aspenes, E., Moe, R. W., Baldwin, B. A., Moradi, A., Stevens, J., & Tobola, D. P. 2001a. MRI Tomography of Saturation Development in Fractures During Waterfloods at Various Wettability Conditions. Society of Petroleum Engineers, January 2001. DOI:10.2118/71506-MS

Graue, A., Bognø, T., Baldwin, B. A., & Spinler, E. A. 2001b. Wettability Effects on Oil-Recovery Mechanisms in Fractured Reservoirs. Society of Petroleum Engineers. DOI:10.2118/74335-PA

Graue, A., Aspenes, E. Bognø, T., Moe, R.W., and Ramsdal, J. 2002. Alteration of Wettability and Wettability Heterogeneity, Reviewed Proc.: 6th International Symposium on Evaluation of Reservoir Wettability and Its Effect on Oil Recovery, Socorro, NM, USA, Sept. 27-28, 2000. Published in: *J. Petr. Sci. & Eng*. 33(1):3-17, April 2002.

Gray, T.J., 1989. Development Study, East Seminole San Andres Field, Gaines County, Texas. Internal Report, Mobil Exploration and Producing US Inc. Midland Division., March 1989.

Hanssen, J.E., Holt., T., and Surguchev, L.M. 1994. Foam Processes: An Assessment of Their Potential in North Sea Reservoirs Based on a Critical evaluation of Current Field Experience. Presented at the SPE Improved Oil Recovery Conference, Tulsa, Oklahoma, USA, 17-20 April, 1994.

Haugen A., Mani, N., Svenningsen, S., Brattekås, B., Graue, A., Ersland, G., and Fernø, M.A. 2014. Miscible and Immiscible Foam Injection for Mobility Control and EOR in Fractured Oil-Wet Carbonate Rocks. *Transport in Porous Media* 2014 **104**, 109-131. DOI: 10.1007/s11242-014-0323-6

Harpole, K.J., Siemers, W.T. and Gerard, M.G. 1994. CO2 Foam Field Verification Test at EVGSAU: Phase IIIC – Reservoir Characterization and Response to Foam Injection. Presented at the SPE/DOE 9th Symposium on Improved Oil Recovery, Tulsa, OK USA, 17-20 April 1994.

Heller, J.P. 1966. Onset of Instability Patterns between Miscible Fluids in Porous Media. *Journal of Applied Physics 1966*, **37**, 1566-1579.

Heller, J.P., Boone, D.A., and Watts, R.J. 1985. Field Test of CO_2-Foam Mobility Control at Rock Creek. Presented at the SPE 60th Annual Technical Conference and Exhibition, Las Vegas, Nevada USA. September 22-25, 1985. SPE-14395.

Hirasaki, G.J. and Lawson, J.B. 1985. Mechanisms of Foam Flow in Porous Media: Apparent Viscosity in Smooth Capillaries. *Society of Petroleum Engineers Journal*, April 1985, p. 176-190

Hirasaki, G.J. 2017. Personal Communication. October 2017

Hoefner, M.L. and Evans, E.M. 1995. CO_2 Foam: Results from Four Developmental Fields Trials, *SPE Reservoir Engineering*, November 1995, p. 273-281.

Holm, L.W. 1980. Use of Surfactant to Reduce CO_2 Mobility in Oil Displacement. *Society of Petroleum Engineers Journal,* August 1980, 281.

Honarpour, M.M., Nagarajan, N.R., Grijalba Cuenca, A., Valle, M. and Adesoye, K. 2010. Rock-Fluid Characterization for Miscible CO_2 Injection: Residual Oil Zone, Seminole Field, Permian Basin. *SPE Annual Technical Conference and Exhibition,* Florence, Italy, 19-22 September.

Iglaur, S. 2017. CO_2 – Water – Rock Wettability: Variability, Influencing Factors, and implications for CO_2 Geostorage. *Acc. Chem. Res*. 2017, 50, p. 1134-1142. DOI: 10.1021/acs.accounts.6b00602

Jadahunandan, P.P. and Morrow, N.R. 1995. Effect of Wettability on Waterflood Recovery for Crude-Oil/Brine/Rock Systems *SPE Reservoir Engineering* **10** (1): 40-46.

Jian, G., Puerto, M.C., Wehowsky, A., Dong, P., Johnston, K.P., and Hirasaki, G.J. 2016. Static Adsorption of an Ethoxylated Nonionic Surfactant on Carbonate Minerals. *Langmuir*, 10244-10252

Jones, S.A., Laskaris, G., Vincent-Bonnieu, S., and Farajzadeh, R. 2016. Surfactant Effect on Foam: From Core Flood Experiments to Implicit-Texture Foam-Model Parameters. Presented at the SPE Improved Oil Recovery Conference, Tulsa, Oklahoma, USA, 11-13 April, 2016. SPE-179637

Kloet, M.B., Renkema, W.J., and Rossen, W.R. 2009. Optimal Design Criteria for SAG Foam Processes in Heterogeneous Reservoirs. Presented at the 2009 SPE EUROPEC/EAGE Annual Conference and Exhibition, Amsterdam, The Netherlands, 8-11 June 2009. SPE-121581

Krevor, S., Blunt, M J., Bension, S M., Pentland, C H., Reynolds, C., Al-Menhali, A., and Niu, B. 2015. Capillary trapping for geologic carbon dioxide storage – From pore scale physics to field scale implications. *International Journal of Greenhouse Gas Control* **40**: p. 221-237. https://doi.org/10.1016/j.ijggc.2015.04.006.

Lake, L.W., Johns, R.T., Pope, G.A., et al. 2014. *Fundamentals of Enhanced Oil Recovery*, Richardson, Texas, USA. Society of Petroleum Engineers.

Lee, H.O., Heller, J.P. and Hoefer, A.M.W. 1991. Change in Apparent Viscosity of CO_2 Foam With Rock Permeability. *SPE Reservoir Engineering,* November 1991, p. 421-428.

Martin, F.D., Heller., J.P., Weiss, W.W., and Tsau, J.S. 1992. CO2-Foam Field Verification Pilot Test at EVGSAU Injection Project Phase 1: Project Planning and Initial Results. Presented at the SPE Improved Oil Recovery Conference, Tulsa, Oklahoma, USA, 22-24 April, 1992. SPE/DOE-24176

Martin, F.D., Stevens, J.E. and Harpole, K.J. 1995. CO2 Foam Field Test at the East Vacuum Grayburg/San Andres Unit. *SPE Reservoir Engineering*, November 1995, p. 266-272

Matthews, C.S. 1989 in Enhanced Oil Recovery II Processes and Operation, Elsevier Science Publication Company, eds. E.C. Donaldson, G.V. Chilingarian, and T.F. Yen, New York, 1989, p. 129

Melzer, S., Koperna, G.J, and Kuuskraa, V.A. 2006. The Origin and Resources Potential of Residual Oil Zones. Presented at the 2006 SPE Annual Conference and Exhibition, San Antonio, Texas, USA., 24-27 September 2006. SPE-102964

Rossen, W.R. 1996. Foams in Enhanced Oil Recovery. In Foams Theory, Measurements, and Applications. eds. Prud'homme, R.K. and Khan, S.A. volume 57, ch. 11, p 414-464, Marcel Dekker, Inc. New York

Salathiel, R.A. 1973. Oil Recovery by Surface Film Drainage in Mixed-Wettability Rocks. *Journal of Petroleum Technology* **25** (10): p. 1216-1224. SPE-4104-PA. https://doi.org/10.2118/4104-PA.

Schmalz, J.P. and Rahme, H.D. 1950. The Variation of Waterflood Performance with Variation in Permeability Profile. Production Monthly *15*, no. 9, p. 9-12.

Sharma, M., Alcorn, Z.P., Fredriksen, S.B., Fernø, M.A., and Graue, A. 2017. Numerical Modeling Study for Designing CO2-Foam Field Pilot. Presented at the 19th European Symposium on Improved Oil Recovery, Stavanger, Norway, 24 April 2017, DOI**:** 10.3997/2214-4609.201700339

Stephenson, D.J., Graham, A.G., Luhning, R.W. 1993. Mobility Control Experience in the Joffre Viking Miscible CO2 Flood. *SPE Reservoir Engineering*, August 1993, p. 183-188.

Stiles, W.E. 1949. Use of Permeability Distribution in Water Flood Calculations. Petroleum Transactions AIME, *186*, p. 9-13.

Taylor, P. 1998. Ostwald Ripening in Emulsions. *Advances in Colloid and Interface Science* 78 (1998) p 107.163.

Wang, F.P., Lucia, F.J., and Kerans, C. 1994. Critical Scales, Upscaling, and Modeling of Shallow-Water Carbonate Reservoirs. Presented at the 1994 SPE Permian Basin Oil and Gas Recovery Conference, Midland, Texas USA. SPE 27715

Wang, F.P., Lucia, J.F., and Kerans, C. 1998. Integrated Reservoir Characterization Study of a Carbonate Ramp Reservoir: Seminole San Andres Unit, Gaines County, Texas. *SPE Reservoir Evaluation and Engineering*, **1** (2).

Xu, Q., and Rossen, W.R. 2004. Experimental Study of Gas Injection in Surfactant Alternating Gas Foam Process. *SPE Reservoir Evaluation and Engineering*, December 2004, p. 438.448.

Zhou, Z.H. and Rossen, W.R. 1995. Applying Fractional Flow Theory to Foam Process at Limiting Capillary Pressure. *SPE Advanced Technology Series* 3, p. 154-162

Paper IV: Core-Scale Sensitivity Study of CO$_2$ Foam Injection Strategies for Mobility Control, Enhanced Oil Recovery and CO$_2$ Storage

Fredriksen, S.B., Alcorn, Z.P., Sharma, M., Wergeland, C., Fernø, M.A., Graue, A., Ersland, G.

Submitted for publication.

Core-Scale Sensitivity Study of CO_2 Foam Injection Strategies for Mobility Control, Enhanced Oil Recovery and CO_2 Storage

S. B. Fredriksen[1], Z. P. Alcorn[1], M. Sharma[2], C. Wergeland[1], M. A. Fernø[1], A. Graue[1] and G. Ersland[1]

[1]Dept. of Physics and Technology, University of Bergen
[2]National IOR Centre of Norway, University of Stavanger

Abstract

A field pilot research program utilizing CO_2 foam for mobility control, enhanced oil recovery (EOR) and CO_2 storage is ongoing to advance field scale implementation of CO_2 foam. This paper presents experimental and numerical sensitivity studies to assist injection strategy design to increase the success of *in-situ* CO_2 foam generation and propagation. Recommendations are made by evaluating un-steady state *in-situ* foam behavior representative of the near wellbore region. Multi-cycle surfactant-alternating-gas (SAG) provided the highest apparent viscosity foam of 120.2 cP, compared to single-cycle SAG (18.2 cP) and co-injection (56.0 cP) in 100% brine saturated porous media. CO_2 foam EOR corefloods at first-contact miscible (FCM) conditions showed that multi-cycle SAG generated the highest apparent foam viscosity in presence of oil (i.e. *n*-Decane). Multi-cycle SAG demonstrated high viscous displacement forces critical in field implementation where gravity effects and reservoir heterogeneities dominate. At multiple-contact miscible (MCM) conditions, no foam was generated as a result of wettability alteration and foam destabilization in presence of crude oil. In both FCM and MCM corefloods, incremental oil recoveries were on average 30.6% OOIP regardless of injection strategy for CO_2 foam and base cases (i.e. no surfactant). High microscopic sweep by CO_2 diffusion and miscibility dominated oil recovery at core-scale. CO_2 storage potential was 9.0% greater for multi-cycle SAGs compared to co-injections at MCM. A validated core-scale simulation model was used in sensitivity analysis of grid resolution and foam quality. The model was robust in representing the observed foam behavior and will be extended to use in ongoing field scale simulations.

Introduction

The major challenge with CO_2 enhanced oil recovery (EOR) is poor macroscopic displacement, particularly in heterogeneous formations with high permeability contrasts or in fractured reservoirs (Bernard et al. 1980; Latil 1980). The injected CO_2 follows the path of least resistance channeling high permeable zones (layers or fractures) resulting in early breakthrough, high CO_2 recycling, and low incremental oil recoveries (Bond and Holbrook 1958). From viscosity differences between the injected CO_2 and reservoir-fluids in place (water and oil), high mobility CO_2 can also cause viscous fingering that bypass oil-bearing zones (Bond and Holbrook 1958), or low density CO_2 can segregate to the top causing gravity override (Nzekwu and Bennion 1987).

To reduce CO_2 mobility and improve sweep, a foaming agent (i.e. surfactant) mixed in aqueous solution can be injected. The aqueous solution creates lamellas, i.e. interconnected liquid films stabilized by the surfactants surrounding the CO_2. A discontinuous CO_2 phase is formed (Holm 1968), which effectively reduces the relative permeability and propagation of CO_2 through the formation. At reservoir conditions (i.e. high temperature and pressure), the reduced flow rate (Bernard and Holm 1964), entrapment of CO_2 in foam (Bernard et al. 1965) and CO_2-surfactant emulsification (Bernard et al. 1980; Emadi et al. 2013), will increase the CO_2 apparent

viscosity. This effect will be more prominent in high permeable zones and divert flow into less permeable areas with residual oil and increase macroscopic displacement.

In foam EOR the use of CO_2 is favorable due to its high microscopic sweep. At reservoir conditions, CO_2 can develop miscibility with oil and enhance oil recovery significantly. In addition, increased awareness of CO_2 emissions from fossil fuel production and consumption, and its impact on climate, has resulted in a global incentive to mitigate the CO_2 footprint. Carbon capture, utilization and storage (CCUS) is a technology advancement towards more sustainable energy production. CCUS enables the use of captured CO_2 for EOR, while simultaneously storing the injected CO_2 in underground reservoirs.

In the United States, CO_2 for EOR has advanced into a mature technology since the first commercial injection in 1972 (Newton and McClay 1977), while CO_2 foam is less developed at field scale. This paper is part of an ongoing field pilot research program to implement CO_2 foam for mobility control, EOR and CO_2 storage in the Permian Basin of West Texas. The field is a heterogeneous carbonate reservoir with thin, high-permeable zones (up to 300 mD). The field pilot pattern is an inverted 40 acre 5-spot currently producing from tertiary CO_2 and water injection. Early CO_2 breakthrough was observed due to unfavorable effects of channeling. CO_2 foam injection will be implemented to reduce the high gas-oil-ratio, CO_2 recycling, and to provide mobility control and fluid diversion towards un-swept sections of the pilot area and residual oil zone. For more detailed information on the field pilot program see Alcorn et al. (2018).

For the foam treatment to be successful, the injection strategy must balance *in-situ* foam generation, propagation, and injectivity. Operational constraints influence some aspects of the injection design, such as downhole corrosion from carbonic acid during e.g. co-injection. Further, co-injection is difficult to implement due to extremely low injectivity and associated pressure increases (Hoefner, 1995). This has led to a majority of field tests by SAG for better injectivity control, especially when operating close to the fracture pressure (Chou et al. 1992; Harpole et al. 1994; Henry et al. 1996). The reservoir pressure in the pilot area (i.e. 220 bars) is close to the formation fracture pressure of 269 bars (Alcorn et al. 2018). To reduce costs and increase the success of CO_2 foam, recommendations are made in laboratory to help interpret the technology when transferred to field. At laboratory scale, alternating slugs are not typically used due to small fractional flows of gas and the inability to achieve steady state (Groenenboom et al. 2017). Hence, laboratory investigations are designed to represent un-steady state *in-situ* foam generation characterizing behavior near the injection well.

The aim of the paper is to investigate co-injection and SAG for CO_2 foam mobility control, EOR and CO_2 storage to assist in the design of the field pilot. Mobility control by CO_2 foam is evaluated based on apparent foam viscosity, its impact on oil recovery and storage potential. Experimentally, foam behavior by co-injection, single-cycle SAG and multi-cycle SAG are performed in brine saturated systems to generate foam *in-situ* without the presence of oil. CO_2 foam EOR corefloods are then run at FCM and MCM using *n*-Decane and crude oil respectively after waterflooding. Residual oil saturations are high for the core-scale systems after waterflood compared to a near-wellbore region, which can strongly influence foam behavior. A foam model is fitted from foam stability scans, and experimental results from a CO_2 foam EOR coreflood are used to validate a core-scale numerical model to investigate effects of grid resolution and foam quality. The main objective of the numerical sensitivity study is to validate the foam model in representing the observed foam behavior which will be extended to use in ongoing field scale simulations.

Materials and Fluids

Outcrop limestone core plugs were used as reservoir analogues due to limited reservoir cores available from the field pilot area. Limestone is a highly heterogeneous carbonate rock in terms of permeability, and is considered strongly water-wet as it has never been in contact with crude oil (Haugen et al. 2014).

Limestone core plugs were drilled with a 2 inch diameter from larger slabs, cut, cleaned and dried before being 100% saturated with synthetic Permian Basin brine under vacuum. Values of porosity and pore volumes were calculated based on weight differential before and after fluid saturation. Absolute permeability was measured by injecting brine until a stable differential pressure was obtained for three different flood rates. Permeability measured for the single core plugs varied between 8 to 73mD and porosities from 19 to 35%. These values were in the upper range compared to previous measures on field pilot core material of 4-32mD and 9-17% (Alcorn et al. 2018).

Synthetic Permian Basin brine was made based on water analysis from the field, whereas a light North Sea crude oil was used in absence of reservoir crude. The North Sea crude oil has an API of 33.6° (calculated from specific gravity), a little above the API gravity of the Permian Basin crude of 31° at standard conditions (Alcorn et al. 2018). Compositions of brine and crude oil are reported elsewhere (Fredriksen et al. 2018; Graue et al. 1999). The North Sea crude oil is considered MCM with CO_2 at 60°C and 180 bar, with a minimum miscibility pressure (MMP) of 125 bar (Steinsbø et al. 2014). Reservoir conditions in the field, however, are well above MMP for CO_2 and crude oil (Alcorn et al. 2018). N-Decane ($C_{10}H_{22}$) was therefore selected for the first set of EOR corefloods to obtain FCM conditions with CO_2.

A non-ionic surfactant (i.e. Huntsman L24-22) was previously selected for the CO_2 foam field pilot from a surfactant screening study that quantified adsorption on rock with and without CO_2 (Jian et al. 2016). The non-ionic surfactant was also screened for its ability to alter wettability of oil-wet carbonate rocks to weakly oil-wet conditions in favor of foam (Fredriksen et al. 2018). The non-ionic surfactant was used at a 1wt% concentration in Permian Basin Brine.

Procedure

Coreflood setup.

The core-scale system was composed of two stacked core plugs providing a total length of ~25 cm to generate foam *in-situ*. Selection of cores was based on absolute permeability, and cores with similar properties were paired and stacked. An overview of experiments and their stacked system properties are presented in Table 1. All tests were performed horizontally minimizing the influence of gravity. Experimental conditions were set to 60°C, to avoid crude oil wax precipitation. Pore pressure was set to 180 bars, which is slightly above the hydrostatic pressure of the Permian Basin field (i.e. 172 bars) for CO_2 to be MCM with the North Sea crude oil. At these conditions CO_2 is supercritical and will create an emulsified phase with the surfactant solution (Emadi et al. 2013; Dhanuka et al. 2006). Pressure response was measured by a differential pressure transducer and two absolute pressure transducers (i.e. one downstream and one upstream). The standard setup for high-pressure/high-temperature CO_2 foam injections can be found in Steinsbø et al. (2015).

In practice, there are two main injection strategies for *in-situ* CO_2 foam generation (Shan and Rossen 2002; Farajzadeh et al. 2012). The first is simultaneous injection of CO_2 and surfactant solution known as co-injection. In this case, the quality of the foam is determined by the fraction of gas (f_g), i.e. CO_2, and is a function of flow rate (Jones et al. 2016). The second injection strategy is SAG, where the surfactant solution and CO_2 are injected in alternating slugs and the quality of the foam depends on the slug sizes of CO_2-to-surfactant solution. In either case, the *in-situ* foam is evaluated by its apparent viscosity, which is quantified from flow rate

and pressure drop during foam injection (Hirasaki and Lawson 1985). Foam apparent viscosity is calculated by;

$$\mu_{app} = \frac{k\nabla p}{(u_l + u_g)} \tag{1}$$

where k is the permeability of the porous media, ∇p is the pressure gradient measured, and u_l and u_g are the superficial velocities of liquid and gas, respectively (Jones et al. 2016).

In-situ CO_2 foam stability.
Foam stability by SAG

Foam behavior was investigated for two modes of SAG injection. Single-cycle SAG was run at 100% brine saturated conditions prior to multi-cycle SAG on the same core (E2). The SAG injections were separated by a waterflood to re-establish initial conditions with close to zero CO_2 saturation. For both SAG injections, pre-determined slug sizes were injected for 4.0 pore volumes (PVs) targeting a gas fraction of 0.70. For single-cycle SAG, a single slug of surfactant solution was injected (1 PVs) before CO_2 was introduced for foam generation (3 PVs). For multi-cycle SAG, 12 rapid cycles were run: each cycle consisting of a surfactant slug of 0.11 PVs and a CO_2 slug of 0.22 PVs. Apparent foam viscosities were calculated as function of time (i.e. PVs injected) from Equation 1.

ID	Experimental overview	Oil phase	Length [cm]	Porosity [%]	K_{abs} [mD][2]	Swi
D1	Foam Stability: CO-injection	-	7.5 ± 8.8E-03	24.2 ± 0.2	20.5 ± 0.3	1.00 ± 0.01
D2-D3	Foam Stability: CO-injection	-	12.7 ± 3.5E-03	26.2 ± 0.8	31.6 ± 0.2	1.00 ± 0.01
E2	Foam Stability: SAG	-	12.7 ± 2.0E-03	25.4 ± 0.2	42.3 ± 0.1	1.00 ± 0.01
E3-E4	EOR: CO-injection 1.0 ft/day	n-Decane	24.4 ± 2.8E-03	22.3 ± 1.9	15.5 ± 0.2	0.24 ± 7.22E-03
E5-E6	EOR: CO-injection 2.0 ft/day	n-Decane	24.9 ± 2.8E-03	25.8 ± 0.3	21.4 ± 0.3	0.31 ± 7.28E-03
E7-E8	EOR: Single cycle SAG	n-Decane	27.5 ± 2.8E-03	30.7 ± 2.8	24.0 ± 0.0	0.38 ± 7.59E-03
E9-E10	EOR: Multi-cycle SAG	n-Decane	24.8 ± 2.8E-03	25.1 ± 1.5	38.4 ± 0.4	0.29 ± 7.27E-03
E11-E12	EOR: CO-injection 1.0 ft/day	Crude oil	25.3 ± 2.8E-03	28.2 ± 0.4	28.4 ± 0.1	0.23 ± 7.44E-03
E13-E14	Foam stability/EOR: CO-injection 1.0 ft/day	Crude oil	24.7 ± 2.8E-03	27.5 ± 0.4	31.4 ± 0.5	0.24 ± 7.13E-03
E15-E16	Foam stability/EOR: CO-injection 1.0 ft/day (base case[1])	Crude oil	27.4 ± 2.8E-03	22.5 ± 2.3	14.3 ± 1.3	0.15 ± 7.04E-03
E17-E18	EOR: Multi-cycle SAG 1.0 ft/day	Crude oil	24.9 ± 2.8E-03	28.4 ± 1.7	31.6 ± 0.2	0.25 ± 7.20E-03
E19-E20	EOR: Multi-cycle SAG 1.0 ft/day	Crude oil	27.5 ± 2.8E-03	26.5 ± 0.7	11.0 ± 0.1	0.20 ± 7.14E-03
E21-E22	EOR: Multi-cycle WAG 1.0 ft/day (base case[1])	Crude oil	25.0 ± 2.8E-03	25.8 ± 1.8	21.3 ± 0.7	0.24 ± 7.18E-03

[1]Base case = without surfactant solution.
[2]Uncertainty calculated as standard deviation of the mean.
Table 1 – Experimental overview and stacked-system properties

Foam stability by co-injection

Foam behavior during co-injection was investigated by foam quality and rate scans. Tests were run in 100% brine saturated cores, where one system was composed of a single core (D1) and the other a stacked system (D2-D3). Scans were also performed at residual oil saturation after CO_2 foam EOR to assess the effect of crude oil on foam stability (E13-E14), and equivalently for a base case without surfactant (E15-E16). See Table 1 for experimental overview.

Foam quality scans determine the optimal CO_2-to-surfactant solution ratio that will generate the highest apparent viscosity during co-injection. CO_2 fractions were changed from 0.0 to 0.90 for drainage-like co-injection (i.e. increasing CO_2 fraction) at a total superficial injection rate of 1.0 ft/day. Each fraction was maintained until steady state pressure drop was achieved before increasing to next preset value. The apparent foam viscosity was calculated from Equation 1.

Rate scans were performed following foam quality scans on the same core(s) to estimate rate-dependency on shear-thinning behavior (which is desirable in field applications to avoid injectivity issues near the injection well). Rate scans for co-injection were run by increasing the total injection rate at the optimal CO_2 fraction from quality scans. Starting at a superficial

velocity of 1.0 ft/day, the injection rate was raised to 2.0, 3.0, and 4.0 ft/day after reaching steady state conditions.

CO₂ foam EOR.

Core plugs were initially 100% brine saturated, stacked, and drained with either *n*-Decane or crude oil to irreducible water saturation (S_{wi}) at a constant pressure drop of 2 bar/cm. A waterflood was performed for 1 PV prior to CO_2 foam injection. Injection strategies during CO_2 foam were either co-injection, single-cycle or multi-cycle SAG. The CO_2 foam injections lasted for no more than 2 PVs considering volumetric and economic limitations when upscaling to field.

CO_2 foam EOR was performed at FCM conditions using mineral oil (i.e. n-Decane) and at MCM conditions with North Sea crude oil. At FCM conditions, CO_2 foam by co-injection used two injection rates (1.0 ft/day for E3-E4 and 2.0 ft/day for E5-E6) to investigate shear-thinning on foam generation and EOR. Co-injection results were then compared with single cycle (E7-E8) and multi cycle SAG (E9-E10). The most promising injection strategies were evaluated at MCM conditions with crude oil and compared with base case experiments without surfactant solution.

Core-Scale Model Set-up.

Laboratory data from a co-injection experiment (i.e. E13-E14) was utilized for a core-scale simulation model. Stacked system properties are found in Table 1. The model was initialized to represent the stacked system during waterflood and co-injection. For the waterflood, simulations were conducted with ECLIPSE 100 Blackoil simulator while the compositional simulator E300 (Schlumberger, 2015.2) was used for co-injection. Experimental data validated the model through matching bottom hole pressure (BHP) and oil/water production rates. The validated model was used to conduct a sensitivity analysis on the effect of grid cell size and foam quality on oil recovery and CO_2 mobility reduction. A case without surfactant solution was also evaluated. The main objective was to ensure model robustness at representing the observed foam behavior which can be extended to use in ongoing field scale simulations.

Simulation Design.

The base case model consisted of a grid with dimensions 1 x 1 x 100. The injector was completed in the first grid block (inlet), while the producer was completed in the last grid block (outlet). The production well was placed on BHP control and the injector was controlled by rate both of which were measured in the laboratory. Relative permeability data for the waterflood was derived from JBN analysis of oil and water displacement during the laboratory experiment (Johnson et al. 1959). Oil and water densities and viscosities were available from PVT-analysis of the crude oil. The model was initiated with S_{wi} of 0.24 at a system pressure of 182 bars.

The co-injection was initialized at pressure and saturations from the history-matched waterflood. The grid size, orientation, well completions and controls were kept identical, except two injection wells were used to represent the single co-injection well from the experiment (one for CO_2 and one for surfactant solution). A compositional simulation case was generated which contained 14 oil components and 2 water components (water and surfactant). Relative permeability curves were derived from CO_2/brine displacement experiments on similar core material described elsewhere (Alcorn et al. 2018). Capillary pressure effects were not included in this study. The injection schedule was identical to the experimental procedure and a foam quality of 0.70 was targeted using a surfactant solution concentration of 1.0 wt%. The effect of foam was modeled using an empirical local-equilibrium approach, where a gas mobility-reduction-factor is introduced to scale the gas relative permeability in absence of foam as described by Sharma et al. (2017).

Results and Discussions

Apparent viscosities and oil recoveries were used to evaluate mobility control during CO_2 foam. Several mechanisms will contribute to the foam apparent viscosity including lamella creation, trapped gas and CO_2-surfactant emulsification, all of which increase pressure response and inferred higher apparent viscosities.

In-situ CO_2 foam stability.

CO$_2$ foam stability scans by single-cycle and multi-cycle SAG injections were compared to co-injection foam quality scans in brine saturated systems without oil. Foam apparent viscosity during single-cycle SAG was 18.2 ± 12.7 cP at steady state (dashed curve, Figure 1), and 120.2 ± 0.3 cP for multi-cycle SAG (solid curve, Figure 1). Apparent viscosities did not increase before the CO_2 slugs were introduced, leading to lamella creation by mechanisms of leave-behind as the CO_2 saturation increased during the drainage process (Ransohoff and Radke 1988).
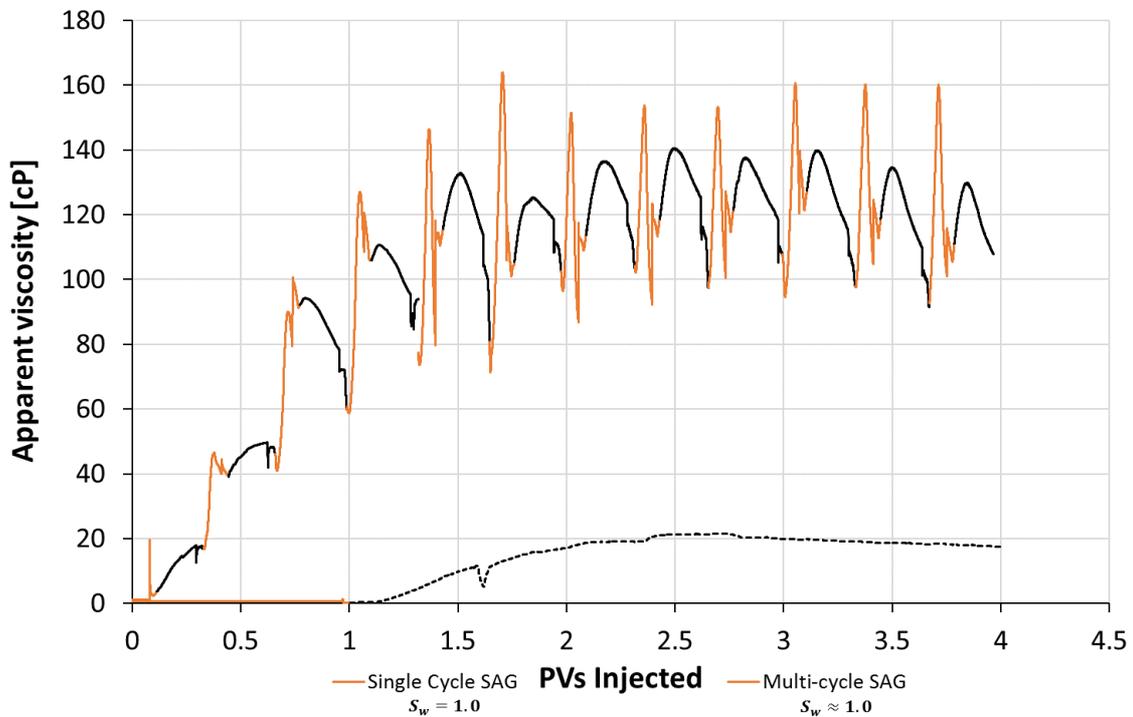
Fig. 1 – Foam apparent viscosity as a function of pore volumes injected during single-cycle SAG (dashed curve) and multi-cycle SAG (solid curve). Orange curves represent injection of surfactant solution slugs and the black curves CO_2 slugs. Single cycle SAG was initiated at $S_w = 1.0$ (no trapped CO_2), whereas multi-cycle SAG injection was initiated with some trapped CO_2 in the core, $S_w \approx 1.0$.

For single-cycle SAG, the formation of lamella by leave-behind occurred only once during drainage (Prud'homme and Khan 1996). After CO_2 was introduced, foam generation depended on fluctuations in local capillary pressures and lamella division to remain stable. However, after several pore volumes CO_2 injected, the foam started to dry out as most of the wetting phase was displaced. The apparent viscosity declined for the last pore-volume CO_2 injected (dashed curve, Figure 1).

Injecting multiple alternating slugs of surfactant solution and CO_2 improved conditions for lamella creation and foam stability. During multi-cycle SAG, surfactant solution was introduced to the system in an imbibition process which caused the capillary pressure to fall and lamella creation by snap-off to dominate foam generation (Ransohoff and Radke 1988). Increased wetting-phase saturation mitigated foam dry-out and a larger degree of fluid diversion

behind the displacement front occurred from mobilizing foam lamella. The growth and propagation of a stable high-viscosity foam region was evident during multi-cycle SAG (solid curve, Figure 1).
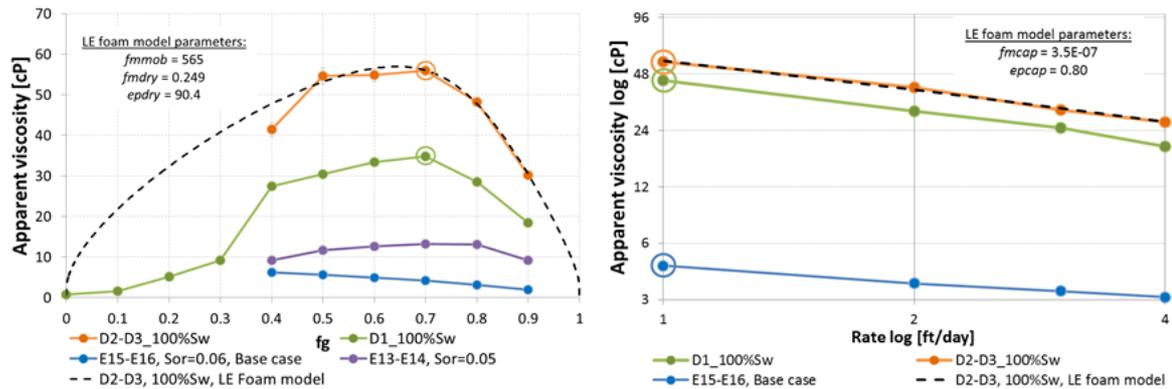
Fig. 2 – Foam stability showing apparent viscosity for foam quality scans f_g=0.0 to 0.90 (left) and foam rate scans at 1.0, 2.0, 3.0 and 4.0 ft/day (right) during co-injection of CO_2 and surfactant solution. Experiments were performed on 100% brine saturated cores (D1 and D2-D3), in cores at residual oil after EOR (E13-E14) and for a base case (E15-E16) without surfactant. The foam rate scans were performed at constant f_g=0.70 after foam quality on the same cores. Foam quality and rate scans for stacked system D2-D3 was used to calibrate an implicit texture local equilibrium (LE) foam model to be used in core-scale simulations (black dashed curves to the left and right with model parameters displayed). Uncertainties are given as standard deviation of the mean.

Co-injection foam quality scans D1 and D2-D3 (orange and green curves, Figure 2) have previously been published (Fredriksen et al. 2018; Rognmo et al. 2018). It was found that with monotonically increasing CO_2 fraction the transition from low quality to high quality foam occurred at f_g=0.70 as indicated by the orange and green circles (Fredriksen et al. 2018; Rognmo et al. 2018). Above this, foam apparent viscosity decreased with further increase in CO_2 fraction. Apparent foam viscosities at steady state for f_g=0.70 was 34.9 ± 1.0 cP (D1), and 56.0 ± 1.6 cP (D2-D3), higher than single-cycle SAG (18.2 ± 12.7 cP), but lower than multi-cycle SAG (120.2 ± 0.3 cP) in Figure 1.

Both lamella creation and destruction occurred simultaneously during co-injection as imbibition (i.e. surfactant) and drainage (i.e. CO_2) processes dominated foam generation. This resulted in a higher apparent foam viscosity compared to single-cycle SAG. During co-injection, CO_2 and surfactant solution separates upon contact with the core inlet, where the continuous wetting-phase flows through the smaller pores, and continuous-CO_2-foam travels the larger pores (Persoff et al. 1991). This resulted in a more dispersed displacement front and less mobility control for co-injection compared to multi-cycle SAG.

The presence of trapped CO_2 provided a viscous component to the pressure drop during multi-cycle SAG and co-injection foam quality scans. This inadvertently overestimated foam apparent viscosities at steady state. A decrease in effective water permeability was observed for E2 from 42.3mD to 19.8mD by capillary trapped CO_2 prior to multi-cycle SAG foam stability. During foam quality scans, when f_g was increased, the CO_2 saturation also increased for each step. Hysteresis, however, will also be present during CO_2 foam injection in field, as water is currently being injected after tertiary CO_2 flooding.

CO_2 foam for EOR and mobility control.
First-contact miscible conditions.
Co-injection and SAG injection strategies were evaluated for their apparent viscosity and oil recovery at FCM conditions (Figure 3). A clean water cut was observed for all waterfloods (left of the vertical black line). The range in recovery between 31.2 % and 47.7% OOIP is a result of core heterogeneity (Eide et al. 2012). Recovery factors and values of apparent viscosity are listed in Table 2.

CO_2 foam co-injections were performed at two different injection rates (1.0 ft/day and 2.0 ft/day). Foam was generated earlier at higher rate (1.7 PVs injected, E5-E6, orange dashed curve) compared to the lower injection rate (2.3 PVs injected, E3-E4, orange solid curve) from dynamic observations of apparent viscosity in Figure 3. The average apparent viscosity, however, was higher at 1.0 ft/day (28.1 cP, E3-E4) than for 2.0 ft/day (18 cP, E5-E6) for the last 0.5 PVs injected (Table 2).

Foam flow behaves as a non-Newtonian fluid and is shear-thinning at increasing flow rates (Kahrobaei et al. 2017). The shear-thinning behavior was observed in Figure 2 (left). The highest apparent viscosity was observed at the lowest injection rate (1.0 ft/day, green and orange circles). Increasing flow rate to 4.0 ft/day caused the apparent viscosity to drop by 56 – and 52 percentage points for D1 and D2-D3 respectively (green and orange curves, Figure 2 left). The shear-thinning effect was therefore expected during CO_2 foam EOR as confirmed in Figure 3.
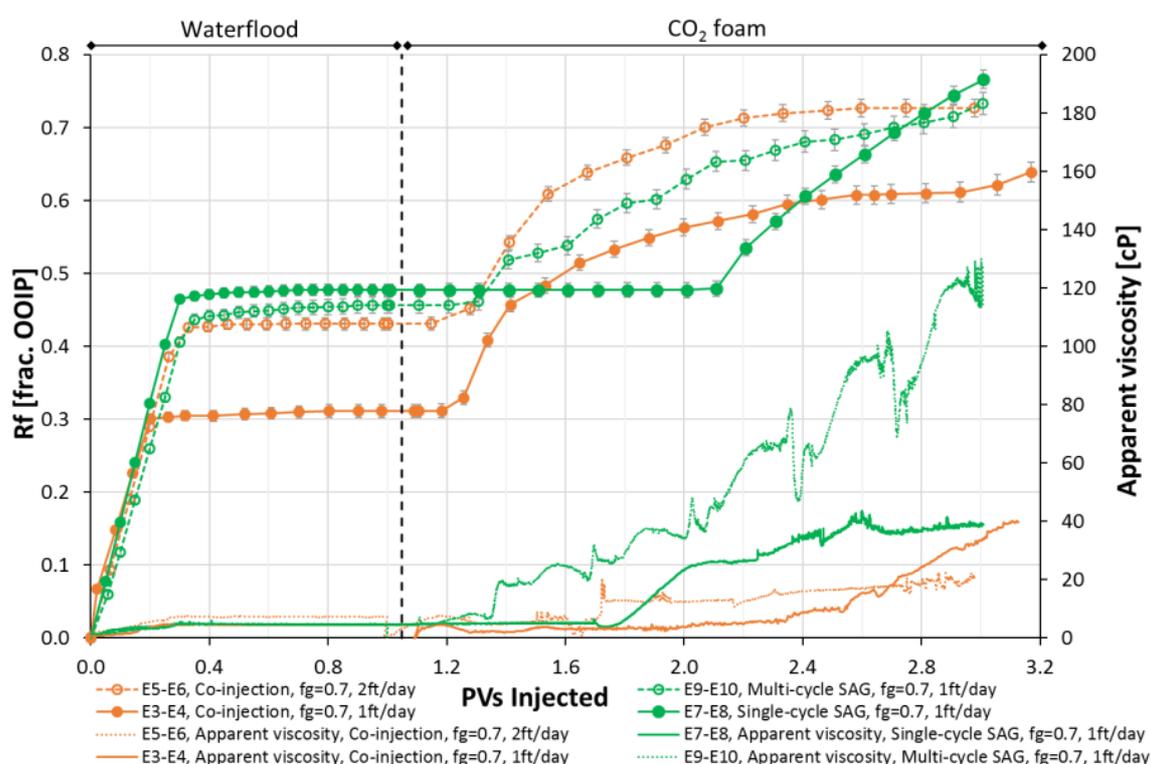
Fig. 3 – CO_2 foam EOR corefloods with co-injection and SAG under FCM conditions using *n*-Decane as the oil-phase. The orange curves represent CO_2 foam by co-injection at rates of 1.0 ft/day (closed circles) and 2.0 ft/day (open circles), and the green curves single-cycle SAG (closed circles) and multi-cycle SAG (open circles). Recovery factor vs. PVs injected to the left of the vertical dashed black line is from waterflood and to the left CO_2 foam. The secondary y-axis shows apparent viscosity for the displacement processes.

Apparent viscosity trends during SAG EOR (green curves, Figure 3) were the same as for foam stability scans (Figure 1). No increase in apparent viscosity was observed prior to CO_2 injection. Steady state apparent viscosity was higher for single-cycle SAG (green solid curve), than either of the co-injection experiments (orange curves) and reached a plateau at 37.9 cP (Table 2). However, a higher apparent viscosity could have been obtained by continuing the co-injection at 1.0 ft/day (solid orange curve). CO_2 foam viscosity for multi-cycle SAG (dashed green curve) increased continuously for each cycle and reached an average value of 100.7 cP at the end of injection (Table 2). In terms of mobility control, multi-cycle SAG was superior in creating conditions for high viscous displacement in both foam stability scans (Figure 1) and EOR corefloods at FCM conditions (Figure 3).

Accelerated oil recovery rate was observed from the start of both co-injections (open and closed orange circles) in Figure 3 and most of the oil was produced after 1.0 PV CO_2 foam injected. For single-cycle SAG (solid green circles), no oil was recovered during the initial surfactant slug before CO_2 was introduced. Steady oil production, however, was observed for multi-cycle SAG after the first CO_2 slug injected (open green circles). The stepwise trend in oil production reflected the shift between slugs during the SAG process.

At FCM conditions, diffusive mixing dominated oil recovery above that of viscous displacement by foam. CO_2 diffusion is a dominant recovery mechanism at core-scale with the potential to recover near 100% of the oil (Eide et al. 2016; Fernø et al. 2015). At constant f_g=0.70, CO_2 diffusion recovered the same amount of oil regardless of injection mode, on average 29.7 ± 2.2% OOIP (Figure 3). As observed in Figure 3, however, total recoveries did not reach the ultimate recovery potential of 100% OOIP as lamellas can create barriers that hinder direct contact between the discontinuous CO_2 phase and unrecovered oil. At high pressures, CO_2 density increases and a shift towards greater surfactant solvation at the water-CO_2 interface causes the CO_2 emulsions to become increasingly stable (Dhanuka et al. 2006). Values of incremental oil recovery during CO_2 foam are listed in Table 2.

Core ID	Oil phase	$R_{f, WF}$ [%OOIP]	$R_{f, CO2\ foam}$ [%OOIP]	$R_{f, tot}$ [%OOIP]	App. visc. CO_2 foam [cP][1]	S_o (after WF) ± 0.01
E3-E4	n-Decane	31.2 ± 0.9	32.7 ± 1.7	63.9 ± 1.4	28.1 ± 7.7	0.48
E5-E6	n-Decane	43.1 ± 0.8	29.6 ± 1.5	72.7 ± 1.2	18.0 ± 1.4	0.39
E7-E8	n-Decane	47.7 ± 0.8	28.9 ± 1.5	76.6 ± 1.2	37.9 ± 1.1	0.48
E9-E10	n-Decane	45.7 ± 1.1	27.6 ± 1.9	73.3 ± 1.6	100.7 ± 14.6	0.46
E11-E12	Crude oil	62.2 ± 0.9	24.5 ± 1.6	86.7 ± 1.3	n/a	0.29
E13-E14	Crude oil	62.0 ± 0.9	31.0 ± 1.6	93.0 ± 1.3	5.5 ± 0.5	0.29
E15-E16	Crude oil	58.6 ± 1.0	34.9 ± 1.7	93.5 ± 1.4	7.3 ± 0.1	0.35
E17-E18	Crude oil	62.3 ± 0.9	30.5 ± 1.6	92.8 ± 1.3	7.0 ± 3.0	0.28
E19-E20	Crude oil	59.8 ± 0.9	33.5 ± 1.5	93.9 ± 1.2	n/a	0.32
E21-E22	Crude oil	66.8 ± 1.0	33.2 ± 1.8	100.0 ± 1.4	7.3 ± 1.6	0.25

$R_{f,WF}$ = recovery factor by waterflood; $R_{f, CO2foam}$ = recovery factor by CO_2 foam; $R_{f,tot}$ = total recovery factor
n/a = not applicable due to missing pressure logs.
[1]Mean average last 0.5PVs at the end of the CO_2 foam flood. Uncertainties are given as standard deviation of the mean.
Table 2 – Recovery factors for CO_2 foam EOR corefloods.

Multiple-contact miscible conditions.

Viscous forces are desirable for mobility control and fluid diversion during *in-situ* CO_2 foam EOR in field. Co-injection at 1.0 ft/day and multi-cycle SAG gave best results in terms of both mobility control and EOR. These injection strategies were used to determine sensitivity in presence of crude oil at MCM conditions. Base case experiments were also run without surfactant solution as a reference to the performance during CO_2 foam. Results are presented in Figure 4.

Waterflood recovery indicated less water-wet conditions with characteristic two-phase production (Jadahunandan and Morrow 1995), and recovered on average 62.0 ± 2.8% OOIP (blue curves, Figure 4). Calculations of apparent viscosities during CO_2 foam demonstrated little to no *in-situ* foam generation. No increase in foam apparent viscosity was observed above that of the base cases without surfactant. Two possible explanations are offered for the absence foam generation in Figure 4 (black and grey curves).

Oil composition is known to influence lamella creation and foam stability, and its presence can make some foams more unstable than others. Schramm and Novosau (1992) found that foam stability was reduced with decreasing carbon content in crude oils. Others have reported that lower number alkanes are more destabilizing than higher number alkanes, because their shorter hydrocarbon chains are more easily imbibed into foam plateau borders to solubilize with surfactants leading to oil spreading and foam instability (Suffridge et al. 1989; Vikingstad et al. 2005; Kristiansen and Holt 1992).
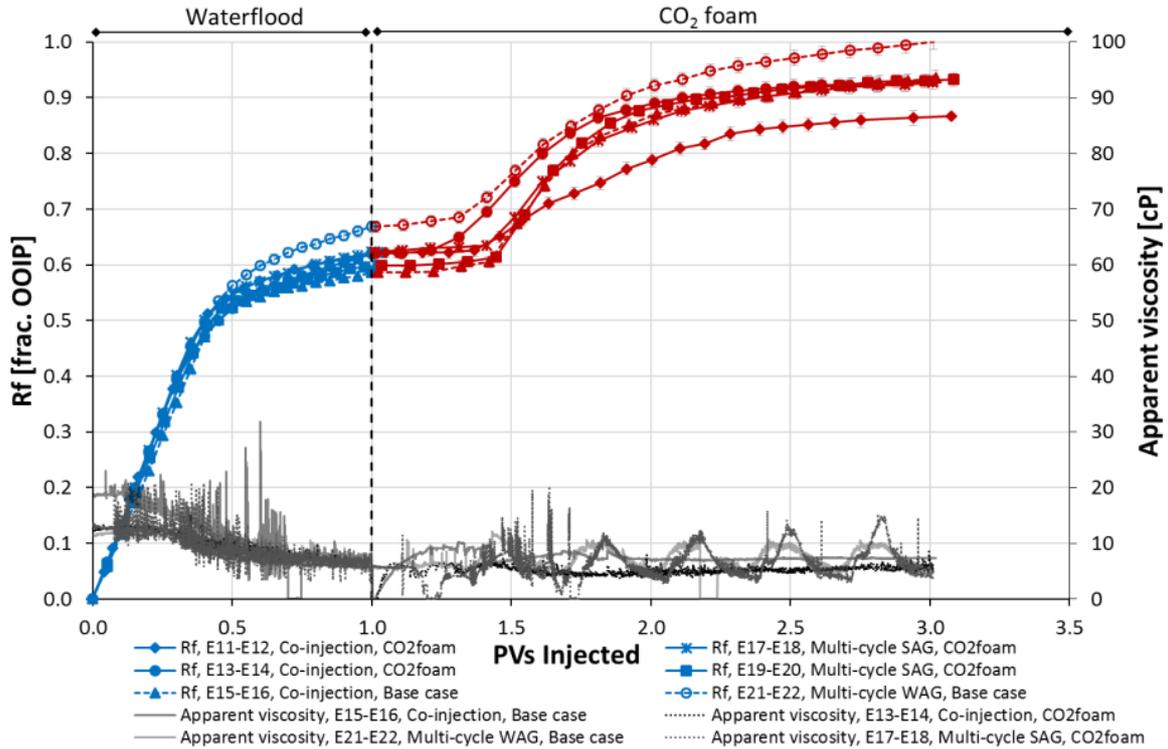
Fig. 4 – CO$_2$ foam EOR corefloods by co-injection and multi-cycle SAG under MCM conditions using North Sea crude oil. Recovery factor vs. PVs injected to the left of the vertical dashed black line is from waterflood (blue curves) and to the left CO$_2$ foam (red curves). CO$_2$ foam injections are represented by the solid lined curves, while the base cases are dashed. The secondary y-axis shows apparent viscosity for the displacement processes.

Wettability alteration towards less water-wet conditions occurs in presence of crude oil (Buckley and Liu 1998). It has previously been reported that foam cannot be generated at other wettability conditions other than strongly water-wet due to the lack of water-wet snap-off sites (Prud'homme and Khan 1996). At strongly water-wet conditions, water-wet films covering the rock surfaces maintain the continuous foam structure throughout the porous media (Farajzadeh et al. 2012). A shift to oil-wet can causes the lamellas to detach from the pore walls, and foam may not be generated. Schramm and Mannhardt (1996) confirmed reduced foam effectiveness at intermediate to oil-wet conditions, and Fredriksen et al. (2018) induced surfactant wettability alteration in oil-wet fractures for CO$_2$ foam to generate in matrix below a critical oil saturation (Fredriksen et al. 2018).

At FCM conditions (Figure 3), the presence of an alkane mineral oil (i.e. *n*-Decane) did not negatively affect foam generation or propagation for either injection strategy. *N*-Decane is a non-polar oil molecule with no ability to alter wetting-state like that of heavy polar molecules (i.e. asphaltenes and resins). Aging carbonate rock in *n*-Decane does not alter wettability (Graue et al. 1994), and so stable lamellas were able to create *in-situ* foam even in the presence of oil.

Co-injection foam quality scans confirmed the influence of crude oil on foam stability. Experiment E13-E14 in Figure 2 (left, purple curve) was performed after CO$_2$ foam EOR with crude oil at residual oil (i.e. $S_{or} = 0.05$). Reduced apparent foam viscosity was observed for every f_g compared to D1 and D2-D3 (i.e. strongly water-wet) in Figure 2 (left, orange and green curve). However, compared to the base case without surfactant (E15-E16, blue curve, Figure 2), the apparent viscosities for E13-E14 (purple curve) were 68 times higher. Hence, it is possible to generate foam with low apparent viscosities under destabilizing conditions with crude oil.

Incremental oil recoveries were also diffusion driven at MCM conditions (Figure 4). Oil recoveries were on average $30.6 \pm 3.0\%$ OOIP for all injection strategies with and without

surfactant at both FCM and MCM conditions. Bernard et al. (1980) observed the same effect in their core-flood experiments with CO_2 foam. This restricted evaluation of injection strategies in terms of production efficiency. Longer induction periods were observed, however, for continuous oil banks to develop under MCM conditions in Figure 4. Between 0.3 to 0.4 PVs of CO_2 foam were injected before oil production was observed (red curves). Total recoveries were higher at MCM conditions (93.2 ± 2.7% OOIP) compared to FCM conditions (71.2 ± 3.2% OOIP) as the waterfloods left behind lower residual oil saturations (Table 2). Further sensitivity analysis on the effect of CO_2 fractions on foam behavior were run using the history-matched core-scale simulation model.

CO_2 storage potential for CCUS.

A secondary objective for implementing CO_2 foam for mobility control and EOR is the potential for storing CO_2 as a part of CCUS. To calculate CO_2 stored, volume of CO_2 produced was measured from volumetric conservation of injected and produced fluids, and subtracted from the volume CO_2 injected. The value for CO_2 storage (given as a fraction of total PV) was compared to the saturation change of oil and water in the core after CO_2 foam. Figure 5 shows CO_2 storage in fraction of PV for both co-injections (left) and multi-cycle (right). A direct correlation between the amounts of CO_2 stored and the water/oil saturation change was observed regardless of injection strategy. For every amount of fluid produced the equivalent amount of CO_2 was stored.
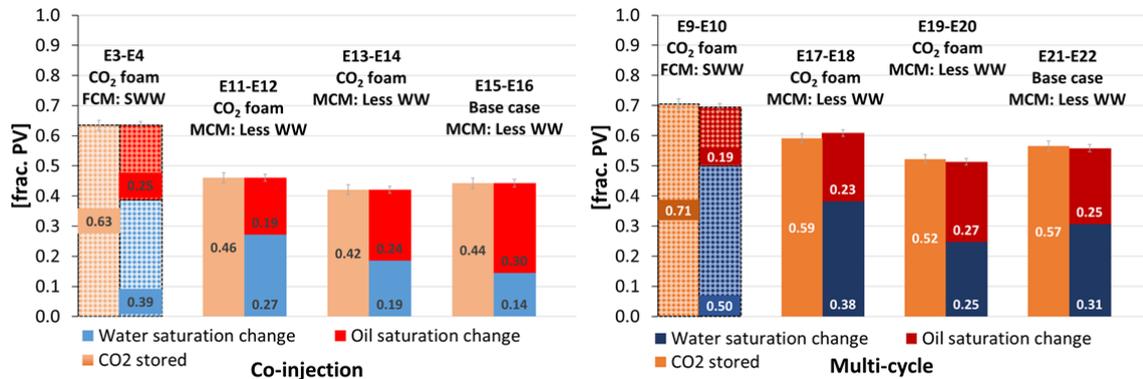
Fig. 5 – CO_2 storage potential during CO_2 foam EOR corefloods at FMC and MCM conditions. Left: Co-injection with/without surfactant. Right: Multi-cycle SAG with/without surfactant. Orange bars represent CO_2 stored in fraction of total PV calculated from volumetric conservation, and the blue and red bars are fractional change in water and oil saturation respectively during injection. Bars with dashed borders and patterned texture indicate FCM conditions, while bars with solid borders and colors show MCM conditions

Storage potential at FCM conditions using *n*-Decane in Figure 5 (E3-E4 and E9-E10) was on average 17.1 ± 4.0% greater than the average storage at MCM conditions with crude oil. This was consistent with the improved CO_2 foam performance and higher apparent foam viscosity at FCM conditions. An overall trend was observed where multi-cycle SAGs and base case WAG at MCM stored on average 9.0 % more CO_2 than co-injections at the same conditions. The difference was related to higher water displacement for multi-cycle SAGs and base case WAG (see higher change in water saturation, Figure 5, right, blue bars).

The effect became clear when plotting CO_2 storage as a function of oil produced in Figure 6. The observed fraction of CO_2 stored to oil produced was above unity (black diagonal), even with no oil produced. This indicated a higher water production rate at the start of injection in favor of CO_2 storage. Capillary trapping is the main mechanism for storing CO_2 in the subsurface (Ali-Menhali and Krevor 2016). At strongly water-wet (FCM) –and at less water-wet conditions (MCM) water was still the preferred wetting-phase, and so capillary trapping remained the main mechanism for storing CO_2 in the core in addition to producing oil.

Improved CO_2 storage was observed at the end multi-cycle SAG and WAG (orange curves) compared to co-injections (blue curves) accounting for the higher storage potential in terms of water displacement as observed in Figure 5.
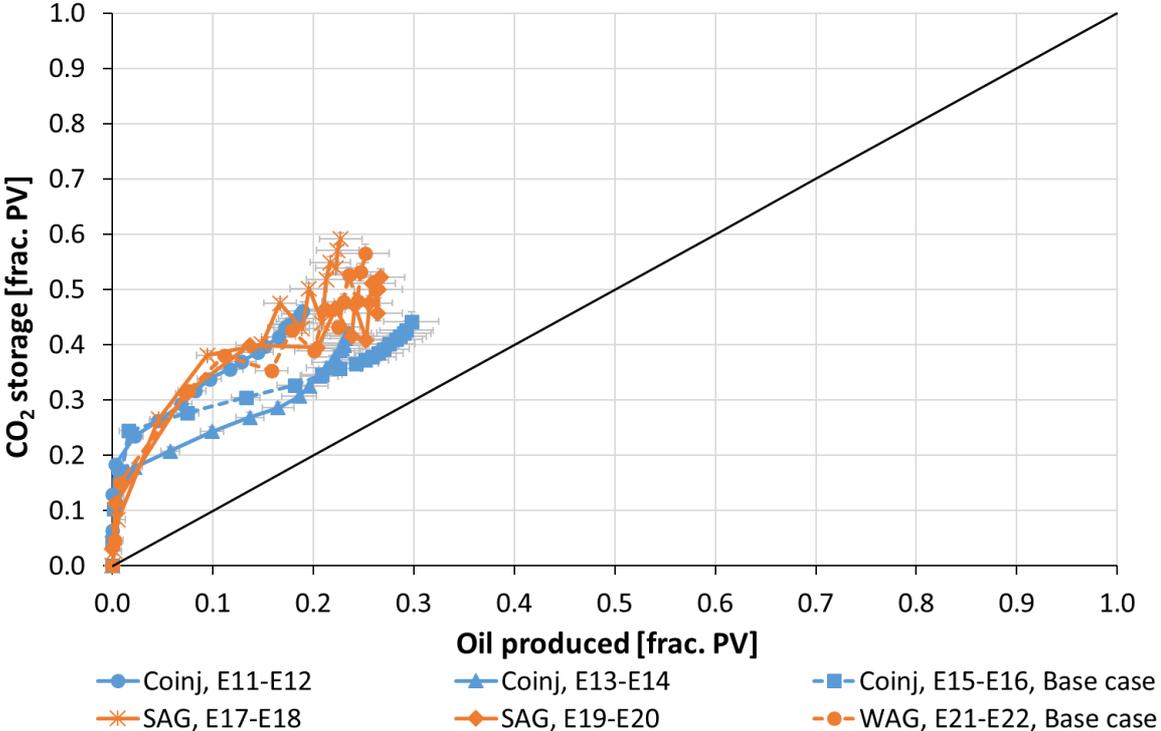
Figure 6 – CO_2 storage as a function of oil produced for CO_2 foam co-injection (blue solid curves) and base case without surfactant solution (blue dashed curve), and for multi-cycle SAG (orange solid curves) and base case WAG (orange dashed curve). The black line represents unity where the amount of CO_2 stored equals oil produced.

Core-Scale Sensitivity Study and Model Validation.

The core-scale simulation model utilized the foam stability measurements in Figure 2 to fit the empirical foam model by curve fitting regression (Alcorn et al. 2018; Sharma et al. 2018; Rognmo et al. 2017). The value for *fmmob*, however, was reduced to 41.5 in accordance with previous findings on field core material to reflect more realistic conditions for the field system. An acceptable history-match for E13-E14 was obtained for both waterflood and co-injection. The waterflood match was achieved by tuning the oil relative permeability curve to match oil/water production rate and BHP. The co-injection was matched by tuning the oil and water relative permeabilities to match cumulative oil/water production and BHP. Figure 7 shows the history-match.
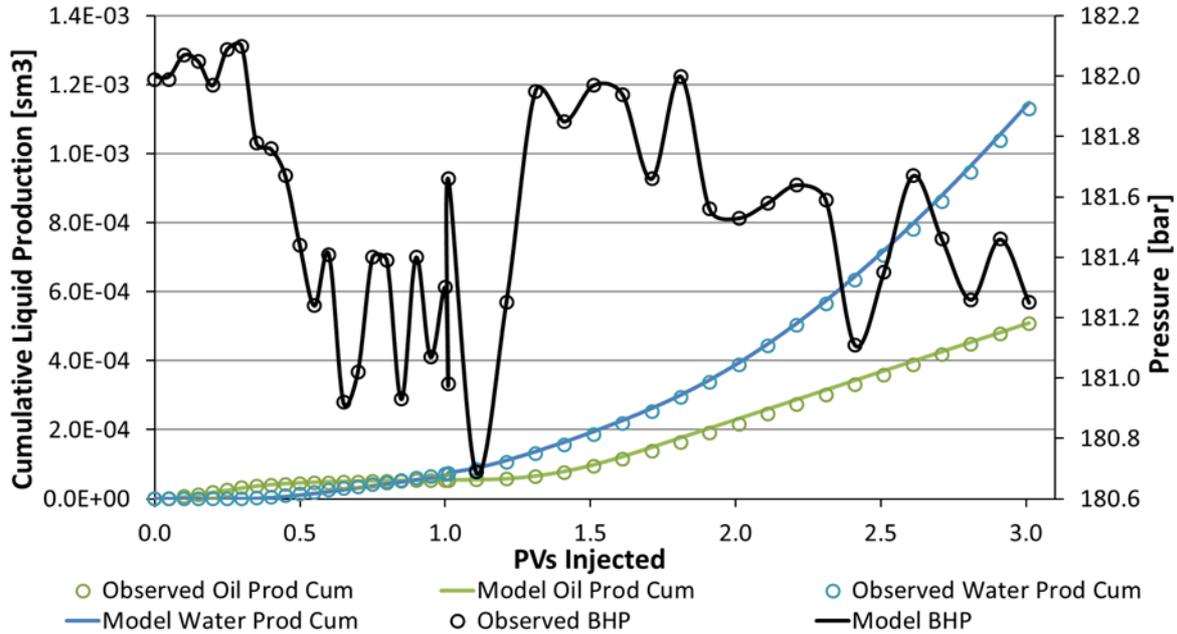
Fig. 7 – Observed (open circles) and modeled (curves) cumulative oil/water production during waterflood and co-injection of the history-matched experiment. Production well BHP is shown on the secondary y-axis.

Effect of Grid Resolution.

The validated model was used to conduct a sensitivity study on the effect of grid resolution during co-injection. A fine scale grid was generated with dimensions 5 x 5 x 200. See Table 3 for comparison of the two grid resolutions. The simulation model was identical to the base case history-match, but used the fine scale grid to evaluate change in CO_2 mobility reduction and oil recovery.

	Coarse base grid	Fine grid
Dimensions	1 x 1 x 100	5 x 5 x 200
Active cells	100	5000
Individual cell size (cm)	4 x 4 x 0.24	0.8 x 0.8 x 0.12

Table 3 – Overview of the coarse base grid and fine grid used for sensitivity study.

CO_2 mobility reduction is generally inferred from delayed CO_2 breakthrough and an increased response in injection pressure. Simulation results showed limited effect of grid resolution on co-injection (Figure 8, left). Comparison of the coarse base grid and fine grid showed a slight variation in injection well pressures (black curves, Figure 8, left), where the fine grid followed the same pressure trend as the coarse grid only 0.5 to 1.0 bars higher. This was less than a 0.5% change (dashed black curve), which did not affect CO_2 breakthrough (red curves, Figure 8, left).

Figure 8 (right) shows cumulative recoveries for the coarse base grid and fine grid during co-injection to study the effect of grid resolution on oil recovery. The coarse base grid recovers more oil initially, but the final difference in cumulative volumes is negligible. Oil recovery was insensitive to grid resolution. As limited variations were seen with the fine grid model, further sensitivity studies utilized the coarser base grid to reduce run time.

13
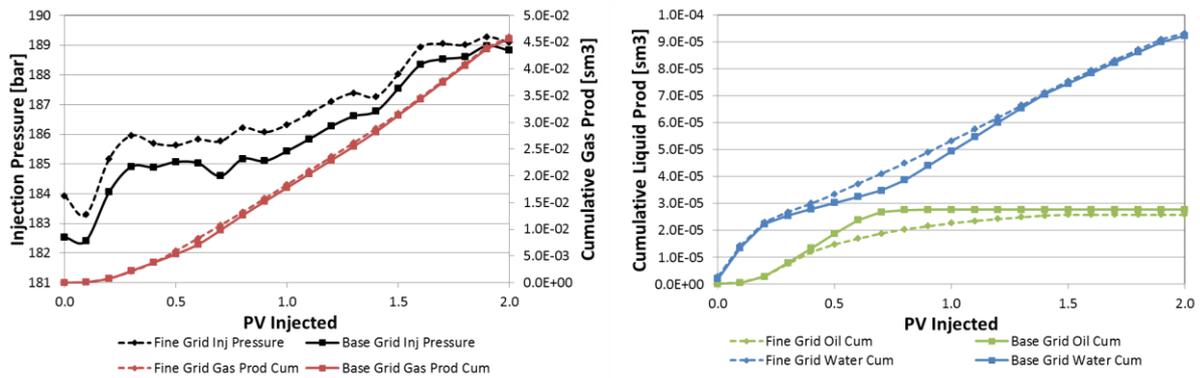
Fig. 8 – Left: Injection well BHP during the co-injection phase of the experiment for the base grid (black, solid curve) and the fine grid (black, dashed curve). Cumulative gas (CO_2) production is shown on the secondary y-axis (red curves). Right: Cumulative oil and water production for the base grid (solid curves) and the fine grid (dashed curves).

Oil saturation development for three different time-steps during co-injection for the coarse base and fine grids are shown in Figure 9. Shortly after the start of co-injection ($t = 1$) an oil bank formed ahead of the injection front and resulted in piston-like displacement for the coarse base case (Figure 9, top). Visual analysis of the fine grid co-injection indicated a more dispersed injection front in the x- and y-directions (Figure 9, bottom), from the completion of the injection well at the center of the grid. Hence, improved fluid displacement was observed in adjacent cells contacting the well connection.
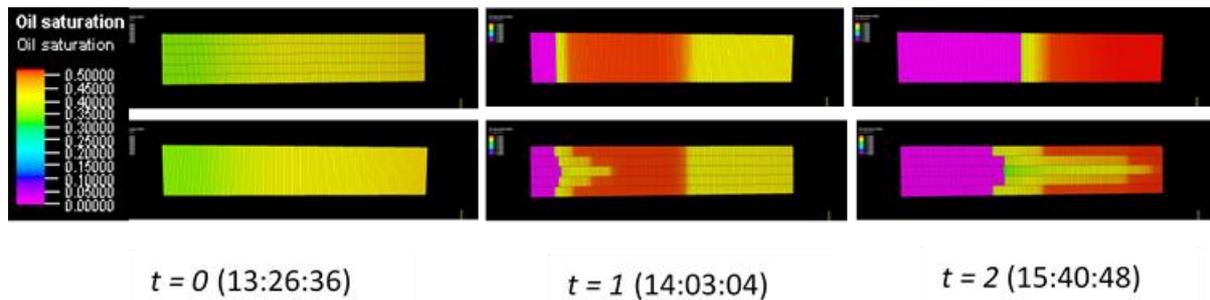
Fig. 9 - Oil saturation development at three different times (*t*) during the base case run (top) and fine grid run (bottom). Injection is from left to right. Warm colors represent higher oil saturations while cool colors represent lower oil saturations.

Effect of Foam Quality.

To determine its impacts on oil recovery and CO_2 mobility reduction the effect of foam quality (CO_2 fraction) was studied using the coarse base grid. Cases injecting higher CO_2 fractions were set to assess model sensitivity on amounts of CO_2 injected and its influence on oil recovery. The base case history-matched model used the optimal CO_2 fraction of 0.70 measured in laboratory (cf. Figure 2, left, orange and green circles). Further sensitivity cases were set to CO_2 fractions of 0.80, 0.90, and 0.95. Figure 10 shows cumulative oil production (solid curves) for the base case ($f_g=0.70$) and CO_2 fraction sensitives. With increasing CO_2 fractions the oil recovery rate accelerated, but all cases recovered the same volume of cumulative oil. Hence, CO_2 miscibility dominated oil displacement, corroborating the previous observations during the CO_2 foam EOR coreflood experiments in Figure 3 and 4.
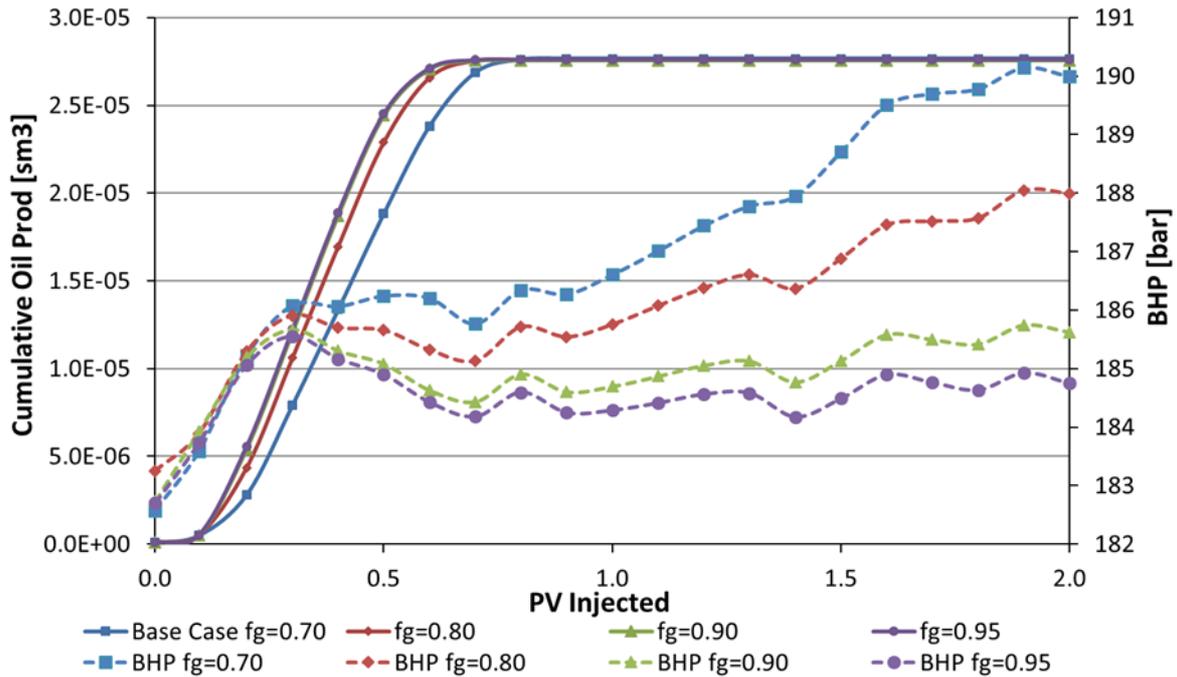
Fig. 10 – Cumulative oil production versus time for the base case (blue solid curve), and three sensitivities with different gas (CO_2) fractions. Injection pressure versus time shown on the secondary y-axis for the base case (blue dashed curve), and three sensitivities with different gas (CO_2) fractions.

Injection pressures for the various CO_2 fractions are shown in Figure 10 (dashed curves). All injection pressures followed the same trend. Higher pressures, however, were observed as the fraction of CO_2 decreased and the fraction of surfactant solution increased, creating a higher apparent viscosity foam (blue and red dashed curves, Figure 10). This is consistent with trends observed in foam quality scans where the optimal CO_2 fraction and highest apparent viscosity was observed at 0.70 (cf. Figure 2, left, green and orange circles). At fractions above this, apparent viscosities declined.

Effect of Surfactant: CO_2/surfactant solution vs CO_2/water.

CO_2 diffusion and miscibility were the main oil recovery mechanisms in both simulation and laboratory experiments. A similar case to the history-matched experiment was therefore set-up without surfactant to investigate CO_2 against CO_2 foam displacement. The injection schedule was kept identical to the base case co-injection, except only water was injected as the aqueous phase. Figure 11 shows injection pressure (dashed curves) and cumulative CO_2 production (solid curves) during co-injection with surfactant (blue curves) and without surfactant (red curves).

15
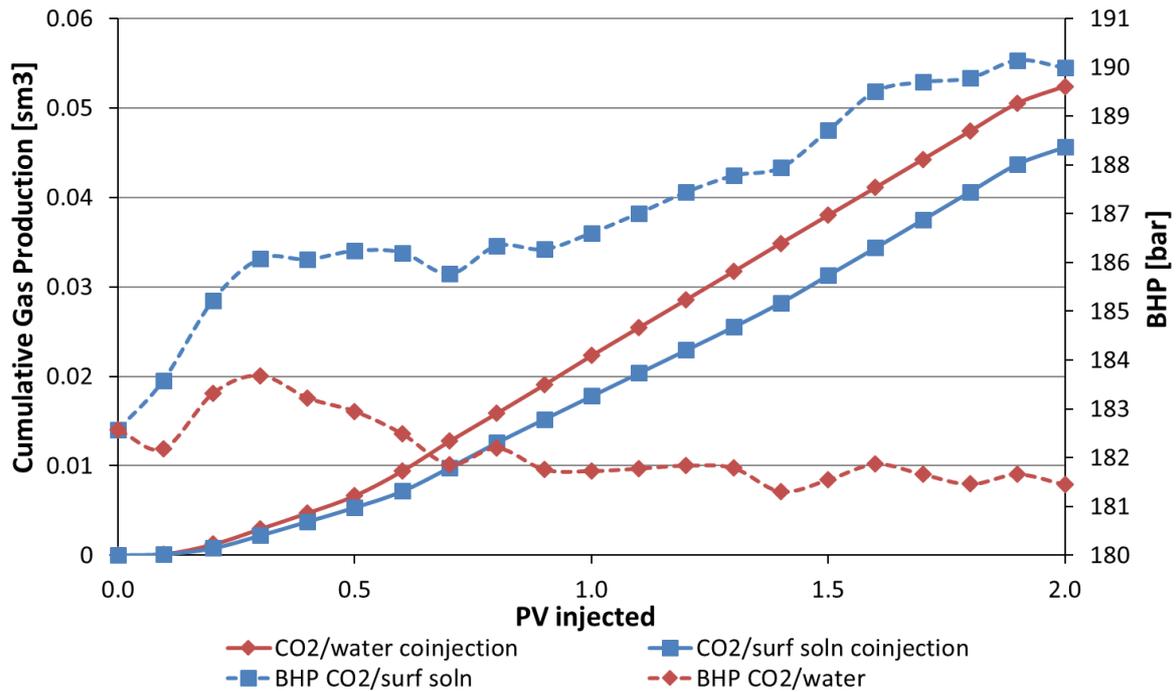
Fig 11 – Injection well pressure (dashed curves) and cumulative gas (CO₂) production (solid curves) for the base case with surfactant present (blue curve) and a case without surfactant present (red curves).

The injection well pressure was significantly lower for the case without surfactant compared to the base case with surfactant (Figure 11, red dashed curve). This indicated higher CO_2 mobility and increased CO_2 production in absence of foam (Figure 11, red solid curve). Analysis of liquid production showed the same cumulative volume of oil recovered in both cases (green curves, Figure 12), but additional water was produced when surfactant solution and CO_2 generated foam (blue dashed curve). Hence, a larger storage potential for CO_2 was obtained with CO_2 foam displacement. This corroborates the observations in Figure 5, where CO_2 storage was higher for multi-cycle SAG because of higher water displacement.

The similar volumes of oil produced with and without surfactant, demonstrated the dominance of miscible CO_2 injection over viscous displacement by foam (green curves, Figure 12). The core-scale model is consistent with laboratory observations indicating that miscibility and diffusion are the governing displacement forces in small core-scale systems. This creates a challenge when upscaling foam behavior to field as reservoir heterogeneity and gravity effects require mobility control by foam to improve macroscopic sweep.
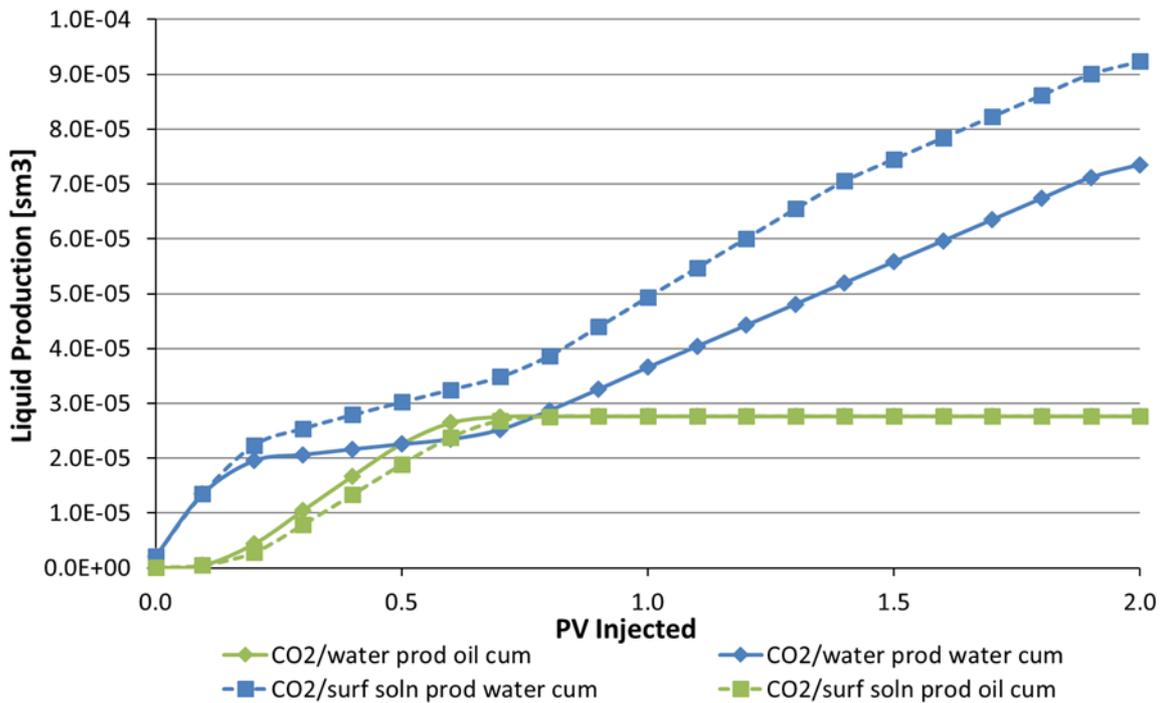
Fig. 12 – Cumulative liquid production during CO₂/water co-injection (solid curves) and CO₂/surfactant solution (dashed curves). Green curves correspond to cumulative oil produced and blue to cumulative water.

Conclusions

This work investigated various injections strategies (i.e. co-injection and SAG) for CO_2 foam mobility control, EOR and CO_2 storage to assist in the design of a CO_2 foam field pilot. The sensitivity study involved both experimental laboratory work and numerical analysis. Foam behavior in brine saturated systems was investigated to generate foam *in-situ* without the presence of oil. CO_2 foam EOR corefloods were run at first-contact miscible (FCM) conditions and multiple-contact miscible (MCM) conditions using *n*-Decane and crude oil, respectively, after waterflooding. Key findings from this work were:

- Multi-cycle SAG showed the highest apparent viscosity foam of 120.2 cP during *in-situ* CO_2 foam stability scans compared to single-cycle SAG (18.2 cP) and co-injection (56.0 cP) without oil present, and for CO_2 foam EOR at FCM conditions (100.7 cP).
- Incremental oil recoveries during tertiary CO_2 foam injections were on average 30.6% OOIP for all injection strategies with and without surfactant at both FCM and MCM conditions. At MCM conditions, CO_2 foam was not generated as a result of wettability alteration and foam destabilization in presence of crude oil.
- A validated numerical core-scale model captured the observed foam behavior from laboratory corefloods. The foam model was not sensitive to grid resolution, which provided confidence in model robustness for upscaling foam transport to field scale simulations.
- CO_2 diffusion and miscibility with the oil in place were the main recovery mechanisms in favor of viscous displacement by CO_2 foam and corroborated by laboratory corefloods and numerical core-scale sensitivity studies on foam quality.
- CO_2 storage potential was 17.1% greater at FCM conditions, compared to MCM, due to improved CO_2 foam performance and CO_2 trapping by capillary forces in more water-wet core plugs. Core-scale simulations indicated high CO_2 storage potential with CO_2 foam because of improved water displacement.

17

The achieved foam apparent viscosity of multi-cycle SAG is encouraging for field application as foam is intended to divert flow from high permeability, well swept regions, to lower permeability un-swept regions of the reservoir. Optimal mobility control is required to counteract the impact of reservoir heterogeneities and gravity on macroscopic displacement. SAG can also provide better control on injectivity while operating close to formation fracture pressure with the ability to switch to CO_2 injection for foam dry-out. Reported oil recoveries, however, cannot be upscaled to represent field performance as CO_2 diffusion will have less effect on displacement at the length scales existing in field.

Acknowledgements

Nomenclature

API	American Petroleum Institute
BHP	bottom hole pressure
CCUS	carbon capture utilization and storage
EOR	enhanced oil recovery
FCM	first-contact miscible
f_g	gas fraction
K	permeability
MCM	multiple-contact miscible
MMP	minimum miscibility pressure
OOIP	oil originally in place
PV	pore volume
PVT	pressure, volume, temperature
$R_{f,tot}$	total recovery factor
$R_{f,WF}$	recovery factor by waterflood
$R_{f, CO2\ foam}$	recovery factor by CO_2 foam
SAG	surfactant-alternating-gas
S_{wi}	irreducible water saturation
S_o	oil saturation
S_{or}	residual oil saturation
t	time
u_g	gas superficial velocity
u_{liq}	liquid superficial velocity
μ_{app}	apparent viscosity
∇p	pressure gradient

References

Alcorn, Z.P., Fredriksen, S.B., Sharma, M., Rognmo, A.U., Føyen, T., Fernø, M.A. and Graue, A. 2018. An Integrated CO_2 Foam EOR Pilot Program with Combined CCUS in an Onshore Texas Heterogeneous Carbonate Field. SPE Improved Oil recovery Conference, 14-18 April, Tulsa, Oklahoma. SPE-190204-MS.

Ali-Menhali, A.S. and Krevor, S. 2016. Capillary Trapping of CO_2 in Oil Reservoirs: Observations in a Mixed-Wet Carbonate Rock. *Environmental Science and Technology* **50** (2016): 2727-2734.

Bernard, G.G. and Holm, L.W. 1964. Effect of Foam on Permeability of Porous Media to Gas. SPE Annual Fall Meeting, 11-14 October, Houston, Texas, US. SPE-983.

Bernard, G.G., Holm, L.W. and Jacobs, W.L. 1965. Effect of Foam on Trapped Gas Saturation and on Permeability of Porous Media to Water. SPE Annual Fall Meeting, 3-6 October, Denver, Colorado, US. SPE-1204.

Bernard, G.G., Holm, L.W. and Harvey, C.P. 1980. Use of Surfactant to Reduce CO_2 Mobility in Oil Displacement. *SPE Journal* **20** (4): 281-292.

Bond, D.C. and Holbrook, O.C. Gas Drive Oil Recovery Process. 1958. United States Patent Office. 30 December. Patented number 2,866,507.

Chou, S.I., Vasicek, S.L., Pisio, D.L., Jasek, D.E., Goodgame, J.A. 1992. CO2 Foam Field Trial at North Ward Estes. 67th SPE Annual Technical Conference and Exhibition, October 4-7, Washington, D.C..

Buckley, J.S. and Liu, Y. 1998. Some mechanisms of crude oil/brine/solid interactions. *Journal of Petroleum Engineering* **20** (3-4): 155-160.

Dhanuka, V.V., Dickson, J.L., Ryoo, W. and Johnston, K.P. 2006. High internal phase CO_2-in-water emulsions stabilized with a branched nonionic hydrocarbon surfactant. *Journal of Colloid and Interface Science* **298** (1): 406-418.

Eide, Ø., Haugen, Å., Svenningsen, S., Hoff, K., Ersland, G., Fernø, M.A. and Graue, A. 2012. Tertiary Liquid and Supercritical CO_2 injection in Chalk and Limestone at Strongly Water-Wet and Near Neutral-Wet Conditions. International Symposium of the Society of Core Analysts, 27-30 August, Aberdeen, Scotland.

Eide, Ø., Fernø, M.A., Alcorn, Z.P. and Graue, A. 2016. Visualization of Carbon Dioxide Enhanced Oil Recovery by Diffusion in Fractured Chalk. *SPE Journal* **21** (1): 112-120.

Emadi, A., Sohrabi, M., Farzaneh, S.A. and Ireland, S. 2013. Experimental Investigation of Liquid-CO2 and CO2-Emulsion Application for Enhanced Heavy Oil Recovery. SPE EAGE and SPE Europec, 10-13 June, London, United Kingdom. SPE-164798-MS.

Farajzadeh, R., Andrianov, A., Krastev, R., Hirasaki, G.J. and Rossen, W.R. 2012. Foam-oil interactions in porous media: Implications for foam assisted enhanced oil recovery. *Advances in Colloid and Interface Science* **183-184** (2012): 1-13.

Fernø, M A., Steinsbø, M., Eide, Ø., Ahmed, A., Ahmed, K. and Graue, A. 2015. Parametric study of oil recovery during CO_2 injections in fractured chalk: Influence of fracture permeability, diffusion length and water saturation. *Journal of Natural Gas Science and Engineering* **27** (2): 1063-1073.

Fredriksen, S.B., Alcorn, Z.P., Frøland, A., Viken, A., Rognmo, A.U., Seland, J.G., Ersland, G., Fernø, M.A. and Graue, A. 2018. Surfactant Pre-Floods during CO_2 Foam for Integrated Enhanced Oil Recovery in Fractured Oil-Wet Carbonates. SPE Improved Oil recovery Conference, 14-18 April, Tulsa, Oklahoma. SPE-190168-MS.

Graue, A., Tonheim, E. and Baldwin, B. 1994. Control and Alteration of Wettability in Low-Permeable Chalk". Proceedings of the 3rd International Symposium on Evaluation of Reservoir Wettability and its Effect on Oil Recovery, 21-23 September, Laramie, WY.

Graue, A., Viksund, B G. and Baldwin, B A. 1999. Reproducible Wettability Alteration of Low-Permeable Utcrop Chalk. *SPE Reservoir Evaluation and Engineering* **2** (02): 134-140. SPE-55904-PA.

Groenenboom, J., Kechut, N.I., Mar-Or, A., Vincent-Bonnieu, S. 2017. Foam Assisted WAG: Injection Strategies to Optimize Performance. SPE/IATMI Asia Pacific Oil & Gas Exhibition, 17-19 October, Jakarta, Indonesia. SPE-186991-MS.

Haugen, Å., Mani, N., Svenningsen, S., Brattekås, B., Graue, A., Ersland, G. and Fernø, M A. 2014. Miscible and Immiscible Foam Injection for Mobility Control and EOR in Fractured Oil-Wet Carbonates. *Transport in Porous Media* **104** (1): 109-131.

Harpole, K.J., Siemers, W.T. and Gerard, M.G. 1994. CO_2 Foam Field Verification Test at EVGSAU: Phase IIIC – Reservoir Characterization and Response to Foam Injection. SPE/DOE 9th Symposium on Improved Oil Recovery, 17-20 April, Tulsa, OK, USA.

Henry, R.L.; Fisher, D.R.; Pennel, S. P.; Honnert, M.A.: Field Test of Foam to Reduce CO2 Cycling. SPE/DOE Tenth Symposium on Improved Oil Recovery, April 21–24, Tulsa, OK, US. SPE/DOE 35402

Hirasaki, G. J. and Lawson, J.B. 1985. Mechanisms of Foam Flow in Porous Media: Apparent Viscosity in Smooth Capillaries. *SPE Journal* **25** (2): 176-190.

Hoefner, M.L. and Evans, E.M. 1995. CO_2 Foam: Results from Four Developmental Fields Trials. *SPE Reservoir Engineering* **10** (4): 273-281.

Holm, L.W. 1968. The Mechanisms of Gas and Liquid Flow Through Porous Media in the Presence of Foam. *Transactions* **243** (1968): 359-369.

Jadahunandan, P.P. and Morrow, N.R. 1995. Effect of Wettability on Waterflood Recovery for Crude-Oil/Brine/Rock Systems. *SPE Reservoir Engineering* **10** (1): 40-46.

Jian, B., Puerto, M C., Wehowsky, A., Dong, P., Johnston, K P. and Hirasaki, G J. 2016. Static Adsorption of an Ethoxylated Nonionic Surfactant on Carbonate Minerals. *Langmuir* **32** (40): 10244-10252.

Johnson, E.F., Bossler, D.P. and Naumann, V.O. 1959. Calculation of Relative Permeability From Displacement Experiments. Trans. AIME 1959, *216*, 370.372.

Jones, S.A., Laskaris, G., Vincent-Bonnieu, S., Farajzadeh, R. and Rossen, W.R. 2016. Surfactant Effect on Foam: From Core Flood Experiments To Implicit-Texture Foam Model Parameters. SPE Improved Oil Recovery Conference, 11-13 April, Tulsa, Oklahoma. SPE-179637-MS.

Kahrobaei, A., Vincent-Bonnieu, S. and Farajzadeh, R. 2017. Experimental Study of Hysterisis behavior of Foam Generation in Porous Media. *Nature* **7** (8986): 1-9.

Latil, M. *Enhanced Oil recovery*. 1980. Paris: Editions Technip.

Newton, L.E. and McClay, R.A. 1977. Corrosion and Operational Problems, CO2 Project, Sacroc Unit. SPE Permian Basin Oil and Gas Recovery Conference, 10-11 March, Midland, Texas. SPE-6391-MS.

Nzekwu, B.I. and Bennion, D.W. 1987. Mobility control in dynamic gravity segregation flow systems. *Journal of Canadian Petroleum Technology* **26** (4): 80-87. JCPT87-04-08.

Ransohoff, T.C. and Radke, C.J. 1988. Mechanisms of Foam Generation in Glass-Bead Packs. *SPE Reservoir Engineering* **3** (2): 573-858. SPE-15441-PA.

Rognmo, A.U., Fredriksen, S.B., Alcorn, Z.P., Sharma, M., Føyen, T., Eide, Ø., Graue, A. and Fernø, M. 2018. Pore-to-Core EOR Upscaling for CO2-foam for CCUS. SPE EUROPEC featured at the 80th EAGE Annual Conference and Exhibition, 11-14 June, Copenhage, Denmark. SPE-190869-MS.

Schramm, L.L. and Novosad. 1992. "The destabilization of foams for improved oil recovery by crude oils: Effect of the nature of the oil". *Journal of Petroleum Science and Engineering* **7** (1-2): 77-90.

Schramm, L.L. and Mannhardt, K. 1996. The effect of wettability on foam sensitivity to crude oil in porous media". *Journal of Petroleum and Engineering* **15** (1): 101-113.

Shan, D. and Rossen, W.R. 2002. Optimal Injection Strategies for Foam IOR. SPE/DOE Improved Oil Recovery Symposium, 13-17 April, Tulsa, Oklahoma. SPE-75180-MS.

Sharma, M., Alcorn Z.P., Fredriksen, S.B., Fernø, M., Graue, A. 2017. Numerical Modeling Study for Designing CO2 Foam Filed Pilot. EAGE IOR Symposium, 24-27 April, Stavanger, Norway.

Steinsbø, M., Brattekås, B., Fernø, M.A., Ersland, G. and Graue, A. 2014. Supercritical CO_2 Injection for Enhanced Oil Recovery in Fracture Chalk. International Symposium of the Society of Core Analysts, 8-12 September, Avignon, France. SCA2014-092.

Steinsbø, M., Brattekås, B., Ersland, G., Bø, K., Opdal, I.E., Tunli, R., Graue, A. and Fernø, M.A. 2015. Foam as Mobility Control for Integrated CO2-EOR in Fractured Carbonates. 18th European Symposium on Improved Oil Recovery, 14-16 April, Dresden, Germany.

Suffridge, F.E., Raterman, K.T. and Russell, G.C. 1989. Foam Performance Under Reservoir Conditions. 64th SPE ATCE, 8-11 October, San Antonio, Texas, US. SPE-19691-MS.

Persoff, P., Radke, C. J., Preuss, K., Benson, S.M. and Witherspoon P.A. 1991. A Laboratory Investigation of Foam Flow in Sandstone at Elevated Pressure. *SPE Reservoir Engineering* **6** (3): 365-378. SPE-18781-PA.

Prud'homme, R K. and Khan, S A. 1996. *Foams, Theory, Measurements, and Applications*. New York: Marcel Dekker Incorporated.

Vikingstad, A. K., Skauge, A., Høiland, H. and Aarra, M. 2005. Foam-oil interactions analysed by static foam tests. *Colloids and Surfaces A: Physicochem. Eng. Aspects* **260** (2005): 189-198.

Paper V: CO_2 Foam Field Pilot Test for EOR and CO_2 Storage in a Heterogeneous Carbonate Reservoir: Operational Design, Data Collection and Pilot Monitoring Program

Alcorn, Z.P., Sharma, M., Fredriksen, S.B., Rognmo, A.U., Fernø, M.A., Graue, A.

We H 04

CO2 Foam Field Pilot Test for EOR and CO2 Storage in a Heterogeneous Carbonate Reservoir: Operational Design, Data Colle

Z.P. Alcorn* (University of Bergen), M. Sharma (The National IOR Centre of Norway, University of Stavanger), S.B. Fredriksen (University of Bergen), A.U. Rognmo (University of Bergen), M. Fernø (University of Bergen), A. Graue (University of Bergen)

Summary

A field demonstration test using CO2 foam for enhanced oil recovery (EOR) is being implemented in a heterogeneous carbonate reservoir in the Permian Basin of Texas. CO2 as an oil recovery agent part of carbon capture, utilization, and storage (CCUS) has gained recent attention due to growing concerns regarding greenhouse gas emissions. Current CO2 flood performance suffers due to an unfavorable mobility ratio between injected CO2 and reservoir fluids resulting in poor macroscopic sweep efficiency. Foam aims to mitigate the technical challenges of ongoing CO2 injection by improving macroscopic sweep efficiency and oil recovery while storing CO2. As part of a field pilot research program, this study presents project and operational design, baseline data collection program, and pilot monitoring to mitigate the technical challenges with current CO2 injection and verify foam mobility control and CO2 storage. Pilot performance is assessed with the data collection program and includes a tracer program to characterize interwell connectivity, time lapse cross well seismic to improve the reservoir characterization and monitor saturations, injection profiles and fall-off tests to determine zones of injection and injection pressure, and daily measurements of rate and pressure at various stages throughout pilot operation.

Introduction

A field demonstration test using CO_2 foam for enhanced oil recovery (EOR) is being implemented in a heterogeneous carbonate reservoir in the Permian Basin of west Texas. CO_2 as an oil recovery agent part of carbon capture, utilization, and storage (CCUS) has gained recent attention due to growing concerns regarding greenhouse gas emissions. Current CO_2 flood performance suffers due to an unfavorable mobility ratio between injected CO_2 and reservoir fluids resulting in poor macroscopic sweep efficiency from CO_2 channelling through high permeability zones. Foam aims to mitigate the technical challenges of ongoing CO_2 injection by improving macroscopic sweep efficiency and oil recovery while storing CO_2. Earlier CO_2 foam field pilot tests report mixed results most often due to difficulty monitoring the CO_2, surfactant, and water system in the reservoir and attributing additional oil displacement specifically to CO_2 foam (Chou et al., 1992; Stephenson et al., 1993; Martin et al., 1992, 1995). As part of an ongoing field pilot research program, this study presents project and operational design, baseline data collection program, and pilot monitoring to mitigate the technical challenges with current CO_2 injection and verify foam mobility control.

East Seminole field produces from the San Andres unit, a heterogeneous cyclical carbonate reservoir with 110 ft of net pay. The main reservoir zones are predominately subtidal dolostone deposits interbedded with, non-reservoir quality, shaley mudstones. Hydrostatic reservoir pressure was 2500 psi at an average bottom hole temperature of 104°F (40°C) and a formation fracture pressure of 3900 psi. The current reservoir pressure is 3200 psi, well above the 1500 psi minimum miscibility pressure (MMP) of CO_2 and crude oil. The field has produced from the San Andres main producing zone (MPZ) for over 50 years, through primary and secondary waterflood recovery. As seen in other areas of the Permian Basin, tilted fluid contacts presumed from basin activity and/or a breach of seal have created a deeper residual oil zone (ROZ) which is now an economically attractive target for CO_2 EOR (Melzer, 2006). CO_2 has been injected into the MPZ and ROZ in an inverted 40 acre 5-spot pattern since October 2013. Initial production response to miscible CO_2 injection was favorable as oil production increased from 5 bbl/day to 35 bbl/day in the peripheral producers. However, production rates soon dropped and stabilized around 20 bbl/day while gas production continued to rise. In addition, two production wells experienced rapid CO_2 breakthrough compared to other peripheral producers, suggesting the presence of high permeability zones and/or factures transporting the bulk of the CO_2 resulting in poor CO_2 utilization, high producing gas oil ratio (GOR) and CO_2 cycling.

In layered reservoir systems, mobility control is a form of conformance control technology where foams are capable of inhibiting CO_2 flow into high permeability regions and redirecting it into less permeable, higher oil saturated zones impacting in-depth fluid displacement (Sydansk and Romero-Zeron, 2011). Thus, the current CO_2 injector has been selected for a foam treatment to divert flow from high permeability layers into low permeability, unswept regions of the reservoir to improve sweep efficiency, reduce GOR, and improve CO_2 utilization.

Project and operational design presents project objectives and includes foam system design, foam injection schedule, and necessary surface facility modifications and additions. The data collection program aims to establish baseline from ongoing CO_2 injection to characterize interwell connectivity, determine zones of injectivity, and monitor production and injection. Baseline values serve as the basis for assessing pilot performance and verifying CO_2 diversion from high permeability zones resulting in improved sweep efficiency and mobility control.

Project and Operational Design

Project design is guided by objectives which have been identified by members of a multidisciplinary team. The objectives demonstrate the balance between running a controlled experiment at field scale, for future use of foam, and making the foam process economically feasible by reducing operating costs. The foam treatment is designed to mitigate the technical challenges with current CO_2 injection to increase field performance by improving sweep efficiency of CO_2 and increasing incremental oil

production, reducing producing GOR and CO_2 cycling, improving CO_2 utilization, and investigating associated CO_2 storage.

To achieve the objectives, the foam system was designed to maximize the success of the foam generation in the reservoir through minimizing surfactant adsorption and optimizing surfactant concentration and foam strength, considering field economic limits. A number of important foam system design parameters can be measured in the laboratory when preparing for a foam field pilot. These include (but are not limited to) surfactant adsorption levels, surfactant concentration (soluble in injection brine), and foam quality (fraction of CO_2 to fraction of liquid). A surfactant was screened and selected based upon minimal adsorption on dolomite (Jian, et al. 2016). CO_2 foam EOR corefloods indicate that a surfactant concentration of 0.5 wt% is sufficient to reduce gas mobility by a factor of 340, compared to CO_2 at the same conditions, and recovers significant oil after waterflood (35% OOIP). Foam quality scans showed the strongest foam at foam quality of 70%, when considering field scale economic limits (Alcorn et al., 2018). Laboratory measured foam parameters have been recommended for field testing and are used in injection design.

Foam is typically injected into a reservoir via surfactant alternating gas (SAG) or simultaneous injection of gas and surfactant solution (coinjection). Operational constraints control some aspects of field injection design method. For instance, coinjection of CO_2 and surfactant solution brine can create carbonic acid which is known to cause corrosion in many standard oil field casings and pipelines (Matthews, 1989). In addition, pressure increases during coinjection often lead to abrupt increases in bottom hole injection pressure, problematic when operating close to the fracture pressure of the formation. Therefore, it is preferred to inject alternating slugs of CO_2 and surfactant solution to minimize corrosion and offer more flexibility when injection pressure increases. Multiple cycle SAG and rapid SAG emerged as the two most attractive injection strategies based upon the need to limit CO_2 channeling through high permeability zones, mobility control to increase areal sweep efficiency, reduce the producing GOR, and preference to control foam quality.

Data Collection Program and Pilot Monitoring

Considering SAG injection, after CO_2 flood, efforts were made to establish baseline in the field from ongoing CO_2 injection to characterize interwell connectivity and injectivity. Further baseline data collection includes accurately monitoring injection and production well pressure and rates and improving current knowledge of reservoir saturations. Data is collected at various stages of baseline and pilot injection to assess foam performance (**Table 1**). Overall, data collection and pilot monitoring can be divided into three distinct phases: baseline data collection for ongoing CO_2 injection (pre SAG), pilot phase (SAG) monitoring of rates, pressures, and injectivity, and pilot assessment to verify mobility control and improved sweep efficiency (post SAG).

Stage	Pre SAG (baseline)	Pilot Phase (3 SAG cycles)						Post SAG
Slug	Ongoing CO_2 Injection	Surfactant	CO_2	Surfactant	CO_2	Surfactant	CO_2	
Tracers	CO2 (L14)							
Injection Profiles (L14)	X		X					X
Fall off test	X		X					X
Crosswell Seismic (L14/L25)	X							X

Table 1. Schedule of data to be collected to establish baseline from current CO_2 injection (pre SAG), monitoring pilot phase operations (SAG), and assessment of pilot performance (Post SAG). A three cycle, multiple cycle SAG is assumed.

An interwell tracer test (IWTT) was implemented to characterize interwell connectivity. Non-radioactive tracer was injected into the selected pilot well (IL-1) to determine breakthrough time and the volume of the reservoir contacted by the current CO_2 injection. All peripheral producers were

monitored on a 10 month sampling schedule first focusing on two of the wells which had most rapid CO_2 breakthrough (PL-1 and PL-4, **Figure 1**). Samples from PL-1 and PL-4 were collected twice a week for the first month of tracer injection with frequency decreased to once a week, thereafter. Once breakthrough was observed in PL-1 and PL-4, sampling began for the remaining peripheral production wells. Tracer breakthrough times and volume of reservoir contacted give baseline measurements to compare foam injection.
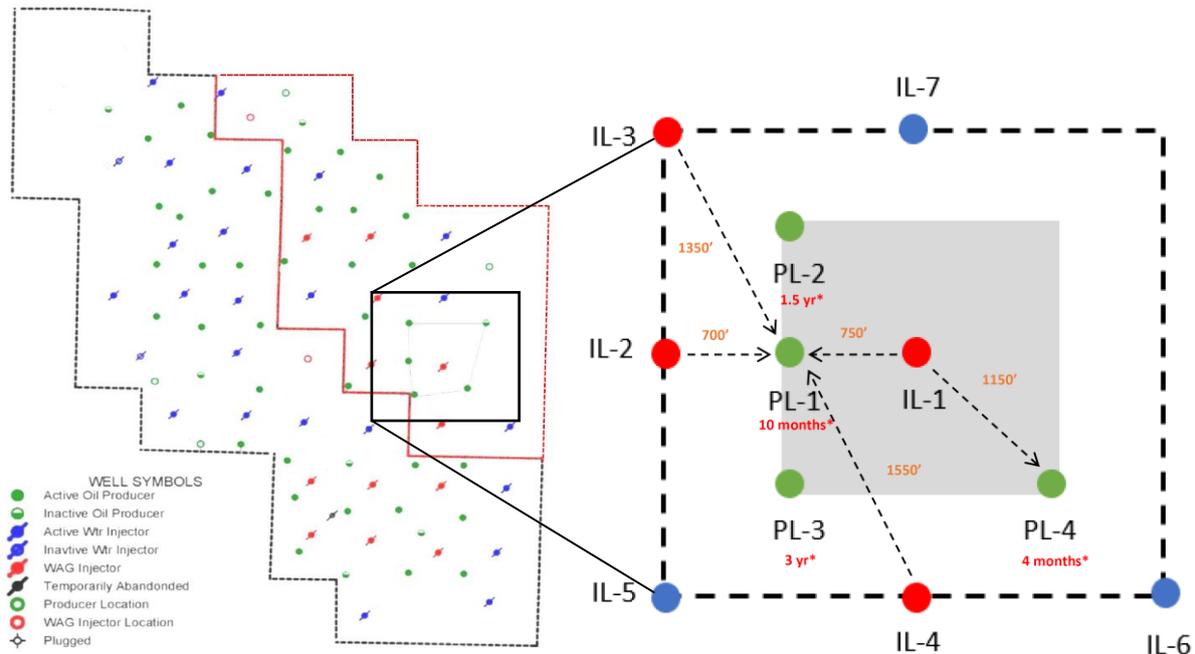
Figure 1. Field map showing selected pilot area location, at right. Shaded area represents selected inverted 5-spot pattern for the pilot test. Interwell distances and breakthrough time are shown for selected wells. Foam will be injected into IL-1 and all peripheral production wells (shown in green) will be monitored during baseline data gathering and pilot test.

Five injection profiles have been taken at various stages throughout CO_2 injection operations in PL-1. Profiles indicate good injectivity in only the lower section of the MPZ with injectivity in the ROZ improved with time. The most recent injection profile, taken July 2017, showed 65% of injection into the MPZ and 35% into the ROZ. Foam is intended to divert flow from the previously swept zones and reach oil in the ROZ which has not been contacted by CO_2. Thus, additional injection profiles taken pre SAG, after the first complete SAG cycle, and post SAG will provide information on near wellbore fluid diversion from the foam treatment.

Limited historical information is available to provide insight on injection well bottom hole pressure (BHP). Currently IL-1 injects at a tubing head pressure (THP) of 1900psi. Fall-off test are planned pre SAG, to establish baseline CO_2 injection BHP, and post SAG to measure pressures from foam injection. Time-lapse cross well seismic has been considered to improve current knowledge of reservoir saturations and enhance the reservoir characterization. More importantly, time lapse seismic can provide CO_2 saturation monitoring between the injection well and peripheral producers. Seismic applications used in conjunction with tracer travel time information offer the best case scenario for measuring baseline values and assessing pilot performance. In addition to tracer technology, injection profiling, fall-off tests, and time lapse seismic, daily rates and pressures will be monitored during the baseline CO_2 injection and pilot operations.

Conclusions and Expected Outcomes

A data collection and monitoring program for a CO_2 foam for mobility control and EOR field pilot is proposed to establish baseline from ongoing CO_2 injection, monitor pilot operations, and assess CO_2 foam's impact on sweep efficiency, incremental oil production, CO_2 cycling and utilization, and reservoir pressure. Current CO_2 operations suffer from the poor mobility ratio between CO_2 and reservoir fluids resulting in poor macroscopic sweep efficiency due to CO_2 channeling through high permeability zones. A foam treatment has been selected to alleviate the technical challenges of ongoing CO_2 injection by improving macroscopic sweep efficiency and oil recovery, while storing CO_2.

The data collection program is used to assess pilot performance and includes a tracer program to characterize interwell connectivity, time lapse cross well seismic to improve the reservoir characterization and monitor saturations, injection profiles and fall-off tests to determine zones of injection and injection pressure, and daily measurements of rate and pressure at various stages of the current CO_2 injection (pre SAG), during SAG, and post SAG. Expected outcomes from the baseline data collection program and foam treatment are: increased injection pressure during SAG, change in injection profiles showing diversion of fluids into unswept reservoir zones, measurable change in CO_2 saturations, reduced producing GOR in peripheral production wells, delayed CO_2 breakthrough during foam injection, improved sweep efficiency and increased incremental oil recovery, and verification of CO_2 storage which provides more sustainable oil production.

References

Alcorn, Z.P., Fredriksen, S.B., Sharma, M., Rognmo, A.U., Føyen, T.L., Fernø, M.A., and Graue, A. [2018]. An Integrated CO_2 Foam EOR Field Pilot Program with Combined CCUS in an Onshore Texas Heterogeneous Carbonate Field. Accepted and to be presented at the SPE Improved Oil Recovery Conference, Tulsa, OK USA. 14-18 April 2018.

Chou, S.I., Vasicek, S.L., Pisio, D.L., Jasek, D.E., Goodgame, J.A. [1992] CO2 Foam Field Trial at North Ward Estes. Presented at the 67th SPE Annual Technical Conference and Exhibition, Washington, D.C., October 4-7, 1992.

Jian, G., Puerto, M.C., Wehowsky, A., Dong, P., Johnston, K.P., and Hirasaki, G.J. [2016]. Static Adsorption of an Ethoxylated Nonionic Surfactant on Carbonate Minerals. *Langmuir*, 10244-10252

Martin, F.D., Heller., J.P., Weiss, W.W., and Tsau, J.S. [1992]. CO2-Foam Field Verification Pilot Test at EVGSAU Injection Project Phase 1: Project Planning and Initial Results. Presented at the SPE Improved Oil Recovery Conference, Tulsa, Oklahoma, USA, 22-24 April, 1992. SPE/DOE-24176

Martin, F.D., Stevens, J.E. and Harpole, K.J. [1995]. CO2 Foam Field Test at the East Vacuum Grayburg/San Andres Unit. *SPE Reservoir Engineering*, November 1995, p. 266-272

Matthews, C.S. [1989] in Enhanced Oil Recovery II Processes and Operation, Elsevier Science Publication Company, eds. E.C. Donaldson, G.V. Chilingarian, and T.F. Yen, New York, 1989, p. 129

Melzer, S., Koperna, G.J:, and Kuuskraa, V.A. [2006]. The Origin and Resources Potential of Residual Oil Zones. Presented at the 2006 SPE Annual Conference and Exhibition, San Antonio, Texas, USA., 24-27 September 2006. SPE-102964

Stephenson, D.J., Graham, A.G., Luhning, R.W. [1993]. Mobility Control Experience in the Joffre Viking Miscible CO2 Flood. *SPE Reservoir Engineering*, August 1993, p. 183-188.

Sydansk R.D. and Romero, L. [2011] Reservoir Conformance Improvement, Society of Petroleum Engineers, Richardson, TX USA

Paper VI: Model Calibration for Forecasting CO₂-Foam EOR Field Pilot Performance in a Carbonate Reservoir

Sharma, M., Alcorn, Z.P., Fredriksen, S.B., Rognmo, A.U., Fernø, M.A., Skjæveland, S.M., Graue, A.

Model Calibration for Forecasting CO_2-Foam EOR Field Pilot Performance in a Carbonate Reservoir

M. Sharma [a], Z. P. Alcorn [b], S. B. Fredriksen [b], A. U. Rognmo [b], M. A. Fernø [b], S. M. Skjæveland [a] and A. Graue [b]
[a] The National IOR Centre of Norway, University of Stavanger
[b] Department of Physics and Technology, University of Bergen

Abstract

Application of foam has been found to mitigate challenges associated with field-scale CO_2 floods for Enhanced Oil Recovery (EOR) by providing in-depth mobility control. The field pilots that have been run so far have shown varying results, inferred mainly from interwell tracer studies and production data analysis. A research collaboration has been setup to advance the technology of using foam as mobility control agent for CO_2 EOR, with focus on integrated reservoir modelling to assist technology transfer to high cost environment. A heterogeneous carbonate reservoir onshore in west Texas, USA has been selected for field trial. The reservoir has been waterflooded for more than fifty years, and a significant part of it has been on continuous CO_2 injection for last five years. An inverted five-spot pattern, which had rapid CO_2 breakthrough in adjacent producers and is currently recycling significant amounts of CO_2, has been selected for the study. The pilot is planned for two years with surfactant-alternating-gas injection in the first year, followed by CO_2 injection in the next year.

A reservoir model was created by integrating available static and dynamic information. Since the measurement of static information and production performance is usually imprecise, even the most carefully constructed models do not exactly represent reality. In this paper, we present a workflow that was used to calibrate the reservoir model to historical data for practical forecasting, which takes into account a wide range of uncertainties caused by inaccessibility of information. Laboratory studies were performed with reservoir cores, fluids and selected surfactant to obtain the base values of foam model parameters. As an output, distributions for Key Performance Indicators such as cumulative oil production and CO_2 retention were generated for the proposed pilot to guide further decision making.

1. Introduction

The miscible and immiscible CO_2 flood technology for Enhanced Oil Recovery (EOR) has evolved over last four decades in terms of laboratory studies, numerical modelling and field operations. A large number of commercial CO_2 floods have been operated since the first commercial CO_2 injection in SACROC Unit in 1972 (Merchant 2010). Some of these projects are still operational with CO_2 injection reaching over 80% HCPV and tertiary recovery ranging between 15 to 20% of oil initially in-place (OIIP). Based on the knowledge gained from field-scale projects, it has been realised that a substantial volume of reservoir remains unswept during CO_2 floods leading to lower oil recovery compared to recovery at core-scale. This is mainly because of low density and viscosity of CO_2 and reservoir heterogeneity resulting in viscous fingering, gravity segregation and poor sweep (Jarrell et al. 1990). Several technologies have been tested to improve CO_2 flood performance including near well polymer or gel treatment, cementing for zonal isolation, alternating CO_2 injection with water, and smart completions with inflow control valves (Sharma et al. 2016), with limited to moderate success for in-depth mobility control.

The laboratory studies and field pilots conducted so far confirm the viability of foam for CO_2 mobility control away from the injector (Heller 1994). Also, it offers a better control during field operations because of dynamic state of foam, allowing its effect to be completely reversed if required. Previous field trials with foam (Heller et al. 1985, Holm and Garrison 1988, Jonas et al. 1990, Chou et al. 1992, Hoefner and Evans 1995, Harpole and Hallenbeck 1996, Sanders et al. 2012, Mukherjee et al. 2016) have demonstrated the benefits of this technology to variable extent, with a few meeting all planned objectives and making a good return on investment.

A research collaboration has been setup between industry and universities to design and execute a field pilot with foam in a heterogeneous field onshore Texas, to better understand the large-scale displacement process using integrated reservoir modelling. The secondary objective is to demonstrate the application of foam in improving CO_2 storage efficiency through selective isolation of high permeability regions, and mobilization of water from pore space to allow more room for CO_2 than in conventional injection schemes. The field selected for the pilot study is located onshore in Permian basin, west Texas. It came online in early 1940s and produced 12% of OIIP until late 1960s. Waterflood began in early 1970s with wells on an 80-acre pattern. The field was developed throughout early 1980s with infill drilling to establish 40-acre peripheral waterflood patterns. However, with a low primary plus secondary recovery of only 22% of OIIP by late 1980s, the operator realized the need to reduce pattern size. An infill program was run to develop field on a 20-acre five spot pattern. Infill drilling yielded excellent results with increase in oil production rate from 400 STB/D to 1200 STB/D. However, a steep decline in production and high residual oil saturations in the reservoir rock after waterflood indicated the potential for tertiary oil recovery. Tertiary CO_2 injection for EOR started in eastern part of the field in October 2013 to target remaining oil, and further expanded to other patterns which has resulted in an increase in oil production rate from 250 STB/D in October 2013 to 800 STB/D in March 2018 (**Fig. 1**). The peripheral producers of most of the patterns, however, have already experienced CO_2 breakthrough, with breakthrough occurring as early as within four months from start of CO_2 injection in nearby injectors. The reservoir has poor volumetric sweep due to reservoir heterogeneity and unfavourable mobility of CO_2, which makes it a good candidate to test foam for improving sweep and reducing CO_2 recycling.

After discussions with the field operator, an inverted five-spot pattern around well 1 (**Fig. 2**) was selected for injection for field trial, which has representative geology, good well injectivity, short CO_2 travel time and high gas-oil ratio. The reservoir exhibits large vertical heterogeneity with Dykstra-Parsons permeability variation coefficient of 0.79 and Lorenz coefficient of 0.84. Because of short interwell distances of around 700 feet, the reservoir is expected to respond to foam in a much shorter time interval.

This paper presents a workflow for history matching previous waterflood and CO_2 injection to obtain a revised estimate of uncertainty about the static characteristics and dynamic behaviour of the field. Laboratory coreflood experiments performed with reservoir core and selected surfactant under representative conditions were used to characterize foam behaviour. The uncertainties in modelling foam behaviour were added to the uncertainties in the reservoir model to obtain reliable forecast for the pilot performance in terms of distributions for Key Performance Indicators (KPIs) like cumulative oil production and CO_2 retention.

2. Methodology

2.1. History Matching Approach

To assist the numerical modelling work for pilot design, a three-dimensional geologic model was setup for a sector which included the wells in the pilot area, and peripheral water and CO_2 injectors. Wells 1 to 11 (Fig. 2) were included in the sector model which had 28 layers and

around 70,000 active cells with areal dimensions of 50 feet. The plan is to inject surfactant in well 1 and observe the response at wells 3 and 5.

Limited core and log data was available for geologic modelling. The information was used to define structural and stratigraphic framework, and identify three petrophysical classes (Wang et al. 1998). The main reservoir zones are composed of grainstones and packstones (Petrophysical class 1 and 2) interbedded with low permeability shaley mudstones (Petrophysical class 3). The range in permeability values for class 1 and 2 arises from dissolution of carbonate material resulting in high local values of permeability. The layers – 4, 8, 10 and 16, which correspond to the grain dominated facies of Petrophysical class 1, were input deterministically after the initial geomodel was built. Petrophysical properties for these 'Enhanced Permeability Zones' were assigned a constant value throughout the layer. The details on the geologic and reservoir modelling are available in Sharma et al. (2017) and Alcorn et al. (2018). **Fig. 3** shows the permeability distribution in the initial geologic model for a cross-section connecting wells 8, 3, 1, 5 and 10, highlighting the vertical heterogeneity in the reservoir.

The reservoir model was then tuned to available production data in two stages: Phase-I for historical water injection from January 1971 until September 2013, and Phase-II for historical CO_2 injection from October 2013 until March 2018. The historical injection rates for wells 6, 7, 8, 9, 10 and 11 were adjusted corresponding to the area the well was feeding in the sector model for simulation purpose, as shown in **Fig. 4**. Since the well status has changed during these phases, a prefix of 'P','WI' or 'GI' has been used in this paper to denote the state of the well as producer, water injector or CO_2 injector, respectively.

It was realized that large uncertainties exist in modelling inputs because of absence of seismic information, limited core availability, gaps in production data and limited information on well operations or workovers. Since the main objective of reservoir modelling was to create a reliable forecast that reflects all the available information, the geologic model was history matched to reduce the range in uncertainties before using it for pilot design. Integration of dynamic data requires solution of flow equations several times in an iterative fashion. The workflow that was used for assisted history matching is outlined in **Fig. 5**. The workflow transforms uncertainty about input information into an ensemble of predictions that describes the uncertainty in production. As we proceeded, initial views about uncertainties were revised to get a reasonable fit to observations using more than one set of values for model parameters. The history matching results are presented in section 3, which were obtained by following the steps below:

2.1.1. Setting up an Uncertainty Matrix

To begin with, a matrix was setup with uncertainty parameters (UPs) after discussion with different stakeholders, which listed important model parameters, their ranges and distributions. The framing discussion was based on the review of the prior knowledge of the field including previous uncertainty work about volumetrics, and the available historical data.

2.1.2. Setting up the Objective Function

The progress of the history matching process depends on the quality of the setup of the objective function, which is the misfit or mismatch between the observed data and the simulator response. The objective function is minimized for a set of uncertain parameters using optimisation algorithms. Since different data types carry different values during model calibration, it was necessary to identify whether each type of data should be included as a target for matching or simply monitored. Also, it is important to place more emphasis on data which has a lower error

associated with the measurements. The available historical data was therefore evaluated to eliminate outliers. Judgements about the weighting of different data types were made, and misfits for different wells and data types were used to obtain the global objective function value as

$$GV = \sum_i \sum_j W_i \, W_j \left(\frac{Sim_i^j - Obs_i^j}{Std_i} \right)^2 \tag{1}$$

where GV is the global value, i refers to the mismatch parameter (MP) like observations of oil rate at a well, j refers to an individual time step that contains an observation, W_i is the global weight factor of MP i which defaults to 1, W_j is the weight of timestep j which defaults to equal weighting for all time steps, Sim_i^j refers to the simulated value of observation i at time j, Obs_i^j refers to the observed history match value of parameter i at time j and Std_i is the standard deviation of MP i.

2.1.3. Model Validation

A well set up assisted history matching workflow has advantages over trial and error approaches, provided the initial-set up is good and the range of UPs is validated. The validation stage involved:
- Sensitivity analysis: Running simulations by varying one variable at a time to get relative impact of each UP on various MPs in form of Tornado plots.
- Boundary analysis: Running simulations using Plackett-Burmann (PB) sampling, where low values of some UPs were combined with high values of other UPs. This was used to ensure that simulations based on the input range of UPs cover measured data and match shape for simulated cases. A wider range of the solution space gets sampled with the Plackett-Burmann experiment compared to Latin Hypercube runs, and is therefore an efficient (in terms of simulations required) method to validate UPs' ranges.

2.1.4. Selecting Starting Points for Assisted History Matching

Once the model was validated by adjusting range of UPs and adding more UPs if required, Latin Hypercube (LHC) sampling technique was used to generate approximately 10 times the number of UPs simulations. Pareto plots and Correlation charts were generated based on LHC runs to understand the relation among MPs and dependence of MPs on UPs. Multiple start points were selected, with large initial step sizes for UPs to initialize an efficient search process and obtain a range of alternate HM solutions.

2.1.5. Completing History Matching Phase

Evolution strategy (ES) was used for assisted history matching, which is one implementation of an evolutionary algorithm (Back 1996, Schulze-Riegert et al. 2002) with local and global search capabilities. Evolutionary algorithms are widely used to solve complex optimization problems. They use only the objective function value to determine new search steps and do not require any gradient information. They can be used in cases where traditional algorithms fail because of significant non-linearities or discontinuities in the search space. In ES, transition functions describe a process of transforming a set of candidate solutions into a subsequent one by applying mutation operators and selection criteria. In addition to a sufficient match quality, the other criteria that were found important for a successful HM were to have sampled a wide

enough selection from the input UP distribution and to have obtained as many alternative solutions as realistically possible.

2.2. Prediction Approach

2.2.1. Reservoir Management Plan

The current reservoir pressure is 600 to 800 psi higher than hydrostatic pressure (2300 psi). The injectors operated at flowing bottom-hole pressure constraint of 3950 psi, close to fracture pressure, until March 2018. The reservoir management plan going forward is to inject at a lower rate at levels almost half of historic injection rate. For the sector model, it is equivalent to reduction in injection rate from 0.1 pore volume (PV) a year to 0.05 PV a year. A disposal well, completed in a separate deeper reservoir, is being used to depressurize the reservoir before start of pilot. The gas injectors, after conversion from either a producer or a water injector, have been on continuous CO_2 injection in past. The revised plan is based on water alternating gas (WAG) injection with water injection for one year followed by CO_2 injection for six months. Based on discussions with operator, it has been agreed to implement surfactant alternating gas (SAG) injection in the chosen injector. Optimization of slug sizes for WAG and foam pilot was not considered for this part of the study.

2.2.2. Transition to Prediction Phase

The well controls typically changes from controlling on set rates (voidage rate, liquid rate, oil rate) for history matching to controlling on set pressures (normally tubing-head pressure) for prediction, which introduces a discontinuity in well performance. This can be avoided by calibrating well productivities when starting predictions to ensure smooth transition between the history match phase and the prediction phase. Where a single history matched model is being sought, this is usually overcome by adjusting well productivity index (PI) multipliers or skin to reproduce flowing bottom-hole pressure and rate behaviour. The process however is extraordinarily time consuming, particularly if a large number of wells are involved. Where multiple history matched models are sought, such a process is impractical because of the engineering intervention required in each model.

We handled this issue of a smooth and physically reasonable transition into prediction by applying the same process to the prediction as applied during history matching. The injectors will operate on a constant injection rate at levels almost half of historic injection rate, which is used as primary constraint for prediction. Well injectivity was tuned to reduce the misfit between observed data and model's response before using flowing bottom-hole pressure as secondary constraint. All producers in the field have been on artificial lift for a very long time, with no flowing bottom hole pressure data available. The producers are kept on constant liquid rate at same level reported on last step in historic data, assuming no modification in the lift capacity during prediction phase.

2.2.3. Modelling Foam Rheology

There are two general approaches available to model foam rheology and its effect on gas flow in porous media. The Explicit-texture approach (Falls et al. 1988, Rossen et al. 1999), allows direct simulation of foam generation, propagation, and coalescence, which in turn, control the changes in the gas mobility and pressure gradient. The Implicit-texture approach (Cheng et al. 2000¸ Alvarez et al. 2001), uses an empirical relation to capture the effect of surfactant concentration, water saturation, oil saturation and shear thinning due to flow velocity on foam

mobility. Because of several uncertainties associated with modelling and simulation of field processes, and excessive numerical cost associated with explicit-texture approach, the second approach was found more appropriate for prediction phase. In this approach, the gas permeability in presence of foam (k_{rg}^{f}) is modified by multiplying the gas relative permeability without foam (k_{rg}^{nf}) at a specific water saturation with a mobility reduction factor (MRF):

$$k_{rg}^{f} = k_{rg}^{nf} \times MRF \qquad (2)$$

The water permeability in presence of foam remains unchanged. We studied the effect of water saturation, shear rate, surfactant concentration, oil saturation (Farajzadeh et al. 2012) and permeability on mobility reduction factor in numerical modelling, given by the expression:

$$MRF = \frac{1}{1 + fmmmob \times F_{water} \times F_{shear} \times F_{surf} \times F_{oil}} \qquad (3)$$

where $fmmmob$ refers to the maximum gas mobility reduction that can be achieved. F_{water}, F_{shear}, F_{surf} and F_{oil} with expressions below capture the effect of water saturation, shear rate, surfactant concentration and oil saturation dependence, with all lying in the range of 0 to 1. The capillary number N_{ca} represents the relative effect of viscous and capillary forces.

$$F_{water} = 0.5 + \frac{arctan[epdry(S_w - fmdry)]}{\pi} \qquad (4)$$

$$F_{shear} = \begin{cases} \left(\frac{fmcap}{N_{ca}}\right)^{epcap} & if\ N_{ca} > fmcap \\ 1 & otherwise \end{cases} \qquad (5)$$

$$F_{surf} = \left(\frac{Surfactant\ concentration}{fmsurf}\right)^{epsurf} \qquad (6)$$

$$F_{oil} = \left(\frac{fmoil - S_o}{fmoil}\right)^{epoil} \qquad (7)$$

A non-ionic water-soluble surfactant – Surfonic L24-22 was selected for field pilot based on surfactant screening studies for the reservoir (Nguyen et al. 2015). Surfonic L24-22 is a linear alcohol ethoxylate produced by the addition of ethylene oxide (EO) to linear, primary alcohols. It is a 22 mole ethoxylate of linear, primary 12-14 carbon number alcohol. Three sets of experiments – EOR, foam quality scan and foam rate scan, were performed with the chosen surfactant, reservoir core and fluids under representative conditions. The foam quality scan (Osterloh and Jante 1992, Xu and Rossen 2004, Kim et al. 2005) involved obtaining steady state pressure drop for constant total injection rate with foam quality varying between 0.3 to 1, and was used to obtain values for *fmmmob*, *fmdry* and *epdry*. The foam rate scan, on the other hand, involved obtaining steady state pressure drop for constant foam quality (below transition foam quality from quality scan) with total injection rate varying between 1 to 8 ft/d. *fmcap* and *epcap* were obtained by fitting rate scan, instead of using lowest capillary number in dynamic model as *fmcap*. The details on experimental setup and analysis are available in Alcorn et al. 2018, Rognmo et al. 2018 and Fredriksen et al. 2018, and are not repeated here. Foam model

parameters were obtained by fitting different set of laboratory data, and are presented further in section 3. The surfactant selected for the pilot shows very low adsorption of 0.08 mg/g (Jian et al. 2016) on reservoir material. Surfactant adsorption and wettability alteration were therefore not considered in this study because of runtime issues.

In order to account for the effect of permeability, the grid was divided into three regions depending upon the grid cell permeability- less than 10mD, 10-50 mD and greater than 50mD. These regions were assigned different fmmob, fmdry and epdry. The grid cells connecting to proposed injector were refined areally from 50 ft x 50 ft to 10 ft x 10 ft by introducing local grid refinement. In order to model foam dry-out during SAG near injector, cells (within refined grid) connecting to injector were assigned an fmmob of 0 to mimic foam absence within a radius of 5 ft around injector.

3. Results and Discussion

3.1. Waterflood Match

Thirty years of waterflood data was available for wells (**Fig. 6**) in the pilot area that was used to calibrate the geologic model. Based on the regional data, it has been identified that the reservoir consists of two zones (**Fig. 7**):
- Main Pay Zone (MPZ), which has produced by primary depletion and waterflood
- Residual Oil Zone (ROZ), which is thought to be formed by structural tilting or seal breach events, and has been naturally waterflooded over geologic time. This zone has significant immobile oil (20-40% of OIIP), which cannot be technically drained by primary or secondary mechanisms.

The only information available on reservoir pressure was that the reservoir stayed close to hydrostatic condition during the waterflood. The bubble point pressure for the reservoir fluid was measured to be 1400 psi, which is lower than hydrostatic pressure of 2300 psi at top of MPZ at 5300 ft. A black oil fluid model with oil and water phase was therefore found sufficient to model waterflood. Fluids were assumed to have constant compressibility and viscosity. The relative permeability curves were based upon SCAL measurement with fit using Modified Brooks-Corey relation for oil and water respectively:

$$k_{row} = k_{row}^0 \left(\frac{S_o - S_{orw}}{1 - S_{orw} - S_{wcon}} \right)^{n_{ow}} \tag{8}$$

$$k_{rw} = k_{rw}^0 \left(\frac{S_w - S_{wcon}}{1 - S_{orw} - S_{wcon}} \right)^{n_w} \tag{9}$$

where, k_{row}^0 and k_{rw}^0 are oil and water end-point relative permeability, while n_{ow} and n_w are Corey exponents for oil (in presence of water) and water respectively.

The water saturation in the model was assigned through enumeration, with MPZ at initial saturation of 0.1 and ROZ at higher saturation of 0.68 in base model (Honarpour et al. 2010). The wells were completed in MPZ only. Monthly production and injection data was available for each well during waterflood period. Simulations were run with producers on historic liquid rate control and injectors on historic water injection rate adjusted as shown in Fig. 4. The objective function was setup by adding mismatch between simulated and observed cumulative oil production for each producer. The weighting was assigned in proportion to fraction of cumulative oil produced by each well at sector level to improve the match for P-1, P-2 and P-4. As shown in **Fig. 8**, the response from the base geologic model deviates significantly from the observed behaviour for all the producers.

Table 1 lists the 48 UPs that were initially identified around pore volume, permeability, and oil and water relative permeabilities based on initial discussions with various stakeholders. 97 experiments were run as part of Sensitivity analysis, and 49 additional experiments were run as part of Boundary analysis. **Fig. 9** shows the tornado plot for various MPs which became available after Sensitivity analysis. The x-axis shows the relative change in mismatch of cumulative oil production from base, which is the geologic model at this point. Each UP in the model has its own bar, where red and blue bars corresponds to low and high values of that UP, respectively.

200 experiments were run with LHC sampling to search the possible solution space and identify requirement to introduce more UPs or revise the range of existing ones. As shown in **Fig. 10**, Pareto plots for MPs were generated based on the results from LHC runs to understand the relative impact of an UP on a MP. Fig. 10a shows that the mismatch in cumulative oil production for P-1 is positively correlated to the UP – *PORVMULT*, which is the pore volume multiplier for the entire sector. This means that reducing the value of *PORVMULT* will reduce the mismatch in cumulative oil production for P-1. Similarly, increasing the value of the UP – *PERMMULT08*, which is the areal permeability multiplier for layer 8, will reduce the mismatch in cumulative oil production for P-1 because of the negative correlation between them. On the other hand, Figs. 10b and 10c suggest that the same UPs – *PORVMULT* and *PERMMULT08* have a reverse relation with the mismatch in cumulative oil production for P-2 and P-4. The correlations of various MP to the global value, and among themselves were also analysed using cross plots. A trend with negative correlation between two MPs suggests that they cannot be reduced at the same time, without introducing local updates around wells. **Figs. 11a through 11c** shows that mismatch in cumulative oil production for P-1 is negatively correlated to the mismatch for P-2 and P-4, and positively correlated to mismatch for P-5.

Findings from LHC runs were then used to identify four regions marked A to F, as shown in **Fig. 12** to make local update within MPZ. Because of absence of seismic data, the geologic model was setup as layer cake model with areal continuity in individual layer. This may not be the case in the reservoir owing to discontinuity of facies or presence of faults. The initial results from an interwell tracer study also confirm a discontinuity between wells 1 and 2, and wells 1 and 4. The list with UPs was further revised, and Sensitivity analysis was rerun. Only 15 most significant UPs, which were found to influence the mismatch in the cumulative oil production the most, were carried forward. These UPs are listed in Table 2. The Boundary analysis was also rerun. **Figs. 13a and 13b** compare the simulation response for the PB experiments with the observed data for the entire sector for cumulative oil production and water-cut respectively. **Fig. 14** shows the simulation response for cumulative oil production for each producer for the experiments generated using PB, and suggests that the optimizer will more likely provide a successful history match with the screened UPs. 150 LHC experiments were run, and four start points were identified for running ES to reduce the global objective function value.

Figs. 15a and 15b show the cumulative oil production and water-cut for the entire sector respectively for cases selected to update the range for the 15 UPs after history match. Similarly, **Figs. 16 and 17** compare the cumulative oil production and water-cut respectively for the five producers (P-1, P-2, P-3, P-4 and P-5) for the selected cases. Table 2 shows the range and distribution for various UPs after match.

3.2. CO$_2$ Injection Match

CO$_2$ flood data was available for 4.5 years (**Figs. 18 and 19**) for wells in the pilot area which was used to further calibrate the reservoir model. A compositional fluid model was used to simulate historical CO$_2$ injection, for which Peng-Robinson Equation of State model was tuned to available PVT data with six components, including CO$_2$ as a separate component (Sharma et

al. 2017). Because of the assumption that the reservoir pressure does not go below bubble point pressure, only oil and water phases were considered to be present at the start of simulation of CO_2 injection. The pressure and water saturation in the model were initialized from the saturation state post waterflood simulation. The oil composition was based on composition data available from PVT study, and was assumed uniform in all cells at start of simulation for this phase.

Wettability measurements (Honarpour et al. 2010) showed mixed-wet behaviour with a tendency toward oil-wet condition similar to most carbonate reservoirs. In order to model hysteresis, separate saturation functions were specified for drainage and imbibition processes, which were parameterized to allow variation in critical gas saturation, relative permeability end-points, and Corey exponents during history match process, using relations below:

$$k_{rog} = k_{rog}^0 \left(\frac{S_l - S_{org} - S_{wcon}}{1 - S_{gcon} - S_{org} - S_{wcon}} \right)^{n_{og}} \tag{10}$$

$$k_{rg} = k_{rg}^0 \left(\frac{S_g - S_{gcon}}{1 - S_{gcon} - S_{org} - S_{wcon}} \right)^{n_g} \tag{11}$$

where, k_{rog}^0 and k_{rg}^0 are oil and gas end-point relative permeability, while n_{og} and n_g are Corey exponents to oil (in presence of gas) and gas respectively. Killough's non-wetting model was used to model hysteresis, the mathematical details for which are available in the ECLIPSE Technical Description (Schlumberger 2018) and are not discussed here.

Monthly oil and water production, and injection volumes were available for each well. Gas production, however, could only be measured from January 2016 onwards because of facility constraints in field. Shut-in reservoir pressure was not recorded for wells in the pilot area during CO_2 injection phase. Only one measurement was available for reservoir pressure from a well outside of pilot area but at a close distance, which suggested that the reservoir pressure increased from hydrostatic (2300 psi) in October 2013 to 3300 psi in July 2017. Flowing tubing-head pressure data was available for injectors since January 2016, with producers on artificial lift and no flowing pressure measurement. Because of presence of lift equipment in well, low well productivity and high operational costs involved in running a production log, there exists a large uncertainty around how much fluid is being produced from each reservoir layer.

The producers and CO_2 injectors were completed in both MPZ and ROZ in the model, in-line with the perforation activities performed in field at the start of CO_2 injection. Simulations were run with producers on liquid rate control, with an objective to match cumulative oil and water production, and gas-oil ratio for last two years. The injectors were set on historic water and CO_2 injection rate with adjustments as shown in Fig. 4. The objective function was setup by adding mismatch between simulated and observed response for – cumulative oil production for each producer, gas production rate for last two years and flowing bottom-hole pressure for injectors. The weighting was assigned in proportion to fraction of cumulative oil produced by each well at sector level to improve the match for P-3 and P-5, which are the key producers for pilot with surfactant injection planned in well 1.

Deepening of producers into ROZ resulted in significant amount of water production in field, which could not be matched until introduction of aquifer support to ROZ in the model. Once all the wells could produce on liquid rate control with bottom-hole pressure above 1000 psi, runs for Sensitivity analysis were made. 70 UPs were identified in addition to the 15 UPs from waterflood match, mainly around pore volume and transmissibility in interwell regions for MPZ and ROZ; three-phase relative permeabilities; and well injectivities. All studies for CO_2 match were performed by fixing the 15 UPs from waterflood match at their mean values. Based on the

results from sensitivity analysis, 43 (out of 70) UPs were carried forward in history matching, which are listed in Table 3.

200 LHC experiments were run, and four start points were identified for running ES to reduce the global objective function value. **Figs. 20a through 20d** compare the observed and simulation response for cumulative oil production, water cut and gas-oil ratio for the entire sector after history match. The relative error in cumulative oil production was reduced to less than 10% after history match. **Figs. 21 and 22** compare the observed and simulation response after history match for cumulative oil production, water cut and gas-oil ratio for P-3 and P-5 respectively.

The well injectivity indices were modified for the injectors to get a match on flowing bottom-hole pressure, which were estimated from tubing-head pressure using correlations for water and CO_2 phases. Because of absence of flowing gradient surveys, the vertical lift performance could not be validated, and the estimated flowing bottom-hole pressure was expected to have error of a few 100 psi. This, however, was not a concern for prediction because of change in operation strategy from injection at fixed pressure to a fixed rate at levels half of the historic rates. The weight assigned to the mismatch for bottom-hole pressure was therefore kept low in the objective function setup. **Fig. 23** compares the observed and simulation response for flowing bottom-hole pressure after match for well 1. The cell connection (transmissibility) factor, which is defined below, had to be significantly reduced for most of the wells:

$$Cell\ Connection\ Factor = \frac{PIMULT * Kh}{\ln\left(\frac{r_o}{r_w}\right) + s} \tag{12}$$

where PIMULT is a user-specified number, Kh is the effective permeability times the net thickness of the connection, r_o is the 'pressure equivalent radius' of the grid block, r_w is the wellbore radius and s is the skin factor. For well 1, the ratio between the connection factors for history matched models to the geologic model, which was setup using petrophysical logs, was found to be 0.1 to 0.4. **Fig. 24** shows that the reservoir pressure at the sector level in March 2018 (at the end of CO_2 injection match) for cases selected to update posterior UPs lies in the range of 2800 – 3000 psi, close to the expected value.

As shown in **Fig. 25**, four injection profiles have been recorded for GI-1 at a year's interval since start of CO_2 injection in October 2013. The profiles were recorded using radioactive tracer logging tool in slug tracking mode, where a 'shot' of tracer was injected into the wellbore. A gamma-ray detector was used to record the location of slug and amplitude variation with time by successive upward and downward passes or 'drags'. For each drag, the area under the trace and above the common baseline of the traces was used to quantify the fraction of injection fluid still in or near the wellbore. Even though the technique is economic for multi-well surveys and broadly identifies zones of injection, it has poor vertical resolution. The profiles were therefore not used directly for model calibration. The fractions of injected CO_2 entering into each of the two pay zones were calculated instead, and were used to test the predictive capability of the history matched models. **Fig. 26** shows the simulation results for the fraction of injected CO_2 entering into MPZ after calibration, which reduces from 100% at the beginning of CO_2 injection to around 70% after 2 years of injection. Well 1 was a producer during waterflood phase with completions in MPZ, and the formation in ROZ was perforated when it was converted into a CO_2 injector. Because of selective depletion in MPZ around well 1 due to production, CO_2 preferentially flowed into MPZ until local equilibration between the zones was achieved. Since the last injection profile for well 1 is two years old, a new survey is planned before start of the pilot which will act as a baseline for future profiles during pilot phase.

An interwell tracer study was initiated on 9 January 2018, with injection of a passive non-radioactive gas tracer (Khan et al. 2016) in GI-1, to characterize the communication between GI-1 and surrounding producers P-2, P-3, P-4 and P-5. The first set of data received from the field until March 2018 showed tracer breakthrough in P-3 and P-5 in 17 days. P-3 and P-5 were sampled twice a week and have produced 16.5% and 6% during this period. No tracer has been observed in P-2 and P-4. The tracer study is still in progress, with a reduced sampling frequency of one sample every two weeks. The tracer response was not a part of the objective function for the current history match cycle, and was only used to validate the quality of matched models. **Fig. 27** compares the simulation results for the cumulative tracer production for both the wells as a fraction of the total amount of tracer injected. Even though the models predict lower tracer production, mainly because of presence of high resolution features in reservoir which cannot be captured in current model, their performance was found acceptable.

3.3. Foam Pilot Performance Prediction

In order to simulate foam behaviour in the reservoir model, a surfactant component was added to the aqueous phase which had the water component present during CO_2 history match as default (Islam and Farouq-Ali 1990). As mentioned earlier, the dynamic model was divided into three regions to capture effect of permeability on foam behaviour – Region 1 with permeability less than 10 mD, Region 2 with permeability in range of 10 to 50 mD and Region 3 with permeability greater than 50 mD. Before using a specific model for forecasting, an external script was run to assign regions based on the permeability in that model. **Fig. 28a** shows permeability distribution for a cross-section along wells 3, 1 and 5 for one the models after history match, while the regions for same are shown in Fig. 28b.

Most of the experiments in laboratory were performed with reservoir cores having permeability in range of 20 to 30 mD. The experiments were performed using reservoir oil and brine under representative conditions. The base values for foam model parameters - *fmmob*, *fmdry* and *epdry* for Region 2 were obtained by performing regression on the quality scan data to fit the empirical foam model as shown in **Fig. 29a**. The base values for *fmcap* and *epcap* were obtained by performing regression on the rate scan data to fit the empirical foam model as shown in Fig. 29b, assuming *fmmob*, *fmdry* and *epdry* (estimated earlier) to be invariable while fitting rate scan data. The details on fitting the empirical foam model are available in Zeng et al. (2016). In absence of cores from Region 1 and Region 3, assumptions were made about *fmmob*, *fmdry* and *epdry* to characterize foam behaviour. The values were assumed such that no foam generates in Region 1, and apparent viscosity of foam in Region 3 is twice of that in Region 2. Table 4 lists the base values of these parameters along with the range considered for pilot performance prediction.

The minimum concentration for foam generation in numerical model was set at the critical micellar concentration (CMC), which was found to be 0.01 wt% (0.035 lb/bbl) for the selected surfactant. The experiments for foam quality scan and foam rate scan were performed with 0.5 wt% and 1 wt% surfactant solutions in laboratory, and based upon the finding that 0.5 wt% solution yields equally strong foam as 1 wt% solution, injection in well 1 is planned at 0.5 wt% concentration. The base value of *fmsurf*, which corresponds to reference concentration for transition from weak to strong foam was assumed to be 0.05 wt% (0.175 lb/bbl), which is five times the CMC. The base value for *epsurf*, which controls the steepness in the change of mobility reduction due to surfactant concentration, was assumed 1. The base value of *fmoil*, which corresponds to maximum oil saturation above which foam ceases to exist, was considered as 0.28 based upon CO_2-Foam EOR experiments. The base value of *epoil*, which controls the steepness in the change of mobility reduction due to oil saturation, was assumed 1. Table 4 lists

the range of values for all foam model parameters which were considered for pilot performance prediction.

12 UPs were considered for modelling foam behaviour, which were combined with the 58 UPs from history matching phase, to generate 100 LHC cases under two scenarios. As shown in **Fig. 30a**, the first scenario is based on operators' current plan to implement WAG in the pilot area with one year of water injection followed by six months of CO_2 injection. The second scenario (Fig. 30b) considers 12 cycles of SAG starting 1 November 2018, followed by continuous CO_2 injection. The SAG strategy, which is based on discussions with the operator and cross-section numerical modelling, includes 10 days of surfactant injection and 20 days of CO_2 injection. Water and CO_2 injection will be limited to 300 STB/D and 1000 Mscfd respectively, which are around half of the maximum rates that can be injected in well 1 at maximum allowable flowing bottom-hole pressure. These injection schemes result in a similar injection of around 1.1 million barrels under reservoir conditions for both the scenarios. For each case, simulations were run using the sampled values of the UPs for all three phases – waterflood, CO_2 injection and forecast for three years. The initial pressure, saturation and composition for each case for second and third phase were based on the values extracted from the last step of previous phase.

Fig. 31 shows the forecasts for gas-oil ratio for both the scenarios from LHC cases. Even though water injection reduces gas recycling, it is not significant enough compared to mobility control provided by foam, even with continuous CO_2 injection after pilot. **Fig. 32a** shows the cumulative probability distribution for incremental oil forecasted using LHC cases for Scenario 2 with respect to Scenario 1 after 1 year, 2 years and 3 years of start of pilot. Because of injection at low rate (0.05 PV a year), it is expected that the incremental volume of oil produced with foam will reach a significant level only after the SAG cycles have completed. In addition to incremental oil production, CO_2 retention was evaluated which is defined as:

$$CO_2 \ Retention \ = \frac{CO_2 \ Injected - CO_2 \ Produced}{CO_2 \ Injected} \tag{13}$$

In the above expression, produced CO_2 volume corresponds to recycled CO_2 volume assuming no CO_2 loss at surface, while injected CO_2 volume corresponds to sum of purchased and recycled CO_2 volumes. Fig. 32b shows the cumulative probability distribution for CO_2 retention factor for both the scenarios after 2 years and 3 years of start of pilot. The selective foam generation in high permeability regions allows diversion of CO_2 into low permeability regions, resulting in a higher CO_2 retention. CO_2 storage is slightly different from CO_2 retention, as given below (Melzer 2012),

$$CO_2 \ Storage \ = \frac{CO_2 \ Injected - CO_2 \ Produced - CO_2 \ Losses}{Purchased \ CO_2 \ Injected} \tag{14}$$

Since the above definition requires the operator to disclose the purchased volumes in addition to measurement of losses, CO_2 retention was found a more suitable metric for this study. Table 5 lists the P90, P50 and P10 values for incremental oil and increase in CO_2 retention with foam. **Fig. 33** shows the correlation between the two KPIs – incremental oil and increase in CO_2 retention with respect to various UPs after 2 years of start of pilot based upon the 100 LHC cases. A higher value of a particular UP which is positively correlated with a particular KPI will result in higher KPI, like 'M9' in Fig. 33a. Most of the UP were found to have weak correlation with the KPIs, and the relevant UPs were not only limited to foam model parameters.

4. Conclusions

A research program has been initiated to advance the technology of using foam as mobility control agent for CO_2 EOR and storage as part of CCUS value chain, with focus on integrated reservoir modelling to assist technology transfer to high risk and high cost environment. A heterogeneous carbonate reservoir onshore in west Texas, USA has been selected for field trial.

In this paper, we discussed a workflow to create reliable forecasts of future field behaviour which honours all the available information including core and petrophysical data, production data and laboratory data. It relies on applying engineering judgement while using a reservoir model to obtain an understanding about the uncertainty in the production forecasts, as accurately as possible. Inputs from all stakeholders were used to understand the uncertainties in the initial numerical model, which were revised while calibrating the model performance to match historical production data. The predictive capability of the calibrated models were tested for injection profiles and interwell tracer test data, which were excluded during history matching. Even though the input data was sparse and had uncertainties, the calibrated models were found to be fit-for-purpose. The workflow was then used to generate a spread of forecast to predict foam pilot performance. A baseline injection profile and fall-off test is planned before start of the pilot, which will be further used to improve the model quality and guide decision making during field operation.

Acknowledgements

Nomenclature

epcap	Parameter that captures shear-thinning behavior in the low quality regime
epdry	Parameter controlling the abruptness of foam collapse
epoil	Parameter controlling the effect of oil saturation
epsurf	Parameter controlling the effect of surfactant concentration
fmcap	Parameter set to the smallest capillary number expected in the simulation
fmdry	Water saturation in vicinity of which foam collapses
fmmob	Reference gas mobility-reduction factor for foam
fmsurf	Reference surfactant concentration
fmoil	Reference high oil saturation for foam collapse
Kh	Permeability-thickness
s	Skin factor
k_{rg}^{nf}	Gas relative permeability without foam
k_{rg}^{f}	Gas relative permeability with foam
k_{rg}^{0}	Gas end-point relative permeability
k_{rog}^{0}	Oil end-point relative permeability in presence of gas (and connate water)
k_{row}^{0}	Oil end-point relative permeability
k_{rw}^{0}	Water end-point relative permeability

n_g	Corey exponents to gas
n_{og}	Corey exponents to oil in presence of gas and connate water
n_{ow}	Corey exponent to oil in presence of water
n_w	Corey exponent for water
r_o	Pressure equivalent radius of a grid
r_w	Wellbore radius
N_{ca}	Capillary number
Obs_i^j	Observed history match value of parameter i at time j
Sim_i^j	Simulated value of observation i at time j
Std_i	Standard deviation of mismatch parameter i
S_{orw}	Residual oil saturation to waterflood
S_{wcon}	Connate water saturation
W_i	Global weight factor of mismatch parameter i
W_j	Weight of timestep j

Abbreviations

BOPD	Barrels of oil per day
CCUS	Carbon capture, utilization and storage
EOR	Enhanced oil recovery
ES	Evolution strategy
GV	Global objective function value
KPI	Key performance indicator
LHC	Latin hypercube
Mscfd	Thousand standard cubic feet per day
MP	Mismatch parameter
MPZ	Main producing zone
MRF	Mobility reduction factor
OIIP	Oil Initially In-Place
PB	Plackett-Burmann
PI	Productivity (injectivity) index
PIMULT	Productivity (Injectivity) index multiplier
PV	Pore volume
PVT	Pressure Volume Temperature
ROZ	Residual oil zone
SAG	Surfactant alternating gas
SCAL	Special core analysis
STB/D	Stock tank barrels per day
UP	Uncertainty parameter
WAG	Water alternating gas
Wt %	Weight percent

References

Alcorn, Z.P., Fredriksen, S., Sharma, M., Rognmo, A., Fernø, M. and Graue, A. 2018. An Integrated CO_2 Foam EOR Pilot Program with Combined CCUS in an Onshore Texas Heterogeneous Carbonate Field. SPE Improved Oil Recovery Conference, Tulsa, USA, 14-18 April

Alvarez, J.M., Rivas, H., and Rossen, W.R., 2001. A Unified Model for Steady-State Foam Behavior at High and Low Foam Qualities. SPE J. 6, 325-333.

Back, T., 1996. Evolutionary Algorithms in Theory and Practice. Oxford U. Press, Oxford, U.K.

Cheng, L., Reme, A.B., Shan, D., Coombe, D.A. and Rossen, W.R., 2000. Simulating Foam Processes at High and Low Foam Qualities. SPE/DOE Symposium on Improved Oil Recovery, Tulsa, OK, 3-5 April.

Chou, S.I., Vasicek, S.L., Pisio, D.L., Jasek, D.E. and Goodgame, J.A., 1992. CO_2 Foam Field Trial at North Ward-Estes. SPE Annual Technical Conference and Exhibition, Washington, D.C., 4-7 October.

Falls, A.H., Hirasaki, G.J., Patzek, T.W., Gauglitz, D.A., Miller, D.D. and Ratulowski, J., 1988. Development of a Mechanistic Foam Simulator: The Population Balance and Generation by Snap-Off. SPE Res. Eng. 3, 884-892.

Farajzadeh, R., Andrianov, A., Krastev, R., Hirasaki, G.J. and Rossen, W.R., 2012. Foam-Oil Interaction in Porous Media: Implications for Foam Assisted Enhanced Oil Recovery. Adv. Colloid Interface Sci. 183-184, 1-13.

Fredriksen, S. B., Alcorn, Z. P., Sharma, M., Wergeland, C., Fernø, M.A., Graue, A. and Ersland, G. 2018. Core-Scale Sensitivity Study of CO_2 Foam Injection Strategies for Mobility Control, Enhanced Oil Recovery and CO2 Storage. Manuscript submitted for publication in SPE Journal.

Harpole, K.J. and Hallenbeck, L.D., 1996. East Vacuum Grayburg San Andres Unit CO_2 Flood Ten Year Performance Review: Evolution of a Reservoir Management Strategy and Results of WAG Optimization. SPE Annual Technical Conference and Exhibition, Denver, Colorado, 6-9 October.

Heller, J.P., 1994. CO_2 Foams in Enhanced Oil Recovery. In Foams: Fundamentals and Applications in the Petroleum Industry, Advances in Chemistry 242, ed. L. L. Schramm, Chapter 5, 201-234. American Chemical Society.

Heller, J.P., Boone, D.A. and Watts, R.J., 1985. Field Test of CO_2 Mobility Control at Rock Creek. SPE Annual Technical Conference and Exhibition, Las Vegas, Nevada, 22-26 September.

Holm, L.W. and Garrison, W.H., 1988. CO_2 Diversion With Foam in an Immiscible CO_2 Field Project. SPE Res. Eng. 3 (1), 112-118.

Hoefner, M. L. and Evans, E. M., 1995. CO_2 Foam: Results from Four Developmental Field Trials. SPE Res. Eng. 10 (4), 273-281.

Honarpour, M.M., Nagarajan, N.R., Grijalba Cuenca, A., Valle, M. and Adesoye, K., 2010. Rock-Fluid Characterization for Miscible CO_2 Injection: Residual Oil Zone, Seminole Field, Permian Basin. SPE Annual Technical Conference and Exhibition, Florence, Italy, 19-22 September.

Islam, M.R. and Farouq-Ali, S.M., 1990. Numerical Simulation of Foam Flow in Porous Media. J. Can. Pet. Tech. 29(4), 47-51.

Jarrell, P.M., Fox, C.E., Stein, M.H. and Webb, S.L., 1990. Practical Aspects of CO_2 Flooding. SPE Monograph Series, 22.

Jian, G., Puerto, M.C., Wehowsky, A., Dong, P., Johnston, K.P. and Hirasaki, G.J., 2016. Static Adsorption of an Ethoxylated Nonionic Surfactant on Carbonate Minerals. Langmuir 32(40), 10244-10252.

Jonas, T.M., Chou, S.I. and Vasicek, S.L., 1990. Evaluation of a CO_2 Foam Field Trial: Rangely Weber Sand Unit. SPE Annual Technical Conference and Exhibition, New Orleans, Louisiana, 23-26 September.

Khan, M.N., Iwama, H., Al-Neaimi, A., Al-Shehhi, O. and Chatterjee, M., 2016. A to Z of Gas Tracers – A Decade of Learning and Experience. SPE Abu Dhabi International Petroleum Exhibition & Conference, Abu Dhabi, UAE, 7-10 November.

Kim, J.S., Dong, Y. and Rossen, W.R., 2005. Steady-State Flow Behavior of CO_2 Foam. SPE J. 10, 405-415.

Melzer, L.S., 2012. Carbon Dioxide Enhanced Oil Recovery (CO_2 EOR): Factors Involved in Adding Carbon Capture, Utilization and Storage (CCUS) to Enhanced Oil Recovery. Report prepared for the National Enhanced Oil Recovery Initiative, Center for Climate and Energy Solutions.

Merchant, D.H., 2010. Life Beyond 80: A look at Conventional WAG Recovery Beyond 80% HCPV Injection in CO_2 Tertiary Floods. SPE International Conference on CO_2 Capture, Storage, and Utilization, New Orleans, Louisiana, USA, 10-12 November.

Mukherjee, J., Nguyen, Q. P., Scherlin, J., Vanderwal, P.G. and Rozowski, P., 2016. CO_2 Foam Pilot in Salt Creek Field, Natrona County, Wyoming: Phase III: Analysis of Pilot Performance. SPE Improved Oil Recovery Symposium, Tulsa, Oklahoma, USA, 11-13 April 2016.

Nguyen, Q.P., Hirasaki, G.J. and Johnston, K. P., 2015. Novel CO_2 Foam Concepts and Injection Schemes for Improving CO_2 Sweep Efficiency in Sandstone and Carbonate Hydrocarbon Formations. Technical Report, U.S. Department of Energy / National Energy Technology Laboratory.

Osterloh, W.T. and Jante, M.J., 1992. Effects of Gas and Liquid Velocity on Steady-State Foam Flow at High Temperature. SPE/DOE EOR symposium, Tulsa, OK, April 22-24.

Rognmo, A.U., Fredriksen, S., Eide, Ø., Føyen, T.L., Graue, A., Alcorn, Z.P., Sharma, M., Fernø, M., 2018. Pore-to Core EOR Upscaling for CO_2-Foam for CCUS. SPE EUROPEC featured at 80th EAGE Conference and Exhibition, Copenhagen, Denmark, 11-14 June.

Rossen, W.R., Zeilinger, S.C., Shi, J.X. and Lim, M.T., 1999. Simplified Mechanistic Simulation of Foam Processes in Porous Media. SPE J. 4, 279-287.

Sanders, A., Jones, R. M., Linroth, M.A. and Nguyen, Q. P., 2012. Implementation of a CO_2 Foam Pilot Study in the SACROC Field: Performance Evaluation. SPE Annual Technical Conference and Exhibition, San Antonio, Texas, USA, 8-10 October.

Schlumberger, 2018. Technical Description. ECLIPSE Reservoir Simulation Software.

Schulze-Riegert, R.W., Axmann, J.K., Haase, O., Rian, D.T. and You, Y.,-L., 2002. Evolutionary Algorithms Applied to History Matching of Complex Reservoirs. SPE Res. Eval. Eng. 5 (2), 163-173.

Sharma, M., Taware, S.V. and Datta-Gupta, A., 2016. Optimizing CO_2 Floods Using Rate Control with Smart Wells Under Geologic Uncertainty. SPE Abu Dhabi International Petroleum Exhibition & Conference, Abu Dhabi, UAE, 7-10 November.

Sharma, M., Alcorn, Z.P., Fredriksen, S., Fernø, M. and Graue, A. 2017. Numerical Modelling Study for Designing CO_2-Foam Field Pilot. IOR 2017 – 19th European Symposium on Improved Oil Recovery, Stavanger, Norway, 24-27 April.

Wang, F.P., Lucia, J.F. and Kerans, C., 1998. Integrated Reservoir Characterization Study of a Carbonate Ramp Reservoir: Seminole San Andres Unit, Gaines County, Texas. SPE Res. Eval. Eng. 1(2), 105-113.

Xu, Q. and Rossen, W.R., 2004. Experimental Study of Gas Injection in Surfactant-Alternating-Gas Foam Process. SPE Res. Eval. Eng. 7, 438-448.

Zeng, Y., Muthuswamy, A., Ma, K., Wang, L., Farajzadeh, F., Puerto, M., Vincent-Bonnieu, S., Eftekhari, A.A., Wang, Y., Da, C., Joyce, J.C., Biswal, S.L. and Hirasaki, G.J., 2016. Insights on Foam Transport from a Texture-Implicit Local Equilibrium Model with an Improved Parameter Estimation Algorithm. Ind. Eng. Chem. Res., 2016, 55 (28), 7819–7829.

Parameter	Scope	Distribution	Min	Mean	Max	Count
SwCrit	Entire Model	Uniform	0.1	0.2	0.25	1
Sor	Entire Model	Uniform	0.3	0.35	0.4	1
KroSwMin	Entire Model	Uniform	0.65	0.75	0.85	1
KrwSor	Entire Model	Uniform	0.6	0.7	0.8	1
Nw	Entire Model	Uniform	1.2	1.4	3.0	1
No	Entire Model	Uniform	4.0	4.5	5.0	1
PORVMULT (Pore Volume Multiplier)	Entire Model	Uniform	0.7	1.0	1.3	1
PERMMULT (Permeability Multplier)	Layer-based	Uniform	0.7	1.0	1.3	20
KYKX	Entire Model	Uniform	0.7	1.0	1.3	1
KVKH: Good layers	Layer-based	Uniform	0.4	0.6	0.8	17
KVKH: Poor layers	Layer-based	Uniform	0	0.16	0.25	3

Table 1—Initial uncertainty matrix for water injection match.

Parameter	Region	Layer(s)	Distribution	Min	Max	Mean	Std. Dev.	P10	P90
SwCrit	All	All	Log Normal			0.24	0.03	0.21	0.27
Sorw	All	All	Normal			0.41	0.03	0.37	0.44
KroSwMin	All	All	Uniform	0.59	0.80			0.61	0.78
KrwSorw	All	All	Uniform	0.61	0.80			0.63	0.78
Nw	All	All	Uniform	1.04	1.31			1.07	1.28
Now	All	All	Log Normal			5.03	0.44	4.48	5.60
PVMult1	A	1 - 16	Triangular			1.91	0.02	1.72	2.14
PVMult2	B	1 - 16	Log Normal			0.98	0.08	0.88	1.08
PVMult3	C	1 - 16	Normal			0.10	0.01	0.08	0.11
PVMult4	D	1 - 16	Uniform	0.08	0.12			0.08	0.12
PVMult5	E	1 - 16	Uniform	6.52	8.45			6.71	8.25
PVMult6	F	1 - 16	Uniform	0.08	0.12			0.08	0.12
PermMult1	A, B, E	1 - 16	Uniform	0.43	0.58			0.44	0.57
PermMult2	C, D, F	1 - 16	Uniform	1.28	1.72			1.32	1.68
KYKX	All	All	Uniform	0.59	0.79			0.61	0.77

Table 2—Updated uncertainty parameters (range and distribution) based upon waterflood match.

Parameter	Layer(s)	Distribution	Min	Max	Mean	Std. Dev.	P10	P90
Krg@Connate Liquid	All	Uniform	0.90	1.00			0.91	0.99
Ng	All	Uniform	1.00	1.10			1.01	1.09
Nog	All	Uniform	1.00	1.20			1.02	1.08
SgCritIMB	All	Log-Normal			0.28	0.01	0.26	0.29
SgCritDRN	All	Triangular			0.32	2E-4	0.30	0.34
SwCritDRN	All	Normal			0.33	0.02	0.31	0.36

Parameter	Wells/Region	Distribution						
M4 (Wells 1 - 5: PV Mult)	1 - 16	Log-Normal			5.03	0.27	4.69	5.38
M5 (Wells 1 - 5: Trans Mult)	1 - 16	Normal			0.20	0.02	0.17	0.23
M6 (Wells 5 - 10: PV Mult)	1 - 16	Log-Normal			5.01	0.29	4.64	5.38
M7 (Wells 5 - 10: Trans Mult)	1 - 16	Uniform	0.80	1.00			0.82	0.98
M9 (Wells 1 - 3: Trans Mult)	1 - 16	Uniform	0.17	0.24			0.17	0.24
LY8A (Wells 1 - 3: Trans Mult)	8	Log-Normal			1.99	0.22	1.72	2.27
LY8B (Wells 3 - 8: Trans Mult)	8	Uniform	1.64	2.44			1.72	2.36
OP2 (Wells 1 - 3 Inner Region: Trans Mult)	4	Uniform	1.65	2.38			1.72	2.31
OP3 (Wells 1 - 3 Outer Region: Trans Mult)	4	Log-Normal			1.97	0.22	1.70	2.25
OP4 (Wells 1 - 3 Inner Region: Trans Mult)	7, 8	Log-Normal			1.99	0.23	1.71	2.28
OP5 (Wells 1 - 3 Outer Region: Trans Mult)	7, 8	Uniform	1.58	2.42			1.66	2.34
OP6 (Wells 1 - 3 Inner Region: Trans Mult)	10	Uniform	1.64	2.39			1.72	2.32
OP7 (Wells 1 - 3 Outer Region: Trans Mult)	10	Uniform	1.56	2.40			1.64	2.32
OP10 (Wells 1 - 5 Inner Region: Trans Mult)	4	Normal			1.00	0.13	0.84	1.16
OP11 (Wells 1 - 5 Outer Region: Trans Mult)	4	Log-Normal			1.92	0.22	1.65	2.21
OP12 (Wells 1 - 5 Inner Region: Trans Mult)	7, 8	Uniform	0.80	1.21			0.84	1.17
OP13 (Wells 1 - 5 Outer Region: Trans Mult)	7, 8	Log-Normal			1.97	0.23	1.68	2.27
OP14 (Wells 1 - 5 Inner Region: Trans Mult)	10	Uniform	0.80	1.20			0.84	1.16
OP15 (Wells 1 - 5 Outer Region: Trans Mult)	10	Uniform	1.61	2.39			1.69	2.31
R7 (Wells 5 - 10: PV Mult)	18 - 28	Log-Normal			0.10	0.01	0.09	0.11
R9 (Wells 2 - 6: PV Mult)	18 - 28	Log-Normal			0.10	0.01	0.09	0.11
R10 (Wells 2 - 6: Trans Mult)	18 - 28	Uniform	0.40	0.60			0.42	0.58
R14 (Wells 3 - 8: Trans Mult)	18 - 28	Uniform	1.23	1.81			1.29	1.75
R16 (Wells 1 - 5: Trans Mult)	18 - 28	Log-Normal			2.07	0.18	1.85	2.31
R18 (Wells 2 - 6: Trans Mult)	19	Uniform	0.40	0.61			0.42	0.59
WPIMULT_GI1	Completion	Log-Normal			0.06	0.01	0.05	0.06
WPIMULT_GI6	Completion	Uniform	0.25	0.35			0.26	0.34
WPIMULT_GI8	Completion	Uniform	0.45	0.66			0.47	0.64
WPIMULT_GI9	Completion	Uniform	2.00	3.03			2.10	2.93
WPIMULT_GI10	Completion	Uniform	0.04	0.08			0.04	0.08
WPIMULT_WI1	Completion	Uniform	0.30	0.50			0.32	0.48
WPIMULT_WI6	Completion	Uniform	0.20	0.30			0.21	0.29
WPIMULT_WI7	Completion	Uniform	0.15	0.20			0.16	0.19
WPIMULT_WI8	Completion	Uniform	1.99	3.03			2.09	2.93
WPIMULT_WI9	Completion	Uniform	6.98	8.04			7.09	7.94
WPIMULT_WI10	Completion	Uniform	1.98	2.93			2.08	2.84
WPIMULT_WI11	Completion	Uniform	0.20	0.30			0.21	0.29

Table 3—Updated uncertainty parameters (range and distribution) based upon CO_2 injection match.

Parameter	Region	Low	Base	High	Distribution	Remarks
Fmmob	1		0			Assumed no foam generation
	2	500	630	750	Uniform	Base value based on Quality Scan
	3	900	1200	1500	Uniform	
Fmdry	1		0.32			
	2	0.243	0.27	0.297	Uniform	Base value based on Quality Scan
	3	0.198	0.22	0.297	Uniform	
Epdry	1		500			
	2	80	100	120	Uniform	Base value based on Quality Scan
	3	20	25	30	Uniform	
Fmcap	All	6.2e-7	7.8e-7	9.4e-7	Uniform	Base value based on Rate Scan
Epcap	All	0.52	0.65	0.78	Uniform	Base value based on Rate Scan
Fmsurf	All	0.14	0.175	0.21	Uniform	Base value assumed 5 times of CMC
Epsuf	All	0.8	1	1.2	Uniform	
Fmoil	All	0.21	0.28	0.35	Uniform	Base value from EOR experiments
Epoil	All	0.5	1	2	Uniform	

Table 4—Uncertainties in foam model parameters considered for forecasting.

KPI	Time	P90	P50	P10
Incremental Oil, STB	1 Year	1900	2500	2800
	2 Years	2700	3500	5000
	3 Years	5600	6700	8200
Increase in CO_2 Retention Factor	2 Years	0.16	0.22	0.28
	3 Years	0.07	0.13	0.20

Table 5—Confidence intervals for KPIs based upon simulation cases.
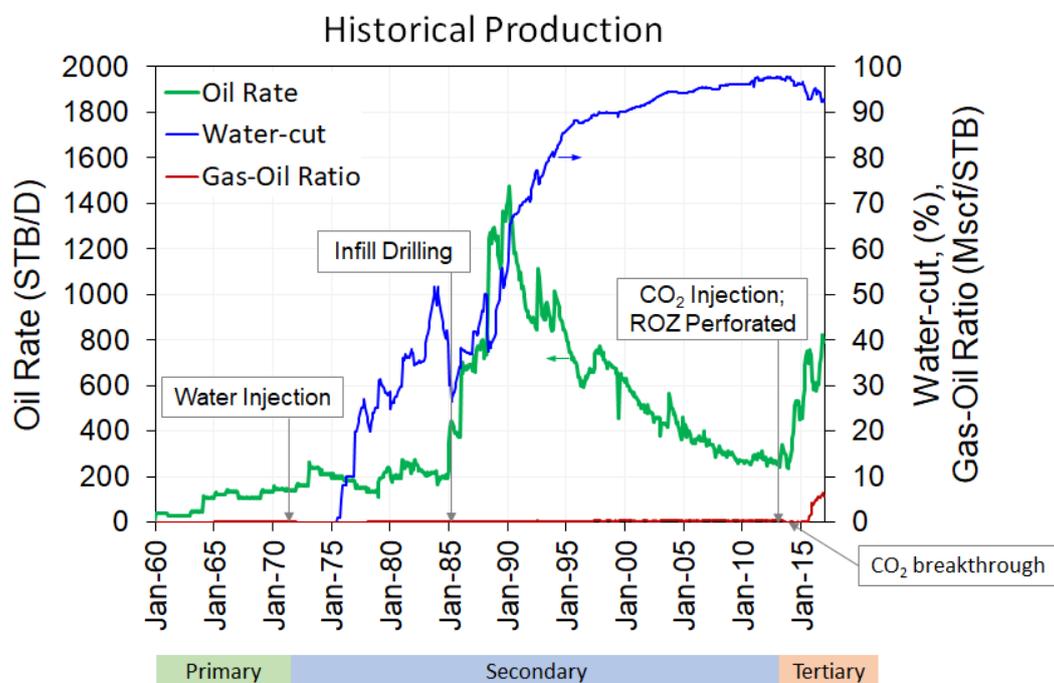
Fig. 1—Field historical production.
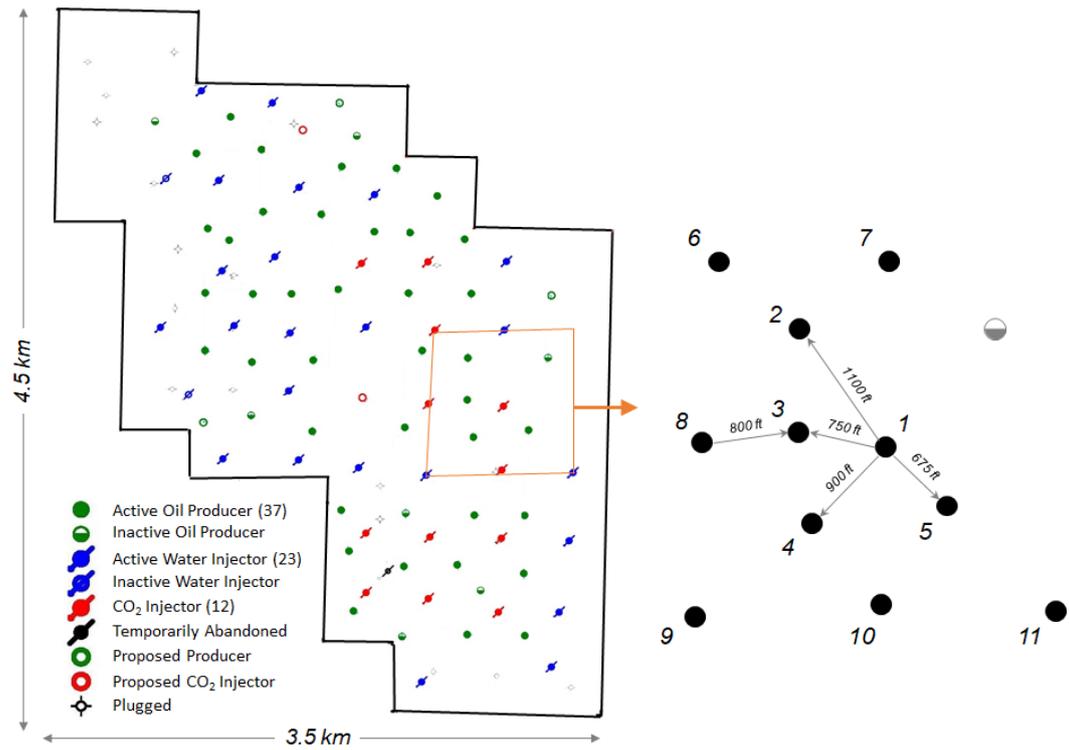
Fig. 2—Field layout and location of selected pilot area. Surfactant will be injected in well 1.
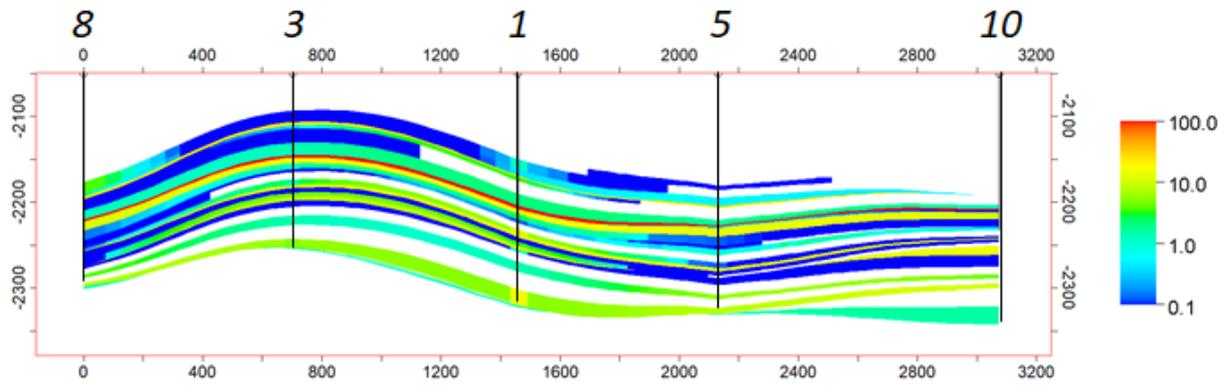
Fig. 3—Cross-section along wells 8, 3, 1, 5 and 10 showing permeability in geologic model.
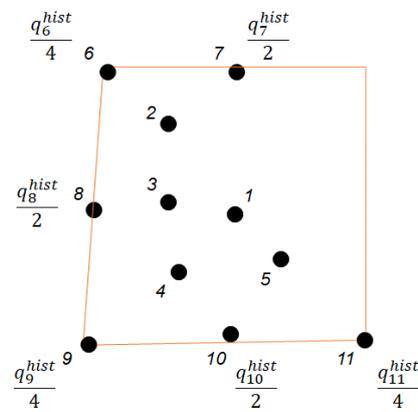
Fig. 4—Injection rates for wells at boundary of sector model - 6, 7, 8, 9, 10 and 11.
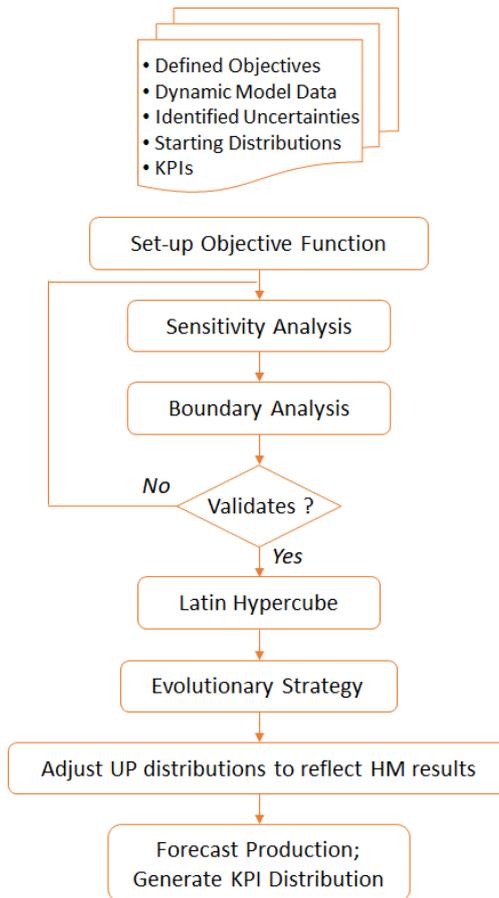
Fig. 5—History matching and forecasting workflow.
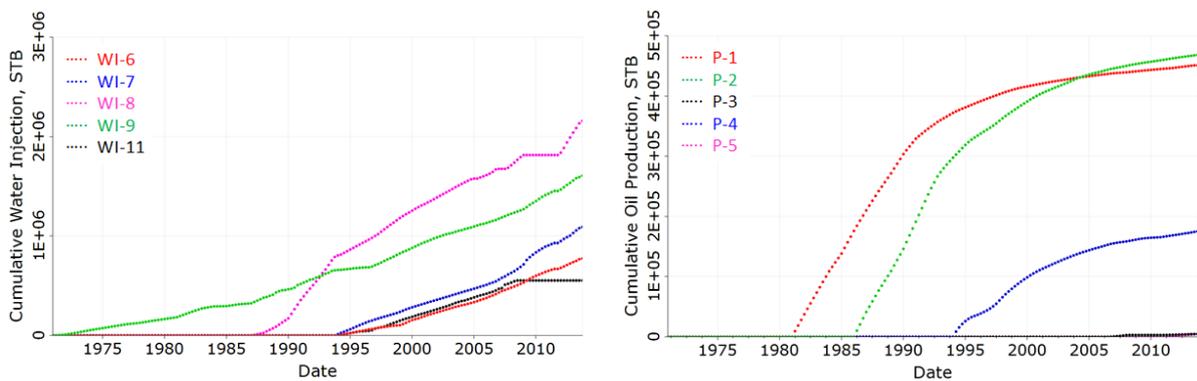
Fig. 6—Historic well performance during waterflood (a) Cumulative water injection (b) Cumulative oil production.
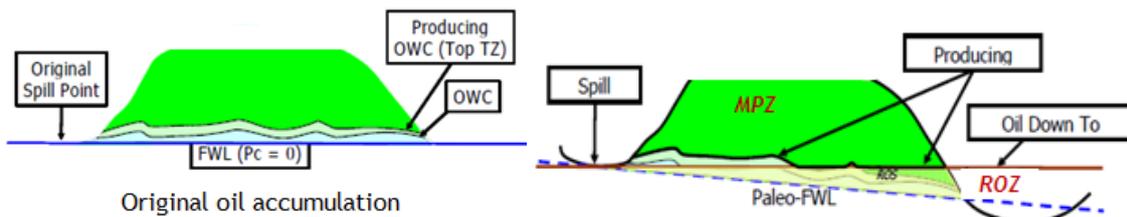
Fig. 7—Effect of tilting on initial hydrocarbon distribution.
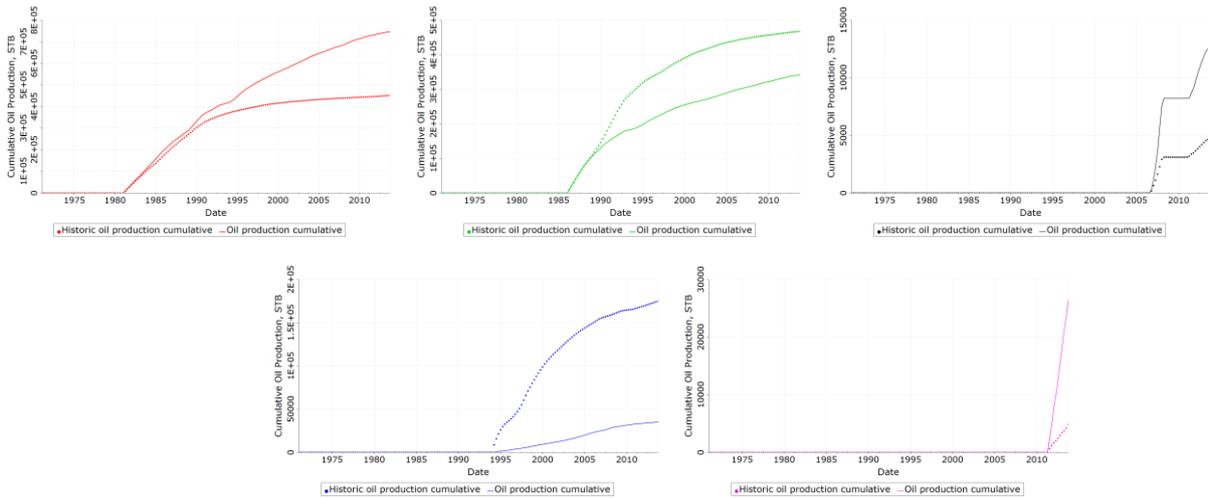
Fig. 8—Mismatch in cumulative oil production based upon base geologic model for producers P-1, P-2, P-3, P-4 and P-5.
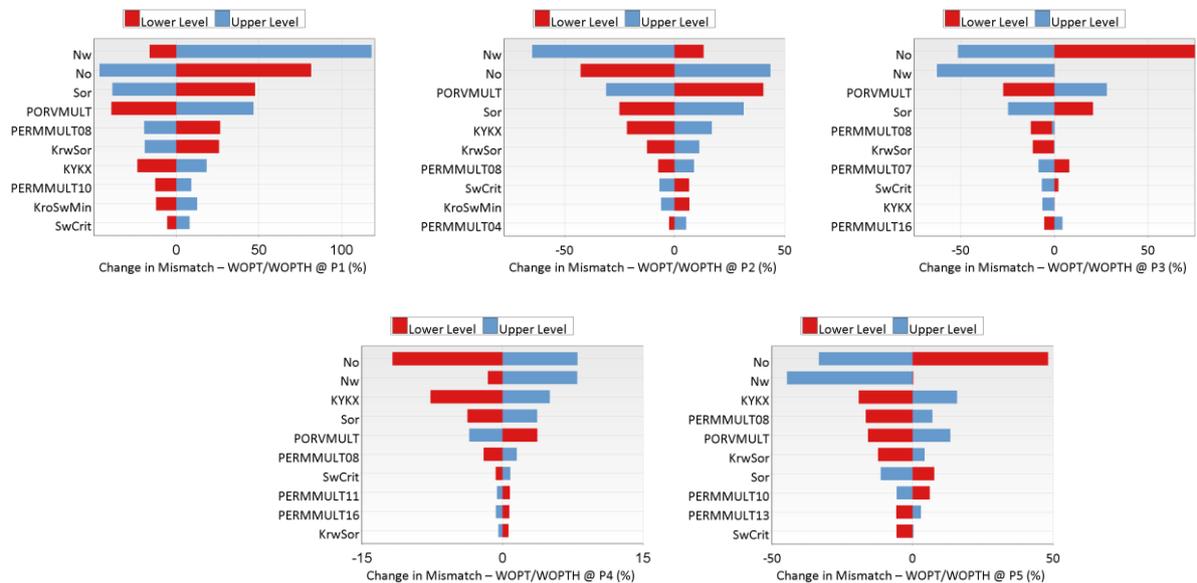
Fig. 9—Sensitivity analysis showing the key uncertainty parameters influencing change in mismatch between observed and simulated cumulative oil production for producers P-1, P-2, P-3, P-4 and P-5.
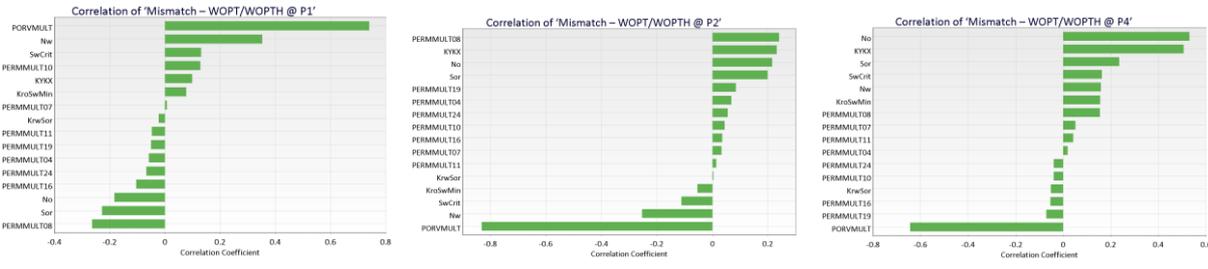
Fig. 10—Pareto plots showing correlation of mismatch between observed and simulated cumulative oil production to the uncertainty parameters based upon LHC runs for producers P-1, P-2 and P-4.

22
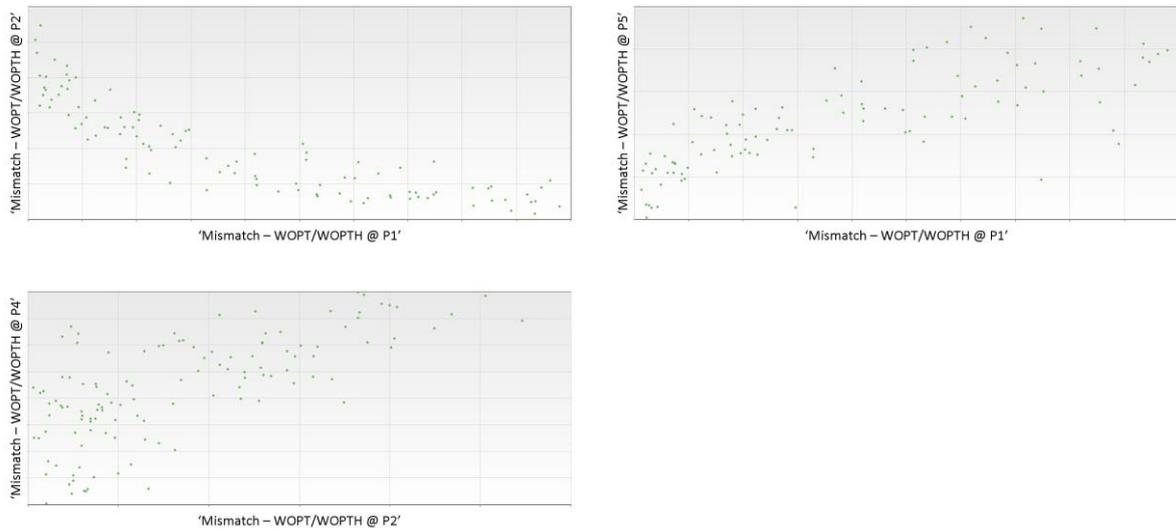
Fig. 11—Plots showing correlation for mismatch between observed and simulated cumulative oil production based upon LHC runs for (a) P-1 vs. P-2 (b) P-1 vs. P-5 and (c) P-2 vs. P-4.
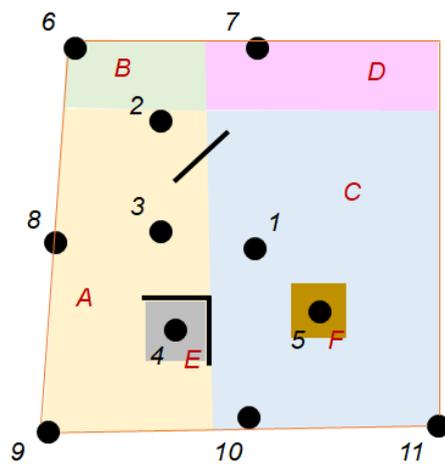
Fig. 12—Regions identified for modification based upon LHC runs, and considered for history matching using ES.
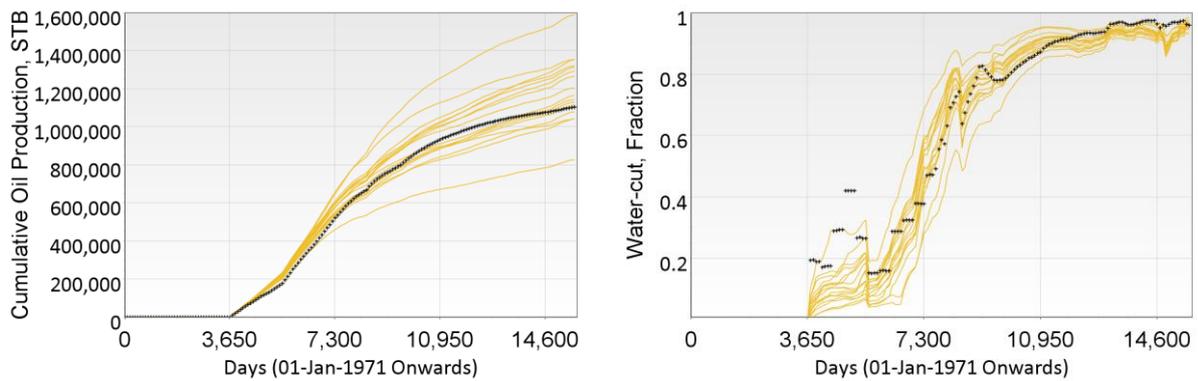
Fig. 13—PB experiments with revised uncertainty parameters showing simulation results covering the observed data at sector level (a) Cumulative oil production (b) Water-cut.
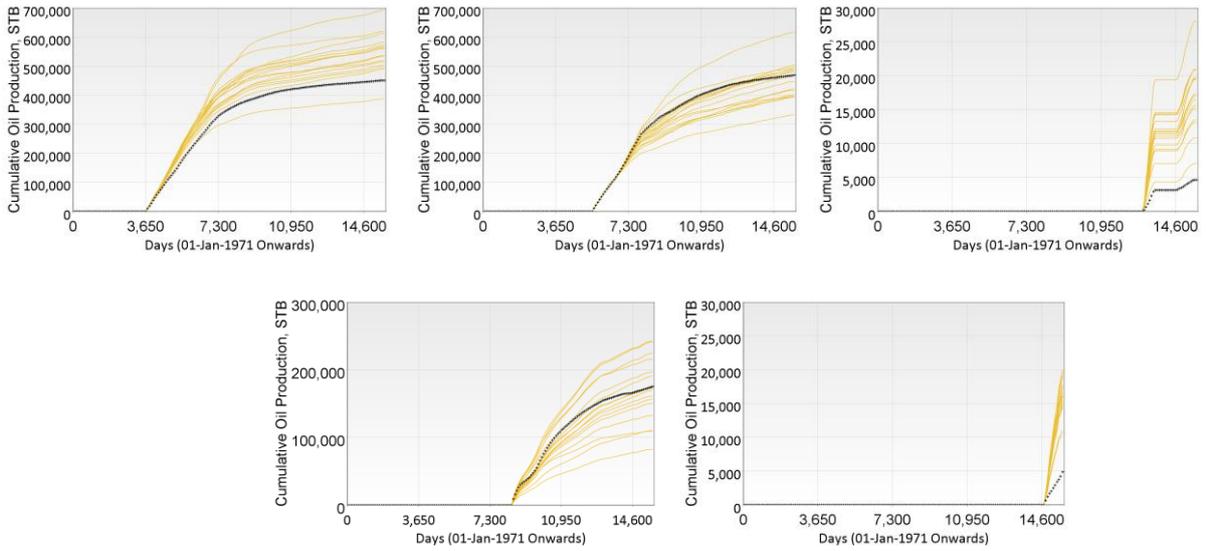
Fig. 14—PB experiments showing cumulative oil production for producers P-1, P-2, P-3, P-4 and P-5.
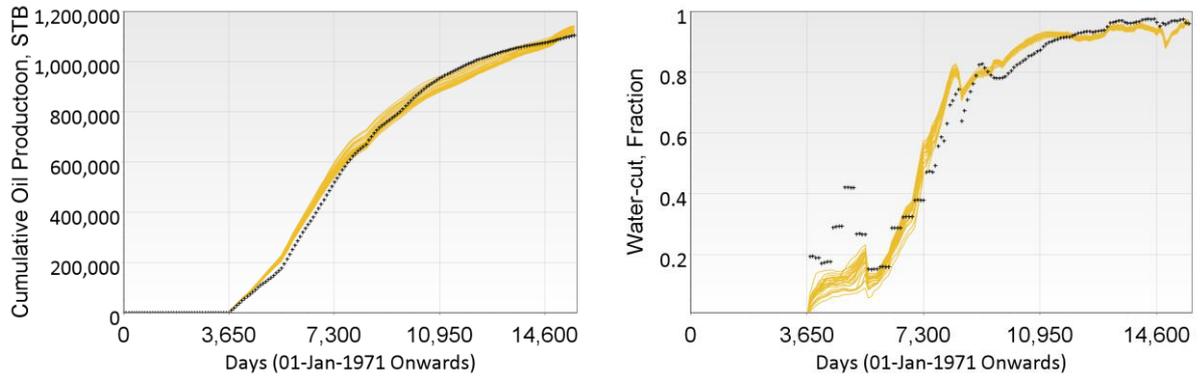
Fig. 15—Simulation results at sector level for cases selected to update (posterior) uncertainty parameter ranges after running ES (a) Cumulative oil production (b) Water-cut.
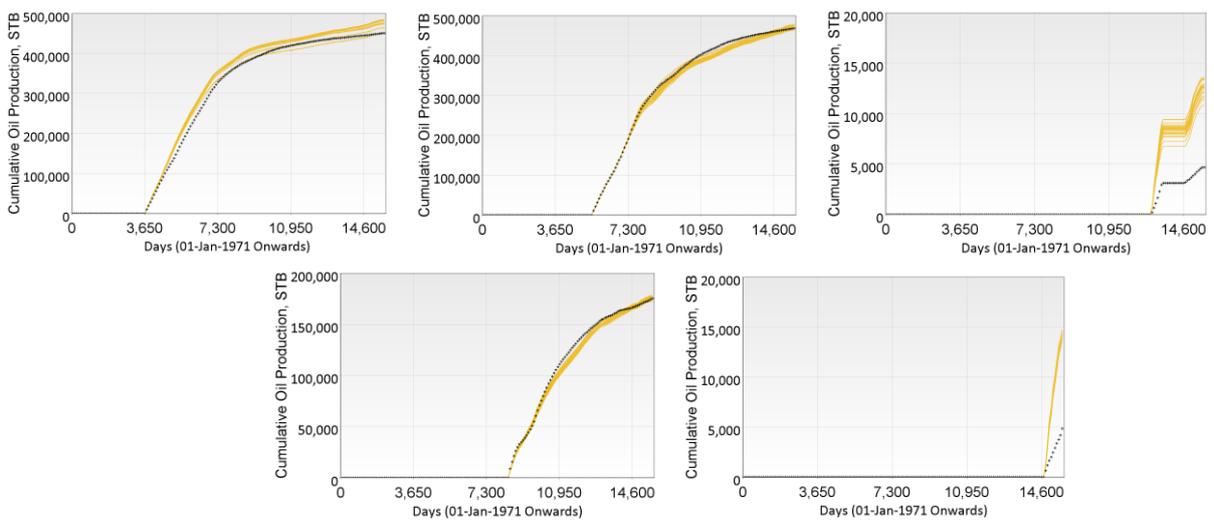
Fig. 16—Cumulative oil production for producers P-1, P-2, P-3, P-4 and P-5, for cases selected to update (posterior) uncertainty parameter ranges after running ES.
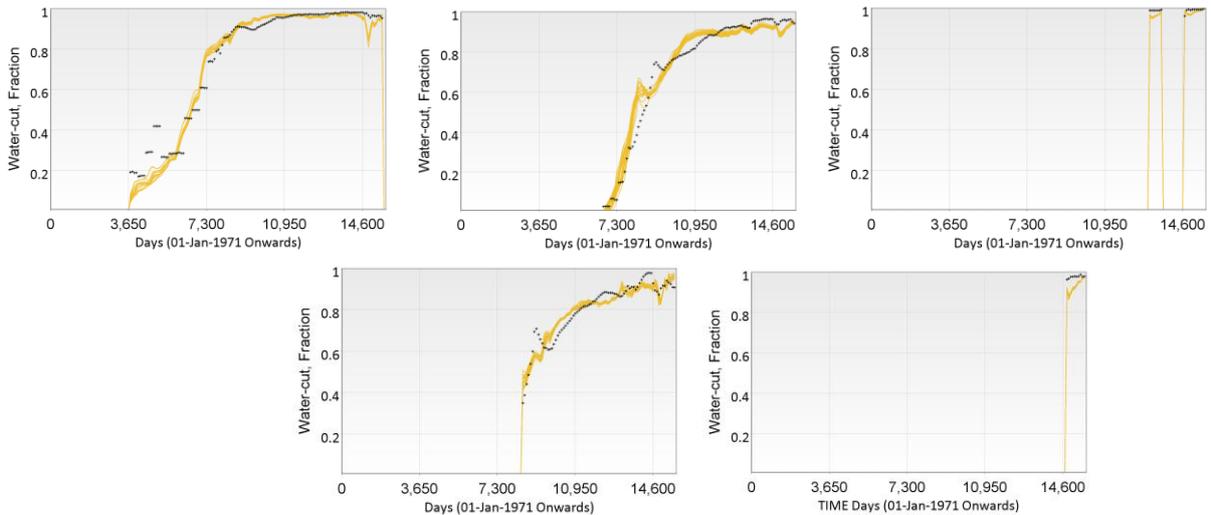
Fig. 17—Water-cut for producers P-1, P-2, P-3, P-4 and P-5, for cases selected to update (posterior) uncertainty parameter ranges after running ES.
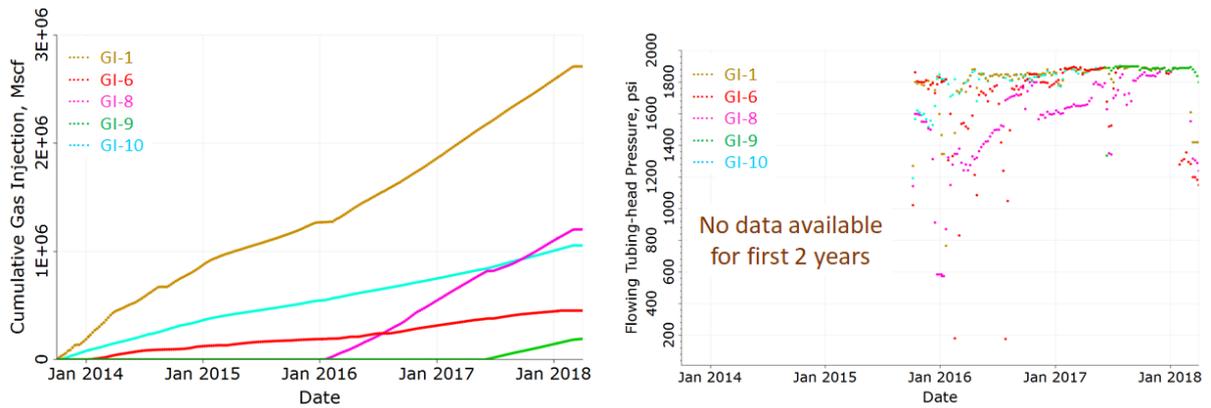
Fig. 18—Historic well performance during CO_2 injection (a) Cumulative CO_2 injection (b) Tubing-head pressure.
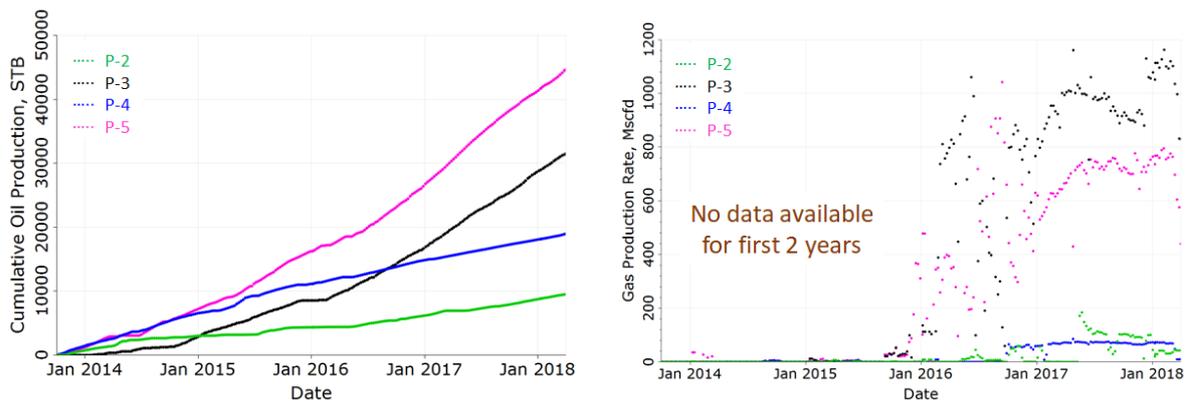
Fig. 19—Historic well performance during CO_2 injection (a) Cumulative oil production (b) Gas production rate.
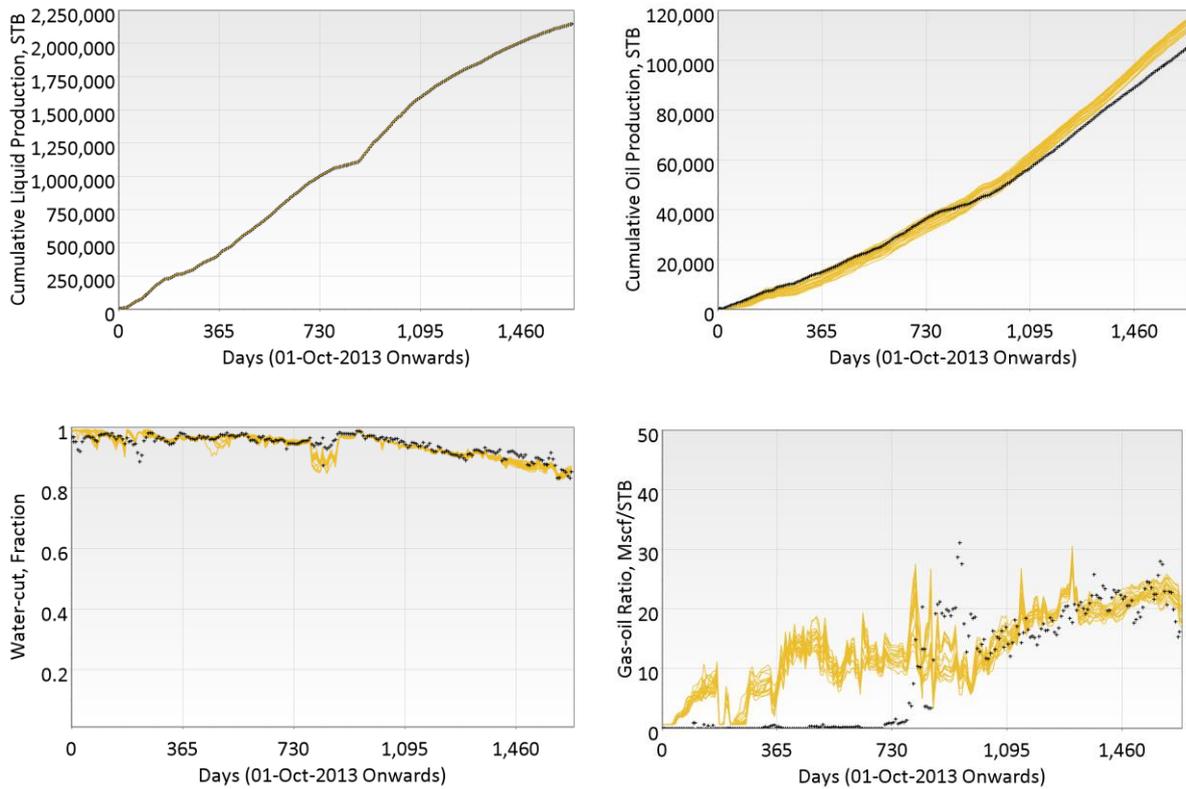
Fig. 20—Simulation results at sector level for cases selected to update (posterior) uncertainty parameter ranges (a) Cumulative liquid production, showing producers do not switch from the assigned liquid rate control (b) Cumulative oil production (c) Water-cut (d) Gas-oil ratio.
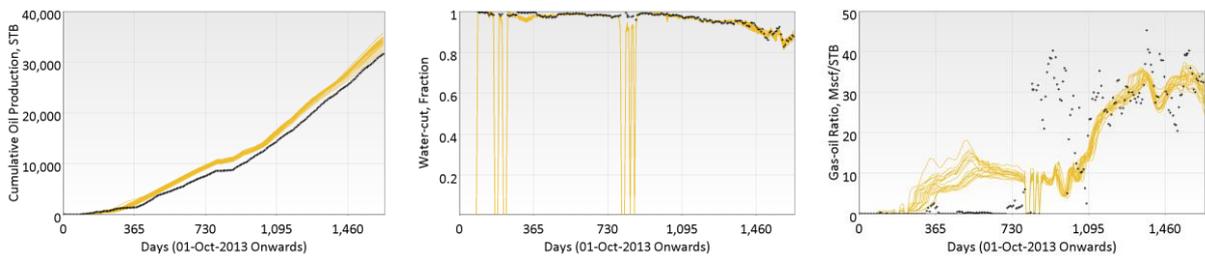
Fig. 21—Simulation results for P-3 for cases selected to update (posterior) uncertainty parameter ranges after running ES (a) Cumulative oil production (b) Water-cut (c) Gas-oil ratio.
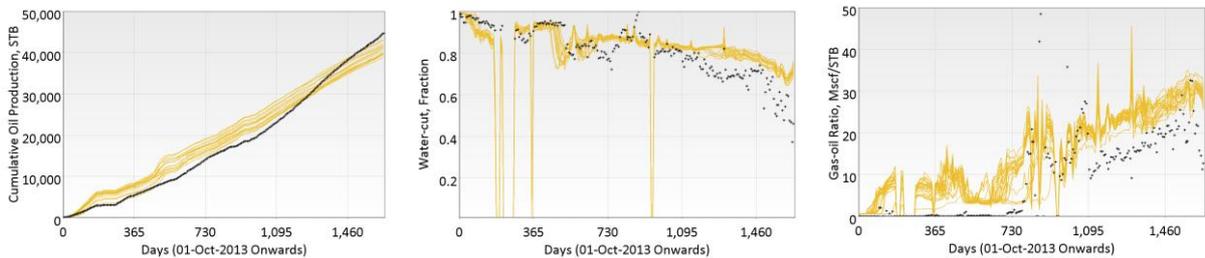
Fig. 22—Simulation results for P-5 for cases selected to update (posterior) uncertainty parameter ranges after running ES (a) Cumulative oil production (b) Water-cut (c) Gas-oil ratio.

Fig. 23—Flowing bottom-hole pressure for GI-1 for cases selected to update posterior uncertainty parameter ranges.

P10	P50	P90
2830	2898	2977
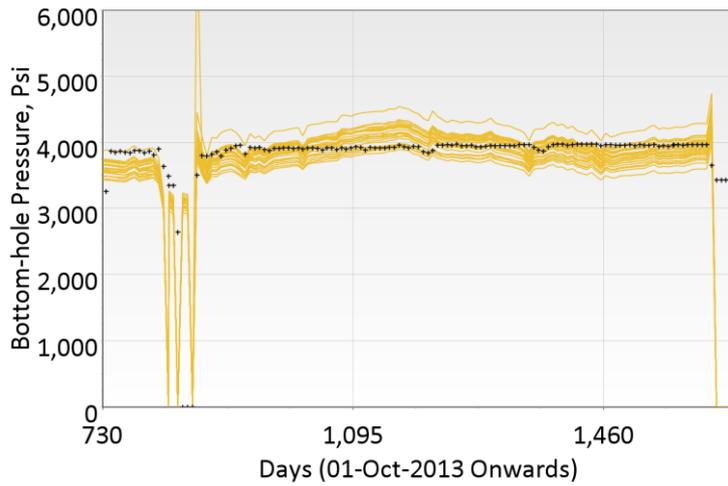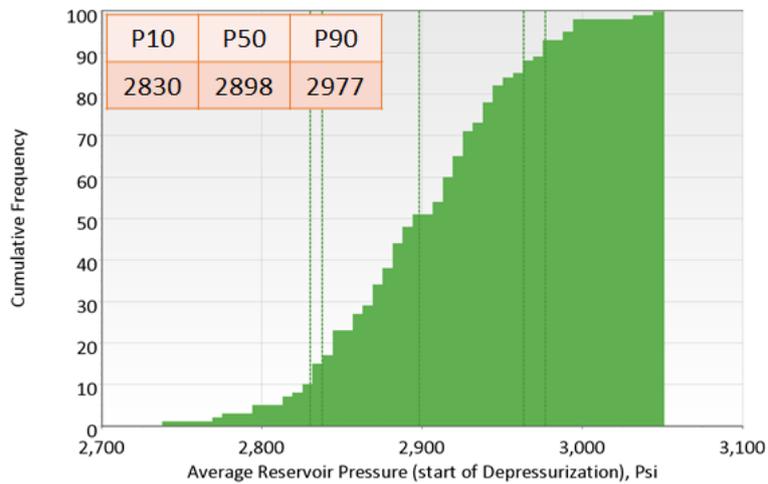
Fig. 24—Cumulative distribution for reservoir pressure at sector level at the start of depressurization (in April 2018) for cases selected to update posterior uncertainty parameter ranges.
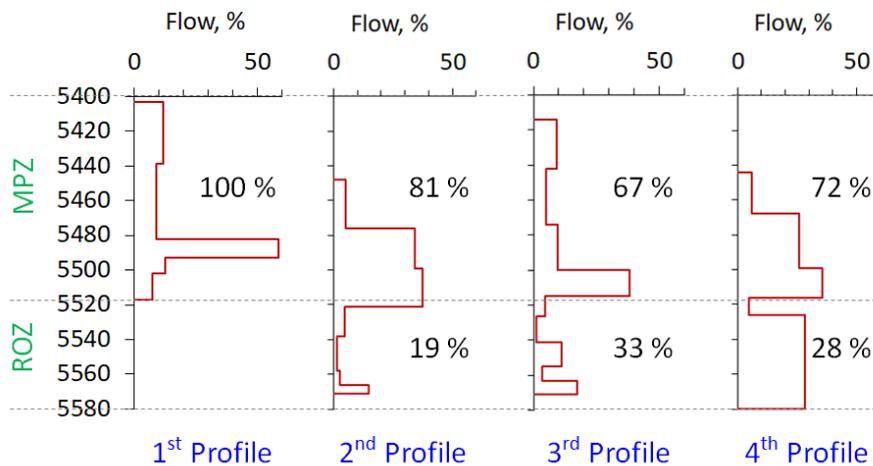
Fig. 25—Historic injection profiles for GI-1 recorded every year since start of CO_2 injection in October 2013, showing fraction of CO_2 entering into MPZ and ROZ.
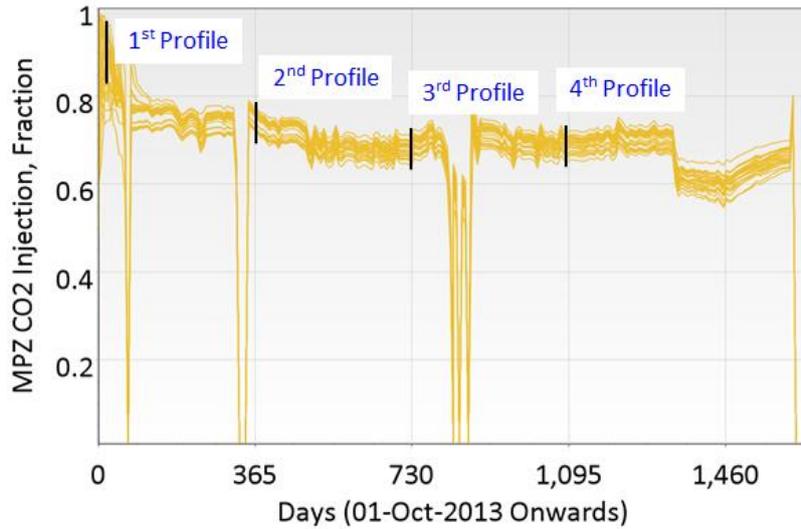
Fig. 26—Fraction of CO_2 injected into GI-1 entering into MPZ for cases selected to update posterior uncertainty parameter ranges after CO_2 injection match.
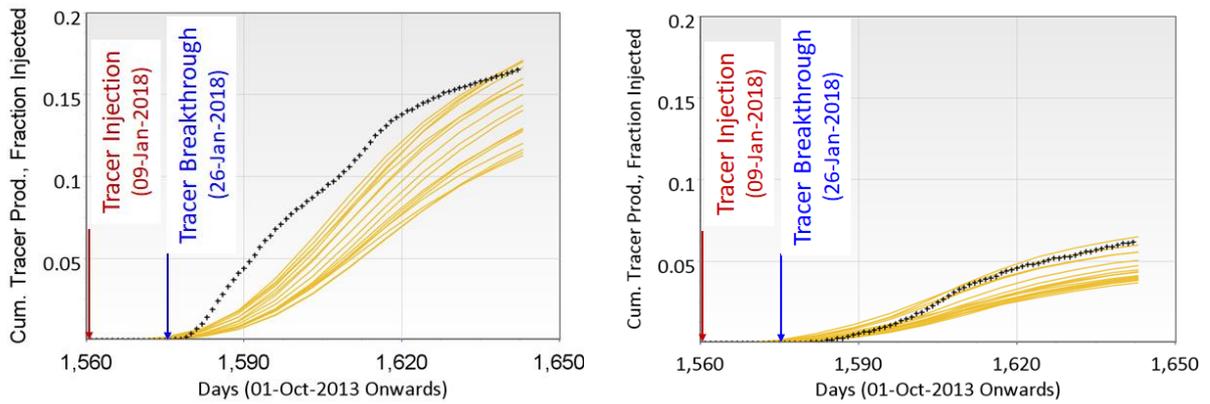
Fig. 27—Cumulative tracer production, as fraction of injected volume, for cases selected to update posterior uncertainty parameter ranges (a) P-3 (b) P-5.
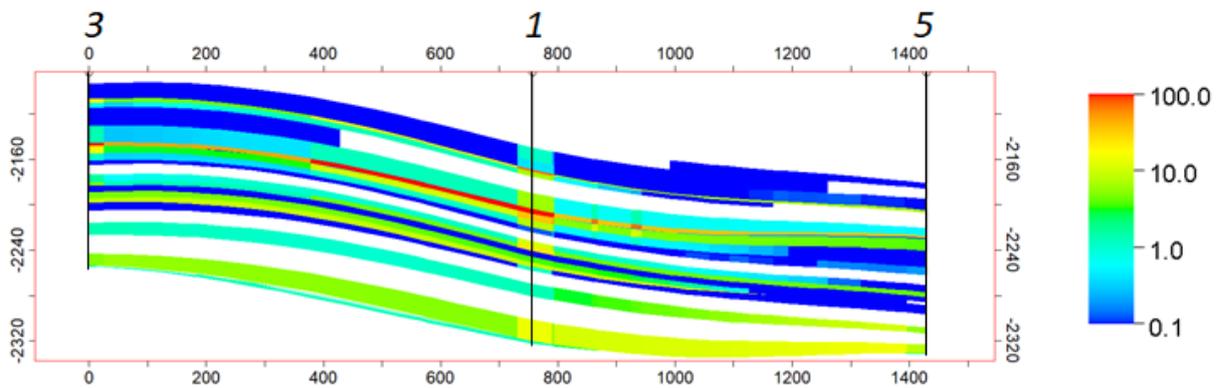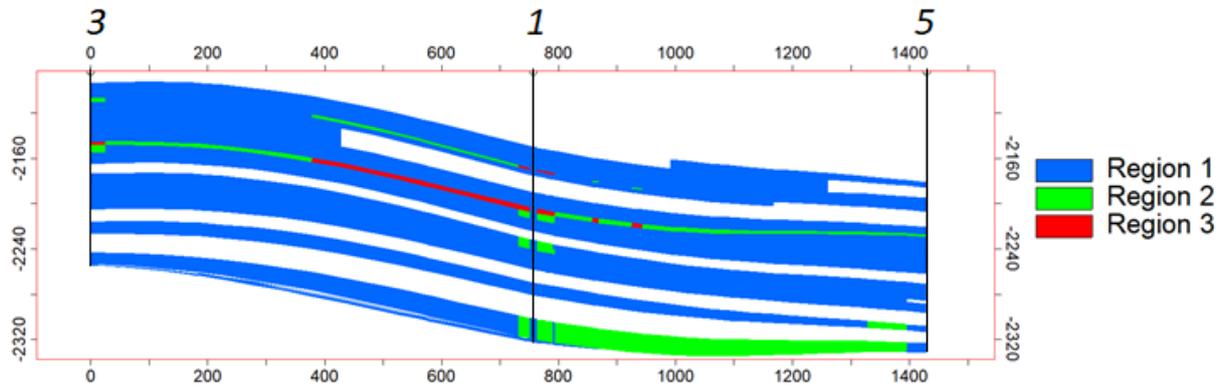
Fig. 28—Cross-section along wells 3, 1 and 5 showing (a) Permeability for a realization after history match (b) Regions identified for that realization based upon permeability. The innermost grid within LGR around well 1 also assigned region 1 irrespective of permeability of cell connecting to that well.
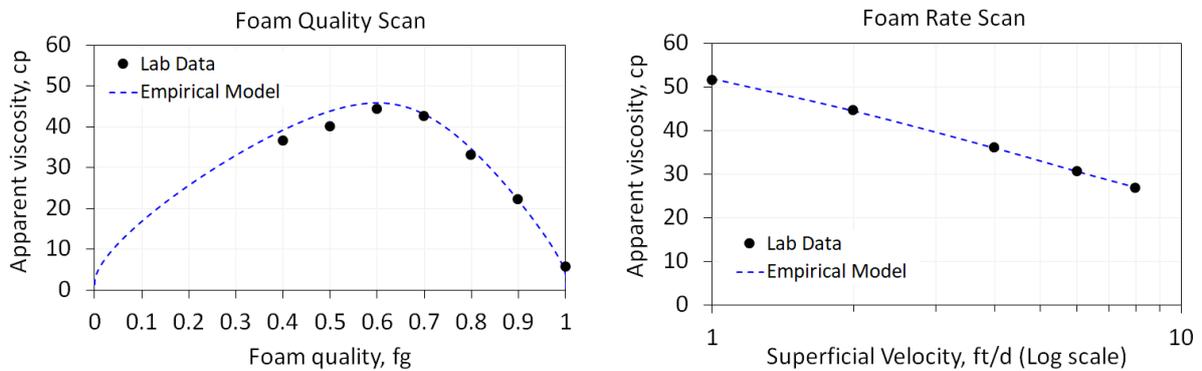
Fig. 29—Experimental data and empirical foam model fit to (a) Quality scan (b) Rate scan.
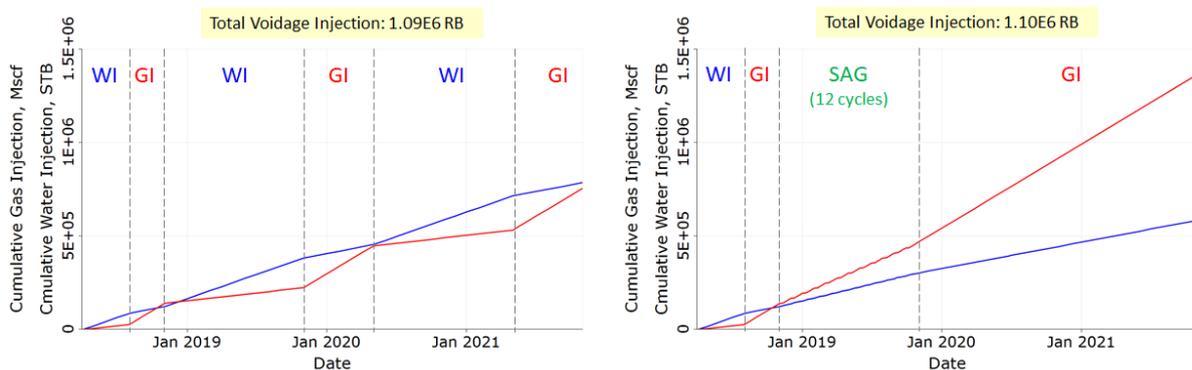
Fig. 30—Injection scheme for (a) Base case scenario with WAG (b) Pilot with 12 SAG cycles followed by CO_2 injection.
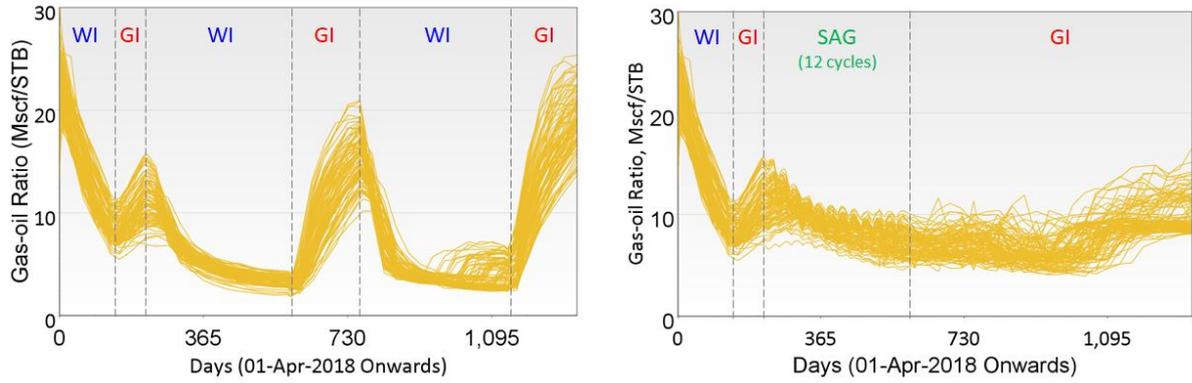
Fig. 31—Gas-oil ratio at the sector level for (a) Base case (b) With SAG.
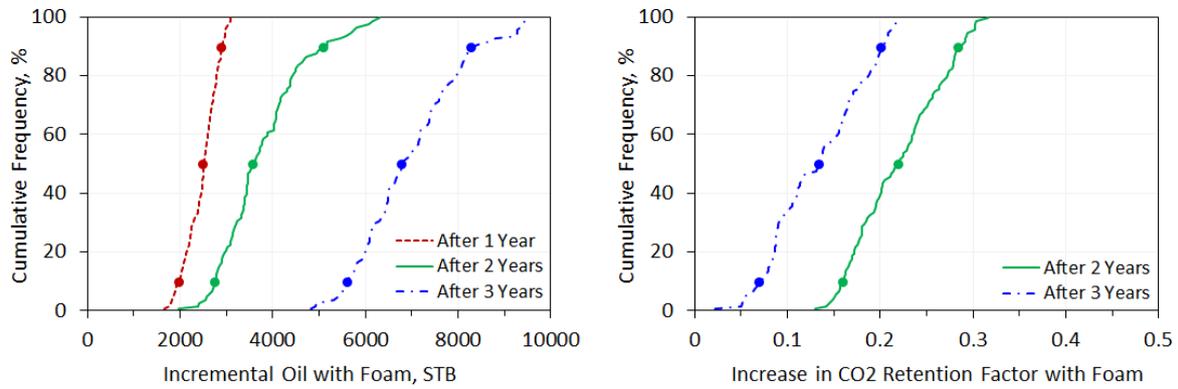
Fig. 32—Cumulative distribution for KPIs (a) Incremental oil (b) Increase in CO_2 retention factor.
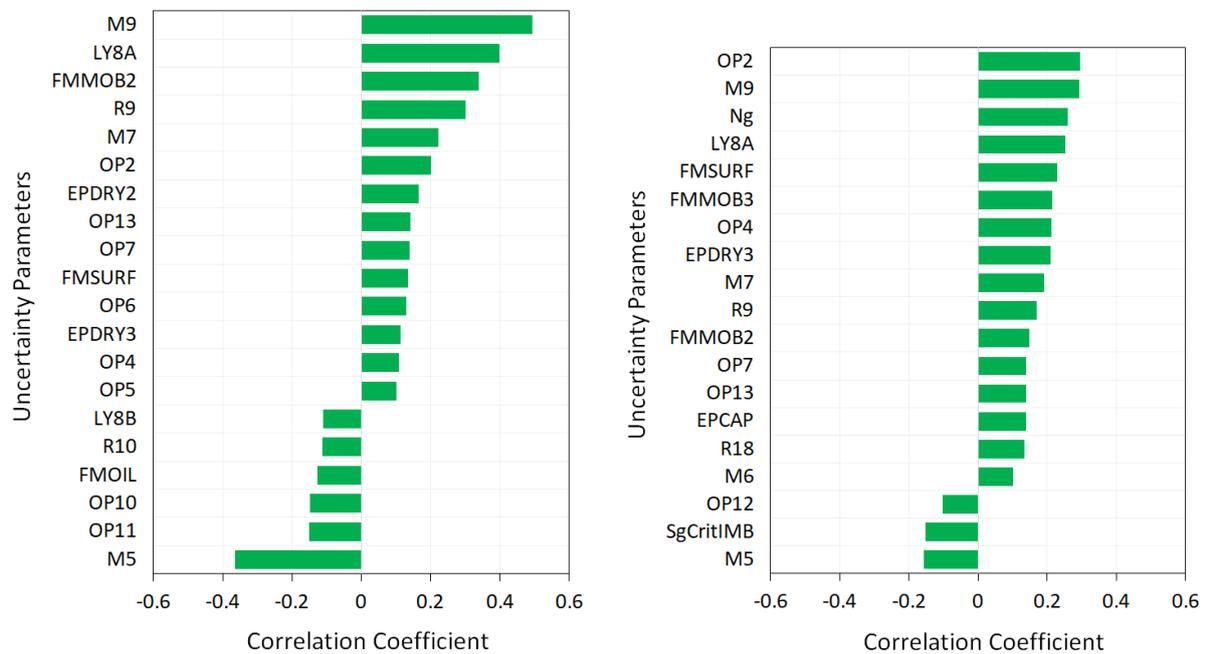
Fig. 33—Pareto plots showing the influence of uncertainty parameters on KPI's after two years of start of pilot (a) Incremental oil (b) Increase in CO_2 retention factor.